THERMAL JOINT CONDUCTANCE OF CONFORMING ROUGH SURFACES: EFFECT OF SURFACE MICRO-HARDNESS VARIATION

by

ADEL ABDEL-HALIM HEGAZY

A thesis
presented to the University of Waterloo
in fulfilment of the
thesis requirement for the degree of
Doctor of Philosophy
in
Mechanical Engineering

Waterloo, Ontario, 1985

© Adel Abdel-Halim Hegazy 1985

I hereby declare that I am the sole author of this thesis.

I authorize the University of Waterloo to lend this thesis to other institutions or individuals for the purpose of scholarly research.

. Adel Hegazy

I further authorize the University of Waterloo to reproduce this thesis by photocopying or by other means, in total or in part, at the request of other institutions or individuals for the purpose of scholarly research.

. Adel Hegazy

The University of Waterloo requires the signatures of all persons using or photocopying this thesis. Please sign below, and give address and date.

ABSTRACT

This work dealt with the problem of predicting contact, gap and joint conductances between conforming rough surfaces. The main purpose of the work was to investigate the effect of surface micro-hardness variation upon the prediction of thermal interface conductances under the first load cycle. A survey of the literature revealed that the title problem has received very little attention in the past three decades, especially from the thermal viewpoint. An investigation of surface micro-hardness variation was carried out. The investigation revealed that most engineering surfaces exhibit micro-hardness variation which depends upon the material type and the machining process. These findings were confirmed by a series of Vickers micro-hardness measurements for several engineering materials. A semi-general micro-hardness variation for these materials has been proposed which should be useful to thermal analysts.

The theoretical thermal conductance models used in this work are those of Yovanovich and his co-workers. These models were reviewed and a mechanical model was proposed to estimate the appropriate contact hardness value required for accurate thermal predictions. The mechanical model was applicable for practical engineering joints and is a function of the surface parameters and the micro-

hardness variation of a particular joint.

An extensive experimental program was carried out employing different materials to verify the theoretical models over a broad range of surface roughnesses, thermophysical properties, micro-hardness variations and contact pressures. More than 400 contact conductance data points for Nickel 200, Stainless Steel 304, Zircolay-4 and Zirconium-2.5wt%Nb joints confirmed the validity the mechanical and contact conductance models. Also, experimental data for stainless steel joints in Nitrogen and Helium environments were obtained. The agreement between the measured and predicted joint conductances was excellent for Nitrogen data but seemed to break down for Helium. The deviations between some of the experimental data and the theoretical predictions were discussed. The discussion has emphasized the importance of the joints' geometric and thermophysical parameters which affected the predictions in vacuum or gaseous environments.

The present work explained the apparent contradictory results obtained by various investigators for similar materials. It showed also that accurate thermal predictions depended more than had been realized upon the appropriate micro-hardness value which must be determined from the micro-hardness variation. The present work confirmed the validity of the investigated models.

ACKNOWLEDGEMENTS

The author wishes to express his gratitude and appreciation to Dr. M.M. Yovanovich for his guidance and encouragement during the course of this investigation. The author also wishes to thank Dr. M.H. Schankula for his kind cooperation and support of this research

The author also thanks Mr. R. Kaptein for his technical assistance and Mr. A. Hodgson for fabrication of the experimental apparatus components.

Thanks must be expressed to Messrs. A. Key and D. Raude of the Engineering Machine Shop for their care and patience in the fabrication of the test specimens.

Thanks are also due to Messrs. M. Reenen, D. Struthers and P. Renkema for their technical assistance with the electronic equipments.

The author is grateful to his colleague Mr. Chris Lane for reviewing the manuscript.

Finally, the author expresses his thanks to his wife for her patience and encouragement, and to his parents for their moral support and encouragement.

Sincere appreciation is expressed to the Atomic Energy of Canada-Whiteshell Nuclear Research Establishment for their financial support which made this work possible.

TABLE OF CONTENTS

Table of Contents (continued...)

Table of Contents (continued...)

Table of Contents (continued...)

LIST OF TABLES

List of Tables (continued...)

List of Tables (continued...)

List of Tables (continued...)

List of Tables (continued...)

List of Tables (continued...)

LIST OF ILLUSTRATION

List of Illustrations (continued...)

List of Illustrations (continued...)

List of Illustrations (continued...)

NOMENCLATURE

A_a	apparent contact area
A_g	projected gap area
A_r	real contact area
a, a_i	mean and individual contact spot radius
a_c	contact radius
b, b_i	mean and individual flux tube radius
b_t	roughness parameter, $b_t = 2(CLA_1 + CLA_2)$
C_c	dimensionless contact conductance, $C_c = \sigma h_c/(mk_s)$
C_g	dimensionless gap conductance, $C_g = \sigma h_g/(mk_s)$
C_g^*	dimensionless gap conductance, $G_g^* = (b_t/\sigma)(\sigma h_g/k_g)$
C_j	dimensionless joint conductance, $C_j = \sigma h_j/(mk_s)$
CLA_1, CLA_2	arithmetic mean roughness heights from the surface mean line of surface 1 and surface 2, respectively
c_1, c_2	constants
d	indentation diagonal
d_v, $\bar{d}_v$	Vickers indentation diagonal and the average value
E_1, E_2	emissivity for surface 1 and surface 2, respectively
g_1, g_2	temperature jump distance for surface 1 and surface 2, respectively
H	micro-hardness
H_c, H_m	contact hardness and macro-hardness
H_v, $\bar{H}_v$	Vickers micro-hardness and the average value

Nomenclature (continued...)

h_c	contact conductance, $h_c = 1/(R_g A_a)$
h_g	gap conductance, $h_g = 1/(R_g A_a)$
h_j	joint conductance, $h_j = 1/(R_j A_a)$
h_r	radiation conductance, $h_r = 1/(R_r A_a)$
K	thermal conductivity ratio, $K = k_g/k_s$
K_n	Knudsen number
k_1, k_2	thermal conductivity of surface 1 and surface 2, respectively
k_g	gas conductivity
k_s	harmonic mean thermal conductivity, $k_s = 2k_1k_2/(k_1 + k_2)$
L	load
M	effective temperature jump distance, $M = g_1 + g_2 = \alpha\beta\Lambda$
MRH_1, MRH_2	height of the highest peaks from the surface mean line of surface 1 and surface 2, respectively
m	effective surface mean absolute slope, $m = \sqrt{m_1^2 + m_2^2}$
m_1, m_2	surface mean absolute slope of surface 1 and surface 2, respectively
N	number of contact spots
n	contact spot density, $n = N/A_a$
P	contact pressure
P_g, P_{go}	gas pressure and gas pressure at reference conditions
Pr	Prandtl number, $Pr = \mu c_p/k_g$
Q	heat flow rate
q	heat flux

Nomenclature (continued...)

R_c	contact resistance
R_g	gap resistance
R_j	joint resistance
R_r	radiation resistance
r	radius
S_u, S_y	ultimate and yield tensile stresses
T, T_o	gas temperature and gas temperature at reference conditions
T_m	joint mean temperature, $T_m = (T_1 + T_2)/2$
T_1, T_2	temperature of the contacting surfaces evaluated by extrapolating the temperature gradients in the solids to the interface
t, t_e	local and effective gap thicknesses
X	gas parameter, $X = b_t/M$
x	dimensionless parameter, $x = Y/(\sqrt{2}\sigma)$
Y	separation between the mean planes of the contacting surfaces
YH	gap-temperature jump parameter, $YH = (Y/\sigma)/(M/\sigma)$
y	surface height variable
α	accommodation parameter
α_1, α_2	accommodation coefficients for surfaces 1 and 2, respectively
β	gas parameter, $\beta = (2\gamma/\gamma + 1)/Pr$
γ	ratio of specific heats, $\gamma = C_p/C_v$
Δ	change in accompanying variable

Nomenclature (continued...)

ζ	constant
η	constant, $\eta = -0.26$
Λ, Λ_o	molecular mean free path and molecular mean free path at reference conditions
ρ	mean asperity tip radius
σ	effective surface RMS roughness, $\sigma = \sqrt{\sigma_1^2 + \sigma_2^2}$
ϕ	probability function
ψ, ψ_i	mean and individual contact spot constriction parameters

Subscripts

mn	minimum
mx	maximum

CHAPTER 1

INTRODUCTION

1.1 Definition of Joint Conductance

When two conforming rough surfaces are brought in contact under load in a gaseous environment, the heat transfer between them is impeded by the interface resistance. This results in a temperature drop across the interface for a given heat flow through the interface. The thermal resistance caused by the interface is called the thermal joint resistance, R_j, and is defined as follows:

$$R_j = \Delta T / Q \tag{1.1}$$

where Q is the steady-state heat flow normal to the interface. The temperature drop ΔT is obtained by extrapolating to the interface the steady-state temperature profiles far from each side of the interface.

The thermal joint conductance, h_j, is defined as the reciprocal of the product of the thermal joint resistance and the apparent area and is given by:

$$h_j = 1 / R_j A_a \tag{1.2}$$

where A_a is the apparent area of contact.

In general, there are three principle contributions to the heat flow across the interface, Figure 1.1:

a - conduction through the micro-contact spots

b - conduction through the gaseous fluid

c - thermal radiation across the gaps.

The contact resistance R_c, the resistance due to the gaseous fluid present in the gaps R_g, and the radiation resistance R_r are assumed to be thermally connected in parallel, Figure 1.2, and the joint resistance can be expressed approximately by:

$$\frac{1}{R_j} = \frac{1}{R_c} + \frac{1}{R_g} + \frac{1}{R_r} \tag{1.3}$$

and in terms of the thermal conductances as:

$$h_j = h_c + h_g + h_r \tag{1.4}$$

Thus, the problem of determining the thermal joint conductance reduces to separate estimations of its components. If the last two components of heat transfer are absent, i.e., the contact occurs in vacuum with negligible radiation, then the joint conductance is called the contact conductance.

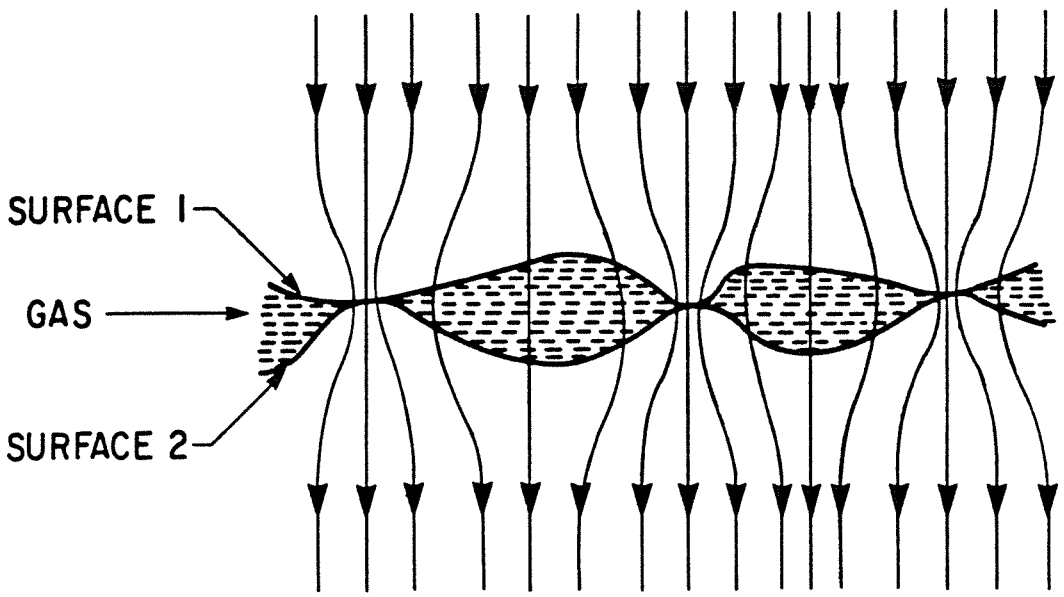

Figure 1.1: Heat Flow Across Contacting Rough Surfaces

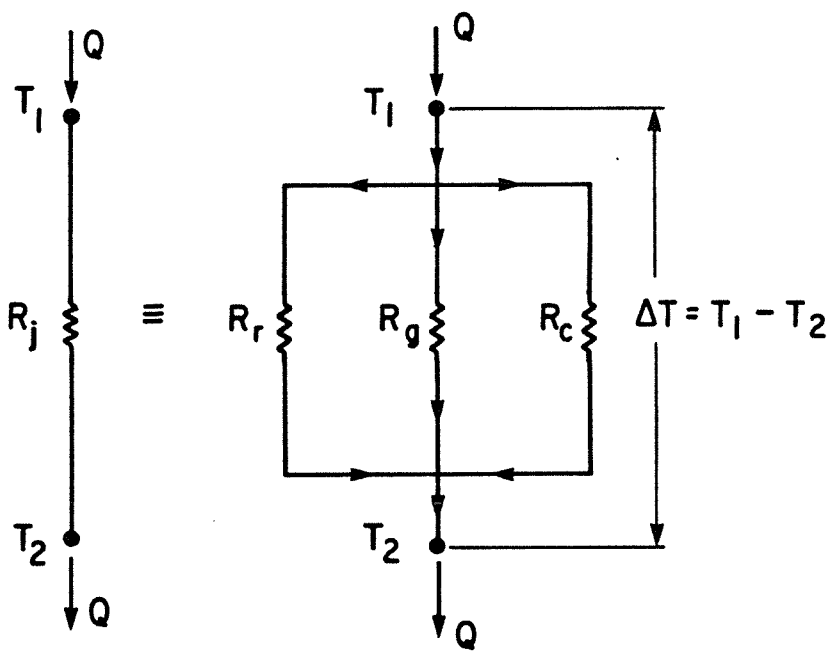

Figure 1.2: Thermal Resistance Circuit of Contacting Rough Surfaces

1.2 Literature Review

The problem of predicting contact and gap conductances has been the subject of numerous research studies during the past three decades, which indicates the degree of importance attached to this subject. This is quite natural, if one considers the special need for more reliable equipment in aerospace, nuclear reactors and the electronics industry, as well as in many other heat transfer systems.

Several comprehensive reviews on the research topic are available [1-9]. The theoretical base of the subject is fairly well established and significant progress has been made in our understanding and ability to predict the thermal conductances [10-22]. The experimental studies have yielded valuable data which provide insights into the complexity of the problem and, in turn, led many investigators to develop simplified models or correlations for predicting contact and gap conductances [11,14,16,17,20,30-31]. However, a striking feature of the published models and experimental results of several investigators has been the very wide discrepancies of these results using nominally similar materials. Also, each of the simplified models that has been advanced generally can be applied only to the experimental results of the investigator.

Although the literature on the subject now amounts to several hundred papers, only a relatively small fraction of the material deals with the influence of surface hardness variation upon the prediction of thermal conductances. Boeschoten and Ven der Held [32], in one of the earlier experimental and analytical studies on thermal joint conductance between aluminum and other metals, reported that the micro-hardness measurements of aluminum rods gave a value seven times larger than the hardness value found in the literature. They attributed this to the drawing of the rods. In their analysis they used the larger value.

Laming [33] considered the effect of hardness variation in his thermal model. From his conductance measurements, and following Mott's [34] analysis, he was able to determine the form of the hardness variation for his specimens. He claimed that the hardness value is very important in correlating thermal conductance data.

Henry [15] made micro-hardness measurements on lapped stainless steel type 416 specimens using Vickers and Knoop micro-hardness testers. Henry concluded that a considerable scatter is indicated, but a definite trend is observed, i.e., the micro-hardness decreases with increasing indentation size. In his model, a micro-hardness value corresponding to an indentation area equal to the average contact size observed during his experiments was employed.

Clausing and Chao [16] measured micro-hardness variations in several metal alloys, such as magnesium, brass, aluminum, and stainless steel, which were used in their experimental program. They reported these hardness values but did not attempt to incorporate them in their model. However, they recommended using the micro-hardness value in microscopic contact area calculations.

Shlykov and Ganin [23] developed a model for predicting thermal conductances between two rough surfaces. In their study, they pointed out that the effect of work-hardening due to machining processes should be taken into consideration by increasing the macro-hardness value. They did not, however, present any analysis or method to show how this effect might be incorporated in their model.

Tsukizoe and Hiskado [51-54] investigated theoretically and experimentally the mechanism of contact between nominally flat rough surfaces and developed a model for predicting thermal joint resistance across such contacts. A number of materials such as aluminum, copper and low carbon steel were employed in their experimental studies. For these metals, they observed a considerable amount of work-hardening on the surface of the test specimens after finishing. To account for this effect they used different Vickers micro-hardness values: measured under 0.098N load [53], 0.245N load [52], and the mean of two values obtained using 0.098N and 0.98N indenter load, for the same material. They gave no explanation at all for choosing these values.

One of the first published studies dealing directly with the effect of micro-hardness variation upon the prediction of thermal conductances was performed by Yovanovich, Hegazy and DeVaal [35]. They proposed four models to handle the effect of micro-hardness variation. These models use contact, gap, and joint conductance correlations developed by Yovanovich [31]. They concluded that the conventional mechanical model (assuming a uniform hardness equal to the bulk value) yields the upper bound on the conductances. Also, they showed that the bulk hardness model [31], with the appropriate micro-hardness value, predicts contact conductance in good agreement with some limited experimental results.

Schankula, Patterson and Yovanovich [36] performed a theoretical and experimental investigation into the effect of oxide films on the thermal resistance bewteen contacting Zircaloy surfaces. In their analysis they considered the effect of surface micro-hardness variation observed in Ref.[35]. Using one of the models suggested in this reference, very good agreement between the experiments and the theoretical predictions was observed for non-oxidized Zircaloy surfaces.

Yovanovich, Hegazy and Antonetti [37] verified the contact conductance models proposed in Ref.[35] using experimental data for Nickel 200 contacts. The experimental data covered a wide range of

geometric characteristics but a limited range of contact pressure. This study showed that the bulk hardness model predictions exceeded the experimental measurements by approximately 55 to 96 percent depending upon the specimen's surface parameters. It was recommended that the simple Direct Approximate Model (DAM), which employs information about the specimen's micro-hardness, surface parameters, and mean contact pressure, should be used to predict contact conductance for conforming, rough surfaces.

Yovanovich and Hegazy [38] presented 45 experimental contact conductance data points for Nickel 200, Stainless Steel 304, and Zircaloy conforming rough surfaces [36,37] obtained by three groups of researchers in two countries employing nominally similar test equipments and procedures. When the experimental data are nondimensionalized and plotted against the contact pressure which is also normalized with respect to the Effective Surface Micro-Hardness (ESMH), excellent agreement between the theoretical predictions and the experiments was observed. They concluded that the contact conductance correlation of Yovanovich [31], in conjuntion with the DAM of determining the ESMH, is an accurate, universal contact conductance correlation for conforming, rough surfaces.

1.3 Problem Statement

At present in the thermal literature, many investigators have reported attempts to correlate the thermal conductance data. Most of those correlations are inadequate for realistic thermal conductance predictions. One obvious reason is the difficulty to specify correctly the micro-hardness values that exist in engineering surfaces. This difficulty is often circumvented by going to well-defined micro-hardness values, i.e., experimental measurements. However, even for this simplified method the majority of thermal researchers have failed to predict accurately all the important micro-hardness variation because of the shortcomings in the assumed models. In addition, the existing models do not recognize and, in turn, do not adequately describe the influence of micro-hardness variation on the prediction of thermal conductances. It is believed that the failure of these investigators to realize the presence and importance of micro-hardness variation gives their models limited value.

While a large amount of literature exists on the general topic of thermal conductance, there is very little information to clarify the effect of hardness variation on the prediciton of thermal conductances. In addition, the relatively small amount of experimental data which is reported in some detail in a number of studies on interfaces in vacuum or gaseous environments, does not show any promise for successful use. Unfortunately, most of this data does

not include information on surface parameters or hardness variation and often the test details are incomplete. Also, in many cases the experimental program was carried out over a narrow range of surface parameters and contact pressures as well as for one or two different materials. It is not possible to use such incomplete information in developing or verifying a model dealing with the problem at hand.

Thus, the objectives of the present work are:

1. To investigate experimentally the micro-hardness variation of selected engineering materials and derive a general expression for the resultant data which will be suitable for thermal analysts.

2. To develop a mechanical model for predicting the contact micro-hardness of a machined surface incorporating the micro-hardness variation and the surface parameters (σ,m).

3. To modify the theoretical thermal conductance models proposed in Refs.[31,38,55] to include the effect of micro-hardness variation.

4. To verify experimentally the mechanical and thermal conductance models in different environments over a wide range of surface parameters, hardness variations and contact pressures for these selected materials.

5. To compare the experimental results with the theoretical predictions as well as with the available models in the literature.

Chapter 2 deals with the hardness investigation and consists of two parts. The first part includes a brief discussion of the micro-hardness load dependence and the contradictions found in the thermal literature with respect to hardness. The second part contains correlations for the micro-hardness variations of selected materials and a semi-general expression for these variations. Other empirical evidence is given to support this view.

The theoretical analysis of the problem, including the mechanical model for determining the appropriate contact hardness for thermal predictions, is presented in Chapter 3. Also, the thermal conductance models of Yovanovich et al [31,55] are reviewed.

Chapter 4 presents a description of the experimental apparatus and test procedure. Emphasis is placed on specimen preparation and the estimation of surface parameters. The comparison between the experimentally measured and theoretically predicted thermal conductances is presented in Chapter 5. Chapter 6 is devoted to a comparison between the present thermal models and the available models in the literature.

The conclusions drawn from this work, as well as the recommendations for future work, are given in Chapter 7.

CHAPTER 2

HARDNESS INVESTIGATION

2.1 Introduction

The hardness quality of materials is an important property from the standpoint of contact phenomena such as the formation of contact area, friction and wear. However, hardness as a term has a different meaning to different researchers and, therefore, different definitions and measurement methods exist. Hardness definitions and tests are adequately presented in various standard textbooks [34,39-41] on hardness and metallography which should be consulted for full details. The wide variety of hardness tests has been classified into groups the most common of which is the static indentation group. Static indentation tests have the advantage of providing a very simple non-destructive means for assessing the resistance of material to plastic deformation. For this reason they are used extensively in contact problem investigations.

In a static indentation test, a steady load is applied to an indenter which may be a ball, cone or pyramid and the hardness is calculated from the area or depth of indentation produced. Depending upon the type of test, the applied load may range from thirty kilonewtons down to 0.05 newtons. For more details the reader is referred to Appendix A. This wide load range and its

effect on indentation size has led many investigators to suggest three ranges of load. According to O'Neill [40], the most widely accepted suggestion was put forward in 1952 by Bückle who reviewed it later [42]. From Bückle's study [42], the following three load ranges can be distinguished:

1. "Micro-hardness" ..... 0.05N - 2.0N

2. "Low-load hardness" ..... 2N - 30N

3. "Macro-hardness" ..... > 30N

As pointed out by Bückle [42], the first two load regions sometimes overlap because their limits depend, not only on load, but also on the material being tested.

Micro-hardness and low-load hardness tests are often carried out with a Vickers indenter, which is a square-based diamond pyramid having an apex angle of 136°. In general, it is agreed that the macro-hardness value is independent of load; but for laods less than 10N it is observed that the hardness value increases with decreasing load. The subject has been extensively reviewed by Mott [34] and others [42]. Since the indentations produced by the Vickers indenter are geometrically similar for all sizes, the variation in hardness values with load must be real, which has been confirmed by numerous investigations. Several possible suggestions have been put forward

to explain this phenomenon. Mott [34] suggested that the slip mechanism for small indentations is different from that for large ones. Bowden and Tabor [43] attributed this phenomenon to the work-hardening of the testing surfaces during mechanical preparation. This suggestion is in line with Mott's results and those of others. In a very recent study, Pethica et al [44] attributed this increase in micro-hardness to a real increase in the plastic yield stress of the metal near the free surface as a result of a local extreme work-hardening. Another possible suggestion, due to Gane and Cox [45], is that this increase in micro-hardness is caused by some surface strengthening mechanism, either by absorbed surface films interfering with dislocation movement, or by the diffusion of some impurity from the bulk. Generally, the increase in micro-hardness with smaller loads and, therefore, smaller indentation size, has been called by Shaw [46] and others [42,44,45] the "Size Effect".

A search of the literature shows that the study of the contact area of a single asperity is fundamental to the development of any model for predicting thermal joint conductance, especially the contact conductance. In other words, the models require knowledge of the plastic flow pressure of the softer of the contacting surfaces to calculate the contact area of a single asperity. It is generally recognized and understood that the plastic flow pressure of the softer surface can be related to the pressure under the indenter in a static

indentation test. However, the approximate nature of these models has led the majority of the investigators to assign the macro-hardness value to the plastic flow pressure, disregarding the size effect. A few authors [14,16,17,20-22] have recognized the importance of the size effect and stated clearly that the micro-hardness must be employed in their models, although they have not said which micro-hardness test or what load conditions should be used. This is obviously due to the shortcomings in the proposed models. However, an example exists in the work of Tsukizoe and Kisakado [51,54]. They reported both the load and the micro-hardness test used (Vickers), but assigned different micro-hardness values for the same material without any reasonable explanation. Generally, this confusion about the hardness has resulted in serious discrepancies between the proposed models and the thermal results of nominally similar materials.

A number of researchres [23,25,29,47,84] have assumed a fixed contact size in the range of 30 μm to 40 μm, though they used the macro-hardness as an equivalent to the plastic flow pressure for this size. Henry [15], however, used a micro-hardness value corresponding to an indentation area equal to the average contact size observed during his experimental work. The observed contact size in his study was approximately 14 μm.

The previous discussion has brought to light a very important point which has been ignored over the past three decades. If the

measured or assumed contact size is, in general, less than 40 μm, then the macro-hardness which is determined from large indentations of the order of 1 mm is totally inadequate and emphasis must be placed on the determination of the appropriate value. This is in line with Greenwood [48] who stated, "For the present discussion the origin of this extra hardness, whether due to an abnormal state of work-hardening, or to frictional restraint, or to a strengthening effect due to a surface film blocking the movement of dislocations, is irrelevant: the important thing is that the use of the bulk hardness is wrong, and quite badly so.". This micro-hardness variation, due to size effect for whatever reasons, does not permit us to neglect its influence upon the determination of the suitable micro-hardness value for thermal predictions. It is the purpose of this chapter to investigate the behaviour of micro-hardness variation in a number of materials which will be used in the thermal investigation. The measured micro-hardness variations will be employed to estimate the appropriate micro-hardness values for the thermal predictions.

2.2 Hardness Measurements

In order to investigate the effect of hardness variation upon the prediction of thermal joint conductance, four different materials with very different properties (Nickel 200, Stainless Steel 304,

Zr-2.5wt%Nb and Zircolay-4) were investigated.† They were selected for their popularity in spacecraft applications, the electronics industry and in nuclear reactor technology. The tested surfaces were prepared on the faces of 25 mm long, 25 mm diameter cylinders. These cylinders were fabricated from commercial bars and prepared using the same machining processes. Each specimen was first turned to the required dimensions, then the two flat surfaces were ground and finally lapped. After the lapping process, the specimens were mechanically polished to a good metallographic finish.

Hardness measurements were made on the cylinder's flat surfaces at room temperature. First, on one of the flat surfaces, Vickers micro-hardness measurements were made using a Leitz Durimet bench type micro-hardness tester with different indenter loads. Typical load values were: 0.147, 0.245, 0.98, 1.96, 2.94 and 4.91 N. Five indentation tests were randomly performed in different locations to reflect any hardness variation, if present, over the surface, i.e., a softer area. It is assumed that by taking five indentations under each load, the average value should be reasonably representative of the micro-hardness behaviour of that surface. On the other flat

---

† At the beginning of this research, the Zirconium specimens were supplied by Whiteshell Nuclear Research Establishment - AECL, while the Ni200 specimen was supplied by V. Antonetti (IBM Corp.) who was investigating the use of metallic coatings to enhance thermal contact conductance.

surface, the macro-hardness values were determined using Brinell and Rockwell standard testers.† Both testers were employed to produce two indentations using the Brinell indenter and three indentations by means of the Rockwell indenter.

Figure 2.1 shows the semi-logarithmic plots of the average hardness values versus the indentation depths. The depth of indentation was employed for presentation convenience. These curves consist of two parts. One corresponds to the macro-hardness, Rockwell and Brinell, where there is no variation in the measured hardness values. The second part represents the Vickers micro-hardness variations. Here the micro-hardness increases with decreasing indentation depth or alternatively with decreasing indentation size; for the Vickers indenter $d_v/t = 7$. It is clear that as the indentation depth (size) increases the micro-hardness values gradually approach those values obtained from the macro- hardness measurements. Furthermore, as the macro-hardness values of these materials increase the amount of micro-hardness variation decreases.

For determining the relation between Vickers micro-hardness and the indentation size, the micro-hardness measurements, H_v, were

---

† Brinell Test: 10 mm diameter steel ball with 29.43kN load.
Rockwell Test: 1.59 mm diameter steel ball with 981N load (Rockwell B).

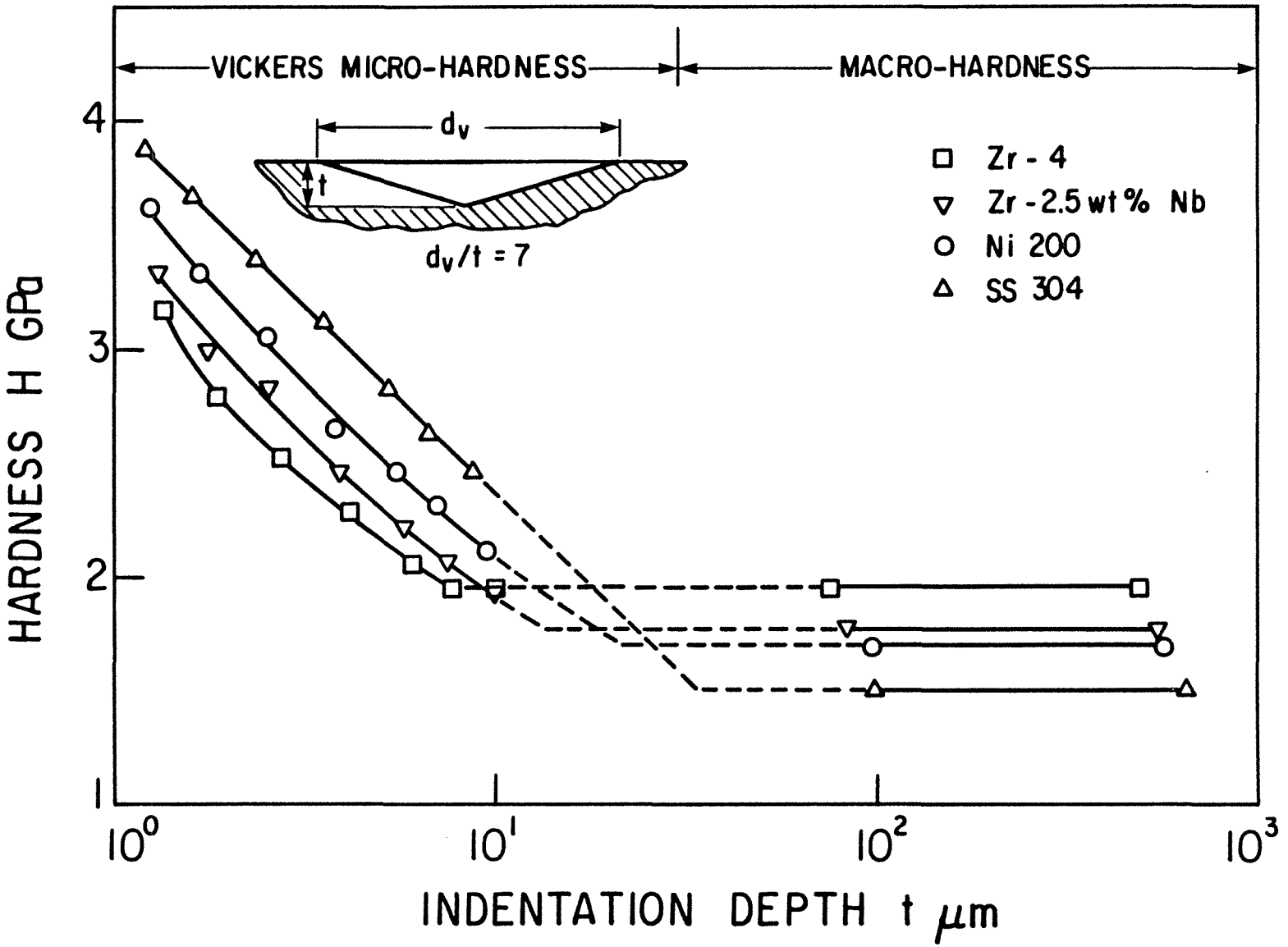

Figure 2.1: Hardness Measurements of Different Materials

plotted as a function of the indentation diagonal, d_v, on a log-log scale as shown in Figure 2.2. It was observed that the micro-hardness measurements of SS304, Ni200, Zr-2.5wt%Nb and Zr-4 could be represented by four straight lines. Therefore, they could be described by a power law in the form:

$$H_v = c_1 d_v^{c_2} \tag{2.1}$$

where

H_v is Vickers micro-hardness Gpa

d_v is Vickers indentation diagonal μm

c_1 is Vickers micro-hardness when $d = 1$ μm

c_2 is a negative exponent which will be denoted as the "size index".

The above equation could be deduced from the following analysis.

Generally, the Vickers hardness is defined as the load divided by the indentation surface area produced by a square-based pyramid having an angle of 136° between the opposite faces and 148° between the edges. Therefore, for a given indentation of diagonal d_v produced under the action of applied load L, we have

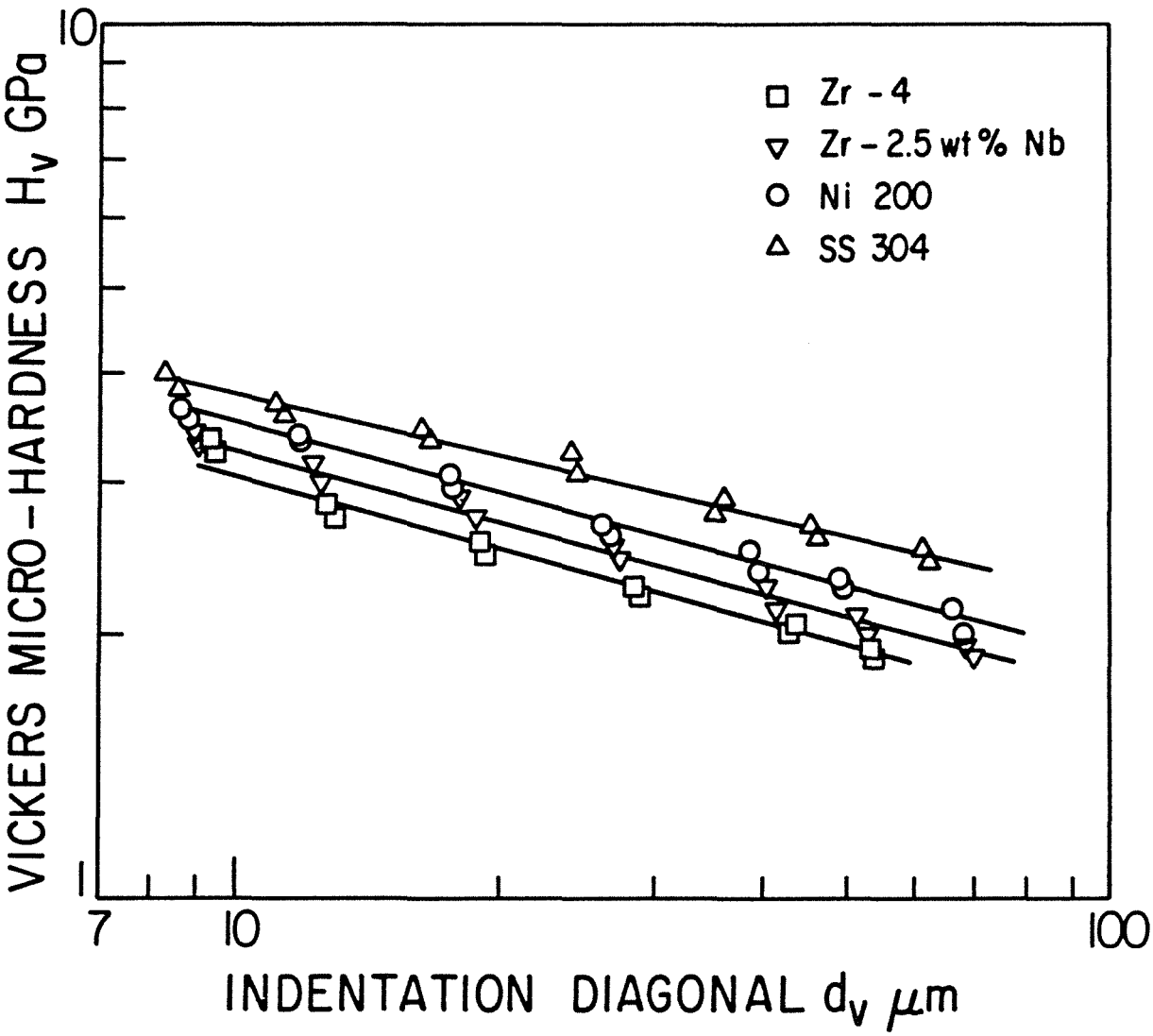

Figure 2.2: Vickers Micro-Hardness Variation of Different Materials with Indentation Diagonal (Maximum and Minimum values)

$$\text{Vickers hardness} = 2L \sin(68°)/d_v^2 \tag{2.2}$$

or

$$H_v = 1.8544L / d_v^2 \quad . \tag{2.3}$$

In micro-hardness tests, very small diamond pyramids are usually used to produce very small indentations. The applied load is usually less than 10N (a typical range is 0.147-4.91N) and the resultant indentation diagonals are measured by a microscope in μm. Thus, Eq.(2.3) becomes:

$$H_v = 1854.4L / d_v^2 \quad \text{GPa} \tag{2.4}$$

where d_v is the Vickers indentation diagonal in μm. Eq.(2.4) shows that the Vickers micro-hardness is a function of the applied load and the indentation diagonal. It is assumed that the relation between the applied load and the resulting diagonal is given by:

$$L = ad_v^n \tag{2.5}$$

which has the form of Meyer's law where a and n are constants. Then, by combining Eqs.(2.4) and (2.5), the following relationship could be obtained for Vickers micro-hardness:

$$H_v = 1854.4\ a\ d_v^{n-2} \quad , \tag{2.6}$$

or alternatively,

$$H_v = c_1 d_v^{c_2}$$

which is obviously Eq.(2.1).

2.3 Hardness Measurement Correlations

A least squares fit of the Vickers micro-hardness measurements for the previously mentioned materials, using Eq.(2.1), gives the following correlations:

1. Zr-4 $H_v = 5.677\ d_v^{-0.278}$ GPa (2.7)

2. Zr-2.5wt%Nb $H_v = 5.884\ d_v^{-0.267}$ GPa (2.8)

3. Ni200 $H_v = 6.304\ d_v^{-0.264}$ GPa (2.9)

4. SS304 $H_v = 6.271\ d_v^{-0.229}$ GPa (2.10)

The above correlations show that the micro-hardness value is inversely proportional to the power of the diagonal so that the micro-hardness increases with decreasing indentation size. A summary of the correlation coefficients c_1 and c_2, along with both the maximum and RMS percent differences between the measured and predicted values, is given in Table 2.1. Figure 2.2 shows a comparison between the predictions based upon the correlations and the experimental measurements. Only the maximum and minimum values

Table 2.1: Vickers Micro-Hardness Correlations, $H_v = c_1 d_v^{c_2}$

Material	H_m,GPa	c_1	c_2	Max % Diff.	RMS % Diff.
Zr-4	1.913	5.677	-0.278	3.4	1.7
Zr-2.5wt%Nb	1.727	5.884	-0.267	10.2	2.7
Ni200	1.668	6.304	-0.264	4.8	1.8
SS304	1.472	6.271	-0.229	4.2	1.4
Average of $c_2 = \eta = -0.26$					

Table 2.2: Vickers Micro-Hardness Correlations using Average Size Index, $H_v = \zeta d_v^{\eta}$

Material	H_m,GPa	ζ	η	Max % Diff.	RMS % Diff.
Zr-4	1.913	5.367	-0.26	3.9	1.8
Zr-2.5wt%Nb	1.727	5.75	-0.26	9.7	2.7
Ni200	1.668	6.217	-0.26	5.2	1.8
SS304	1.472	6.906	-0.26	5.9	2.4

resulting from each load are shown in the Figure. It is interesting to note that for the different types of steel the reported values [39] for the constant c_2 are around -0.25. For nickel c_2 ranges from -0.5 (annealed) to -0.14 (rolled).

As seen from Table 2.1, there is no immediately recognizable inter-relation between the coefficient c_1 from the different correlations and the macro-hardness for these materials. But, as is shown in Figures 2.1 and 2.2, one may expect that the c_1 coefficient will decrease as the material becomes harder. Since the same general correlation form and approximately the same slope are obtained, it is concluded that these differences in the size index values may be affected by the values of the c_1 coefficients. Therefore, an average value η is considered for the size index allowing a direct comparison between the resulting ζ coefficients ($c_1=\zeta$ when $c_2=\eta$) and the macro-hardness values of the materials. Using an average value for the size index ($\eta=-0.26$) the corresponding ζ coefficients are computed and given in Table 2.2 along with the maximum and RMS percent difference between the micro-hardness measurements and the predictions.

It is clear from Table 2.2 that for an average size index, $\eta=-0.26$, the ζ coefficient increases with decreasing macro-hardness value. Furthermore, using $\eta=-0.26$ the excellent

agreement between the predictions and the micro-hardness measurements still exists and is confirmed by the values of the RMS% differences. To demonstrate further the excellent agreement between the predictions and the experimental data, the average micro-hardness $\bar{H}_v$ at each load divided by the ζ coefficient is plotted against the average indentation diagonal $\bar{d}_v$ for all the materials shown in Figure 2.3. The theoretical curve

$$\bar{H}_v / \zeta = \bar{d}_v^{-0.260} \tag{2.11}$$

is seen to be an excellent representation for all the data points. Also, the tabulated values for the predictions, using Eq.(2.11), and the measurements are given in Tables 2.3 through 2.6. Generally, it can be seen that the agreement between the measured and predicted values is excellent. In addition, the overall RMS% difference between the predictions and $\bar{H}_v/\zeta$ values is 1.6. The parameter $\bar{H}_v/\zeta$ may be interpreted as the dimensionless micro-hardness which is normalized with respect to the micro-hardness resulting from an indentation diagonal equal to 1 μm.

In light of the above results, it was decided to use a more direct simple method which would allow the prediction of micro-hardness variation based upon the known or easily measured macro-hardness. Obviously, this suggests a certain kind of relationship between the coefficient ζ and the macro-hardness. To establish this

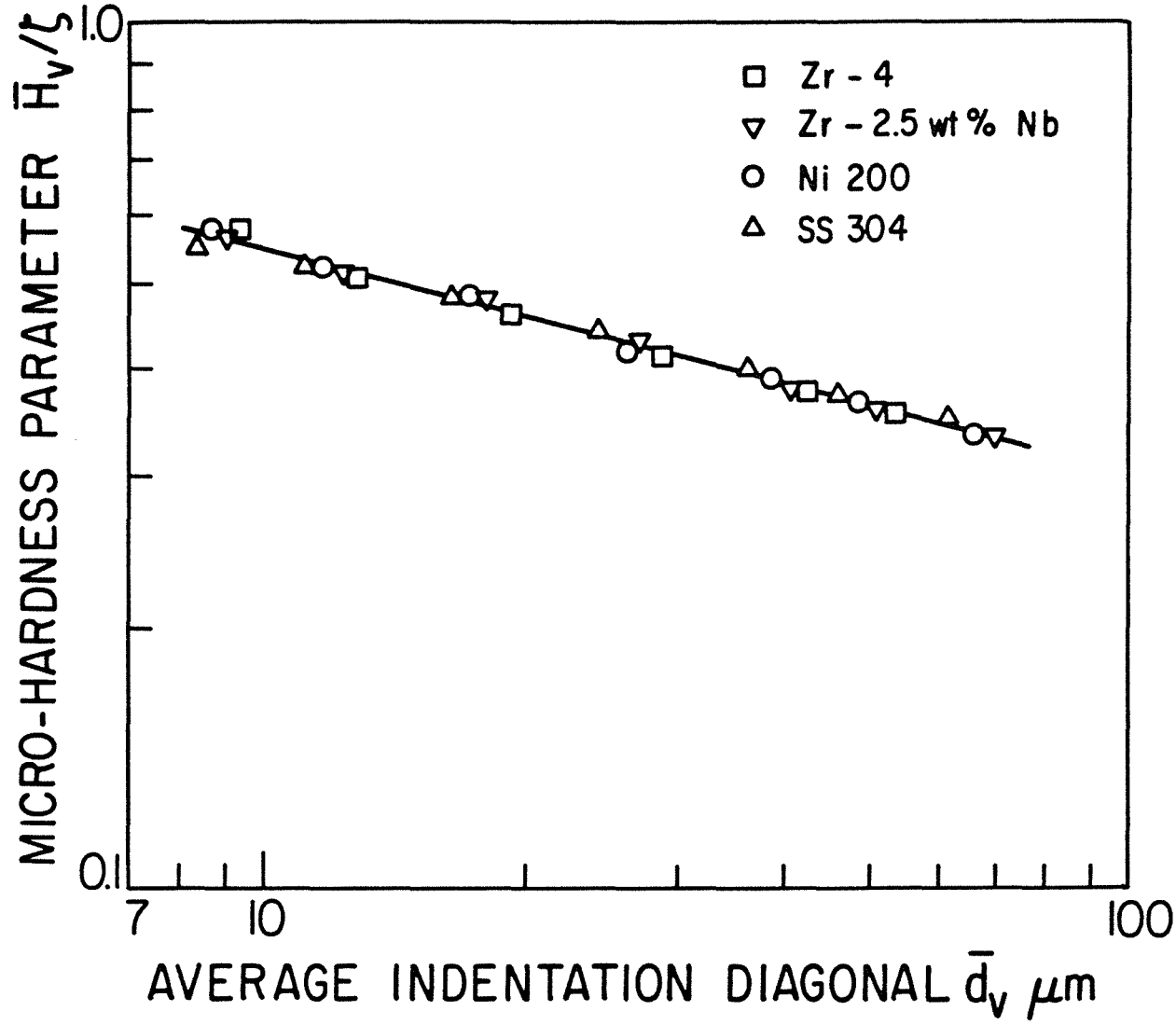

Figure 2.3: Micro-Hardness Parameter $\bar{H}_v/\zeta$ vs. Average Indentation Diagonal $\bar{d}_v$

Table 2.3: Comparison Between the Average Micro-Hardness Values of Zr-4 and the Predictions from Eq.(2.11)

$\bar{d}_v$, μm	$\bar{H}_v$, GPa	$\bar{H}_v / \zeta$	$\bar{d}_v^{-0.26}$	% Diff.
53.33	1.919	0.358	0.356	-0.6
42.51	2.013	0.375	0.377	0.5
28.76	2.200	0.410	0.418	2.0
19.20	2.468	0.460	0.464	0.9
12.88	2.742	0.511	0.515	0.8
9.38	3.102	0.578	0.559	-3.3
RMS% Difference = 1.7				

Table 2.4: Comparison Between the Average Micro-Hardness Values of Zr-2.5wt%Nb and the Predictions from Eq.(2.11)

$\bar{d}_v$, μm	$\bar{H}_v$, GPa	$\bar{H}_v / \zeta$	$\bar{d}_v^{-0.26}$	% Diff.
69.19	1.900	0.333	0.332	0.6
51.67	2.043	0.355	0.359	1.1
40.89	2.177	0.379	0.381	0.5
27.30	2.441	0.425	0.423	-0.5
18.14	2.767	0.482	0.471	-2.3
12.45	2.941	0.511	0.519	1.6
9.13	3.274	0.569	0.563	-1.1
RMS% Difference = 1.3				

Table 2.5: Comparison Between the Average Micro-Hardness Values of Ni200 and the Predictions from Eq.(2.11)

$\bar{d}_v$,μm	$\bar{H}_v$,GPa	$\bar{H}_v / \zeta$	$\bar{d}_v^{-0.26}$	% Diff.
66.26	2.073	0.334	0.336	0.6
49.05	2.268	0.365	0.363	-0.6
38.85	2.419	0.389	0.386	-0.8
26.47	2.597	0.418	0.427	2.2
17.43	2.995	0.482	0.476	-1.2
11.79	3.272	0.526	0.527	0.2
8.76	3.555	0.572	0.569	-0.5
RMS% Difference = 1.1				

Table 2.6: Comparison Between the Average Micro-Hardness Values of SS304 and the Predictions from Eq.(2.11)

$\bar{d}_v$,μm	$\bar{H}_v$,GPa	$\bar{H}_v / \zeta$	$\bar{d}_v^{-0.26}$	% Diff.
61.38	2.414	0.350	0.343	-2.0
46.00	2.579	0.374	0.370	-1.1
36.32	2.758	0.399	0.393	-1.5
24.40	3.056	0.443	0.436	-1.6
16.54	3.325	0.481	0.482	0.2
11.23	3.607	0.522	0.533	2.1
8.47	3.804	0.551	0.574	4.2
RMS% Difference = 2.1				

relationship, the ζ coefficient was plotted as a function of the macro-hardness H_m as shown in Figure 2.4. This gave a linear relationship in the following form:

$$\zeta = 12.04 - 3.49\, H_m \qquad (2.12)$$

A comparison between the actual ζ coefficients and the predictions from Eq.(2.12) is given in Table 2.7.

Table 2.7: Comparison Between the Actual ζ Values and the Predictions from Eq.(2.12)

Material	H_m,GPa	ζ	Eq.(2.12)	% Diff.
Zr-4	1.913	5.367	5.364	-0.06
Zr-2.5wt%Nb	1.727	5.750	6.013	4.60
Ni200	1.668	6.217	6.219	0.03
SS304	1.472	6.906	6.903	-0.04
	RMS% Difference = 2.3			

By combining Eqs.(2.11) and (2.12), the following semi-general micro-hardness correlation is obtained for these metals:

$$\bar{H}_v = (12.04 - 3.49\, H_m)\, \bar{d}_v^{-0.26} \qquad (2.13)$$

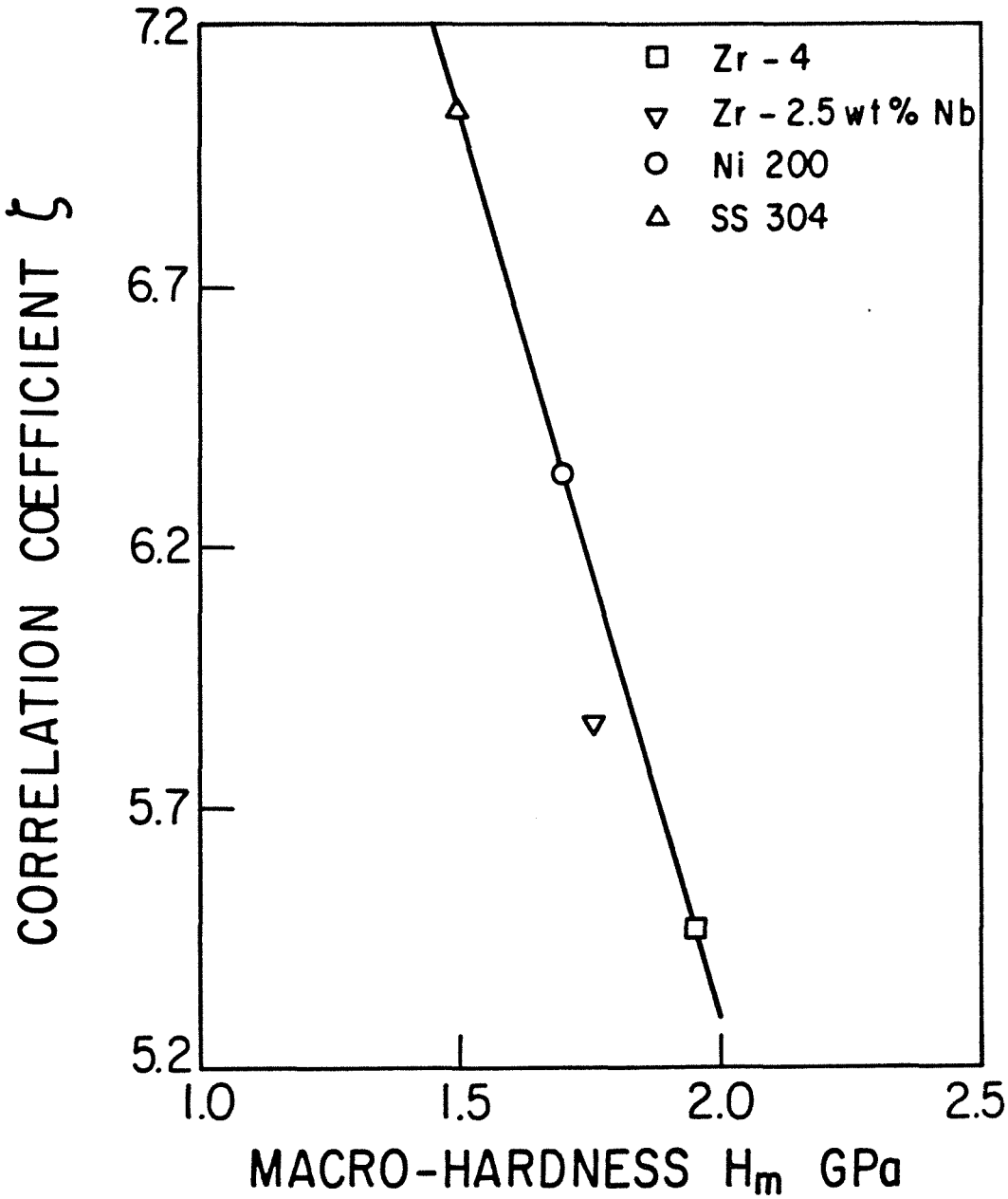

Figure 2.4: Correlation Coefficient ζ vs. the Macro-Hardness Value of Different Materials

A correlation such as this can be useful to the thermal design engineer making it possible to determine a reasonable micro-hardness variation for any metal from this group knowing the macro-hardness value. In this case, the micro-hardness variation is accurate to within a maximum error of 2.2% for Ni200 up to 6.1% for Zr-2.5wt%Nb as seen in Tables 2.8 through 2.11.

2.4 Discussion and Conclusions

In order to eliminate any doubts due to instrumental errors or measurement errors and to check the validity of our micro-hardness measurements, it was decided to test a standard material such as Armco iron which has a well known composition as well as mechanical, electrical and thermal properties. A specimen was prepared in the same manner and tested using the equipment and procedure described earlier. It was observed that the micro-hardness increased with decreasing indentation size as it had in the other materials. However, both size index η and the amount of micro-hardness variation are less, as shown in Figure 2.5. In Figure 2.5, the average measured hardness for each load is shown by the black circles while the solid line represents the prediction from the following correlation:

$$H_v = 3.327\, d_v^{-0.191} \quad \text{GPa} \tag{2.14}$$

Table 2.8: Comparison Between the Average Micro-Hardness Values of Zr-4 and the Predictions from Eq.(2.13)

$\bar{d}_v$,μm	$\bar{H}_v$,GPa	Eq.(2.13)	% Diff.
53.33	1.919	1.907	-0.6
42.51	2.013	2.023	0.5
28.76	2.200	2.240	1.8
19.20	2.468	2.488	0.8
12.88	2.742	2.760	0.7
9.38	3.102	2.997	-3.4
	RMS% Difference = 1.7		

Table 2.9: Comparison Between the Average Micro-Hardness Values of Zr-2.5wt%Nb and the Predictions from Eq.(2.13)

$\bar{d}_v$,μm	$\bar{H}_v$,GPa	Eq.(2.13)	% Diff.
69.19	1.900	1.998	5.2
51.67	2.043	2.156	5.5
40.89	2.177	2.291	5.2
27.30	2.441	2.545	4.3
18.40	2.767	2.820	1.9
12.45	2.941	3.121	6.1
9.13	3.274	3.383	3.3
	RMS% Difference = 4.7		

Table 2.10: Comparison Between the Average Micro-Hardness Values of Ni200 and the Predictions from Eq.(2.13)

$\bar{d}_v$,μm	$\bar{H}_v$,GPa	Eq.(2.13)	% Diff.
66.26	2.073	2.090	0.8
49.05	2.268	2.260	-0.4
38.85	2.419	2.401	-0.7
26.47	2.597	2.653	2.2
17.43	2.995	2.958	-1.2
11.79	3.272	3.274	0.1
8.76	3.555	3.537	-0.5
	RMS% Difference = 1.1		

Table 2.11: Comparison Between the Average Micro-Hardness Values of SS304 and the Predictions from Eq.(2.13)

$\bar{d}_v$,μm	$\bar{H}_v$,GPa	Eq.(2.13)	% Diff.
61.38	2.414	2.367	-1.9
46.00	2.579	2.551	-1.1
36.32	2.758	2.713	-1.6
24.40	3.056	3.008	-1.6
16.54	3.325	3.328	0.1
11.23	3.607	3.681	2.1
8.47	3.804	3.961	4.1
	RMS% Difference = 2.1		

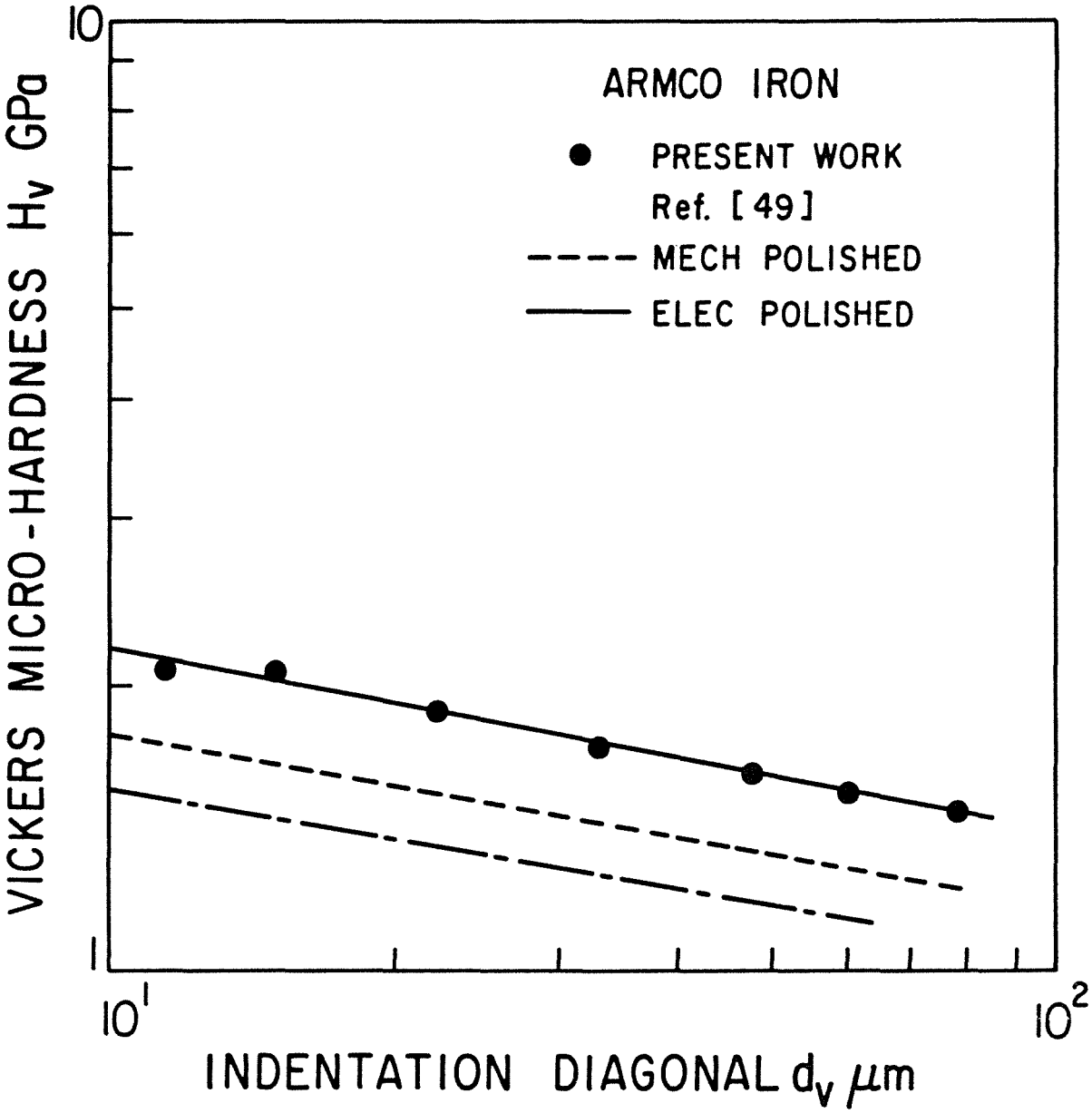

Figure 2.5: Vickers Micro-Hardness Variation of Armco Iron

There is a maximum percent difference of 5.9 and RMS% difference equal to 2.5 between the measured and predicted values.

A search of the literature shows that a similar study was made by Longard [49]. Longard presented numerous sets of Vickers micro-hardness data as hardness versus indentation diagonal on logarithmic scale and showed also that the experimental data was well represented by Eq.(2.1). The micro-hardness data was reported for 99.5% Aluminum, Duraluminum, Steel and Armco iron. Also, the measurements were performed on two groups of specimens. The first group was mechanically polished while the second group was electro-polished. For the same material and under the same load, Longard found that the micro-hardness value for an electropolished specimen is smaller than the value of the mechanically polished one. This difference was attributed to the removal of the work-hardened layer through electropolishing. The reported size index η for the mechanically polished Armco iron was equal to -0.18 (-0.17 for the electropolished specimen) which is in agreement with our findings. However, Longard's Armco iron micro-hardness measurements and, consequently, his predictions are lower, as is shown in Figure 2.5

A particular feature of the curves shown in Figure 2.5 is that the curve from the present study has very similar slope to the curve from Longard's study, but its position has been displaced to higher values of micro-hardness. Since the material composition

is accurately known, it can be said roughly that the difference between the measured micro-hardness values in the two studies may be attributed to the difference in the machining processes used in preparing the test specimens. In other words, the results suggest that for Armco iron the micro-hardness values are influenced by the machining process while the size index η is almost independent of it. Also, the results show clearly that the increase in micro-hardness found in Armco iron, and in the other materials, is a real effect and cannot be ascribed to instrumental errors or dimensional measurement errors.

In light of the foregoing discussion, it becomes necessary to examine the effect of surface preparation upon the micro-hardness profile of a certain material. Thus, a SS304 specimen from the same barstock was prepared by turning, grinding and finally hand-lapping. After lapping the specimen was cleaned to remove the lapping compound and then tested. The results are shown in Figure 2.6; only the maximum and the minimum values are plotted. The measurements of the mechanically-lapped specimen are also included for the purpose of comparison. From Figure 2.6, it is clear that the two sets of measurements have almost the same slope. However, the hand-lapped specimen has lower micro-hardness values due to less degree of surface work-hardening. This conclusion is in line with Longard's observation [49] and others [34,39,41]. A least squares curve fit to the

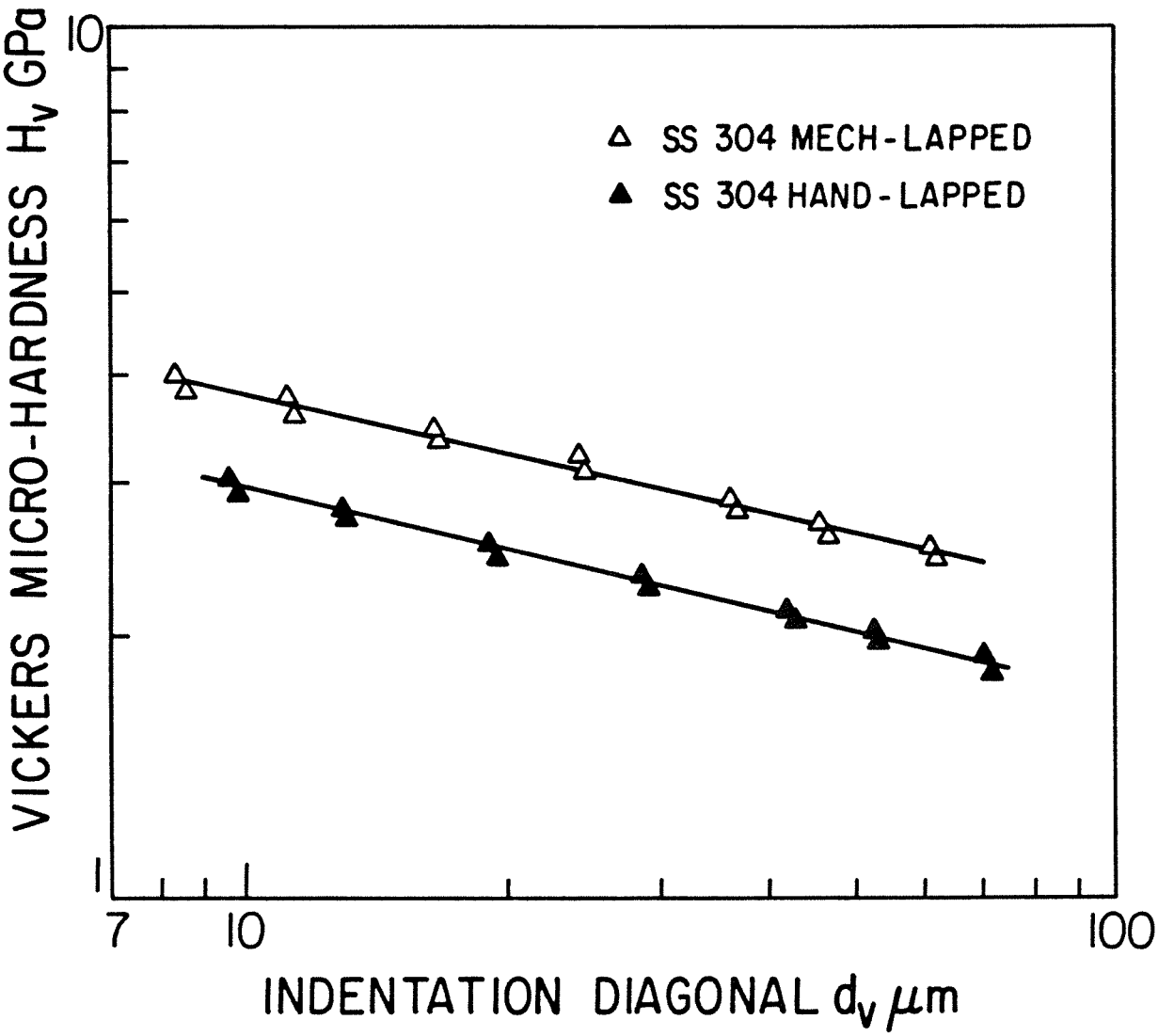

Figure 2.6: Effect of Surface Preparation upon the Micro-Hardness Profile of SS304

hardness measurements, gives the following correlation:

$$H_v = 4.922\ d_v^{-0.233} \quad \text{GPa} \tag{2.15}$$

Note, that this equation contains an exponent, c_2, very similar to that found in Eq.(2.10) but a different value for c_1.

Reference has been made previously to the micro-hardness variation reported by Henry [15] for Stainless Steel 416 (SS416) specimens which were prepared in a similar manner to the specimens in the present study. Thus, the validity of the semi-general correlation, Eq.(2.13), in predicting Vickers micro-hardness variation of other materials from the macro-hardness value was explored. A typical Vickers micro-hardness-indentation area curve, taken from the work of Henry, is shown in Figure 2.7. A replot of his experimental data on H_v-d_v curve is also shown in Figure 2.8. A least squares fit to the experimental measurements, resulted in the following correlation:

$$H_v = 5.176\ d_v^{-0.191} \quad \text{GPa} \tag{2.16}$$

with maximum % difference and RMS% difference of 11.6 and 5.1, respectively. For SS416 the macro-hardness value, as reported in Metals Handbook [50] is equal to 1.53 GPa. Using this value in the semi-general micro-hardness correlation, Eq.(2.13), resulted in the following correlation:

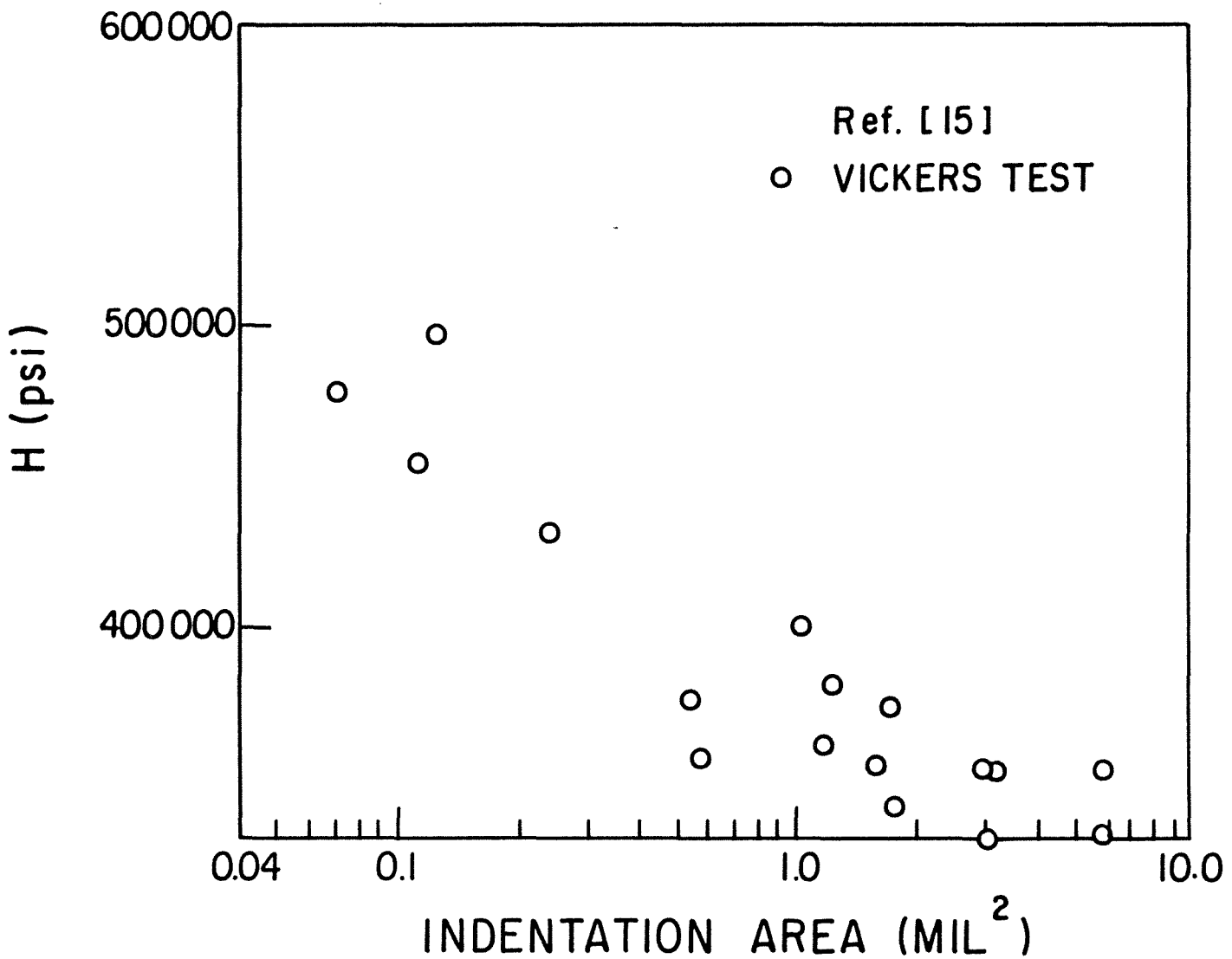

Figure 2.7: Vickers Micro-Hardness Variation of SS416 - Ref.[15]

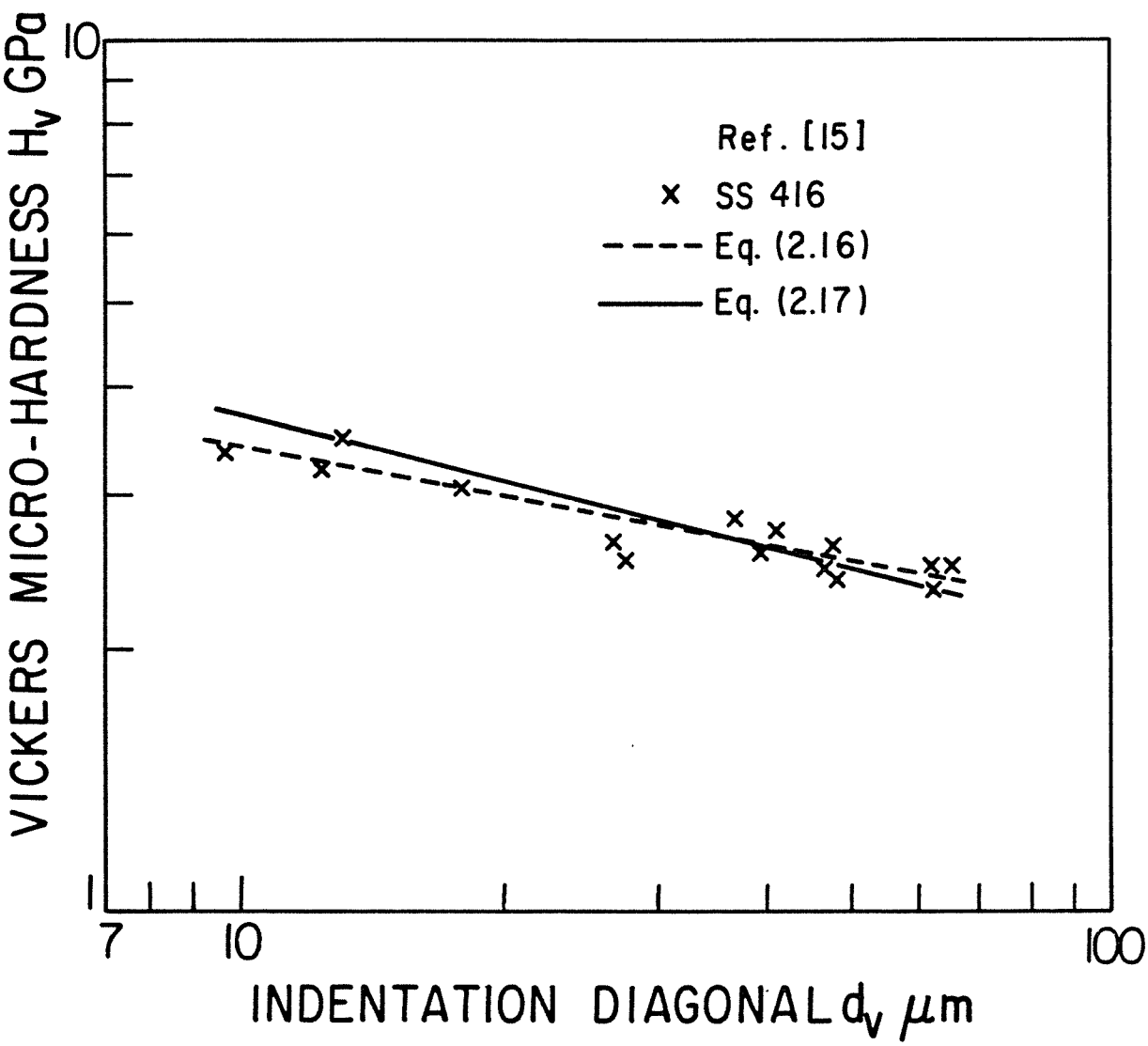

Figure 2.8: Comparison Between Micro-Hardness Measurements of SS416 and the Predictions

$$H_v = 6.7\, d_v^{-0.26} \quad \text{GPa} \tag{2.17}$$

The predicted values from the above correlation match the measurements with maximum % difference of 14.8 and RMS% difference equal to 7.3, as shown in Table 2.12. Keeping in mind that Henry's measurements were performed in a random fashion with arbitrary loads, we concluded that there is a fairly good agreement between the predictions by the semi-general correlation and the Henry data as shown in Figure 2.8.

In conclusion, the results recorded in the previous sections, as well as the above discussion, show clearly that the semi-general micro-hardness correlation, Eq.(2.13), may be used by a thermal design engineer as a satisfactory description of micro-hardness variation in relation to the macro-hardness for this family of materials. However, as shown in Table 2.1, it is quite obvious that the size index for each material is different, so Eq.(2.13) may be unsatisfactory. Also, as is demonstrated, the machining process plays a major role in the creation of this hardness variation, so that Eq.(2.13) will be unsuitable for those who want to know the exact micro-hardness variation of a certain material in this family processed in a different manner. Hence, we cannot proclaim Eq.(2.13) to be a general micro-hardness correlation for these materials. It is recommended, however, that further work be done to clarify the applicability of the semi-general micro-hardness correlation to other materials machined in the same manner.

Table 2.12: Comparison Between Ref.[15] Micro-Hardness Measurements of SS416 and the Predictions from Eq.(2.17)

10^6 Area, in^2	10^{-5} H_v,psif	d_v,μm	H_v,GPa	Eq.(2.13)	% Diff.
0.07	4.80	9.57	3.311	3.724	12.5
0.12	4.56	12.39	3.142	3.483	10.9
0.13	4.98	13.15	3.434	3.429	- 0.1
0.25	4.32	18.07	2.978	3.157	6.0
0.56	3.77	26.78	2.598	2.850	9.7
0.60	3.57	27.71	2.460	2.825	14.8
1.06	4.00	36.98	2.759	2.621	- 5.0
1.23	3.61	39.85	2.491	2.570	3.2
1.31	3.87	41.16	2.669	2.549	- 4.50
1.68	3.53	46.57	2.435	2.468	1.4
1.78	3.74	47.92	2.579	2.450	- 5.0
1.84	3.40	48.66	2.344	2.440	4.1
2.94	3.52	61.63	2.429	2.295	- 5.5
3.00	3.30	62.22	2.279	2.289	- 0.4
3.19	3.52	64.18	2.428	2.271	- 6.5
RMS% Difference = 7.3					

Finally, based upon the good agreement between the micro-hardness measurements and the predictions for these materials, the next problem is in the determination of a suitable micro-hardness value for the thermal predictions from the measured micro-hardness variation. The answer to this problem will be discussed in the next chapter.

CHAPTER 3

THEORETICAL ANALYSIS

3.1 Introduction

During the last three decades a considerable amount of research and study has been devoted to the problem of predicting thermal joint conductance between metallic contacts. The publications on the subject now amount to several hundred papers which not only emphasize the importance of this research topic, but also indicate that the development of a general predictive model has proven to be a difficult task. This is natural if one considers the large number of inter-related factors which can influence the prediction. Some of these factors are: mechanical and thermal properties of the contacting surfaces, the presence of an interstitial fluid as well as its thermal and physical properties, surface roughness or waviness, similar or dissimilar materials, the presence of an oxide layer, contaminant film or metallic coating on the surfaces, etc. For clean, bare metallic joints free of oxide film, the most troublesome of the mechanical factors is the one concerning the micro-hardness variation of the contacting surfaces. Of course, an appropriate hardness value is necessary to calculate the real area of contact. This aspect has been overlooked in the past, as pointed out earlier, but emphasis will be placed on it in this analysis. Also, the analysis is

confined to contact between similar, non-wavy, flat, isotropically rough surfaces in a vacuum or gaseous environment. Since it has been concluded by a number of investigators [9,16] that radiation heat transfer can be neglected for temperatures up to 700K, radiation conductance will be considered negligible throughout this work. For further details the reader is referred to Appendix D.

In this chapter the prediction of the thermal joint conductance is divided into two separate components, the contact conductance and the gap conductance. The contact conductance section consists of three parts. The first part deals with the contact resistance analysis while the second part relates the number of contacts as well as the mean contact spot radius to the surface parameters. The mechanical analysis will be carried out in the third part to develop a model for predicting the appropriate contact hardness, employing information about the surface parameters as well as the micro-hardness variation of the contacting surfaces. Next, the statistical gap conductance model proposed by Yovanovich et al [55] for estimating the contribution of the gas to the joint conductance is reviewed. This model is considered because it provides the most satisfactory approach to this aspect of the problem, although some refinements will be introduced.

The contact and gap conductance models considered here are based upon the following assumptions [31,55]:

1. Contacting surfaces are clean, free of oxides, films, etc.

2. Contacting surfaces are microscopically rough but macroscopically conforming.

3. Contacting surfaces have isotropic Gaussian surface height distributions.

4. The real contact area is uniformly distributed over the apparent area.

5. When the contacting surfaces are pressed together, the asperities of the softer surface deform plastically while the asperities of the harder surface are embedded in the other surface.

6. The average flow pressure between the contacting surfaces is equal to the contact micro-hardness of the softer surface.

7. The contact micro-hardness is a function of the micro-hardness variation of the softer surface and the effective surface parameters.

8. The contact spots, and adjacent surfaces not in contact, are isothermal, each having the temperature extrapolated from the body of the solids.

9. The total heat flow rate can be separated into two independent heat flows through the contact and through the gap.

10. The variable gap thickness will influence the gap conductance and must, therefore, be taken into account.

11. The effective gap thickness is dependent upon the surface roughness and the applied contact pressure.

12. Noncontinuum gas effects must be taken into account.

13. Radiative heat transfer is negligible.

3.2 Thermal Contact Conductance

3.2.1 Thermal Analysis

When two conforming rough surfaces are brought into contact under a static load, intimate contact occurs only at a discrete number of micro-contact spots whose total area is a small fraction of the apparent contact area. The gaps between the contacting surfaces may be filled with a gaseous fluid or may be evacuated. Under vacuum conditions with negligible radiation, heat transfer across the interface takes place by conduction through the micro-contacts. Figure 3.1 shows a representative view of the heat flow lines across an interface. In the regions "far" from the interface, the heat flow lines are

(a)

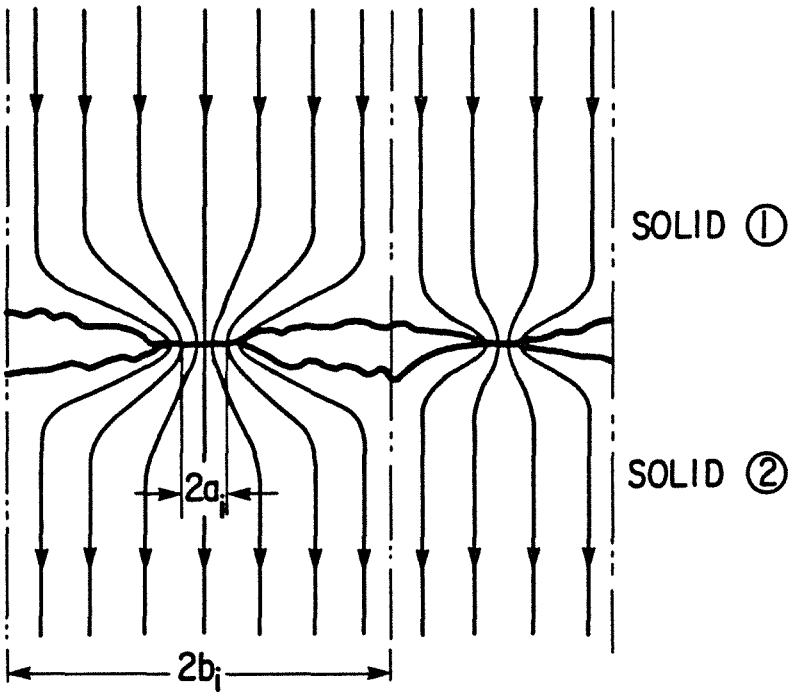

(b)

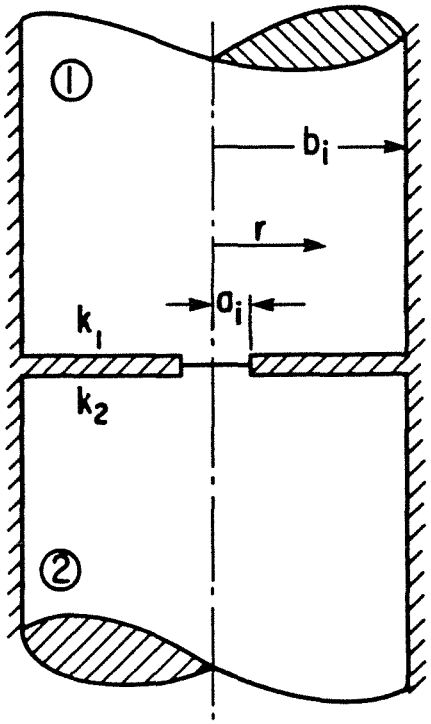

Figure 3.1: Elemental Heat Flux Tube for Individual Micro-contact:
a) Actual
b) Idealization

uniform, parallel to each other, and perpendicular to the interface. As they approach the interface region they converge to the micro-contact areas and spread out on the other side. This convergence and spreading of the flow lines at a single micro-contact area causes a resistance to the heat flow and is denoted as the thermal constriction resistance. In general, the thermal constriction resistance of a single micro-contact is a function of the thermal conductivities of the contacting surfaces, some characteristic dimension of the micro-contact area, and the constriction parameter that depends upon the shape of the micro-contact and the boundary conditions over the micro-contact area. When all the constriction resistances are added in parallel, the sum is defined as the thermal contact resistance.
In order to predict thermal contact resistance analytically, certain assumptions are normally made. It is assumed that there are N isothermal flat micro-contacts randomly distributed over the apparent area and each micro-contact has a circular geometry of radius a_i. An equivalent circular flux tube of radius b_i is associated with each micro-contact that is centrally placed in the flux tube as shown in Figure 3.1. Also, the total area of these flux tubes is equal to the interface apparent area.

The overall thermal contact resistance, R_c, is determined by dividing the temperature drop across the interface, ΔT, by the total heat flow, Q:

$$R_c = \Delta T / Q \tag{3.1}$$

The above equation can be expressed in terms of the constriction resistance of the individual heat flux tube, R_{ci}, as:

$$\frac{1}{R_c} = \sum_{i=1}^{N} \frac{1}{R_{ci}} = \sum_{i=1}^{N} \frac{1}{R_{ci_1} + R_{ci_2}} \tag{3.2}$$

where R_{ci_1} and R_{ci_2} are the respective constriction resistances of the semi-heat flux tube. Therefore, the problem of predicting the thermal contact resistance reduces to the simpler problem of a semi-cylindrical heat flux tube with heat flux specified over part of the contact boundary while the remainder is isothermal. This mixed boundary value problem has not been solved analytically, although various approximate solutions have been presented by a number of investigators.

If it is assumed that the micro-contact, or the contact spot radius, is very small compared with the distance separating it from the neighbouring contacts, the constriction resistance is obtained from the classical solution by Holm [11] for a circular disc of radius a on a half space with thermal conducitivity k:

$$R = \frac{1}{4ka} \tag{3.3}$$

which forms the basis of many of the existing contact conductance models. As the micro-contacts grow in size and increase in number, a constriction parameter $\psi(\varepsilon)$ must be introduced in Eq.(3.3) to allow for the interference between the heat flux tubes.

Roess [56] analytically determined the constriction parameter for the heat flow through a right circular cylinder of radius b, which has an isothermal concentric contact spot of radius a. To overcome the mixed boundary value problem, he replaced the temperature boundary condition by a heat flux distribution proportional to $[1-(r/a)^2]^{-0.5}$ over the contact spot $(0<r<a)$ but is adiabatic outside the contact $(a<r<b)$. This distribution was found to be nearly representative of an isothermal contact spot for small values of relative contact spot radius $\varepsilon(=a/b<0.3)$. Roess presented his results in the form of an infinite series expression given by:

$$\psi(\varepsilon) = 1 - 1.4093\varepsilon + 0.2959\varepsilon^2 + 0.05254\varepsilon^5 + \ldots \qquad (3.4)$$

Mikic [18] examined the isothermal contact case using the above heat flux distribution to replace the prescribed temperature boundary condition. He obtained a different infinite series expression for the constriction parameter. Later, this expression was simplified (Cooper et al [20]) by the following approximate relation:

$$\psi(\varepsilon) = (1-\varepsilon)^{1.5} \qquad (3.5)$$

Yovanovich [57] obtained a general expression for the constriction parameter with the heat flux distribution over the contact spot proportional to $[1-(r/a)^2]^{\mu}$ for three values of μ:-1/2,0,1/2. For $\mu=-1/2$, he found that the contact spot is isothermal provided that $\varepsilon<0.3$. For this case, the following approximate expressions were proposed:

$$\psi(\varepsilon) = 1 - 1.4197\varepsilon \qquad \varepsilon < 0.1 \qquad (3.6)$$

$$\psi(\varepsilon) = (1-\varepsilon)^{1.5} \qquad \varepsilon \leq 0.3 \qquad (3.7)$$

Eq.(3.7) is identical to Eq.(3.5), however, it quite accurately approximates the analytical solution in the specified range of ε.

Gibson [58] solved the same problem by reducing the mixed boundary value problem to a Fredholm integral equation. This integral equation was solved with the help of tabulated integrals available in the literature. He also expressed his results as an infinite series, that is,

$$\psi(\varepsilon) = 1 - 1.4097\varepsilon + 0.3380\varepsilon^3 + 0.0679\varepsilon^5 + \ldots \qquad (3.8)$$

which is remarkably similar to that of Roess, Eq.(3.4).

For the very important range of $\varepsilon<0.3$, it is interesting to note that the results from the various expressions for the constriction

parameter agree remarkably well although they are expressed in different algebraic forms. Therefore, we can conclude that the constriction parameter $\psi(\varepsilon)$ can be expressed accurately by the following simple expression:

$$\psi(\varepsilon) = (1-\varepsilon)^{1.5} \tag{3.9}$$

Now, the thermal constriction resistance for a semi-heat flux tube can be written as:

$$R = \frac{\psi(\varepsilon)}{4ka} \tag{3.10}$$

and the total constriction resistance for the i^{th} heat flux tube as:

$$R_{ci} = \frac{\psi_{i_1}(\varepsilon_i)}{4k_1 a} + \frac{\psi_{i_2}(\varepsilon_i)}{4k_2 a} \tag{3.11}$$

Substituting Eq.(3.11) into Eq.(3.2) yields:

$$\frac{1}{R_c} = \sum_{i=1}^{N} \left[\frac{\psi_{i_1}(\varepsilon_i)}{4k_1 a} + \frac{\psi_{i_2}(\varepsilon_i)}{4k_2 a} \right]^{-1} \tag{3.12}$$

where R_c is the total contact resistance of N circular contact spots.

Because of geometric symmetry about the contact plane, we can put

$$\psi_{i_1} = \psi_{i_2} = \psi_i = (1-\varepsilon_i)^{1.5} \tag{3.13}$$

provided $0 < \varepsilon_i < 0.3$.

Introducing the harmonic mean thermal conductivity as:

$$\frac{1}{k_s} = \frac{1}{2}\left[\frac{1}{k_1} + \frac{1}{k_2}\right] \tag{3.14}$$

allows us to write Eq.(3.12) as:

$$\frac{1}{R_c} = 2k_s \sum_{i=1}^{N} \frac{a_i}{\psi_i} \tag{3.15}$$

Since the contact conductance is defined by:

$$h_c = \frac{1}{R_c A_a} \tag{3.16}$$

therefore, Eq.(3.15) becomes

$$h_c = \frac{2k_s}{A_a} \sum_{i=1}^{N} \frac{a_i}{\psi_i} \tag{3.17}$$

For most engineering applications where $\varepsilon \leq 0.1$ and $0.85 \leq \psi_i \leq 1$, the specific constriction parameter ψ_i appropriate

to each contact spot can be replaced by the mean value of the constriction parameter based upon the total set of contacts [31]. Therefore, Eq.(3.13) can be written as:

$$\psi_i = \psi = (1-\varepsilon)^{1.5} \tag{3.18}$$

where

$$\varepsilon = \sqrt{A_r/A_a} = a/b \tag{3.19}$$

a and b are the mean contact spot and associated flux tube radii respectively, determined from the total real and apparent areas.

Substituting Eq.(3.18) into Eq.(3.17) and replacing the individual contact spot radius a_i by the mean value a yields:

$$h_c = \frac{2k_s\, n\, a}{(1-\varepsilon)^{1.5}} \tag{3.20}$$

where n is the contact spot density defined by:

$$n = N/A_a \tag{3.21}$$

At this stage, the prediction of contact conductance requires knowledge of the mean contact spot radius a as well as the contact spot density n. These two important parameters can be related to the surface characteristics and to the mean separation

between the contacting surfaces. This problem will be considered in the next section.

3.2.2 Surface Analysis

The contact parameters, a and n, required for the prediction of the thermal contact conductance, can be determined using one of the available contact models in the literature. These models require information about the surface characteristics, σ and m, which can be obtained from the profilometer traces of the contacting surfaces before the joint is made.

Greenwood and Williamson [59], among many others [60,61], have shown that the profile heights of many engineering surfaces have a nearly Gaussian distribution; an assumption which is made in most contact models to describe the surface topography. However, their significant contribution was the theoretical treatment of the contact problem which was based upon the application of the probability theory. In other words, they showed that the contact between two Gaussian rough surfaces is equivalent to that between an ideal smooth flat surface and a single Gaussian rough surface having the RMS roughness of the two real surfaces, Figure 3.2. Also, the probability of making contact at any given asperity having height Y above the surface mean plane is:

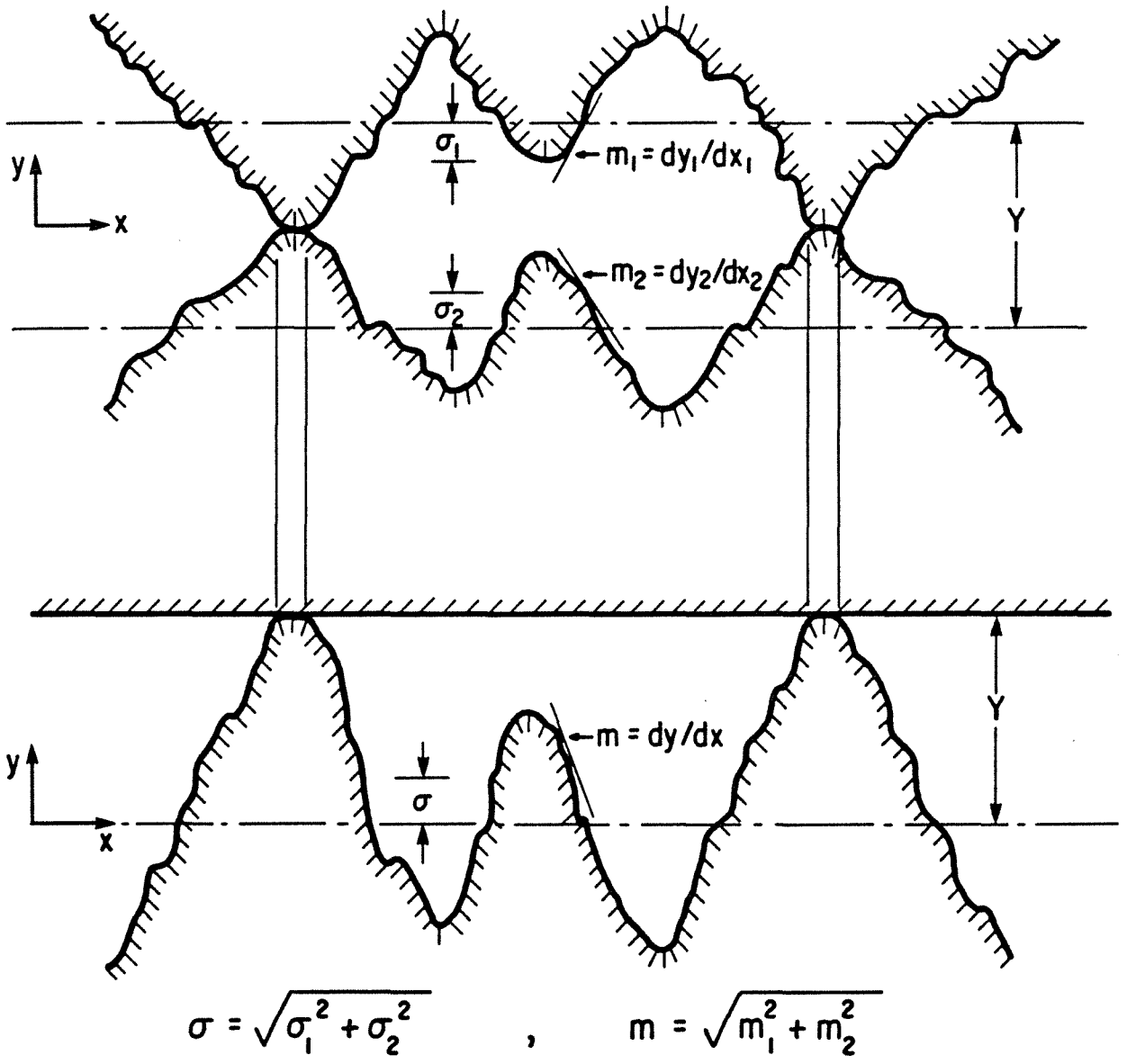

Figure 3.2: Equivalent Contact of Two Gaussian Conforming Rough Surfaces

$$\text{Prob}(y > Y) = \int_{Y}^{\infty} \phi(y)\, dy \tag{3.22}$$

where $\phi(y)$ is the probability function defined by:

$$\phi(y) = \frac{1}{\sigma\sqrt{2\pi}} \exp(-y^2/2\sigma^2) \tag{3.23}$$

and σ is the combined or the effective RMS roughness of the two surfaces which is given by:

$$\sigma = \sqrt{\sigma_1^2 + \sigma_2^2} \tag{3.24}$$

Tsukizoe and Kisakado [51,52] proposed a statistical contact model for predicting the contact spot size and density for an isotropic Gaussian rough surface in contact with an ideal smooth flat surface. In their analysis, it was assumed that the surface asperities have a conical shape of equal base angle which depends on the surface mean absolute slope. On the basis of this assumption and neglecting the asperity interactions, they obtained the following expressions for the contact parameters a and n:

$$a = \frac{\sqrt{2}}{\pi} \left(\frac{\sigma}{m}\right) \frac{1}{x} \tag{3.25}$$

$$n = \frac{\sqrt{\pi}}{8} \left(\frac{m}{\sigma}\right)^2 x \exp(-x^2) \tag{3.26}$$

where $x = Y\sqrt{2}\,\sigma$ and Y is the separation between the surface mean planes as shown in Figure 3.2. m is the effective mean absolute slope of the contacting surfaces and is given by:

$$m = \sqrt{m_1^2 + m_2^2} \tag{3.27}$$

Therefore, the product na can be written as:

$$na = \frac{1}{4\sqrt{2\pi}} \left(\frac{m}{\sigma}\right) \exp(-x^2) \tag{3.28}$$

A different approach, based upon the level-crossing theory, was adopted by Cooper et al [20] in the development of a contact model during their theoretical treatment of the thermal contact conductance problem. Assuming hemispherical asperities whose heights have a Gaussian distribution as well as surface slopes, they showed that the density of the contact spots and the sum of all contact radii can be respectively expressed as functions of the surface parameters:

$$n = \frac{1}{16} \left(\frac{m}{\sigma}\right)^2 \frac{\exp(-2x^2)}{\operatorname{erfc}(x)} \tag{3.29}$$

$$\frac{\Sigma a_i}{A_a} = \frac{1}{4\sqrt{2\pi}} \left(\frac{m}{\sigma}\right) \exp(-x^2) \tag{3.30}$$

Eq.(3.30) can be written in terms of the mean contact radius as:

$$na = \frac{1}{4\sqrt{2\pi}} \left(\frac{m}{\sigma}\right) \exp(-x^2) \tag{3.31}$$

Therefore, from Eqs.(3.29) and (3.31), the mean contact spot radius, a, can be expressed as:

$$a = \sqrt{\frac{8}{\pi}} \left(\frac{\sigma}{m}\right) \exp(x^2)\ \mathrm{erfc}(x) \tag{3.32}$$

Also, they showed that the ratio between the real area of contact and the apparent area, at any given separation between the contacting surface mean planes, can be related to the probability function by:

$$\frac{A_r}{A_a} = \int_Y^\infty \phi(y)\ dy \tag{3.33}$$

which upon integration yields:

$$\frac{A_r}{A_a} = \frac{1}{2}\ \mathrm{erfc}(x) \tag{3.34}$$

Later the above analysis was extended by Mikic [21] who considered the effect of previous loading on the contact parameters and the thermal contact conductance for two conforming rough surfaces. For first loading condition, he obtained the following expression for the mean radius of curvature, ρ, of a hemispherical asperity:

$$\rho = \left(\frac{2}{\pi}\right)^{1.5} \frac{\sigma}{m^2} \frac{x \exp(x^2)\ \mathrm{erfc}(x)}{\left[x - \dfrac{\exp(-x^2)}{2\sqrt{\pi}\ \mathrm{erfc}(x)}\right]} \tag{3.35}$$

Kimura [62] studied statistically the more general case in which an anisotropic rough surface, having asperities of arbitrary shape, contacts an ideal flat surface. The analysis was carried out for "two-dimensional" contact. Again, it was assumed that the asperity heights, as well as slopes, had a Gaussian distribution. Under fully plastic deformation, the following relationships for the micro-contact density, n, and the mean micro-contact area, s, were obtained:

$$n = \frac{1}{4\pi\lambda} \left(\frac{m_x\ m_y}{\sigma^2}\right) \frac{\exp(-2x^2)}{\mathrm{erfc}(x)} \tag{3.36}$$

$$s = 2\pi\lambda \left(\frac{\sigma^2}{m_x\ m_y}\right) [\mathrm{erfc}(x)]^2 \exp(2x^2) \tag{3.37}$$

where m_x and m_y are the surface mean absolute slopes along x and y directions and λ is the micro-contact area shape factor defined by $\lambda = s/(\bar{a}\bar{b})$. $\bar{a}$ and $\bar{b}$ are the mean lengths of the micro-contact area along the principle directions. For rectangular shape, λ is equal to unity while for a circular shape $\lambda = 4/\pi$.

Assuming an isotropic rough surface, i.e., $m_x = m_y$, and circular micro-contacts of radius a, i.e., $s = \pi a^2$ and $\lambda = 4/\pi$, then the contact parameters a, n and na can be written as:

$$a = \sqrt{\frac{\overline{8}}{\pi}} \left(\frac{\sigma}{m}\right) \exp(x^2)\ \mathrm{erfc}(x) \tag{3.38}$$

$$n = \frac{1}{16} \left(\frac{m}{\sigma}\right)^2 \frac{\exp(-2x^2)}{\mathrm{erfc}(x)} \tag{3.39}$$

$$na = \frac{1}{4\sqrt{2\pi}} \left(\frac{m}{\sigma}\right) \exp(-x^2) \tag{3.40}$$

which are similar to the expressions arrived at by Cooper et al [20].

Careful examination of Kimur's results reveals that the contact size is characterized by the square root of the micro-contact area. For the thermal problem in hand, this conclusion was justified by Yovanovich et al [63]. Also, this conclusion is inherent in the thermal analysis through the parameter ε which is actually the square root ratio of the contact spot area to the area of the flux tube associated with it. This result, which apparently was not previously realized, has a significant bearing on the determination of the appropriate contact hardness for the thermal prediction. This will be demonstrated further in the mechanical analysis.

Equally important, the product of the contact parameters a and n from the previous models is identical regardless of the physical geometry and the theoretical treatment employed in formulating the contact model. Consequently, the thermal contact conductance, Eq.(3.20), can be written with confidence as:

$$C_c = \frac{\sigma h_c}{m k_s} = \frac{\exp(-x^2)}{2\sqrt{2\pi}\,(1-\varepsilon)^{1.5}} \tag{3.41}$$

which is a function of the mean plane separation and the square root ratio of the real to the apparent area. The problem of relating these two parameters to the contact pressure will be addressed in the following section.

3.2.3 Mechanical Analysis

When a flat hard smooth surface is placed in contact with a flat soft rough surface under a static load, the hard surface will be supported by the summits of the softer surface's deformed asperities. For the first loading condition, these asperities will deform plastically, and a load balance on the real and apparent areas gives:

$$P\,A_a = P_f\,A_r \tag{3.42}$$

where P_f is the asperity flow pressure. The flow pressure

concept was introduced by Holm [11] to explain the proportionality between the area of contact and the applied load pressure in electric contact problems. It is well established that the flow pressure is related to the pressure under a blunt indenter in a static hardness indentation test [11,39,64,65]. Since there is a little difference between the hardness values obtained from the conventional static indentation test and the material flow pressure, it has become customary to assign the hardness value to the flow pressure. However, it has been shown by Bowden and Tabor [43] that the Vickers hardness value is almost equal to the flow pressure.

If a flat soft smooth surface is pressed against a flat hard rough surface, the hard asperities will penetrate the soft surface in a way similar to the manner of an indenter in hardness indentation tests. Similar concepts apply and, consequently, we can replace the flow pressure by the hardness. Therefore, Eq.(3.42) becomes:

$$\frac{A_r}{A_a} = \frac{P}{H} = \varepsilon^2 = \frac{1}{2}\,\mathrm{erfc}(x) \tag{3.43}$$

Eq.(3.43) relates the ratio of the real to the apparent area, ε^2, as well as the relative mean plane separation, Y/σ, to the applied contact pressure and the hardness of the softer material. With $x = \mathrm{erfc}^{-1}(2P/H)$ and $\varepsilon = \sqrt{P/H}$, Yovanovich [31] correlated the contact conductance exact expression, Eq.(3.41), by the following simple expression:

$$C_c = \frac{\sigma h_c}{m k_s} = 1.25(P/H)^{0.95} \qquad (3.44)$$

which agrees with the exact expression to within ±1.5% for $1 * 10^{-6} \leq P/H \leq 2.3 * 10^{-2}$. Also, he proposed the following approximate expressions for the relative separation and the mean contact spot radius:

$$Y/\sigma = 1.184[-\ln(3.132\ P/H)]^{0.547} \qquad (3.45)$$

$$a = 0.99(\sigma/m)[-\ln(3.132\ P/H)]^{-0.547} \qquad (3.46)$$

In the analysis so far it has been assumed that the hardness of the softer surface is known beforehand. Based upon the conclusions made in the previous chapter, the appropriate hardness value for the thermal prediction has to be determined as a function of the surface micro-hardness variation and the contact size. In seeking this hardness value, it is necessary to state the idea behind the following analysis. The analysis considers a hard rough surface in contact with a soft smooth surface under a given static load. The basic idea is that each asperity can be modelled as a micro-hardness indenter and, through the mechanical and the geometrical characteristics of the asperity, it will be possible to determine the appropriate micro-hardness value under such contact conditions.

It is well known [66] that the asperities of most practical engineering surfaces have rounded summits so that the individual asperity contact can be visualized as a large sphere of radius ρ indenting a flat smooth surface and the resulting indentation has a circular geometry of radius a. In general, spherical indenters are characterized by the following:

i) the sphere hardness is almost equal to the flow pressure;

ii) if a sphere of radius ρ_1 produces an indentation of radius a_1, the hardness will be the same as that obtained with a sphere of radius ρ_2 producing an indentation of radius a_2 provided the indentations are geometrically similar.

In other words, if the ratio a/ρ for both spherical indenters is constant, the hardness will be constant regardless of the indentation size and the load used in producing the indentation. On this basis, it is important to examine the ratio of a/ρ over the important range of the relative contact pressure, i.e., $10^{-4} \leq P/H \leq 10^{-2}$. The radius of the asperity indentation, or the mean contact spot, a, and the asperity tip radius, ρ, are given by:

$$a = \sqrt{\frac{8}{\pi}} \left(\frac{\sigma}{m}\right) \exp(x^2)\ \mathrm{erfc}(x) \tag{3.32}$$

$$\rho = \left(\frac{2}{\pi}\right)^{1.5} \frac{\sigma}{m^2} \frac{x \exp(x^2)\ \mathrm{erfc}(x)}{\left[x - \dfrac{\exp(-x^2)}{2\sqrt{\pi}\ \mathrm{erfc}(x)}\right]} \tag{3.35}$$

Hence, the ratio a/ρ can be written as:

$$\frac{a}{\rho} = \pi m \left[1 - \frac{\exp(-x^2)}{2\sqrt{\pi}\ x\ \mathrm{erfc}(x)}\right] \tag{3.47}$$

which is a function of the relative separation or the relative contact pressure for a given set of contact conditions (applied load, surface roughness, etc.). The ratio (a/ρ), as well as the mean contact radius and the contact density, are computed for selected values of relative contact pressure in the range $10^{-4} \leq P/H \leq 10^{-2}$ and the results are given in Table 3.1.

Examination of Table 3.1 reveals that the mean contact spot radius a increases by a factor of 1.5 for a hundred fold increase in the relative contact pressure, however, the ratio a/ρ increases by only 9.5%. The significance of this result is that the ratio a/ρ remains relatively constant over this wide range of the relative contact pressure and, therefore, the hardness can be assumed approximately constant according to the principle of the geometric similarity. This implies that a unique hardness value, denoted by the Contact Hardness, H_c, can be employed with negligible error in predicting the contact conductance and the relative separation over the specified range of relative contact pressure.

Table 3.1: Contact Parameters a,n and a/ρ at Different Values of Relative Contact Pressure

10^{-4} P/H	Y/σ	$10^4(\sigma/m)a$	$10^4(\sigma/m)^2 n$	$(a/\rho)/m$
1	3.719	3216	3.08	1.47
2	3.540	3360	5.64	1.46
3	3.432	3453	8.01	1.45
4	3.353	3524	10.25	1.45
5	3.291	3582	12.40	1.44
6	3.239	3632	14.48	1.44
7	3.195	3675	16.50	1.44
8	3.156	3714	18.46	1.44
9	3.121	3749	20.38	1.43
10	3.090	3781	22.26	1.43
20	2.878	4016	39.46	1.41
30	2.748	4175	54.79	1.40
40	2.652	4299	68.90	1.39
50	2.576	4403	82.11	1.38
60	2.512	4493	94.61	1.37
70	2.457	4574	106.5	1.36
80	2.409	4647	117.9	1.35
90	2.366	4714	128.9	1.35
100	2.326	4777	139.5	1.34

It should be remembered that the surface micro-hardness variation is a weak function of the indentation size as seen from the semi-general micro-hardness correlation, Eq.(2.13). By means of simple calculations, it can be deduced that an increase by 50% in the indentation size will result in only an 11% decrease in the micro-hardness value. In the remainder of this work the "contact hardness, H_c" will replace the "hardness, H" in all equations and definitions.

In many practical applications of thermal contact conductance, the relative contact pressure lies around $P/H_c = 10^{-3}$ and the surface parameters σ and m are average values. Hence, to minimize the 11% decrease in the hardness over this wide range of relative contact pressure, it seems reasonable to assume that the contact hardness can be determined corresponding to an average contact spot radius, denoted by the contact radius a_c, calculated at $P/H_c = 10^{-3}$. This means that the contact radius, a_c, will be assumed constant over the specified range of relative contact pressure while the number of contacts increases significantly, as shown in Table 3.1, with increasing contact pressure. The above assumption is partially justified by:

1) The fact that, as the applied load increases, the existing contacts grow in size which results in a lower hardness

value. However, the addition of new, but smaller, contacts having higher hardness values may result in an average hardness value which remains relatively constant and equal to the contact hardness.

2) The work of Yovanovich and his co-workers [35-38], over a narrow range of contact pressures and limited experimental data, tended to support this idea.

However, one of the objectives of the experimental program is to verify this assumption for different materials having different micro-hardness variations over a wide range of contact pressures and surface parameters. On the basis of the previous assumption, the contact radius is given by (Table 3.1):

$$a_c = 0.38\ (\sigma/m) \tag{3.48}$$

but it has to be determined as a function of the surface parameters regardless of the value of P/H_c.

For a set of contact conditions, the determination of the appropriate contact hardness H_c corresponding to the contact radius a_c, requires knowledge of the surface micro-hardness variation obtained by means of a spherical indenter. Unfortunately, to the writer's knowledge, such results do not exist. The only choice available is to use Vickers micro-hardness variation. Reti [67]

reported micro-hardness values obtained with triangular and square-based pyramid (Vickers) indenters. The tests were made on different materials, such as steel, beryllium, aluminum alloys and rocksalt, using different loads in the range of 0.05-4.91N. The results showed micro-hardness variation for these materials. However, good agreement between the two hardness values was obtained under the same load for the same material, despite the fact that the two indenters were different in shape and, therefore, gave dissimilar indentation geometries. This finding was also confirmed independently by Williams [68] and Mulhearn [65] for Vickers and spherical indenters. Mulhearn [65] explained this agreement between the hardness values for these indenters by the fact that the deformation patterns for blunt indenters, whose semi-angles are equal to or greater than 68°, are all very similar irrespective of the indenter shape.

In view of the above, one can determine the contact hardness for a set of micro-contacts on the basis of equal indentation areas. In other words, the contact hardness value can be estimated from Vickers micro-hardness variation as a function of the contact radius a_c. The relation between Vickers diagonal d_v and the contact radius a_c, based upon equal areas, is given by:

$$d_v = \sqrt{2\pi}\, a_c \tag{3.49}$$

or

$$d_v = 0.95\ (\sigma/m) \tag{3.50}$$

Since the Vickers micro-hardness variation can be expressed by:

$$H_v = c_1\, d_v^{c_2} \tag{2.1}$$

substituting Eq.(3.50) into Eq.(2.1) results in

$$H_c = c_1(0.95\ \sigma/m)^{c_2} \tag{3.51}$$

where σ is in μm and c_1 and c_2 are the Vickers micro-hardness correlation coefficients. These coefficients must be determined from the micro-hardness measurements of the softer surface.

From the thermal design viewpoint, a simple expression for predicting the contact hardness of the previously mentioned materials would be valuable. Therefore, substituting Eq.(3.50) into the semi-general micro-hardness correlation, Eq.(2.13), yields:

$$H_c = (12.2 - 3.54\ H_m)(\sigma/m)^{-0.26} \tag{3.52}$$

where H_m and H_c are the macro and contact hardnesses respectively in GPa. σ is the effective RMS roughness in μm while m is the effective surface mean absolute slope.

Strictly speaking, Eq.(3.52) is only an approximate expression and should not be used if facilities to measure the actual surface

micro-hardness variation are available. However, it may be useful for the thermal analyst who requires an engineering estimate of the contact hardness. In other words, an engineering estimate of the contact hardness will give a better estimate of the thermal joint conductance than will the macro-hardness.

3.3 Thermal Gap Conductance

The purpose of this section is to review briefly the model proposed by Yovanovich et al [55] for predicting the contribution of heat conduction through a gas filling the gaps between two conforming rough surfaces in contact. Similar to other proposed gas conductance models, this new model incorporates the two parallel isothermal smooth surface gas conductance model and considers the effect of joint surface roughness and gas thermal properties. However, this new model accounts for the statistical local variation in the gap thickness due to the joint roughness and applied contact pressure.

3.3.1 Thermal Resistance Between Two Parallel Isothermal Surfaces

Conduction heat transfer through a gas layer bounded by two parallel isothermal smooth surfaces can take place in different flow regimes. These flow regimes are characterized by the ratio of the gas molecular mean free path, Λ, to the distance separating the two surfaces, t, i.e., Knudsen number K_n.

When the gas molecular mean free path is orders of magnitude smaller than the distance separating the two surfaces ($K_n < 0.01$), the gas can be treated as a continuum. Thus, continuum concepts can be applied to Fourier's equation and the continuum gas resistance is given by:

$$R_{g,c} = t/k_g A_g \tag{3.53}$$

When the gas molecular mean free path is one order of magnitude smaller than the distance separating the two surfaces ($0.1 < K_n < 0.01$), the temperature of the gas molecules next to the surface becomes slightly different from the surface temperature. This is due to the slip of the gas molecules at the surface (temperature jump phenomenon). In this slip flow regime, Kennard [69] showed that Fourier's equation can be applied by increasing the gap thickness at each surface by an additional distance to maintain a linear temperature gradient normal to the two surfaces. This additional distance is called the temperature jump distance, g, and may be expressed by the following equation [69]:

$$g = \frac{(2-\alpha)}{\alpha} \frac{2\gamma}{\gamma+1} \frac{\Lambda}{Pr} \tag{3.54}$$

Therefore, the slip gas resistance is given by:

$$R_{g,s} = (t+M)/(k_g A_g) \tag{3.55}$$

where M is the effective temperature jump distance for the two surfaces defined as:

$$M = g_1 + g_2 = \alpha \beta \Lambda \tag{3.56}$$

For pure gases, the accommodation parameter, α, is given by [31]:

$$\alpha = \frac{(2-\alpha_1)}{\alpha_1} + \frac{(2-\alpha_2)}{\alpha_2} \tag{3.57}$$

and the gas parameter β is defined as:

$$\beta = \frac{2\gamma}{(\gamma+1)} \frac{1}{Pr} \tag{3.58}$$

The gas mean free path must be determined corresponding to the gas pressure and the joint absolute mean temperature using the following relation:

$$\Lambda = \Lambda_o (T/T_o) (P_{go}/P_g) \tag{3.59}$$

The mean free paths of pure gases, Λ_o, are commonly reported in the literature at normal pressures, P_{go}, and absolute temperatures, T_o.

The magnitude of the effective temperature jump distance depends upon a number of factors such as:

1. Gas type and pressure;
2. Gas molecular mean free path;
3. Temperature level of the two surfaces;
4. Surface material and roughness:
5. Presence of oxide or contaminant layers;
6. Presence of adsorbed gases on the surface.

When the gas mean free path is large compared to the distance separating the two surfaces ($K_n > 10$), the collisions between the gas molecules can be considered negligible. In this free molecule regime, heat is transferred by each molecule from the hot surface to the cold one. Therefore, the resistance to heat conduction in this regime can be written as [55]:

$$R_{g,f} = M/(k_g A_g) \tag{3.60}$$

Sherman [91] demonstrated by means of a large number of experimental data that the following simple but accurate relation:

$$Q_t/Q_f = 1/(1+Q_f/Q_c) \tag{3.61}$$

can be used in predicting the heat flow by conduction between the

two surfaces in the transition flow regime. In this regime, the gas molecular mean free path is comparable in size to the distance separating the two surfaces ($0.1 < K_n < 10$).

Since the thermal resistance is defined as:

$$R = \Delta T/Q \tag{3.62}$$

equation (3.61) can be written in terms of the thermal resistance of each regime, after rearranging, as:

$$R_{g,t} = R_{g,c} + R_{g,f} \tag{3.63}$$

Substituting Eqs. (3.53) and (3.60) into Eq. (3.63), the transition thermal resistance across the gas layer can be expressed by:

$$R_{g,t} = (t+M)/(k_g A_g) \tag{3.64}$$

which is exactly the slip flow regime thermal resistance expression, Eq. (3.55).

Careful examination of Eqs. (3.53), (3.55) and (3.60) indicates that Eq. (3.55) can be considered the general form of which the other two equations are special cases. In other words, Eq. (3.55) satisfies the conditions that as the gas mean free path becomes very

small, the effective temperature jump distance, M, can be considered negligible and Eq. (3.55) reduces to Eq. (3.53). On the other hand, when the gas mean free path becomes very large, the gap thickness, t, can be assumed negligible relative to the effective temperature jump distance and, therefore, Eq. (3.55) gives the thermal resistance in the free molecule regime.

More significant is the fact that the conduction modes, across the gap between two parallel isothermal smooth surfaces, are characterized by the ratio of the gap thickness, t, to the effective temperature jump distance, M. This ratio will be denoted by the gap-temperature jump parameter, YH, and defined as:

$$YH = t/M \tag{3.65}$$

The gap-temperature jump parameter will be used to indicate the predominant mode of conduction between conforming rough surfaces in contact. In this case, the gap thickness t will be considered equal to the separation between the mean planes Y.

3.3.2 Application of Parallel Smooth Surface Model to Conforming Rough Surfaces

The gap conductance expression for conforming rough surfaces was developed by:

1. Assuming the variation of the surface temperature due to the surface roughness is negligible;
2. Dividing the gap area into a number of individual flux tubes of equal areas but of different thickness;
3. Determining the resistance of all the flux tubes having a given thickness, corresponding to a certain fraction of the gap area, using Eq. (3.55);
4. Adding this resistance in parallel with the resistance of other gap areas.

The resultant expression from this summation process was expressed by the following integral expression [55]:

$$\frac{1}{R_g} = k_g \int_o^{A_g} \frac{dA_g}{(t+M)} \tag{3.66}$$

By assuming the two contacting surfaces have a Gaussian height distribution, an expression for the fraction of the projected gap area, dA_g, was obtained and is presented directly here as:

$$dA_g = \frac{A_a}{\sqrt{2\pi}} \exp[-(Y/\sigma - t/\sigma)^2/2]\, d(t/\sigma) \tag{3.67}$$

where t is the local gap thickness variation. For more detail the reader is referred to Ref. [55].

By combining Eqs. (3.66) and (3.67) the following integral

expression for the gap resistance between conforming rough surfaces was developed:

$$\frac{1}{R_g} = \frac{k_g A_a}{\sigma\sqrt{2\pi}} \int_o^\infty \frac{\exp[-(Y/\sigma - t/\sigma)^2/2]}{(t/\sigma + M/\sigma)} d(t/\sigma) \tag{3.68}$$

Therefore, the dimensionless gap conductance can be expressed as:

$$C_g = \frac{K}{m\sqrt{2\pi}} \int_o^\infty \frac{\exp[-(Y/\sigma - t/\sigma)^2/2]}{(t/\sigma + M/\sigma)} d(t/\sigma) \tag{3.69}$$

where the dimensionless parameters C_g and K are given by:

$$C_g = \sigma h_g / m k_s \tag{3.70}$$

and

$$K = k_g / k_s \tag{3.71}$$

By setting $u^2 = t/\sigma$, the following transformed expression of Eq. (3.69) was recommended by Zwart [70]:

$$C_g = \sqrt{\frac{2}{\pi}} \frac{K}{m} \int_0^{\infty} \frac{\exp[-(Y/\sigma - u^2)^2/2]}{(u^2 + M/\sigma)} u \, du \qquad (3.72)$$

Also, he suggested the following approximation:

$$C_g = \sqrt{\frac{2}{\pi}} \frac{K}{m} \int_0^{3} \frac{\exp[-(Y/\sigma - u^2)^2/2]}{(u^2 + M/\sigma)} u \, du \qquad (3.73)$$

for numerical computational purposes because the area under the curve becomes negligible for $u > 2.5$.

3.4 Engineering Approximation for the Gap Conductance Model

Inspection of the gap conductance model, Eq. (3.69), reveals that the theoretical prediction is a function of the relative mean plane separation, Y/σ, and the ratio of the effective temperature jump distance to the joint roughness, M/σ. Unfortunately, a closed form expression for the gap conductance model is not available to permit a direct examination of the effect of these two parameters upon the theoretical predictions. The simple gap conductance model proposed by Yovanovich [31], however, has this advantage as well as it can be considered as a good engineering approximation for the proposed gap conductance model. It is the purpose of this section to explore these two advantages.

Yovanovich [31] assumed that the gap heat transfer between two conforming rough surfaces can be modelled as heat transfer between two parallel isothermal flat plates which are separated by an effective gap thickness t_e. He considered the effective gap thickness is equal to the separation between the joint mean planes, Y, and the effective temperature jump distance, M. Thus, the gap conductance can be expressed as [31]:

$$h_g = \frac{k_g}{Y + M} \tag{3.74}$$

and in dimensionless form as:

$$C_g = \frac{K/m}{Y/\sigma + M/\sigma} \tag{3.75}$$

If we define the gap-temperature jump parameter, YH, as:

$$YH = (Y/\sigma)/(M/\sigma) \tag{3.76}$$

then Eq. (3.75) can be written as:

$$C_g = \frac{K/m}{Y/\sigma(1+1/YH)} \tag{3.77}$$

A graphical comparison between the proposed gap model, Eq. (3.69), and the Yovanovich model, Eq. (3.77), in terms of the gap-temperature jump parameter, is shown in Figure 3.3 in the

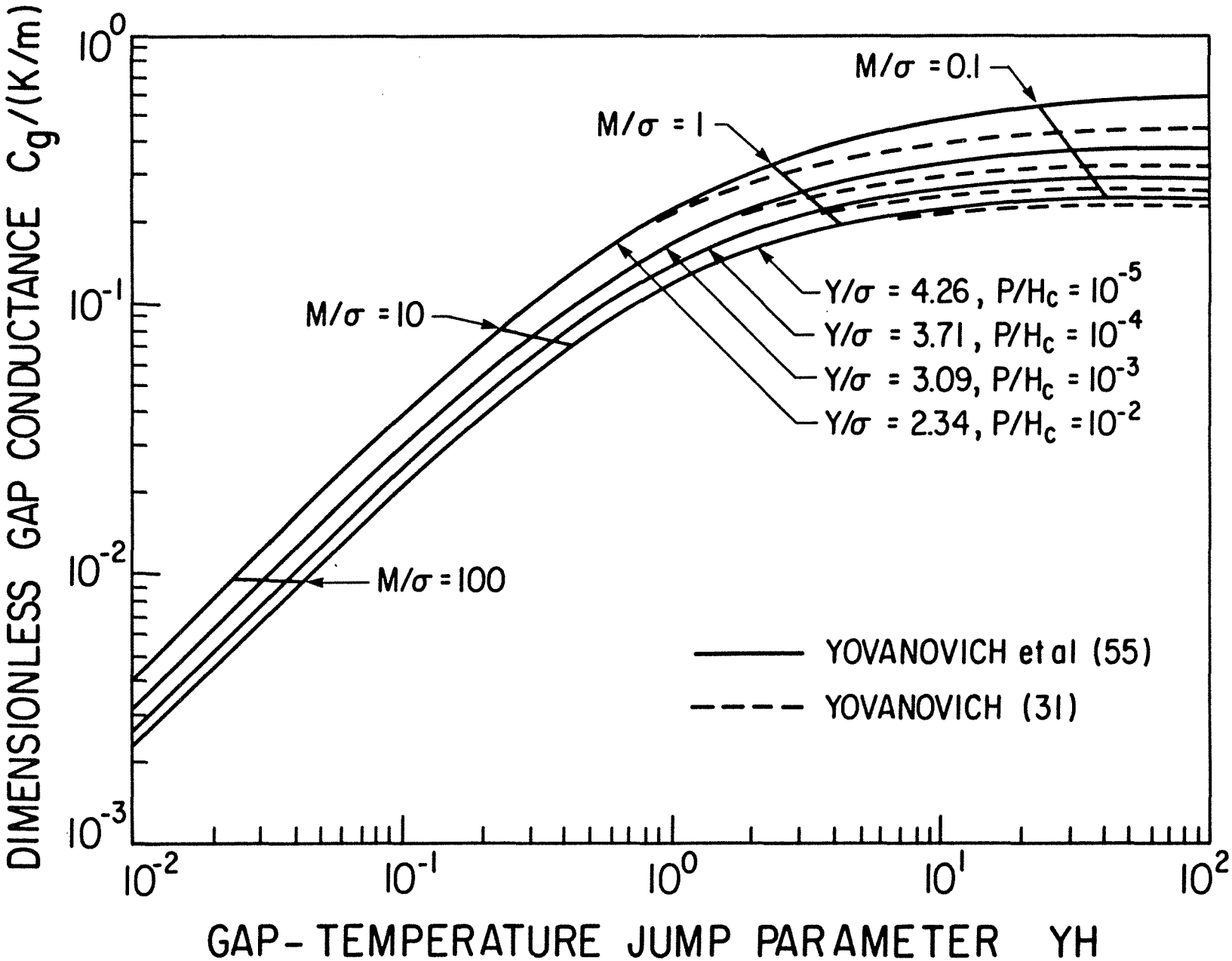

Figure 3.3: Comparison of Different Predictions: The Proposed Gap Conductance Model vs. the Yovanovich Model

range of $2.34 \leq Y/\sigma \leq 4.26$ or, alternatively, in the range of $10^{-2} \geq P/H_c \geq 10^{-5}$.

Figure 3.3 shows that the two gap models predict essentially the same conductance value in the range of $10^{-2} \leq YH < 1$ for any particular value of Y/σ. Also, the prediction is approximately proportional to the parameter YH. In other words, the gap conductance is fully dependent upon the effective temperature jump distance since the latter is, in general, much greater than the separation between the mean planes in the above range of YH.

In the range of $1 \leq YH < 10$, Figure 3.3 shows that the Yovanovich gap conductance model slightly underpredicts the gap conductance relative to the proposed gap model. However, the Yovanovich model can be considered as an accurate approximation for the present model because the deviation between the two models ranges from approximately 5% at $Y/\sigma = 4.26$ up to 17% at $Y/\sigma = 2.34$. Also, Figure 3.3 demonstrates clearly that the gap conductance prediction equally depends upon the mean plane separation and the effective temperature jump distance in this range of YH.

It is evident from Figure 3.3 that the predicted gap conductance by either of the two models is a weak function of the parameter YH in the range of $10 < YH \leq 100$ for any particular value of Y/σ. In this range of YH it can be said that the gap

conductance prediction depends strongly upon the relative separation between the mean planes, Y/σ, and is a weak function of the parameter M/σ. This can be explained by the fact that the relative mean plane separation, Y/σ, is orders of magnitude greater than the ratio of the effective temperature jump distance to the joint roughness, M/σ; this is the continuum flow regime.

On the other hand, Figure 3.3 shows that the Yovanovich gap conductance model underpredicts the gap conductance relative to the proposed model in the same range of YH. The deviation between the two models varies from 6% at $Y/\sigma = 4.26$ up to 15% at $Y/\sigma = 3.09$ and increases to 28% at $Y/\sigma = 2.34$. Keeping in mind that in the range of $2.34 \leq Y/\sigma < 3.09$ $(10^{-2} \geq P/H_c > 10^{-3})$ the contact conductance dominates the prediction of the joint conductance, it can be concluded that the Yovanovich gap model still can be considered as a good approximation for the proposed gap conductance model. From the above discussion the following important conclusions can be drawn:

1. The Yovanovich gap conductance model, Eq. (3.77), is an accurate, simple engineering approximation for the proposed gap conductance model in the range of $10^{-2} \leq YH \leq 10^{2}$.

2. The gap-temperature jump parameter YH successfully characterizes the gap conduction mode between conforming rough surfaces for either of the two models.

3. In the range of $YH < 1$ the gap conductance is fully dependent upon the effective temperature jump distance and the prediction is a strong function of the gas thermal properties.

4. In the range of $1 < YH < 10$ the predicted gap conductance is equally dependent upon the joint mean plane separation and the effective temperature jump distance.

5. In the range of $YH > 10$ the prediction of the gap conductance is fully dependent upon the relative mean plane separation. This strengthens the importance of the appropriate contact hardness value for determining the relative mean plane separation which is essential for the prediction of the gap conductance in this range of YH.

Finally, it should be mentioned that one of the objectives of the experimental program is to verify the validity of the gap conductance model over these three different ranges of the parameter YH.

3.5 Summary of the Formulas

The thermal joint conductance for conforming rough surfaces can be expressed, approximately, as:

$$C_j = C_c + C_g \tag{3.78}$$

where C_c and C_g are the dimensionless contact and gap thermal conductances, respectively.

The dimensionless contact conductance is given by:

$$C_c = \frac{\sigma h_c}{m k_s} = 1.25(P/H_c)^{0.95} \tag{3.44}$$

where h_c is the contact conductance, σ and m are the effective surface parameters, k_s is the harmonic mean thermal conductivity, P is the applied contact pressure and H_c is the contact hardness.

The contact hardness requires knowledge of:

1. the softer surface Vickers micro-hardness variation which can be correlated by:

$$H_v = c_1 d_v^{c_2} \tag{2.1}$$

where d_v is the indentation diagonal, c_1 and c_2 are the correlation coefficients;

2. the contact radius a_c, which is a function of the effective surface parameters, σ and m, and is equal to:

$$a_c = 0.38(\sigma/m) \quad ; \tag{3.48}$$

3. the relation between contact radius a_c and the Vickers indentation diagonal d_v based upon equal areas, which can be expressed by:

$$d_v = \sqrt{2\pi}\, a_c \tag{3.49}$$

or

$$d_v = 0.95(\sigma/m) \quad . \tag{3.50}$$

Therefore, the contact hardness can be expressed by:

$$H_c = c_1(0.95\ \sigma/m)^{c_2} \tag{3.51}$$

The dimensionless gap conductance is given by

$$C_g = \frac{\sigma\, h_g}{m\, k_s} = \frac{K}{m\sqrt{2\pi}} \int_0^\infty \frac{\exp[-(Y/\sigma - t/\sigma)^2/2]}{(t/\sigma + M/\sigma)}\, d(t/\sigma) \tag{3.69}$$

where K is the ratio of the gas conductivity to the harmonic mean thermal conductivity, t/σ is the relative local gap thickness, Y/σ is the relative mean plane separation and M is the effective temperature jump distance.

The transformed approximate version of the above expression for computational purposes is:

$$C_g = \sqrt{\frac{2}{\pi}} \frac{K}{m} \int_0^3 \frac{\exp[-(Y/\sigma - u^2)^2/2]}{(u^2 + M/\sigma)} u \, du \tag{3.73}$$

where $u^2 = t/\sigma$.

The mean plane separation Y/σ is related to the relative contact pressure by the following relation:

$$\frac{P}{H_c} = \frac{A_r}{A_a} = \frac{1}{2} \operatorname{erfc}(Y/\sqrt{2\sigma}) \tag{3.43}$$

The approximate expressions for the relative mean plane separation, Y/σ, and the mean contact spot radius, a, are:

$$Y/\sigma = 1.184 \, [-\ell n(3.132 \, P/H_c)]^{0.547} \tag{3.45}$$

$$a = 0.99(\sigma/m) \, [-\ell n(3.132 \, P/H_c)]^{-0.547} \tag{3.46}$$

CHAPTER 4

EXPERIMENTAL APPARATUS AND TEST PROCEDURE

4.1 Experimental Apparatus

The experimental tests were carried out in a modified vacuum system consisting of: a) test chamber, b) loading mechanism, c) environment control system, and d) measurement system. A general view of the test apparatus components is shown in Figure 4.1.

4.1.1 Test Chamber

The test chamber consisted of a base plate and a pyrex bell jar enclosing a 25mm diameter test column. The test column consisted of, from top to bottom: the heater block, the upper heat meter, the test specimen pair, the lower heat meter, the heat sink and the load cell. An external view of the test column is shown in Figure 4.2 with a representative sketch shown in Figure 4.3.

Generally, two cylindrical specimens, 25mm in diameter by 45mm long, were held coaxially between the upper and lower Armco iron heat flux-meters having the same nominal dimensions. The upper heat meter was fitted into a 25mm diameter recess in a cylindrical brass heating block containing two 100 Watt pencil-type electrical heaters. An aluminum cold plate heat sink, having a 25mm diameter

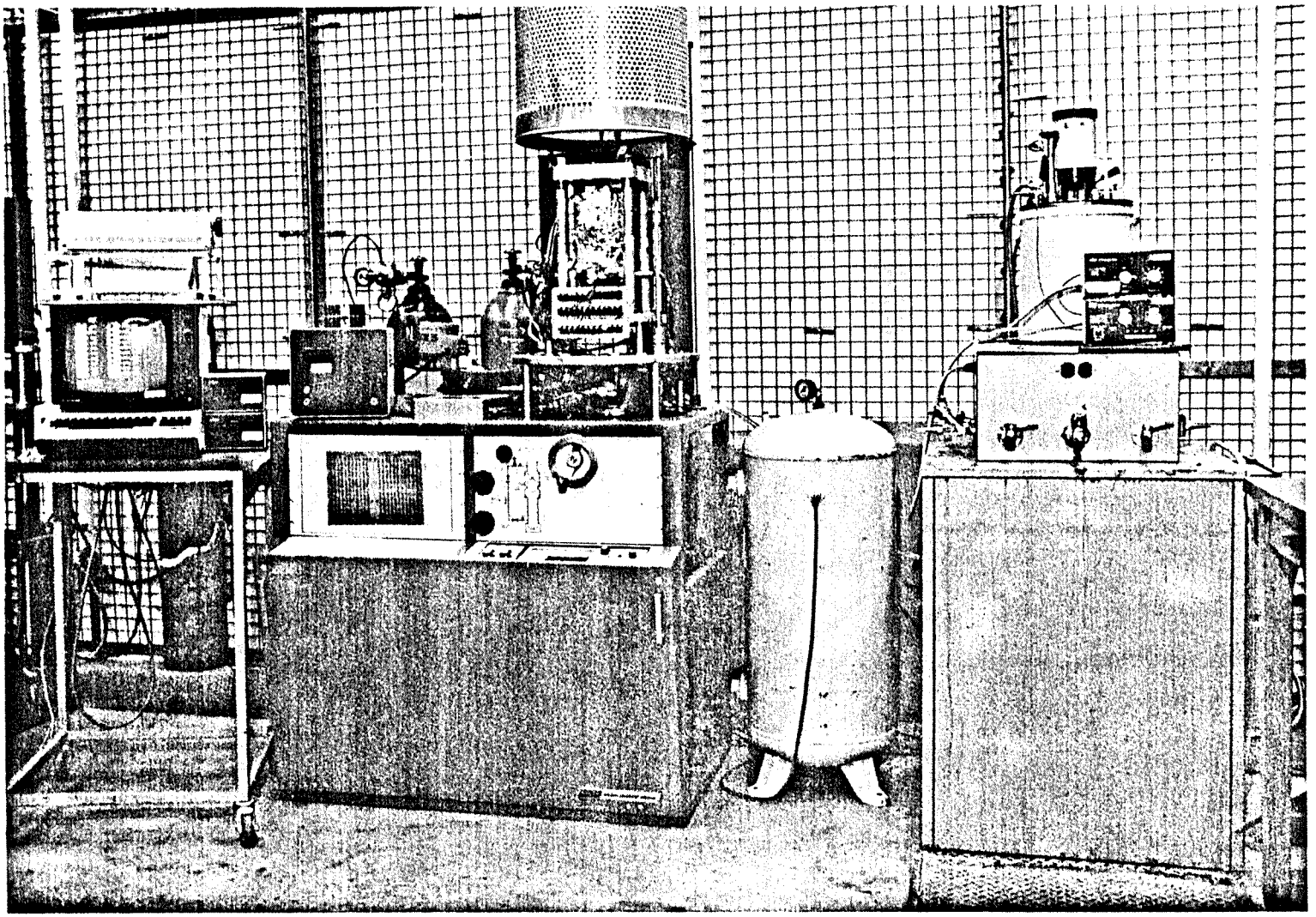

Figure 4.1: General View of Test Apparatus

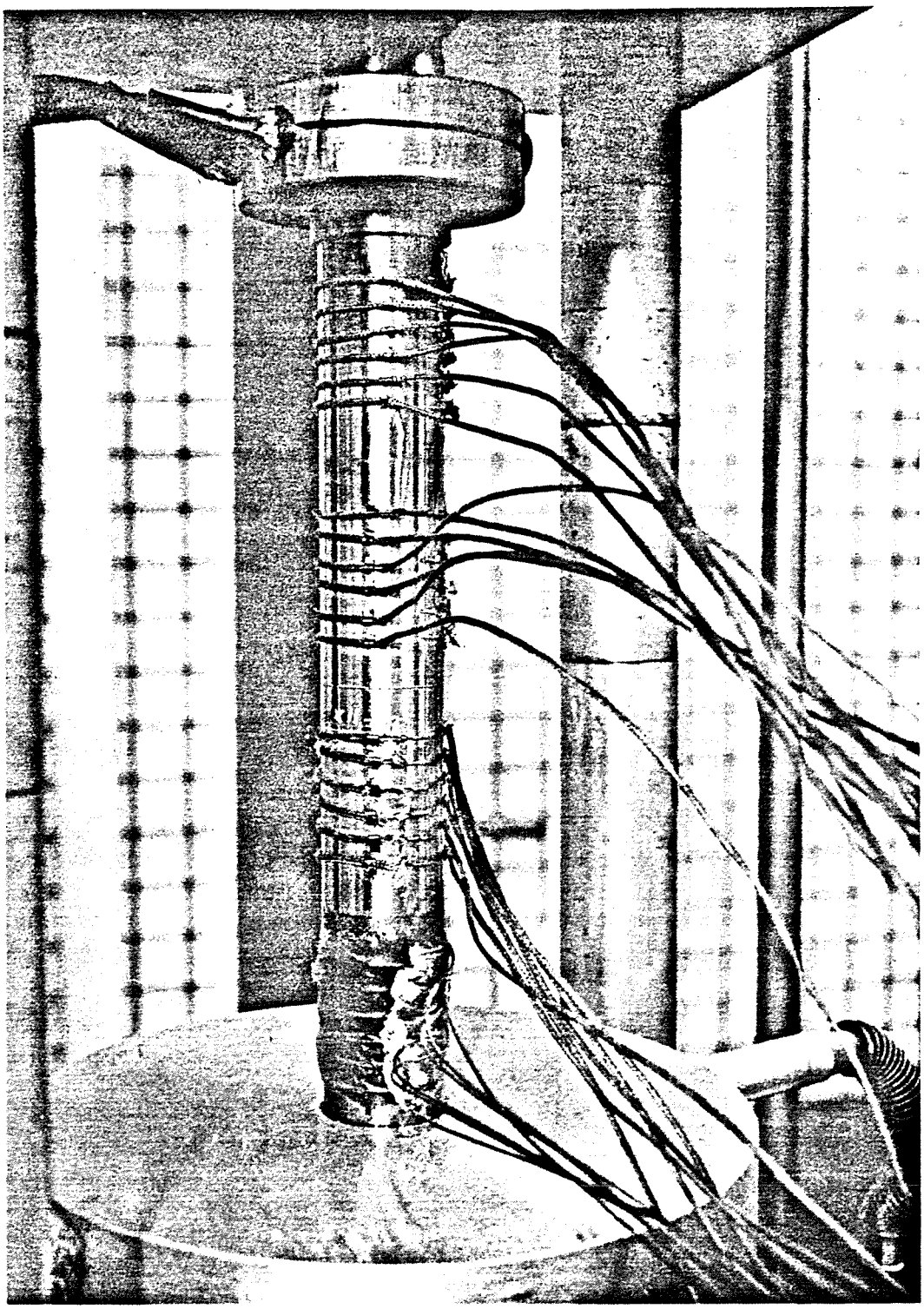

Figure 4.2: General View of Test Column

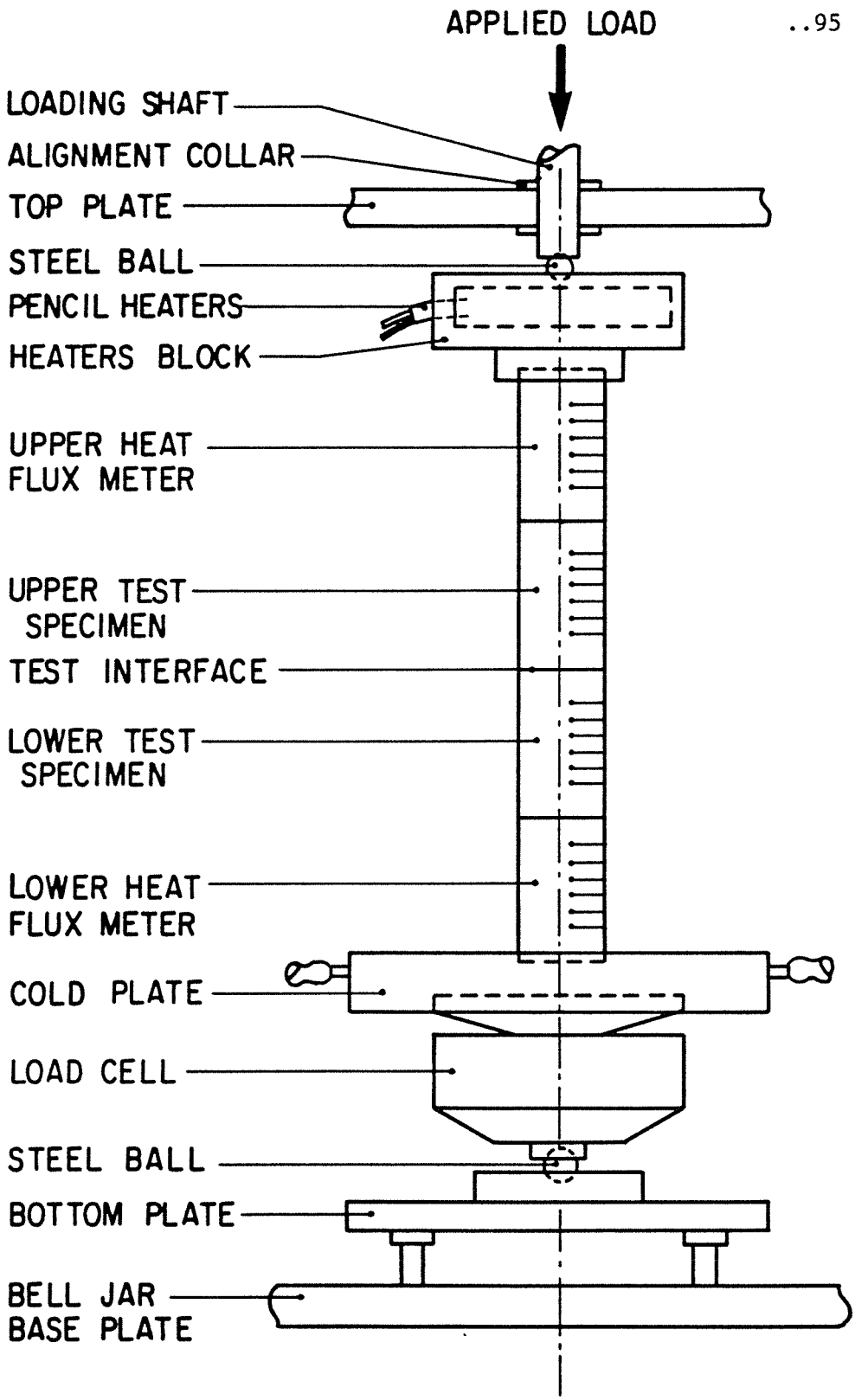

Figure 4.3: Schematic of Test Column

recess, supported and located the lower heat meter coaxially with the column axis.

The main heater was energized by a power supply built in the datalogger and automatically regulated in steps. The voltage supplied to the secondary heater could be adjusted independently via an auto-transformer connected to a separate main. By means of these elements the desired input power level between zero and 200 Watts was obtained.

When tests were conducted in a gaseous environment, the upper Armco iron heat meter was removed to reduce the test column resistance and, consequently, the heat loss. The test specimens were used as heat-flux meters and the heat flux was determined from the temperature gradient along the test specimens and the previously determined thermal conductivities using Fourier's equation. In general, the heat loss from the test column, as determined by the heat meters, was less than 5% under vacuum conditions and less than 10% in the presence of a gaseous medium.

Cooling was accomplished by using a closed loop water chiller system which maintained the cooling water temperature constant and equal to 288K. Flexible bellows were incorporated in the cooling water flow lines inside the test chamber to facilitate the movement of the cold plate under loading. The cold plate was concentrically

mounted on the load cell in order to eliminate the load measurement error due to high working temperatures or a large temperature gradient across the load cell.

Services, such as cooling water lines, heater power lines, load cell cable and thermocouple leads, were introduced into the test chamber through the base plate by means of feedthroughs. Feedthroughs had also been provided for the loading arm, controlled leak and the pressure gauge.

4.1.2 Loading Mechanism

A continuous range of axial loads between 90 and 4460N could be applied to the test column via a lever system having a mechanical advantage approximately 2. The lever system was activated by means of a diaphragm-type air cylinder located outside the test chamber which avoids complications due to an accidental air leak. The loading road feedthrough was sealed by a flexible diaphragm in order to facilitate the movement of the loading arm during loading. The contact pressure could be imposed by pressurizing the air cylinder from a large reservoir connected to a 827 kPa air line via a solenoid valve and a regulating valve.

For a particular run, the required load level was applied automatically with the aid of a microcomputer which:

a) opened the solenoid valve to pressurize the air reservoir and, in turn, the air cylinder;
b) monitored the load cell reading during loading until the required laod level was achieved; then,
c) closed the solenoid valve.

The regulating valve opening was adjusted in a separate experiment in order to avoid second loading effect at any load level; the latter being applied incrementally in 23 steps for each specimen pair.

By means of these elements a stable contact load was applied to the test column via a 5mm ball inserted between two spherical seatings on the loading shaft and the heater block. The contact load was transmitted to an adjustable spherical seating located on the bottom plate through a 13mm ball installed in a load button which was inserted in the centre of the load cell base. Particular attention was paid to the test column alignment in order to ensure that the contact load would be applied centrally and uniformly over the test column interfaces.

4.1.3 Environment Control System

The environment control system consisted of mechanical and oil diffusion pumps, regulated nitrogen and helium supplies, adjustable leak and related valves and piping. For measurements

in vacuum, a vacuum better than 10^{-5} torr was maintained in the test chamber using the mechanical pump in series with the diffusion pump.

The gaseous fluid was introduced into the test chamber by means of the controlled leak feedthrough. The Nitrogen or Helium gas pressure was controlled successfully over a long period of time by:

a) regulating the gas supply;

b) throttling the mechanical pump;

c) equalizing the adjustable leak.

4.1.4 Measurement System

The measurement system consisted of a load cell, a pressure gauge, thermocouples, a datalogger connected to a microcomputer, and related circuits and wiring.

The applied contact load was measured by means of a calibrated load cell, in conjunction with a 10V DC power supply, built into the datalogger. The contact load was determined by monitoring both the sense and output voltages, which eliminated load measurement error due to power supply fluctuation. The sense voltage was measured in microvolts across a 10 ohm resistance in series with a 5600 ohm resistance, both connected in the sense measuring circuit. The load

measurement system, as a whole, was calibrated in a separate experiment, thus, the load was never in error.

A metal diaphragm-type pressure gauge was employed in measuring the test chamber pressure. The pressure gauge is a self-contained unit with the sensor, associated electronics, and power supply mounted in a dust-proof box. The pressure gauge VDC output signal was measured in microvolts by incorporating 3900 ohm, 33 ohm, and 10 ohm resisters, connected in series, in the pressure gauge measuring circuit. The voltage drop across the 33 ohm resistance was used in determining the test chamber pressure in the range of 0.5 to 180 torr. The range between 180 and 760 torr was covered by measuring the voltage drop across the 10 ohm resistance.

In a separate test, the gauge zero was adjusted after the measuring circuit had been electrically screened and calibrated. The gauge zero adjustment was also checked out before conducting any thermal test. The error of this instrument for pressure measurements was ±0.05% full scale, i.e., ±0.5 torr.

All temperature measurements were made with 30 gauge type 'T' copper-constantan thermocouples. Copper-constantan quick change connectors were employed to:

a) facilitate specimen change; and

b) eliminate possible error due to the introduction of additional junctions.

Thermocouple extension leads, 24 gauge, led out of the test chamber through their feedthrough to a terminal strip box. The thermoelectric voltages were measured with a resolution of 0.1μV. Terminal strip temperature compensation was estimated with the aid of a temperature transducer housed in the box. Absolute temperatures were determined from the thermocouple emf after compensation using an eighth order calibration polynomial.

All measuring circuits were screened and calibrated electrically. The voltage signals could be measured accurately to 0.1μV with the datalogger linked to the microcomputer. The software required for the measurement and for the data acquisition were written by the author. The data acquisition program assisted in reading the voltage signals and in processing the data. Another part of the code consisted of a number of subroutines which assisted in controlling the experiment. The vacuum tests were conducted in automatic mode for the 23 load level, while a semi-automatic mode was employed during the gas tests. Generally, the experiment duration for the 23 load level was 5 days for a single environment test and 18 days for a multi-environment test. A schematic representation of the measurement and control system is shown in Figure 4.4.

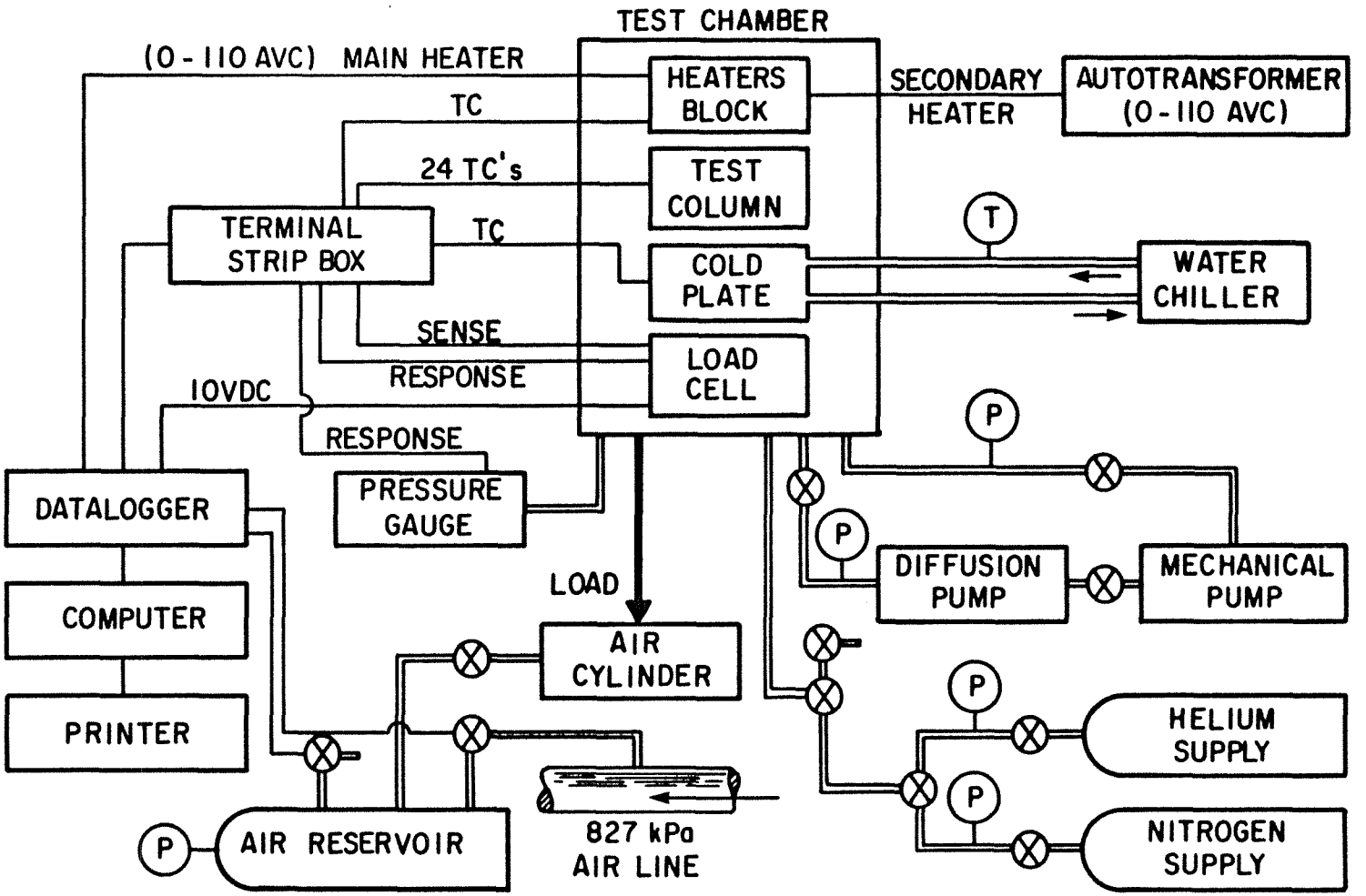

Figure 4.4: Schematic Diagram of Measurement and Control System

4.2 Preparation of Test Specimens

Contact surfaces were prepared on the faces of 25mm diameter by 45mm long cylindrical specimens. The Stainless Steel 304 and Nickel 200 specimens were fabricated from commercial bars taken from stock, while the Zr-2.5wt%Nb and Zr-4 test specimens were cut from bars supplied by the Whiteshell Nuclear Research Establishment, AECL.

Each specimen was first machined on a lathe and then finely ground to the required dimensions. Following this, six holes, of 0.64mm diameter and 2.5mm deep, were radially drilled for the thermocouples. The first hole was located 10mm from the contact surface and the remainder were accurately located 5mm apart. Next, all the contact surfaces were mechanically lapped.

Most of the surfaces prepared by mechanical lapping were found to be non-parallel and approximately spherical. Therefore, these surfaces were lightly re-ground and checked out for parallelism and squareness. Next, the specimens were carefully hand-lapped smooth and ultrasonically cleaned. Specimen cleaning was accomplished through the use of an ultrasonic cleaning bath containing, successively, alkaline detergent, acetone, and distilled water. This procedure ensured the removal of:

a) the residue from the lapping compound;

b) the oily surface films; and

c) the debris from the thermocouple holes.

The specimens were then dried in a stream of warm air.

Finally, the flatness deviation of the contact surface of each specimen was checked out using Krypton 86 monochromatic light source and optical flat. In general, the departure from flatness was estimated to be less than 1μm; typically between one or three fringes of light (one fringe is equal to 0.3μm for Krypton 86). After inspection, the specimens were cleaned again, kept in groups, and stored in vacuum to prevent oxidation until they were used in the thermal tests.

Before testing any material, the cylinders chosen as the upper specimens in the test column were bead-blasted with different grades of glass beads using a device designed by the author. After this process, the roughened specimens were cleaned using the same cleaning procedure. The remaining specimens were used as lapped in the thermal tests. One of these specimens was selected randomly to determine the Vickers micro-hardness variation for this group.

Surface characteristics of each contact surface were estimated by means of a Taylsurf5 profilometer measuring system. Surface

parameters were determined along ten different radial directions using:

a) the maximum permissible higher magnification;

b) different "cut-off" lengths;

c) "filtered" and "unfiltered" profiles; and

d) high resolution pick-up.

The surface parameters were estimated to be accurate to within ±10% employing the information obtained using this technique in conjunction with the methodology outlined in Appendix B. Based upon the texture measurements of the roughened surfaces, as well as their appearance as shown in Figure 4.5, these surfaces were judged to be nearly Gaussian without any directional properties. At this stage, the test specimens were cleaned and kept in pairs. Complete details of the bead-blasting technique, as well as the topographical parameters of each contact surface, are given in Appendix B.

Prior to the thermal test, six copper-constantan thermocouples were inserted in the holes along the specimen, spot welded to the surface, and their relative locations were measured by means of a travelling microscope. The thermocouple leads were wrapped around the specimen to reduce temperature measurement error, and securely fastened to the specimen with small metallic straps. Several

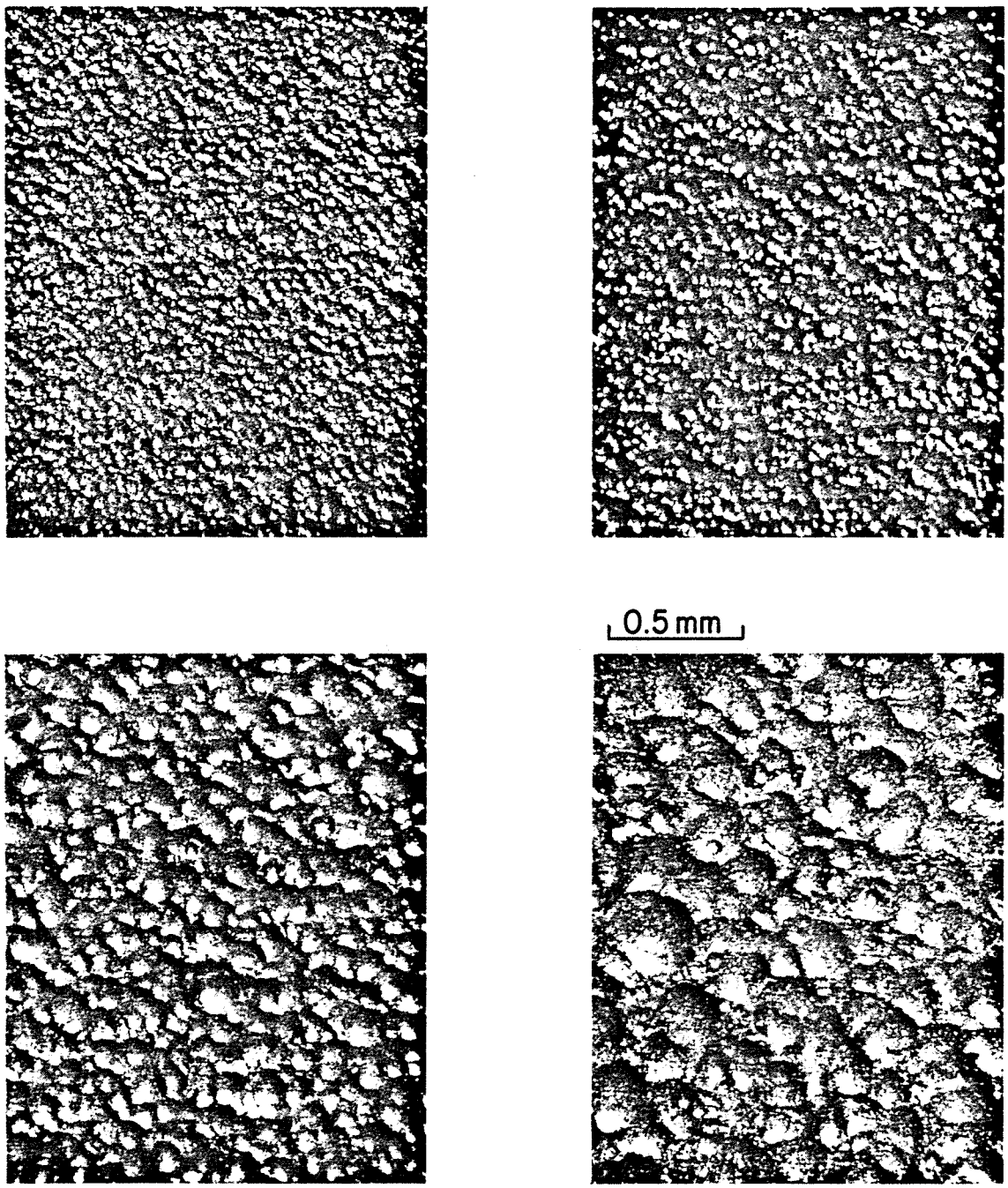

Figure 4.5: Typical Set of Bead Blasted Surfaces

other thermocouple mounting techniques were tried first, but they were found unsatisfactory for high working temperature levels. Before installation in the test column, the thermocouple leads were hooked-up in their connectors and the contact surfaces were cleaned using 1,1,1 trichlorethane.

4.3 Test Procedure

The following test procedure was employed for all of the thermal experiments regardless of the environment type. The datalogger, computer, printer, and the water chiller were powered on. The computer code was loaded and executed, then the test data were entered. All test column interfaces were cleaned and greased with vacuum grease to eliminate contact resistance at these interfaces. Following this, the test specimens were positioned coaxially between the heat-flux meters, and the test column was aligned visually to ensure that the column interfaces remained parallel during testing. An initial load equal to 110N was applied to the test column to assure that misalignment would not occur during evacuation of the bell jar.

The mechanical pump was switched on and the connectors of the thermocouples, as well as the heaters, were plugged in to their respective circuits. The test column was heavily insulated with two layers of Quartz Wool, each 20mm thick. The column was then covered with an aluminum foil heat shield to minimize the heat loss.

The input power to the secondary heater was adjusted manually, the bell jar was carefully lowered, and the test chamber was initially evacuated using the mechanical pump. The diffusion pump was powered on and connected in series with the mechanical pump after 15 minutes. A vacuum pressure below 10^{-5} was achieved after about one hour.

Immediately after lowering the bell jar, the main heater was energized and the initial load was adjusted again via the computer. A routine check for all the measuring circuits was then made and the test chamber was allowed to outgas for approximately three hours. During this period, intermediate temperature checks were made and the secondary heater input power was also adjusted.

After three hours, the computer adjusted the first load level and started to scan the output signals every three minutes. During each scan the computer calculated and displayed all the experimental data such as thermocouple temperatures, contact pressure, test chamber pressure, joint resistance, etc. Also, the computer plotted the change of the joint resistance with time and the temperature gradient along the test pair. When the steady-state criteria were satisfied, the latest experimental data were stored on a disk and printed out. The steady-state criteria were:

1. The joint must be held under these run conditions for at least four hours.

2. The percent difference between the input and output fluxes, determined from the heat meters, must be less than 5% under vacuum conditions, and less than 10% in a gaseous environment.

3. The absolute percent difference between the present joint resistance and the previous one must be less than or equal to 1%.

4. The absolute difference between a particular upper test specimen thermocouple current reading and the previous one must be less than 0.1K.

For vacuum test, the computer increased the contact load automatically to a new preselected level and after about four hours the steady-state was regained and another reading was obtained. This process was repeated for the 23 load levels. In general, the heater electrical power was kept constant and only the contact load was increased. If any subsequent adjustment to the heater power was needed, one hour was allowed before increasing the contact load.

For a single gas test, the test pair was kept at vacuum pressure (better than 10^{-5} torr) for three hours to ensure the gas purity. The heater power and the gas pressure were adjusted and the same procedure was employed. During this type of test, the gas pressure was adjusted from time to time.

For multi-environment tests, the joint was tested under vacuum, nitrogen, and helium conditions. When changing from nitrogen to helium, or vice versa, the test chamber was evacuated to better than 10^{-5} torr for at least 20 minutes, filled with 500 torr of the second gas and then re-evacuated and refilled twice to ensure purity of the gas. The gas pressure was adjusted manually to some chosen value and held almost constant during the run. About one hour was allowed after changing the gas to increase the contact load slightly, then the computer started to scan the different signals. During this period, the heater power was also adjusted to maintain a reasonable interface temperature difference. After the system had attained the new steady-state condtions, another reading was taken. The contact load was either increased by a previously specified increment or held relatively constant while the test chamber environment was changed.

4.4 Uncertainty Analysis

An uncertainty analysis was performed to estimate the maximum uncertainty associated with the measured joint conductance under vacuum, and in Nitrogen and Helium environments. For vacuum tests, the largest uncertainty was found to be 8.1% at the maximum contact pressure for pair PNI0102. The average uncertainty values in the vacuum data were estimated to be: 5.3% for Ni200 pairs, 3.7%

for SS304 joints, 3.6% for Zr-2.5wt%Nb interfaces, and 3.8% for Zr-4 specimens.

For gaseous tests, the largest uncertainty was estimated to be 5.7% at the maximum contact pressure for both Nitrogen and Helium environments. The average uncertainty values in the gaseous tests were: 5.4% under Helium environment, 5.3% in the Nitrogen environment, and 2.7% under vacuum conditions.

For additional details about the maximum uncertainty in the measured joint conductance of each test the reader is referred to Appendix E. Also, Appendix E includes a complete analysis of the estimated maximum uncertainty in the theoretical predictions.

CHAPTER 5

TEST RESULTS AND DISCUSSIONS

5.1 Introduction

An extensive experimental program was carried out under strictly controlled conditions employing carefully prepared and specified contact surfaces to provide accurate data:

1. To verify the assumptions made in the theoretical analysis.

2. To check the validity of the proposed models in vacuum (contact conductance model) and gaseous environments (gap conductance model).

3. To compare other conductance models against the proposed models.

The experimental investigation was restricted to contacts between similar bare metals where one of the contacting surfaces was nearly smooth and flat, and the other was isotropically rough. The roughness parameters of each surface tested, as well as the method of surface preparation, is presented in Table B.4, Appendix B. The materials employed in the test program were Nickel 200, Stainless Steel 304, Zirconium-2.5wt%Nb, and Zircaloy-4. These materials were selected for their wide use in modern technology applications. Also, these

materials possess quite different thermophysical and mechanical properties which allow for a fairly rigorous examination of the proposed models.

The experimental program consisted of two groups of experiments. The first group was performed under vacuum conditions using specimen pairs made of each of the aforementioned materials while the second group was conducted in nitrogen and helium using only Stainless Steel 304 pairs. The experimental data of the two groups are reported in detail in Appendix C. In the following sections the experimental results of each group will be discussed separately.

5.2 Vacuum Tests

Almost four hundred experimental data points have been obtained from four series of tests conducted using joints made from the previously mentioned materials. These series consist of 17 thermal tests, each of about five days duration. These tests covered a broad range of contact pressures, surface textures, and surface micro-hardness variations. In these 17 tests the following procedure was followed:

1. The joint was formed between a rough specimen (odd number) in contact with a "lapped" smooth specimen (even number).

2. Each pair of contacts was made of similar materials and designated by the specimens numbers.

3. The applied contact pressure was automatically increasd by increments over the range of 0.4-8.8 MPa without breaking the vacuum conditions.

4. Contact conductance measurements were determined for the first load cycle under steady-state conditions.

5. Heater electrical input power was maintained as constant, as far as possible, during any particular test.

6. Test results were obtained in vacuum pressures better than 10^{-5} torr.

5.2.1 Data Reduction

Under a given set of contact conditions, the experimental thermal contact conductance value was determined from

$$h_c = \frac{1}{RA_a} = \frac{Q/A_a}{\Delta T} \quad w/m^2K \tag{5.1}$$

where Q/A_a is the heat flux through the joint and ΔT is the temperature drop across the joint. The temperature drop was determined by the microcomputer which performed a linear least-squares fit of the test pair temperatures, extrapolated them to the interface,

and computed the temperature difference between the extrapolated values.

Since the radial heat loss from the test column was less than 5% under vacuum conditions, the heat flux across the joint was assumed to be the average value of the thermal fluxes through the Armco iron heat flux-meters. Each Armco iron heat flux was determined by means of Fourier's equation

$$Q/A = - k \, dT/dz \qquad W/m^2 \tag{5.2}$$

where dT/dz is the temperature gradient along the heat flux-meter and k is the thermal conductivity computed at the mid-plane temperature using the following expression:

$$k(W/m^2K) = 74.6 - 6.9 \times 10^{-2} \, T \, (°C) \tag{5.3}$$

This expression was obtained by correlating the tabulated values of Ref.[71] in the range of 20 to 300°C and has a maximum error of 1.5% at 300°C.

The thermal conductivity of each material tested was determined by correlating the conductivity data generated from the material vacuum tests. For each thermal test run, the microcomputer determined the thermal conductivity of each specimen from the temperature gradient along it and the joint heat flux using Eq.(5.2). Each conductivity value was assigned to the specimen mean temperature.

At the end of a particular test series a linear regression was performed on the thermal conductivity data as a function of the temperature data. The thermal conductivity expressions for these materials are:

1. Nickel 200:

$$k(W/mK) = 83.15 - 6.56 * 10^{-2} T\ (°C) \qquad (5.4)$$

which is accurate to within ±2.5% in the range of 80 to 195°C.

2. Stainless Steel 304:

$$k(W/mK) = 17.02 + 1.52 * 10^{-2} T\ (°C) \qquad (5.5)$$

which is accurate to within ±3% in the range of 60 to 250°C.

3. Zirconium-2.5wt% Nb:

$$k(W/mK) = 18.66 + 8.53 * 10^{-3} T\ (°C) \qquad (5.6)$$

which is accurate to within ±2% in the range of 70 to 268°C.

4. Zircaloy-4:

$$k(W/mK) = 15.47 + 6.88 * 10^{-3} T\ (°C) \qquad (5.7)$$

which is accurate to within ±1% in the range of 76 to 258°C.

These expressions were employed in nondimensionalizing the experimental contact conductance data. It should be mentioned that the Nickel 200 and Stainless Steel 304 expressions yield higher values than those reported in the literature, however, these expressions were independently confirmed for the same bar stock specimens by another researcher [72]. The Zirconium-2.5wt%Nb expression is similar to the expression reported in Ref.[73] while the Zircaloy-4 expression is slightly different from the one reported in the same reference.

The experiments, which will be discussed in the following sections, were performed using 25mm by 45mm cylinders, i.e., the apparent contact area was equal to $4.909*10^{-4} m^2$. The thermal contact conductance data of each series will be compared with the predictions and will be discussed individually in the same sequence in which the data were obtained. The first series of measurements was obtained for Nickel 200 while the second set of experimental data was generated using Stainless Steel 304 pairs. The third and the fourth series of thermal tests were performed using Zirconium alloy contacts.

5.2.2 Nickel 200 Results

The first series of tests was performed using five pairs of Nickel 200 having a broad range of surface parameters as shown in Table 5.1. It can be seen that the joint RMS surface roughness varied from approximately 0.9μm up to 14μm while the corresponding mean absolute slope ranged from approximately 0.11 up to 0.23. Also, the critical surface parameter (σ/m), which is essential for determining the contact hardness as well as for predicting the contact conductance, varied between 8.2μm and 59.8μm.

As shown in Table 5.1, the contact radius varied considerably for Nickel 200 pairs. It ranged from as low as 3.1μm for the "very smooth" pair, PNI0102, up to 22.7μm for the "very rough" pair, PNI0910. The corresponding contact hardness ran from a high value of 3666MPa, for pair PNI0102, to a low value of 2170MPa, for pair PNI0910.

The maximum and minimum measured contact conductances for these pairs are also given in Table 5.1. As might be expected, the highest contact conductance value was obtained for the smoothest pair at the maximum contact pressure of approximately 8830 kPa, while the lowest value was obtained for the roughest pair at the minimum contact pressure of approximately 473 kPa. Table 5.1 shows clearly that these tests were conducted over a fixed range of contact pressures

Table 5.1: Geometric, Mechanical and Thermal Parameters of Ni200 Pairs

PAIR		PNI0102	PNI0304	PNI0506	PNI0708	PNI0910
σ	μm	0.902	3.43	4.24	9.53	13.94
m		0.110	0.190	0.188	0.228	0.233
σ/m	μm	8.20	18.05	22.55	41.80	59.83
a_c	μm	3.12	6.86	8.57	15.88	22.74
d_v	μm	7.79	17.15	21.42	39.71	56.84
H_c	MPa	3666	2977	2807	2385	2170
H_m	MPa	1010	1010	1010	1010	1010
P_{mx}	kPa	8830	8800	8886	8779	8792
P_{mn}	kPa	495	477	493	461	473
10^3 $P/H_{c,mx}$		2.411	2.960	3.170	3.684	4.057
10^3 $P/H_{c,mn}$		0.135	0.160	0.176	0.193	0.218
$T_{m,mx}$	°C	142.2	134.8	138.6	131.1	134.2
$T_{m,mn}$	°C	101.8	97.8	101.6	103.6	99.1
ΔT_{mx}	°C	20.8	36.8	48.7	61.0	84.0
ΔT_{mn}	°C	2.6	4.7	4.6	4.5	8.0
$h_{c,mx}$	W/m^2K	35957	19091	14901	10716	7895
$h_{c,mn}$	W/m^2K	3183	1750	1303	994	670
$H_v(d_v)$	MPa	$6303.8\ d_v^{-0.264}$				
k(T)	W/mk	$83.15 - 6.56 * 10^{-2}\ T\ (°C)$				

having a factor of approximately 19 between its minimum and maximum values. However, the experimental contact conductance data for this series covered a range of relative contact pressures, P/H_c, having a factor of approximately 30 between its limits. This results from the use of different contact hardness values in normalizing the contact pressure.

Since the starting heater input power for this series was maintained constant, the resultant temperature drop across the interface range from a value of approximately 21°C for the "very smooth" pair up to 84°C for the "very rough" pair. This, of course, illustrates the effect of the joint roughness upon the measured contact conductance. Also shown in Table 5.1 are both of the interface mean temperature and temperature difference maximum and minimum values for the Nickel 200 pairs. The test results of this series are reported in detail in Tables C.1-C.5, while the comparison between the experiments and the predictions is given in Tables C6-C.10 in Appendix C.

The graphical comparison between the experimental and theoretical dimensionless contact conductance values, as a function of the relative contact pressure, P/H_c, are presented in Figures 5.1-5.5. The contact pressure in each figure was normalized with respect to the contact hardness of each pair as reported in Table 5.1. Figure 5.1 shows that the experimental conductance for pair PNI0102, the smoothest pair, is slightly higher than the theoretical value for the first few

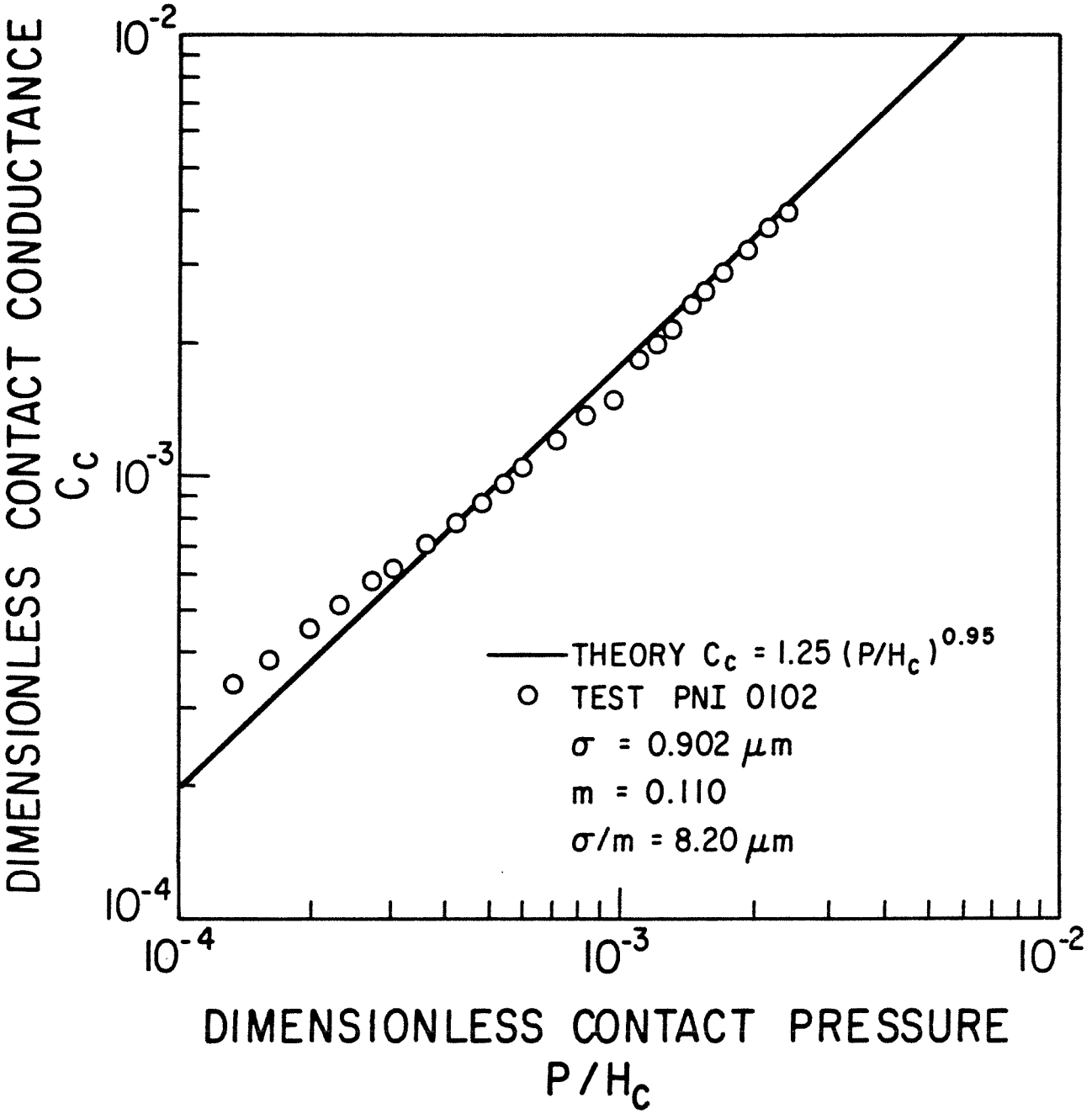

Figure 5.1: Comparison Between Theory and Test Results for Ni200, Pair PNI0102

light load points. However, as the load increases, the measured conductance approaches continually towards the theoretical line up to a relative contact pressure of $5*10^{-4}$. As can be seen from the figure the agreement between the experimental and theoretical values is excellent beyond $P/H_c = 5*10^{-4}$. The RMS precent difference for this pair is only 11.3% and is equal to 6% excluding the first five load points.

The pertinent test results of pair PNI0304 are shown in Figure 5.2. It can be seen that the experimental values are slightly below the predictions with the exception of the first few light load points. Also, the experimental data follow the same trend observed in the previous test. The overall RMS% difference for all the data points is 11.8% and for the last 18 load points is only 7.7%.

The next test was performed on pair PNI0506. As is shown in Figure 5.3, the measured conductance is slightly higher than the prediction for the first three points, equals that predicted by the model at relative contact pressure, $P/H_c = 3*10^{-3}$, decreases with increasing contact pressure up to $P/H_c = 5*10^{-4}$, and then follows the theoretical line with a percent difference of approximately -12%. The reason for this deviation may be attributed to an under-estimation of the surface parameters σ and m. As already mentioned, the surface parameters σ and m are estimated

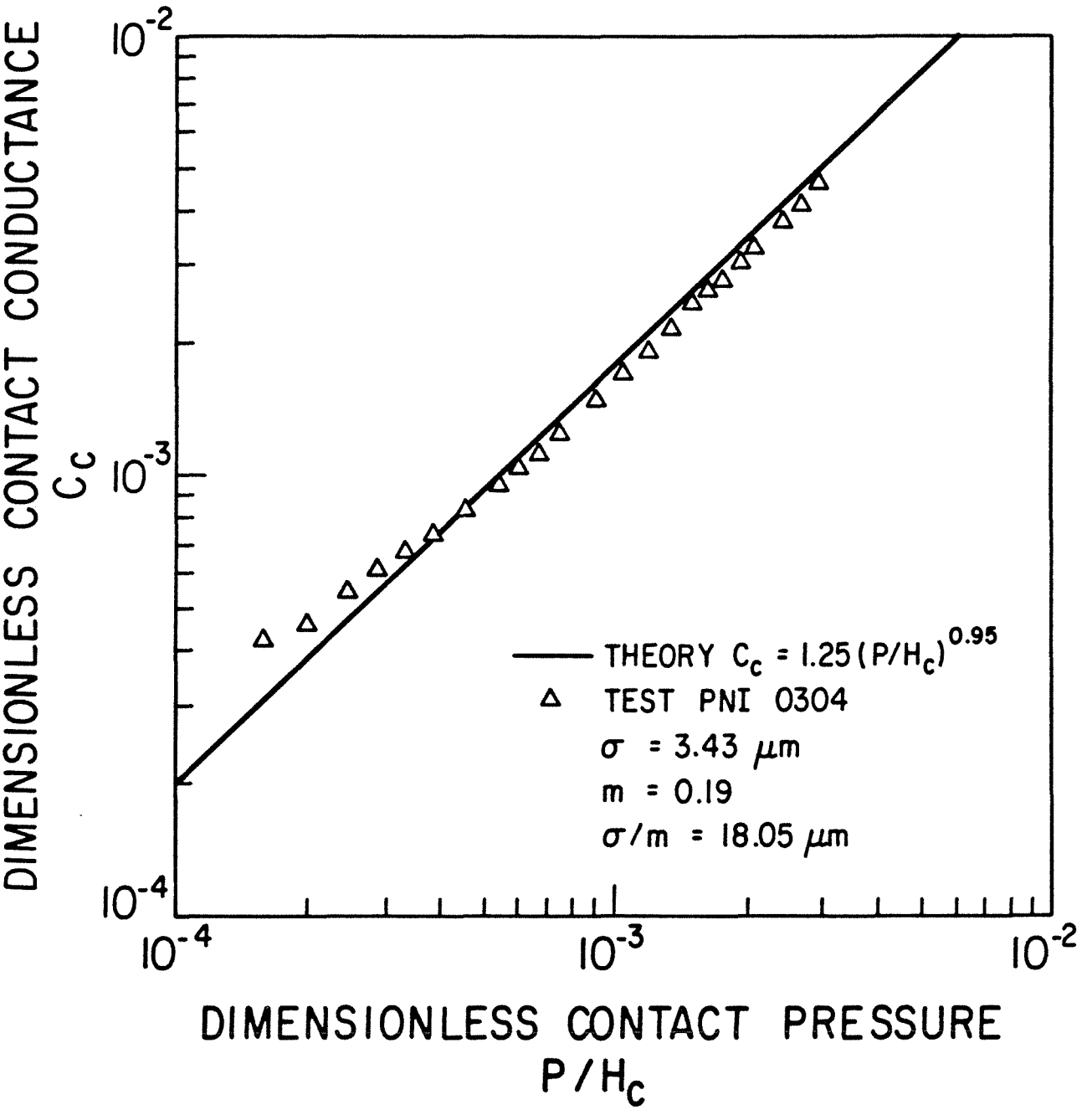

Figure 5.2: Comparison Between Theory and Test Results for Ni200, Pair PNI0304

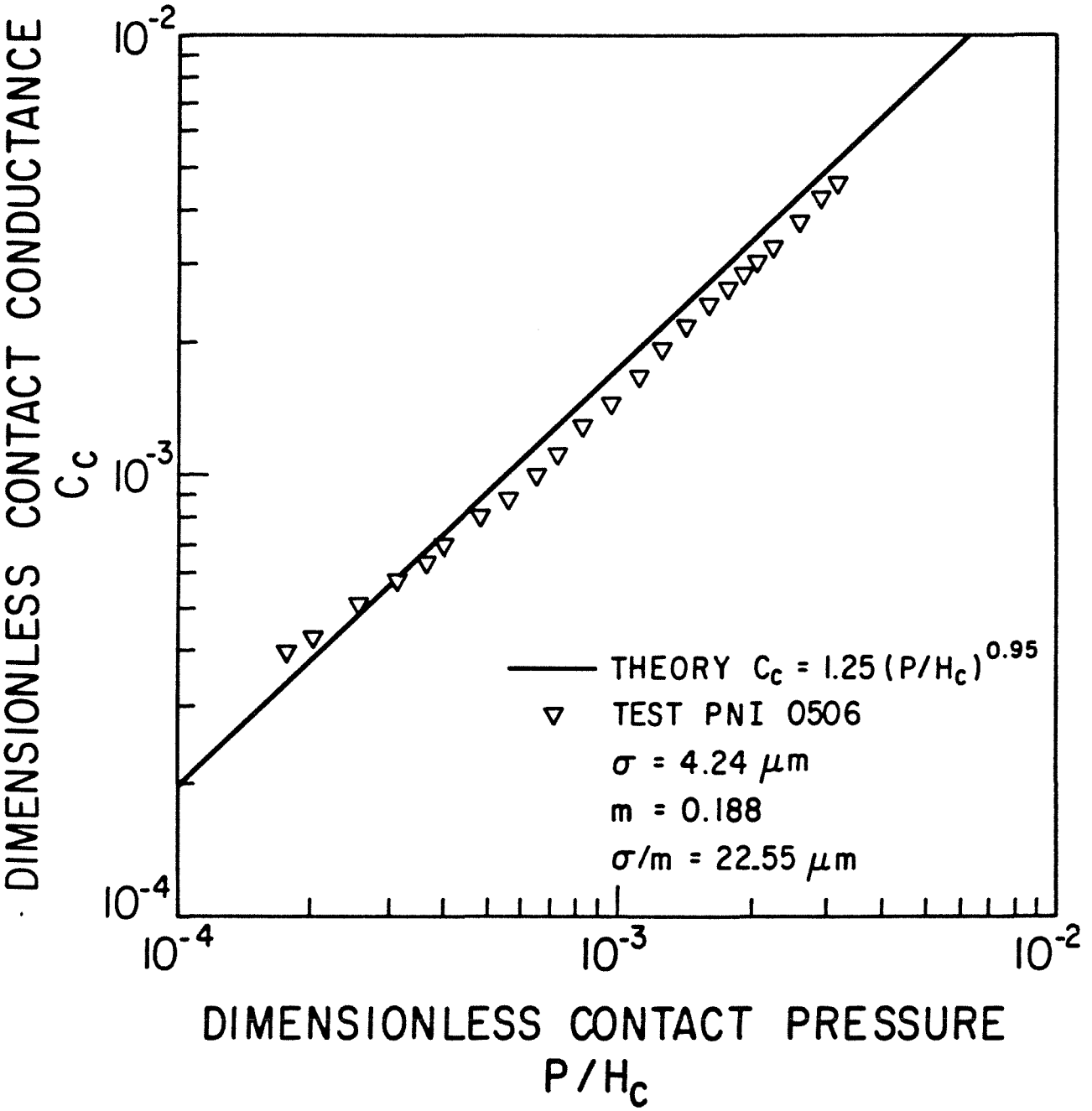

Figure 5.3: Comparison Between Theory and Test Results for Ni200, Pair PNI0506

accurately to within ±10% and according to the uncertainty analysis any experimental data within ±13% of the predictions should be considered satisfactory. Therefore, it is concluded that there is a good agreement between the experiments and the predictions with RMS% difference of 12.3%. These results, however, demonstrate clearly how important the accurate estimation of the surface parameters is in obtaining adequate predictions.

Figure 5.4 shows a comparison between the measured and predicted contact conductances of pair PNI0708. Generally, the experimental values are below the predicted values by approximately 6% for all relative contact pressures greater than $6*10^{-4}$; the RMS% difference is 5.1%. However, the overall RMS% difference between the experiments and the predictions is 13.5%. Once again, the light load data show essentially the same behaviour observed in the previous tests, although the difference between the first data point and the theory was even higher than observed with the other pairs.

The experimental results of pair PNI0910, which has the greatest roughness, are compared with the theoretical predictions in Figure 5.5. As can be seen from the figure, the very light load experimental data exceed the theoretical values while the higher load data points are below the theoretical values. However, the agreement between the experiment and the theory is very good because the RMS% difference is 10%.

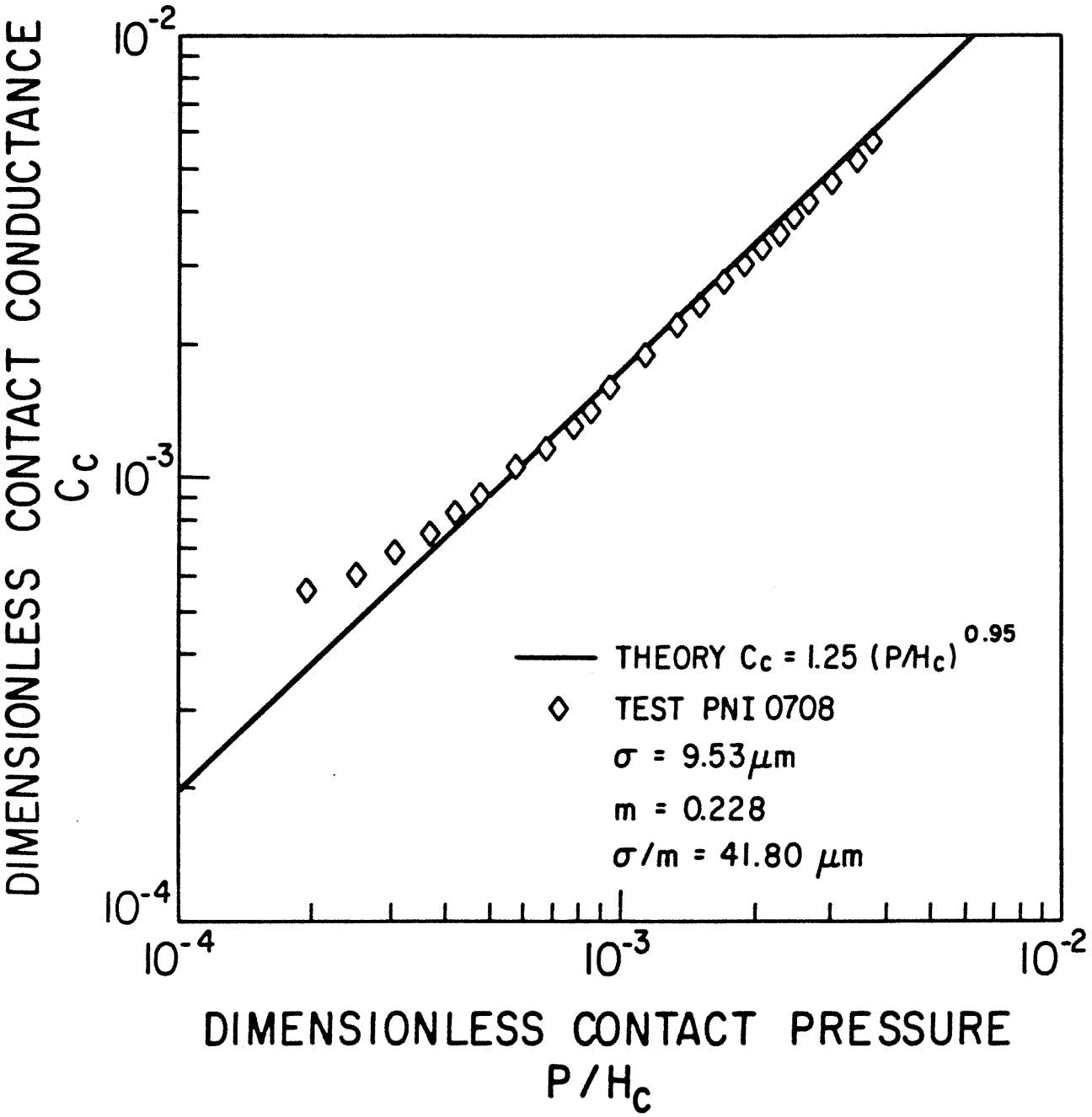

Figure 5.4: Comparison Between Theory and Test Results for Ni200, Pair PNI0708

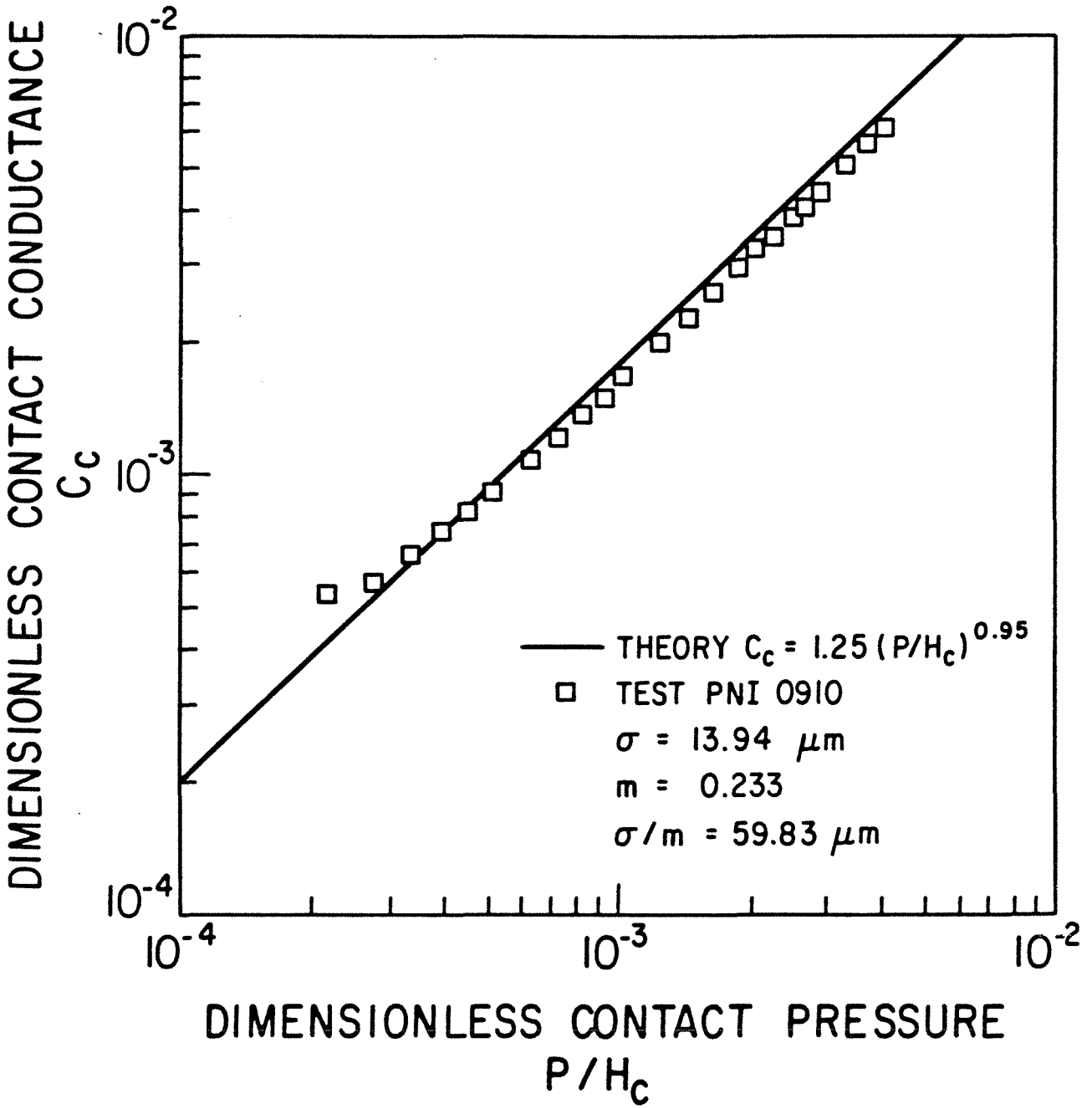

Figure 5.5: Comparison Between Theory and Test Results for Ni200, Pair PNI0910

To demonstrate how important the appropriate contact hardness value is for accurate thermal predictions, the dimensionless experimental data for the two limiting pairs, i.e., PNI0102 and PNI0910, are plotted against the contact pressure in Figure 5.6. The solid lines represent the predictions from the proposed model incorporating the appropriate contact hardness values while the broken line represents the predictions assuming the macro-hardness value of these specimens. It is clear from Figure 5.6 that the theoretical predictions based upon the macro-hardness value are in very poor agreement with the experimental data from these two limiting pairs. Therefore, it can be concluded that, if the macro-hardness value was employed instead of the appropriate contact hardness values, the theoretical predictions would be in error by a factor of 3.4 for the smoothest pair and by a factor of 2.1 for the very rough pair.

Finally, the overall RMS% difference between the measured and predicted conductances for this series of tests is 11.8% which illustrates clearly the importance of the contact hardness in correlating the experimental results as well as the validity of the proposed model. The difference between the light load data and the theory is interesting, but it is too early to draw any conclusion in this regard. This point will be discussed in detail later. It should also be mentioned, that neither the thermal conductivity

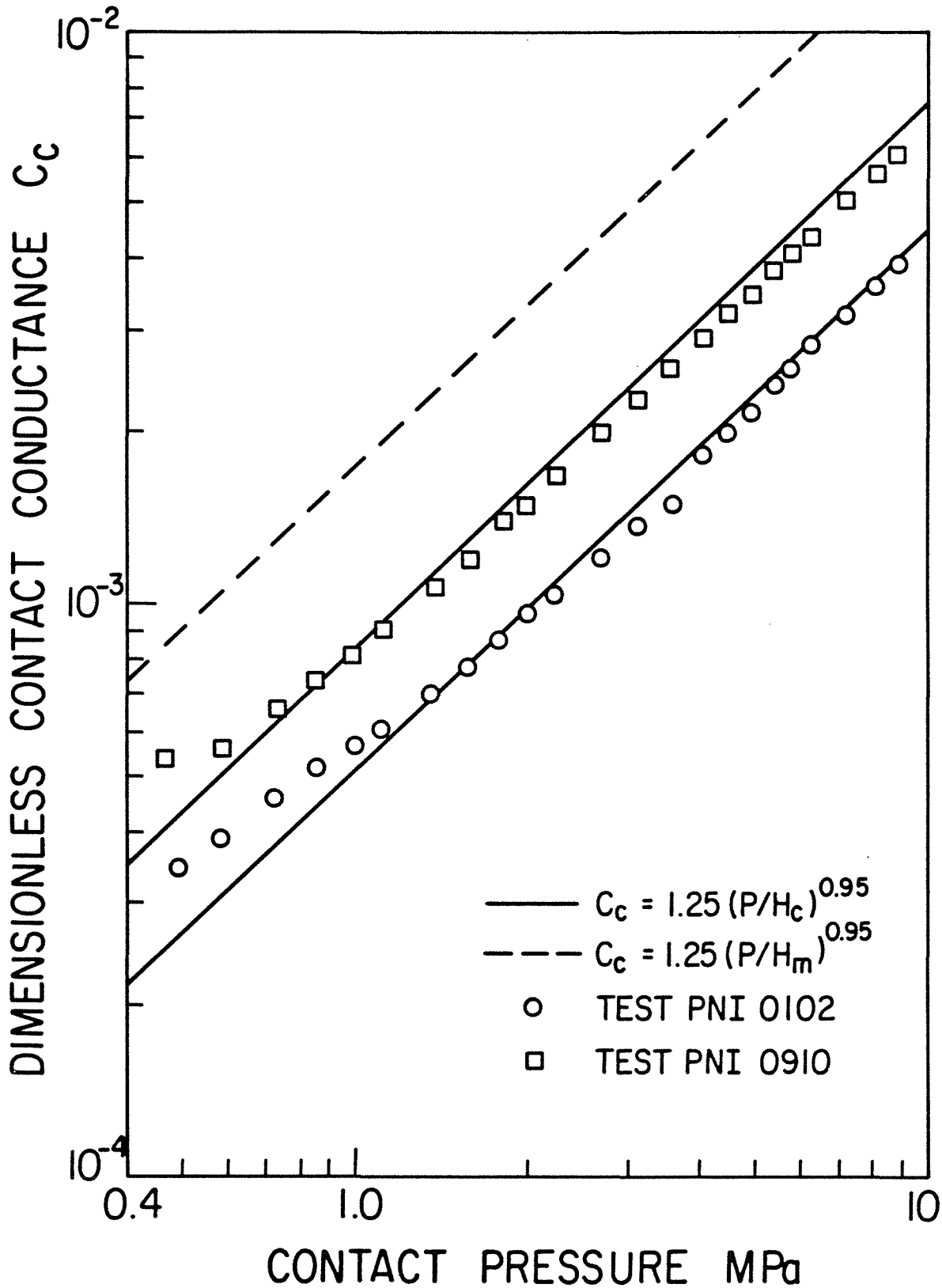

Figure 5.6: Prediction Dependence upon the Appropriate Hardness Value

nor the macro-hardness of these specimens agree with the values reported in Ref.[50]. This interesting observation, as well as the test results of this series, demonstrate how critical the thermal and mechanical properties and the appropriate surface parameters are in obtaining consistent results.

5.2.3 Stainless Steel 304 Results

In contrast to Nickel 200 specimens, Stainless Steel 304 cylinders have a much lower thermal conductivity value but a higher macro-hardness value. At room temperature, the ratio between the Ni200 and the SS304 thermal conductivities is 4.7, while the ratio between their macro-hardness values is 0.7. This large difference in properties provides a useful means of investigating the validity of the proposed contact conductance model.

This series consists of four tests performed on SS304 contacts. The raw data from these tests is reported in Tables C.11-C.14 in Appendix C. The comparisons between the experimental and theoretical dimensionless contact conductances are given in Tables C.15 through C.18.

The range of geometric, mechanical and thermal parameters of this series of tests are summarized in Table 5.2. It can be seen that the surface parameters of the tested joint varied considerably.

Table 5.2: Geometric, Mechanical and Thermal Parameters of SS304 Pairs

PAIR		PSS0102	PSS0304	PSS0506	PSS0708
σ	μm	0.478	2.71	5.88	10.95
m		0.072	0.116	0.146	0.19
σ/m	μm	6.64	23.36	40.27	57.63
a_c	μm	2.52	8.88	15.30	21.90
d_v	μm	6.31	22.19	38.27	54.75
H_c	MPa	4113	3084	2722	2507
H_m	MPa	1472	1472	1472	1472
P_{mx}	kPa	8820	8824	8819	8775
P_{mn}	kPa	446	431	409	445
10^3 $P/H_{c,mx}$		2.146	2.865	3.243	3.503
10^3 $P/H_{c,mn}$		0.109	0.140	0.150	0.178
$T_{m,mx}$	°C	164.5	156.0	147.7	141.4
$T_{m,mn}$	°C	128.2	123.7	110.2	108.8
ΔT_{mx}	°C	47.8	94.5	103.9	114.9
ΔT_{mn}	°C	3.9	9.0	11.2	14.0
$h_{c,mx}$	W/m^2K	11321	3638	2543	1964
$h_{c,mn}$	W/m^2K	706	300	241	185
$H_v(d_v)$	MPa	$6271\ d_v^{-0.229}$			
k(T)	W/mK	$17.02 + 1.52 * 10^{-2}\ T\ (°C)$			

The effective RMS roughness ranged from approximately 0.5μm to 11μm, the effective surface mean absolute slope ranged from 0.072 to 0.19, and the critical surface parameter (σ/m) varied from 6.64μm up to 57.63μm. The corresponding contact radius, a_c, varied from 2.52μm up to 21.90μm while the contact hardness ranged from a high value of 4113MPa down to a low value of 2507MPa.

From Tables 5.1 and 5.2, in conjunction with Table B.5, it is interesting to note that the resultant surface textures of SS304 specimens are less than the corresponding Ni200 specimens roughened by the same grade of glass beads and blast pressure. This demonstrates clearly the effect of the material macro-hardness or, in general, the material mechanical properties upon the resultant surface characteristics. A second interesting observation from these tables is that the critical surface parameter (σ/m) is almost identical for Ni200 and SS304 surfaces roughened by the same grade of glass beads despite the differences in the individual values of σ and m. This observation is in line with the data reported by Henry [15] for SS416.

A third interesting observation from Tables 5.1 and 5.2 is that the SS304 specimens possess a lower micro-hardness variation than those of Ni200 even though the SS304 specimens have the higher macro-hardness value.

The last ten lines in Table 5.2 show the maximum and minimum values of the test data pertaining to this series. The contact pressure ranged from 409 kPa up to 8824 kPa, similar to the previous series. The relative contact pressure, P/H_c, varied approximately from $1.1*10^{-4}$ up to $3.5*10^{-3}$. The mean interface temperature in the four tests were observed to be in the range $165 < T_m < 109°C$. The maximum temperature drop across the interface at the lightest load was between 47.8 and 114.9°C while the minimum value observed during the course of this series was approximately 4°C. As might be expected, the measured contact conductances for SS304 joints were lower than those of Ni200. The lowest value of 185 W/m^2K was observed for the roughest pair PSS0708 at a contact pressure of 445 kPa, while the highest value of 11321 W/m^2K was observed for the smoothest pair at a contact pressure of 8820 kPa.

Figure 5.7 shows that the experimental dimensionless conductances of pair PSS0102, the smoothest joint, slightly exceed the theoretical values up to a relative contact pressure of $3.9*10^{-4}$ with a percent different between 13% and 8%. However, the rest of the data points are in excellent agreement with the theoretical predictions. The RMS% difference for the 23 data points is only 8.8%.

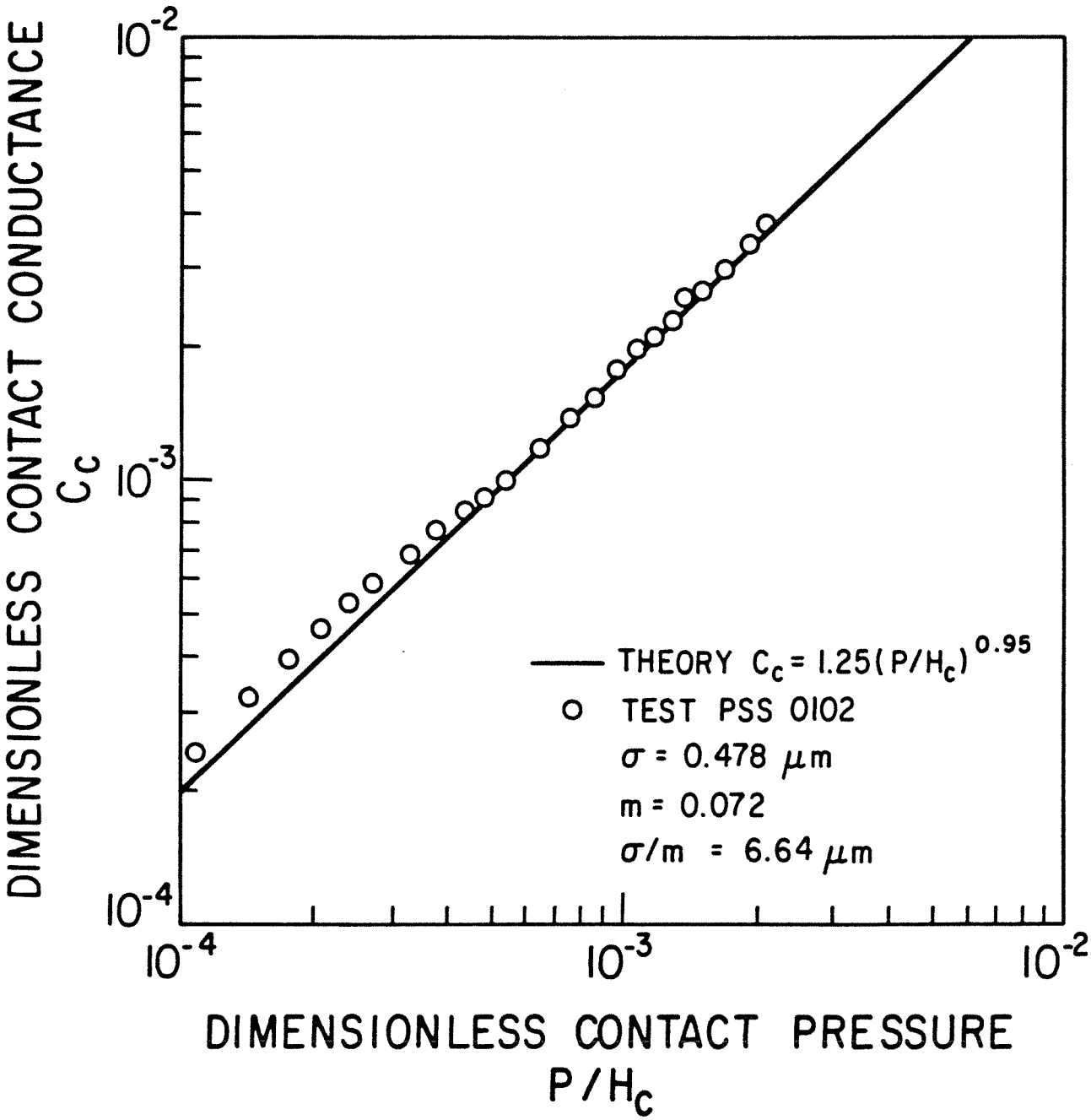

Figure 5.7: Comparison Between Theory and Test Results for SS304, Pair PSS0102

Figure 5.8 pertains to the second pair, PSS0304. It can be seen that the very light load experimental data exceed the predictions, while the higher load data points are below the theoretical values by approximately 9%. Again, the agreement between the experiment and the theory is very good because the RMS% difference is 11%.

Figure 5.9 corresponds to the test performed on pair, PSS0506. Clearly, it can be seen that the agreement between the experiment and the theory is not good at light loads. The measured conductance is consideably higher than the predictions for the first few light load points, but tends towards the theoretical line at moderate contact pressure, and is in excellent agreement with the predicted values at higher contact pressure. The RMS% difference for:

a) the first eight data points is 34.8%;

b) the next eight data points is 6.9%; and

c) the last seven data points is 3.4%.

However, the overall RMS% difference for this test is 21%. Generally, there is no single reason for this unusual behaviour. A number of explanations regarding this phenomenon are presented in Section 5.2.5.

Figure 5.10 shows a comparison between the measured conductances of the roughest pair, PSS0708, and the predicted values. As with

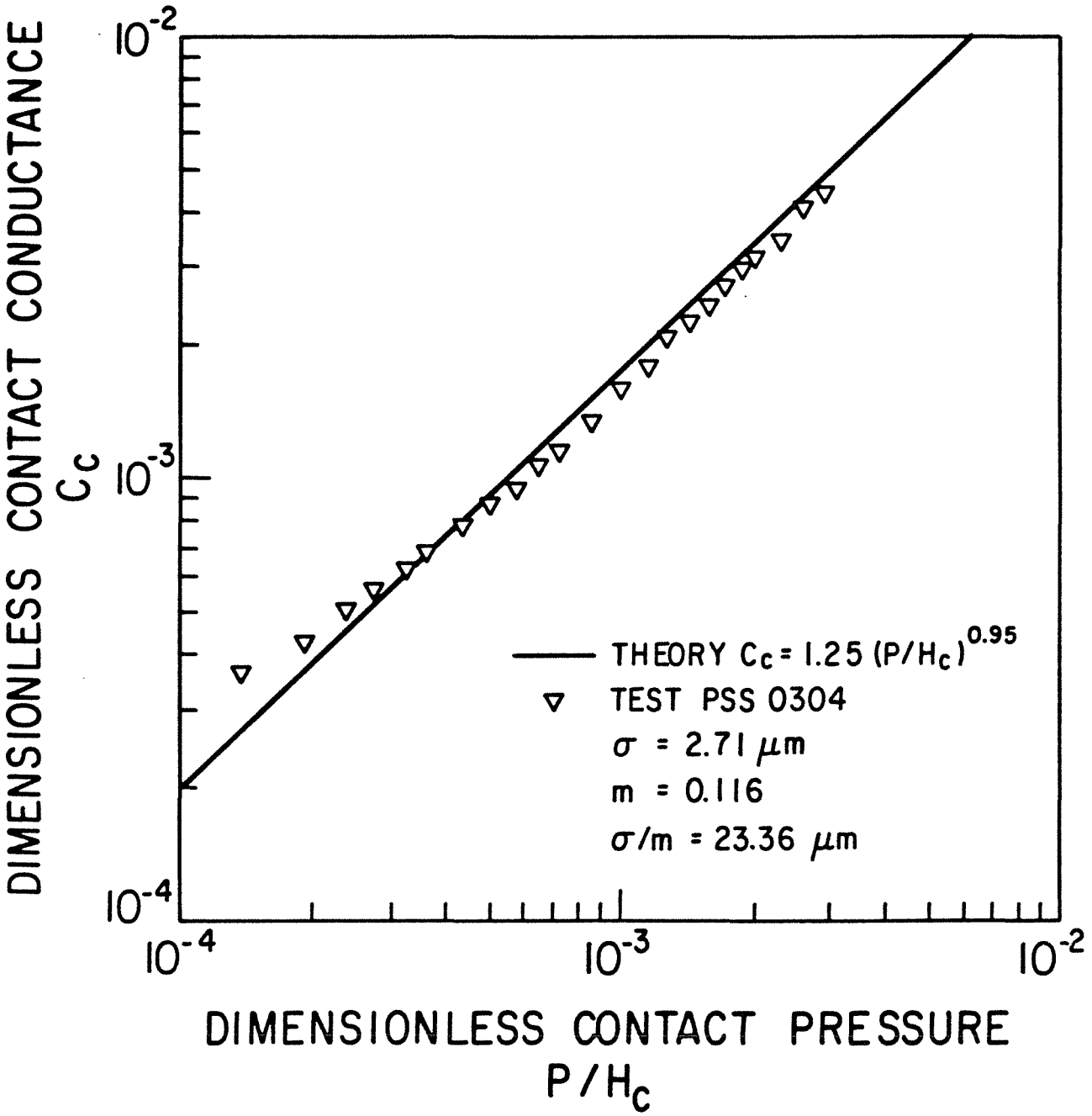

Figure 5.8: Comparison Between Theory and Test Results for SS304, Pair PSS0304

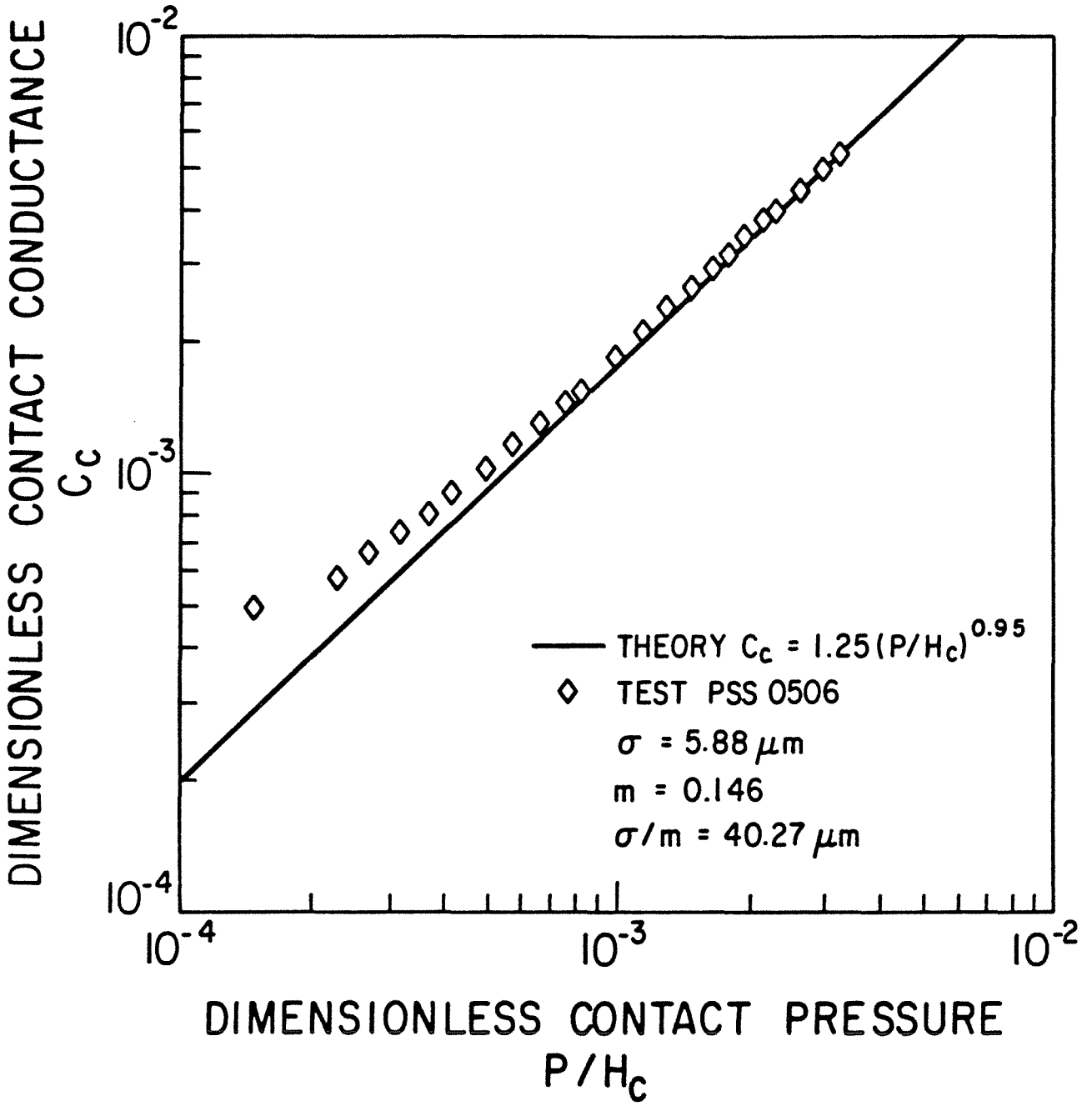

Figure 5.9: Comparison Between Theory and Test Results for SS304, Pair PSS0506

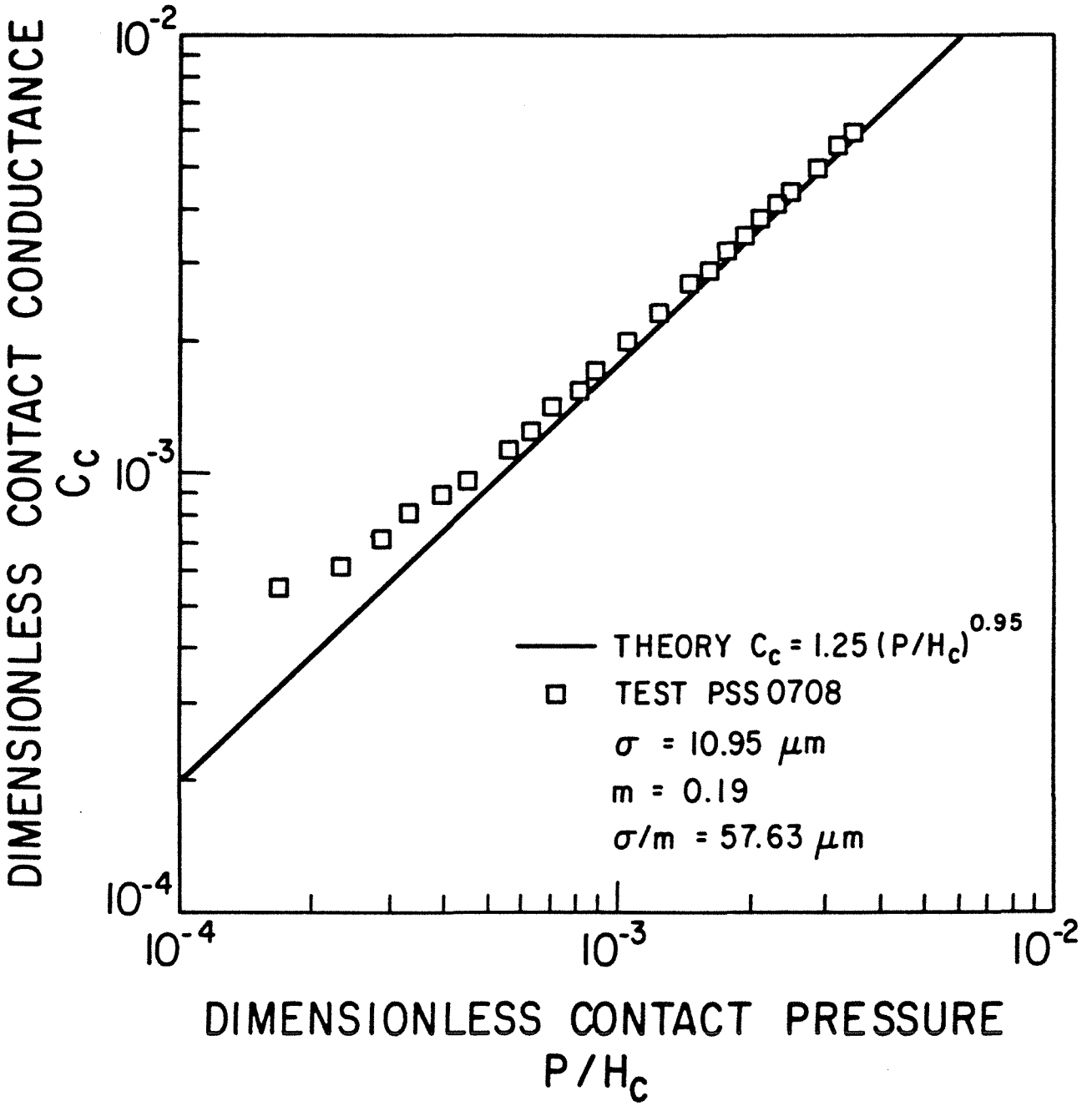

Figure 5.10: Comparison Between Theory and Test Results for SS304, Pair0708

pair PSS0506 the experimental data exceed the theoretical values for all contact pressures, however, the agreement is excellent for relative contact pressures higher than $5*10^{-4}$. Also, it can be seen that the deviation between the first data point and the theory is significantly higher, although this deviation decreases rapidly with increasing applied load. The overall RMS% difference between the experiment and the theory for this joint is 20.2%, while the RMS% difference for the last 18 data points is only 8.1%.

As is shown in Figure 5.11, neglecting the effect of surface micro-hardness variation can result in a very poor agreement between the test data and the thermal predictions assuming the macro-hardness value. The error ranges from approximately 72% for the roughest pair up to approximately 175% for the smoothest pair.

In summary, the experimental data for this series of tests follow the general trend of the Ni200 series. The deviation between the test results and the theoretical values at light loads is more pronounced but appears, however, to increase with increasing surface roughness. At the time, it was thought that the flatness of Ni200 and SS304 rough surfaces had been altered by the bead blasting process since these surfaces were bead blasted twice. This technique was employed to ensure that the resultant surface is random and isotropically rough. However,

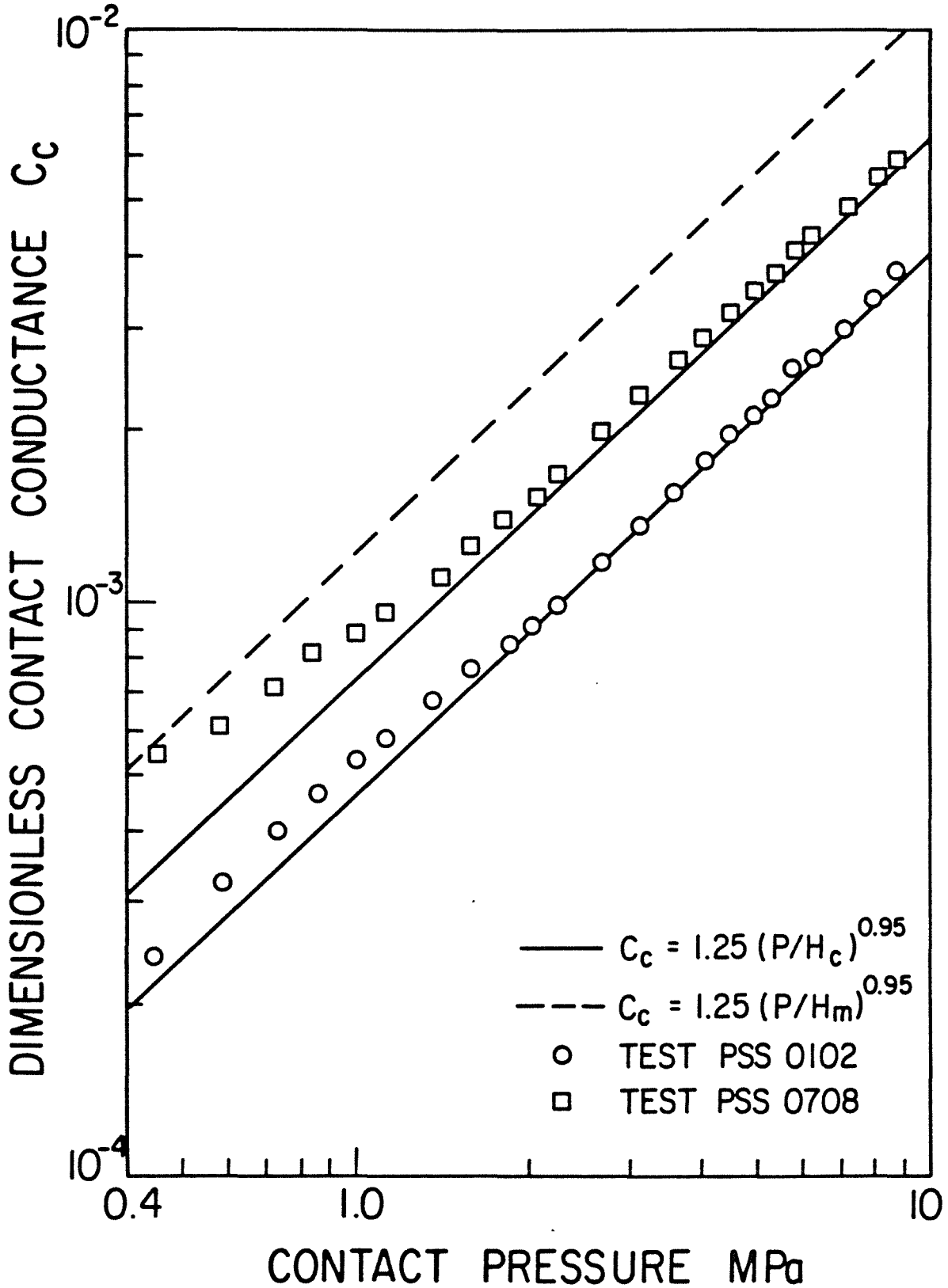

Figure 5.11: Prediction Dependence upon the Appropriate Hardness Value

this technique was modified for the last two series of tests to reduce the scatter of the light load data points. In general, the overall RMS% difference between the experimental and theoretical values for this series of tests is 16.2% and for the last 18 data points of each test is only 7.5%.

5.2.4 Zirconium-2.5wt%Nb Results

Zirconium alloys were included in the experimental program for their wide use in the nuclear reactor industry. These alloys possess thermal conductivity values much closer to that of SS304, however, their macro-hardness values are higher than those of Ni200 and SS304.

The ranges of geometric, mechanical and thermal parameters of Zr-2.5wt%Nb pairs employed in this series of tests are given in Table 5.3. As can be seen, the surface characteristics of the tested pairs did not vary as much as those of Ni200 and SS304. Actually, two main problems were encountered during the bead blasting process. First, a tremendous number of sparks from the surface were noticed when a high blast pressure was used and, second, the roughened surface was covered with a visible oxide film. To overcome these problems it was necessary to use a smaller quantity of glass beads as well as a low blast pressure.

Table 5.3: Geometric, Mechanical and Thermal Parameters of Zr-2.5wt%Nb Pairs

PAIR		PZN0102	PZN0304	PZN0506	PZN0708
σ	μm	0.922	2.50	5.99	8.81
m		0.083	0.162	0.184	0.20
σ/m	μm	11.11	15.43	32.55	44.05
a_c	μm	4.22	5.86	12.37	16.74
d_v	μm	10.55	14.66	30.92	41.85
H_c	MPa	3137	2873	2354	2171
H_m	MPa	1727	1727	1727	1727
P_{mx}	kPa	8749	8738	8785	8851
P_{mn}	kPa	484	462	409	429
10^3 $P/H_{c,mx}$		2.792	3.046	3.736	4.081
10^3 $P/H_{c,mn}$		0.154	0.161	0.174	0.198
$T_{m,mx}$	°C	158.0	169.4	165.4	172.9
$T_{m,mn}$	°C	107.4	147.9	153.3	146.6
ΔT_{mx}	°C	35.1	58.4	102.4	122.1
ΔT_{mn}	°C	5.2	7.1	11.7	13.6
$h_{c,mx}$	W/m^{2}K	8931	7007	3943	3248
$h_{c,mn}$	W/m^{2}K	858	656	327	265
$H_v(d_v)$	MPa	$5884\ d_v^{-0.267}$			
k(T)	W/mK	$18.66 + 8.53 * 10^{-3}$ T (°C)			

Therefore, the range of the surface parameters was relatively narrow.

Table 5.3 shows very clearly that the thermal conductivity of Zr-2.5wt%Nb is a weak function of the temperature and slightly higher than that of SS304. Also from Tables 5.2 and 5.3, it is interesting to note that the micro-hardness variation of Zr-2.5wt%Nb specimens is lower than the micro-hardness variation of SS304 specimens even though the Zr-2.5wt%Nb material has the highest macro-hardness of all the materials tested.

The test results from this series are tabulated in Tables C.19 to C.22 in Appendix C. The comparisons between the experiments and the predictions are reported in Tables C.23 through C.26 and presented in Figures 5.12 through 5.15. Figure 5.12 shows the measured and predicted dimensionless contact conductances plotted against the relative contact pressure for pair PZN0102. A contact hardness value of 3137 MPa is used in normalizing the contact pressure over the whole load range. As can be seen from Figure 5.12, there is excellent agreement between the experiment and the theory for relative contact pressures higher than $5*10^{-4}$; the RMS% difference is only 5.9%. However, the deviation between the experiments and the predictions is significantly larger below this relative contact pressure. The RMS% difference for all the data points is 23.1%.

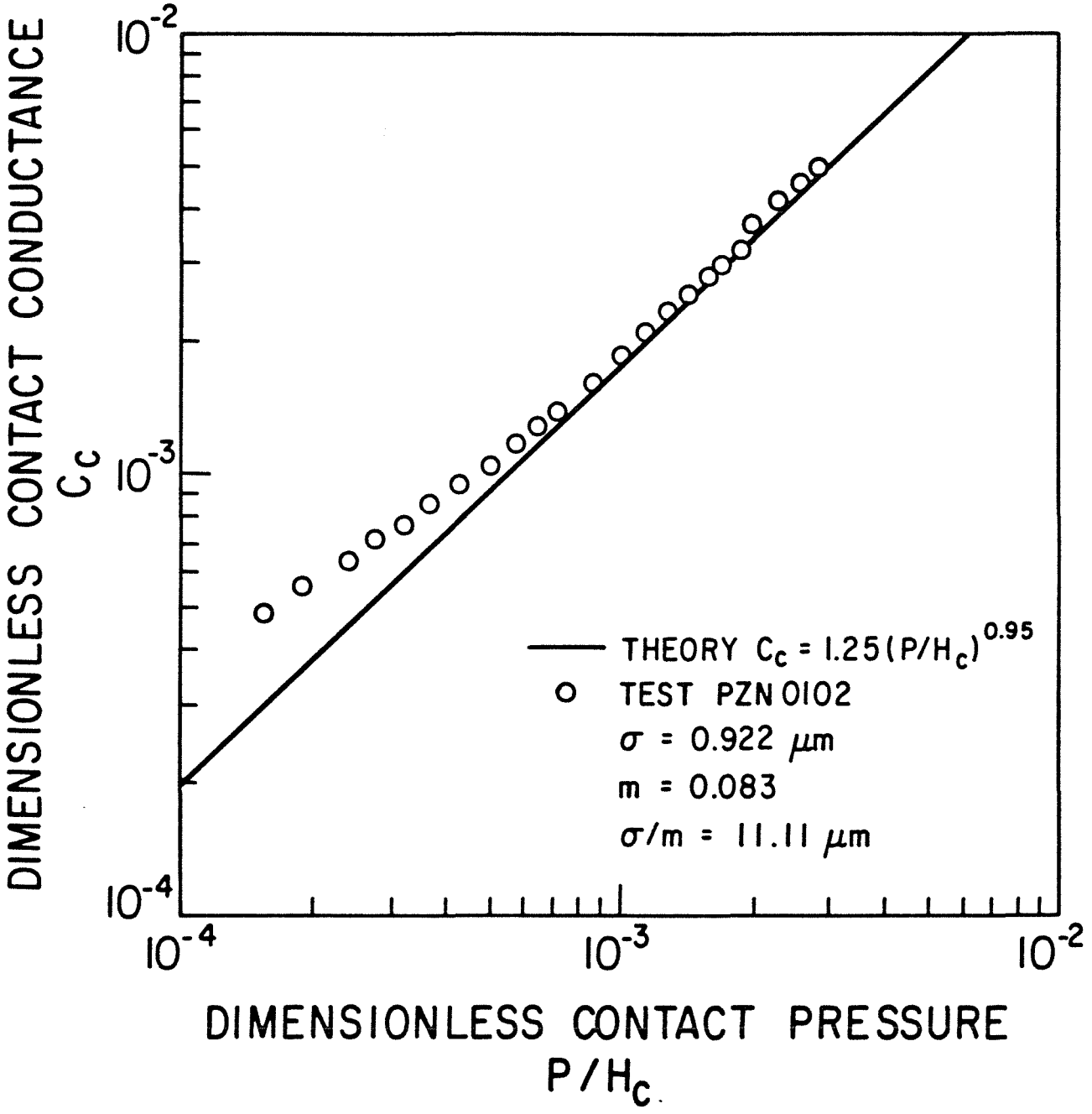

Figure 5.12: Comparison Between Theory and Test Results for Zr-2.5wt%Nb, Pair PZN0102

Since this joint was formed between two lapped surfaces, the bead blasting process could not have caused this significant deviation of the light load data. This ruled out the possibility that the surface out-of-flatness was increased by the bead blasting process. However, it is interesting to note that these test data show a relatively wider scatter than do the results from Ni200 pair PNI0102 and SS304 pair PSS0102. This suggests two other factors which may contribute to this deviation. These two factors are:

a) the original out-of-flatness of the contacting surfaces; and

b) the material type or the material properties, in general.

These factors will be discussed in detail in Section 5.2.6.

The dimensionless contact conductance data of pair PZN0304 is compared with the theoretical values predicted by the proposed model in Figure 5.13. It can be seen that the experiment and the theory are in excellent agreement similar to the previous test for relative contact pressures higher than $5*10^{-4}$; the RMS% difference is 6.7%. However, the total RMS% difference for the test is 21.1% due to the deviation of the light load data points.

The pertinent test results for pair PZN0506 are shown in Figure 5.14. As with the previous two pairs, the agreement between

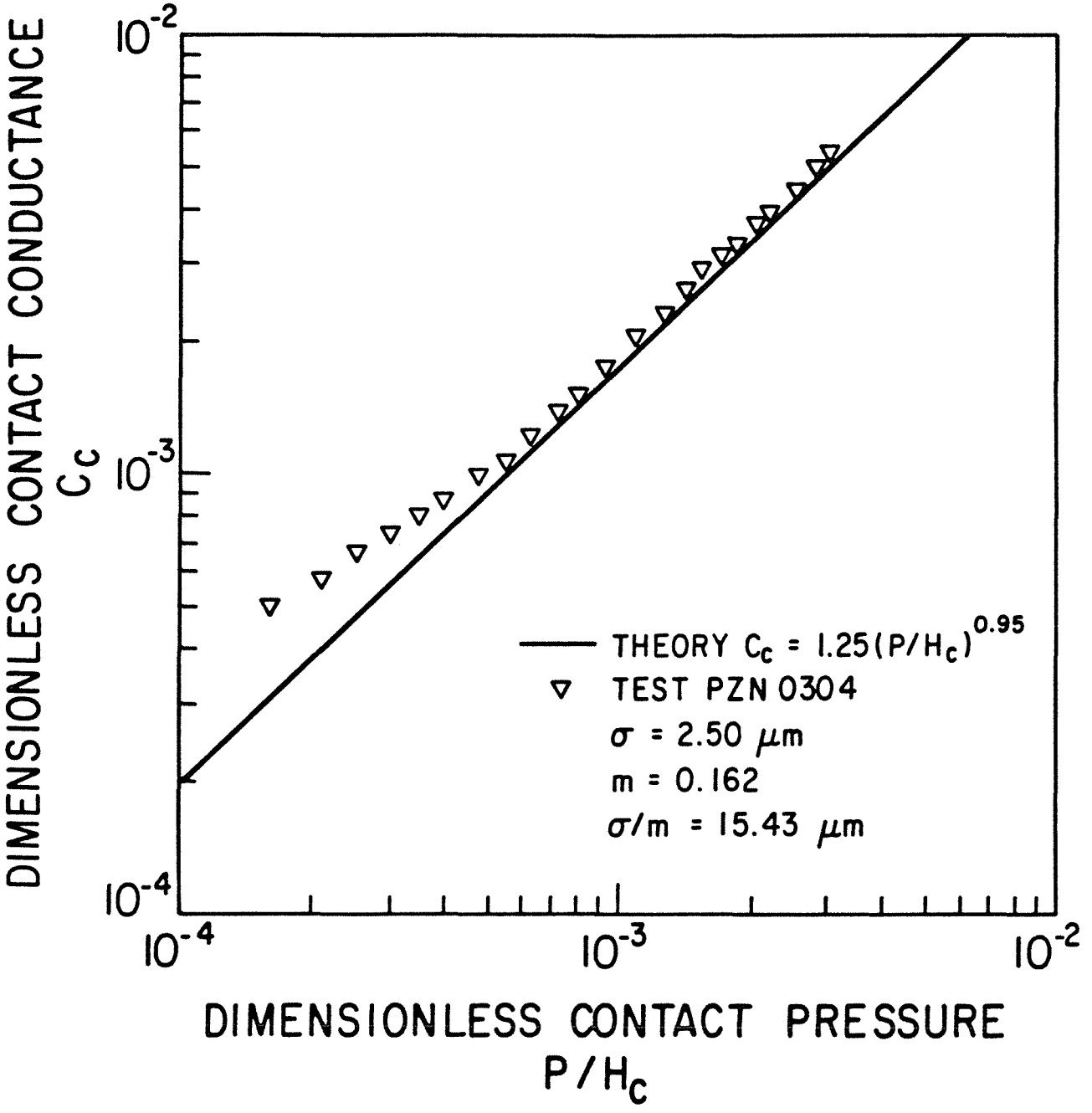

Figure 5.13: Comparison Between Theory and Test Results for Zr-2.5wt%Nb, Pair PZN0304

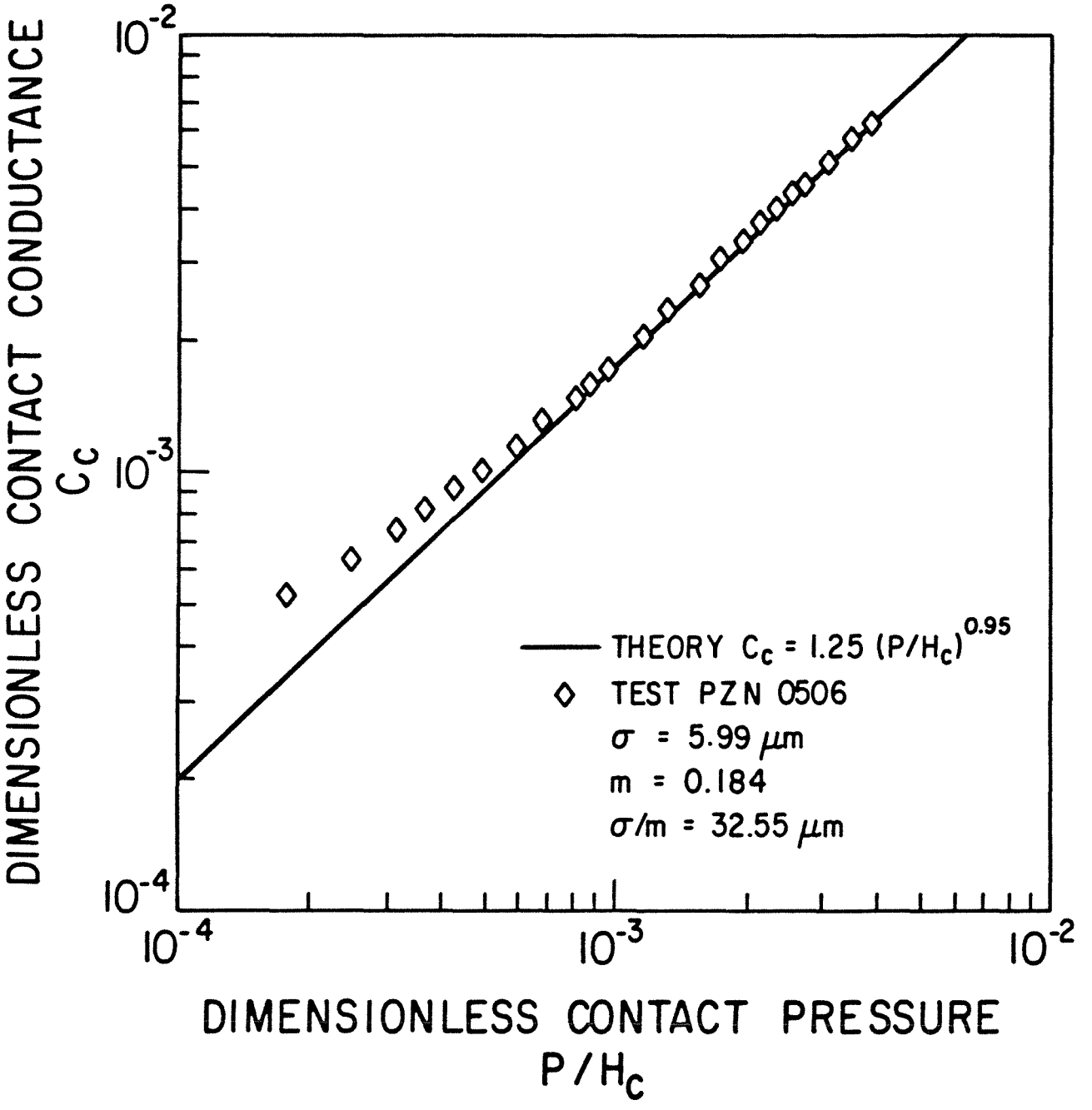

Figure 5.14: Comparison Between Theory and Test Results for Zr-2.5wt%Nb, Pair PZN0506

the experimental and theoretical values is excellent for $P/H_c > 5*10^{-4}$ with RMS% difference of 5.5%. Due to the deviation between the experiments and the predictions at light loads, the RMS% difference for all of the test data points is 17.5%.

Figure 5.15 shows very clearly that the experimental values of pair PZN0708, the roughest pair in this series of tests, exceed the theoretical values for all contact pressures similar to the previous three pairs. Also, the agreement between the last 18 points and the predictions is very good with a RMS% difference of 7.5%. However, the overall test RMS% difference is 16.4%.

Figure 5.16 demonstrates clearly how important the appropriate contact hardness is for accurate thermal predictions. In this figure, the experimental data of pairs PZN0102 and PZN0708, as well as the predicted values from the proposed model, are compared with the theoretical predictions assuming the macro-hardness value of these specimens. As can be seen from the figure, if the macro-hardness value is incorporated into the predictions, the proposed model will predict contact conductance values above the test results by a factor of approximately 1.2 for the very rough pair and by a factor of approximately 1.8 for the very smooth pair.

Generally, it appears that the deviation between the light load data and the theoretical predictions is quite consistent

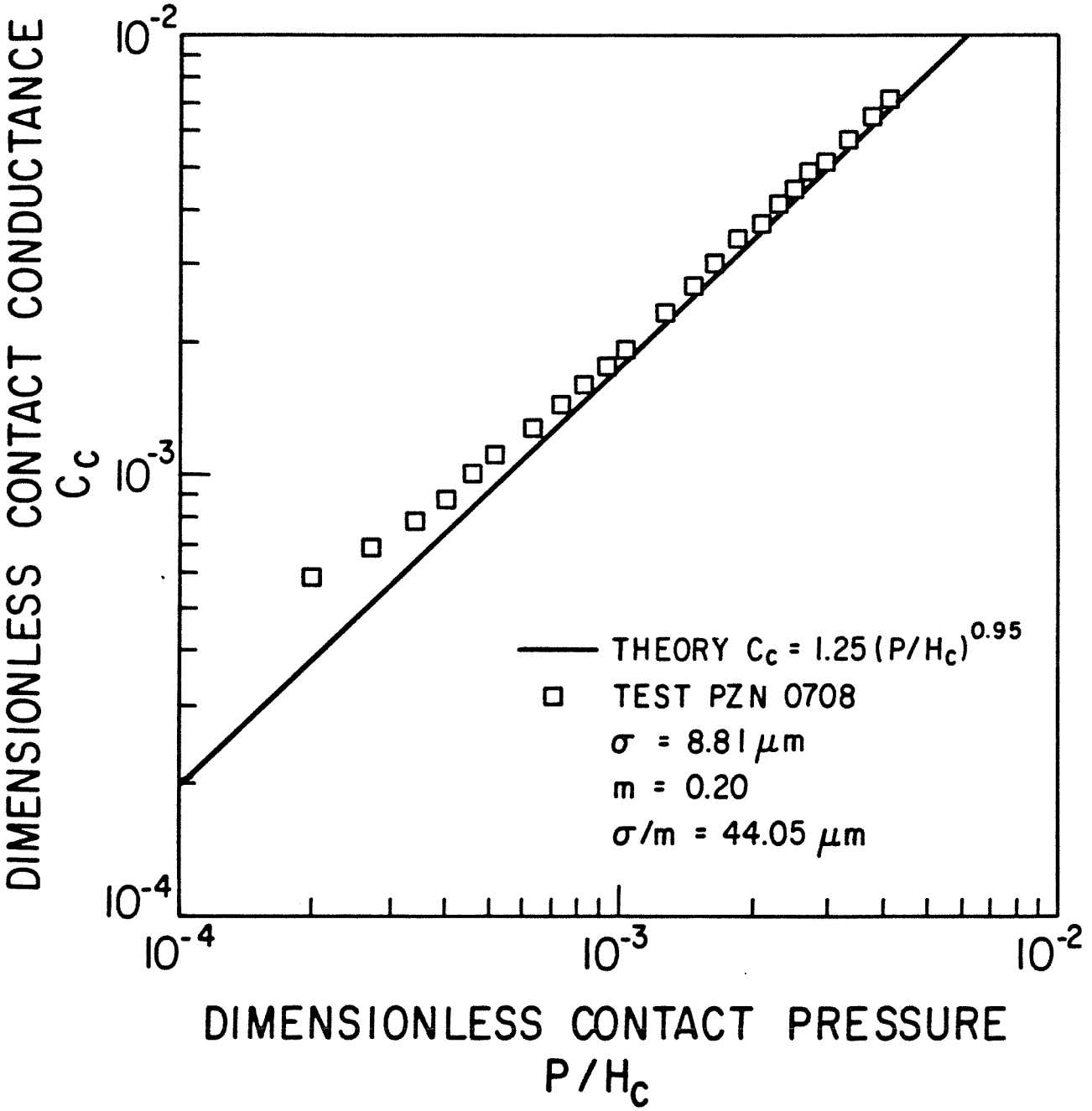

Figure 5.15: Comparison Between Theory and Test Results for Zr-2.5wt%Nb, PZN0708

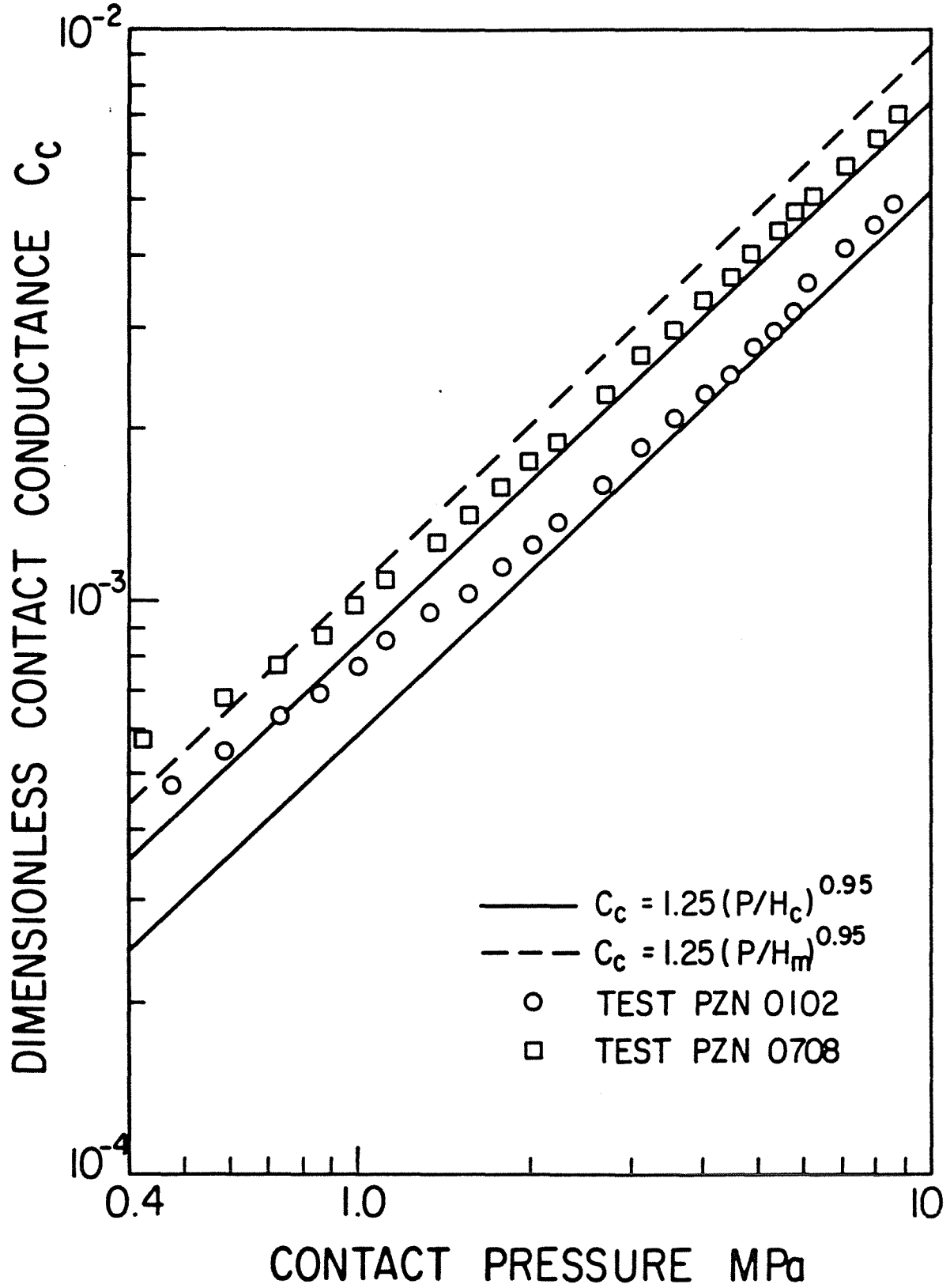

Figure 5.16: Prediction Dependence upon the Appropriate Hardness Value

for this series of tests. However, the agreement between the experimental and theoretical values for relative contact pressures greater than $5*10^{-4}$ is excellent with an overall RMS% difference of 6.4%.

5.2.5 Zircaloy-4 Results

The last series of tests in vacuum was performed on specimens made of Zircaloy-4. The preparation of a satisfactory rough surface with desirable surface textures proved to be a very difficult task for this alloy. Therefore, these pairs have a relatively narrow range of surface parameters as is shown in Table 5.4. The critical surface parameter (σ/m) ran only from 12.43μm up to 38.26μm. The joint RMS surface roughness varied approximately from 0.61μm up to 7.92μm, while the corresponding mean absolute slope varied approximately from 0.05 up to 0.21. The geometrical, mechanical and thermal parameters for the various tests are also given in Table 5.4.

From Table 5.4, it is interesting to note that the Zircaloy-4 specimens possess the lowest micro-hardness and the weakest micro-hardness variation although their macro-hardness value is higher than that of Ni200 and SS304. Consequently, the contact hardness ranged from 2321 MPa for the smoothest pair down to 1972 MPa

Table 5.4: Geometric, Mechanical and Thermal Parameters of Zr-4 Pairs

PAIR		PZ40102	PZ40304	PZ40506	PZ40708
σ	μm	0.609	2.75	3.14	7.92
m		0.049	0.148	0.129	0.207
σ/m	μm	12.43	18.58	24.34	38.26
a_c	μm	4.72	7.06	9.25	14.54
d_v	μm	11.81	17.65	23.12	36.35
H_c	MPa	2321	2190	2105	1972
H_m	MPa	1638	1638	1638	1638
P_{mx}	kPa	8816	8764	8775	8852
P_{mn}	kPa	419	436	415	442
10^3 $P/H_{c,mx}$		3.800	4.005	4.170	4.490
10^3 $P/H_{c,mn}$		0.181	0.199	0.197	0.224
$T_{m,mx}$	°C	178.6	175.1	167.4	167.6
$T_{m,mn}$	°C	154.2	166.2	157.1	154.8
ΔT_{mx}	°C	67.9	76.7	77.2	99.6
ΔT_{mn}	°C	5.0	7.1	7.4	10.8
$h_{c,mx}$	W/m^2K	9144	6163	5419	3644
$h_{c,mn}$	W/m^2K	517	450	432	303
$H_v(d_v)$	MPa	$3320\ d_v^{-0.145}$			
k (T)	W/mK	$15.47 + 6.88 * 10^{-3}$ T (°C)			

for the roughest pair with a factor of only 1.18 between these two values.

The experimental data for this series of tests covered a range of relative contact pressures having a factor of 21 between the minimum ($1.81*10^{-4}$) and the maximum ($4.5*10^{-3}$) values. The maximum and minimum values of the contact conductance, as well as the interface mean temperature and temperature drop are reported in Table 5.4. For more details about the experimental data the reader is referred to Tables C.27 through C.30 in Appendix C. Also, the comparisons between the experimental and theoretical values are presented in Tables C.31 through C.34 and shown in Figures 5.17 through 5.20.

The pertinent test results of the smoothest pair PZ40102 are shown in Figure 5.17 where the dimensionless contact conductance is plotted against the relative contact pressure. From the figure, it can be seen that the agreement between the experimental and theoretical values is excellent over the whole load range. The RMS% difference between the experiments and the predictions is only 6.3%. Moreover, this pair exhibits a minimum deviation between the test data and the predictions at light load. Therefore, after the test was completed the contacting surfaces were checked out again for out-of-flatness which was found to be less than 1μm similar to the other surfaces. This indicates that the material

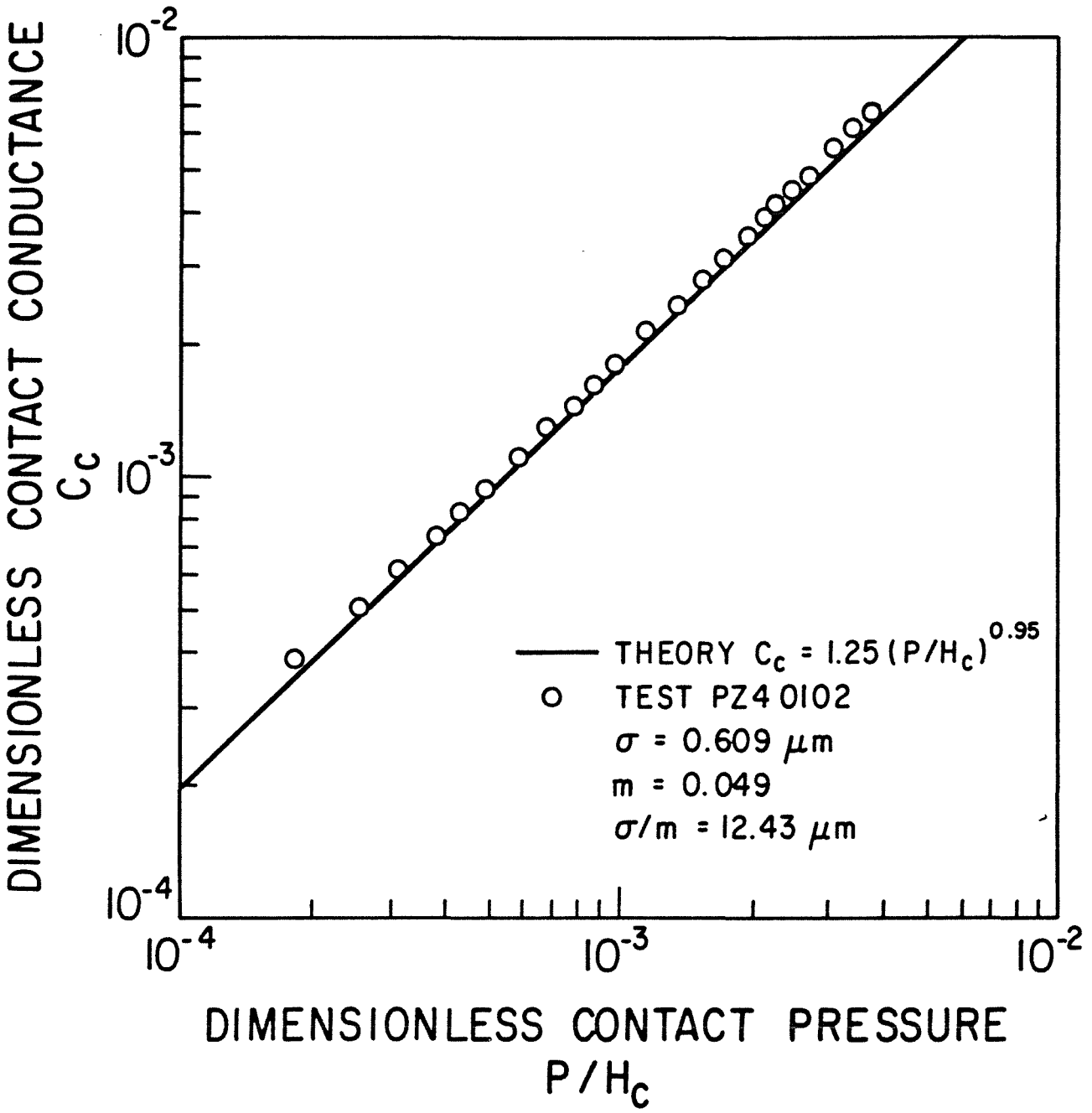

Figure 5.17: Comparison Between Theory and Test Results for Zr-4, Pair PZ40102

type and properties may have a major role in the discrepancies observed at light loads. Further discussion will be devoted to this point in the next section.

Figure 5.18 shows the test results for the next roughest pair of Zircaloy-4 and compares the results with the predictions in dimensionless form. With the exception of the first few light load points, the agreement between the data and the theory is very good. Also, it can be seen that the deviation between the experimental and theoretical values occurs at relative contact pressures less than $5*10^{-4}$.

The test results reported in Table C.28 illustrate an interesting phenomenon which occurred during this test. As can be seen from Figure 5.18, the data point of run 21 shows a marked increase in the measured conductance over its neighbours. Actually during this run, the test column was cooled down to 60°C due to a momentary power failure which disabled the microcomputer, as well as the datalogger. Therefore, the computer program was reloaded and the test continued without making any adjustement in the heater input power. However, when the steady-state was regained after six hours, the measured conductance was higher than the predicted value by 15.4% and above its neighbours by approximately 10%.

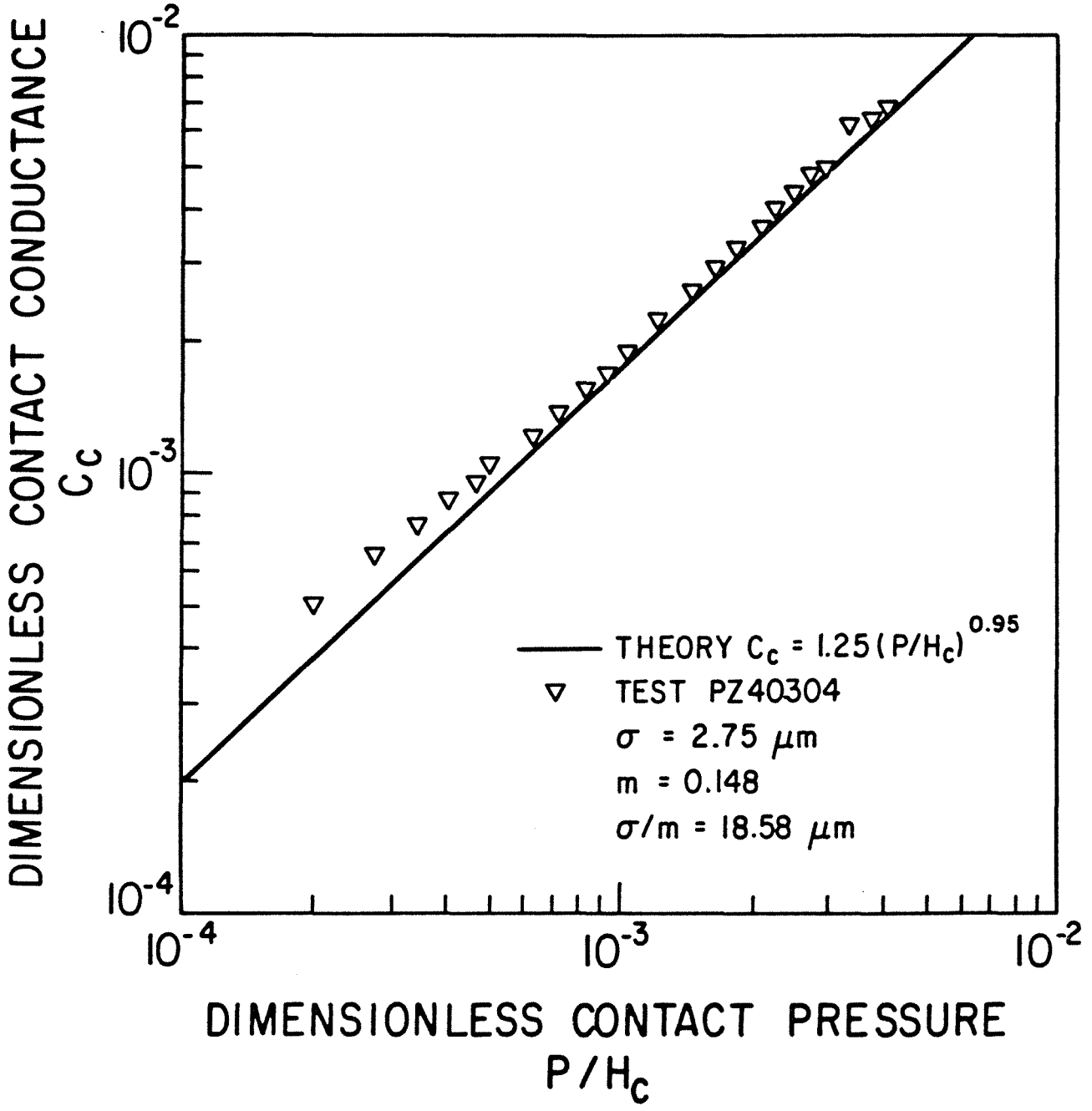

Figure 5.18: Comparison Between Theory and Test Results for Zr-4, Pair PZ40304

It should be stated that the momentary power failure did not affect the mechanical pump or the diffusion pump operation, so the vacuum pressure was always better than 10^{-5} torr. Also, it should be mentioned that a number of instantaneous power failures were experienced during runs 18 and 19. These failures disabled only the the datalogger, interrupting the main heater power for a period of three minutes until the microcomputer reinitialized the data-logger. However, this disturbance resulted in conductance values higher than the expected values by approximately 3-4%.

The measured and predicted contact conductances for pair PZ40506 are shown in Figure 5.19 and are tabulated in Table C.29. From this figure it is clear that the characteristics of the experimental data is quite similar to the previous pair, as well as many other tested pairs. However, these data points seem to be displaced above the theoretical line by approximately 15%. In light of the inherent uncertainty in the experimental data, this deviation can be considered insignificant, although the following may be a plausible explanation.

As mentioned earlier, it was a very difficult task to prepare a satisfactory rough surface on the faces of the Zircaloy-4 specimens. Always, the surfaces roughened by glass beads numbers 3 and 4, Table B.1, had a visible discolouration. This

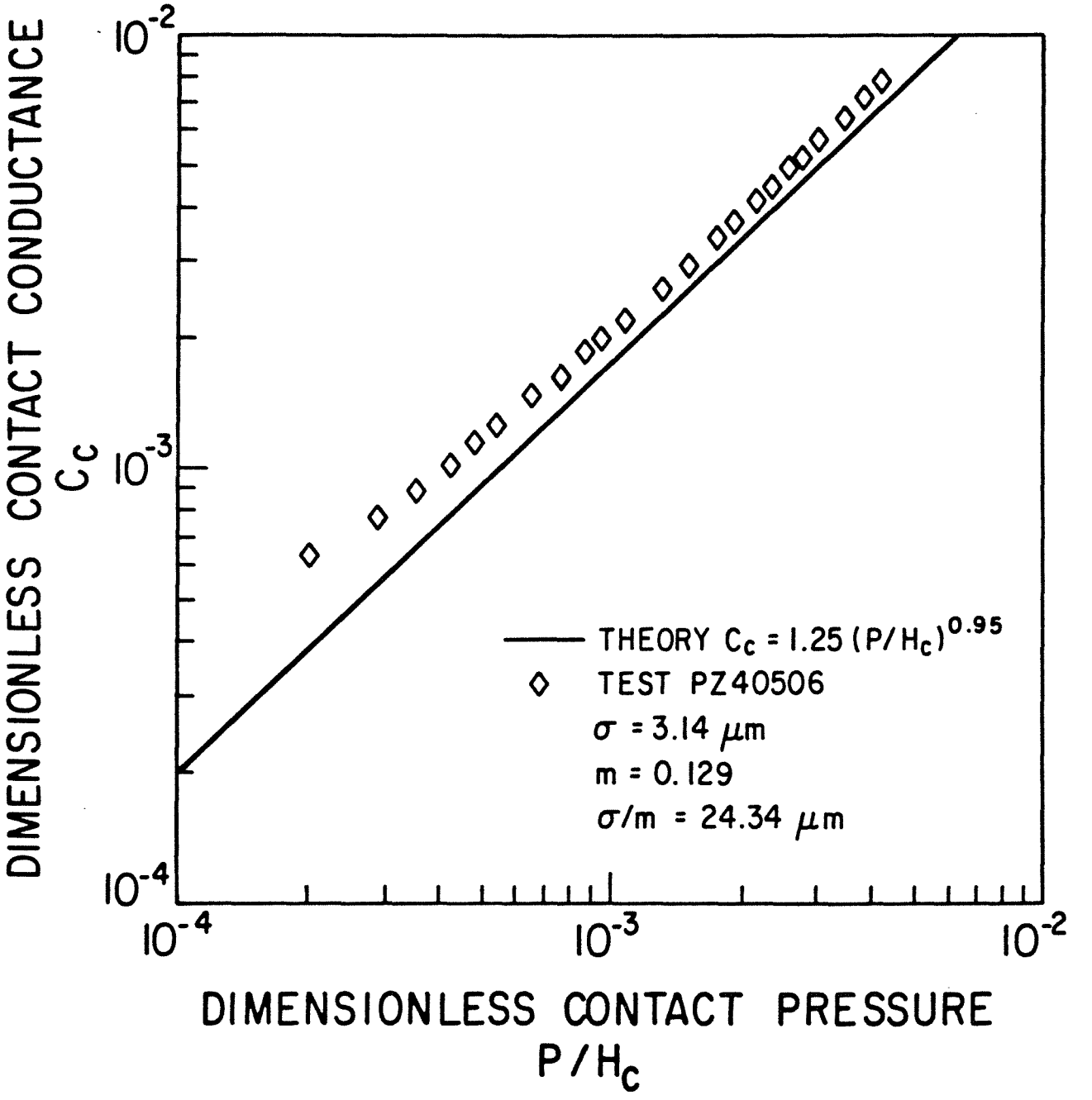

Figure 5.19: Comparison Between Theory and Test Results for Zr-4, Pair PZ40506

discoloration was removed by using an acid mixture of 45mℓ Nitric acid, 45mℓ Lactic acid, and 3mℓ Hydroflouric acid. Several other cleaning solutions were tried first but found to be unsatisfactory. The contact surfaces of pair PZ40506 were cleaned with the acid mixture and distilled water immediately before the test. After the test was completed, the joint surface parameters were remeasured and it was discovered that the acid mixture severely altered the joint surface parameters as is shown in Table 5.4.

Thus, this deviation can be attributed to a change in the measured micro-hardness variation as a result of etching the contacting surfaces with the acid cleaning mixture. The substantial difference in the measured surface parameters before and after the cleaning process lends support to this explanation.

The last test in this series was performed on the roughest pair, PZ40708, which was also cleaned using the acid mixture. As expected, the experimental data shown in Figure 5.20 seem to be higher than the predictions by approximately 14% and exhibit the same characteristic behaviour of the previous pair. The test results are listed in Table C.30 in Appendix C, and the comparisons between the experimental and theoretical values is reported in Table C.34. From these tables and Figure 5.20, it can be seen that the measured conductance of run number 6 is higher than

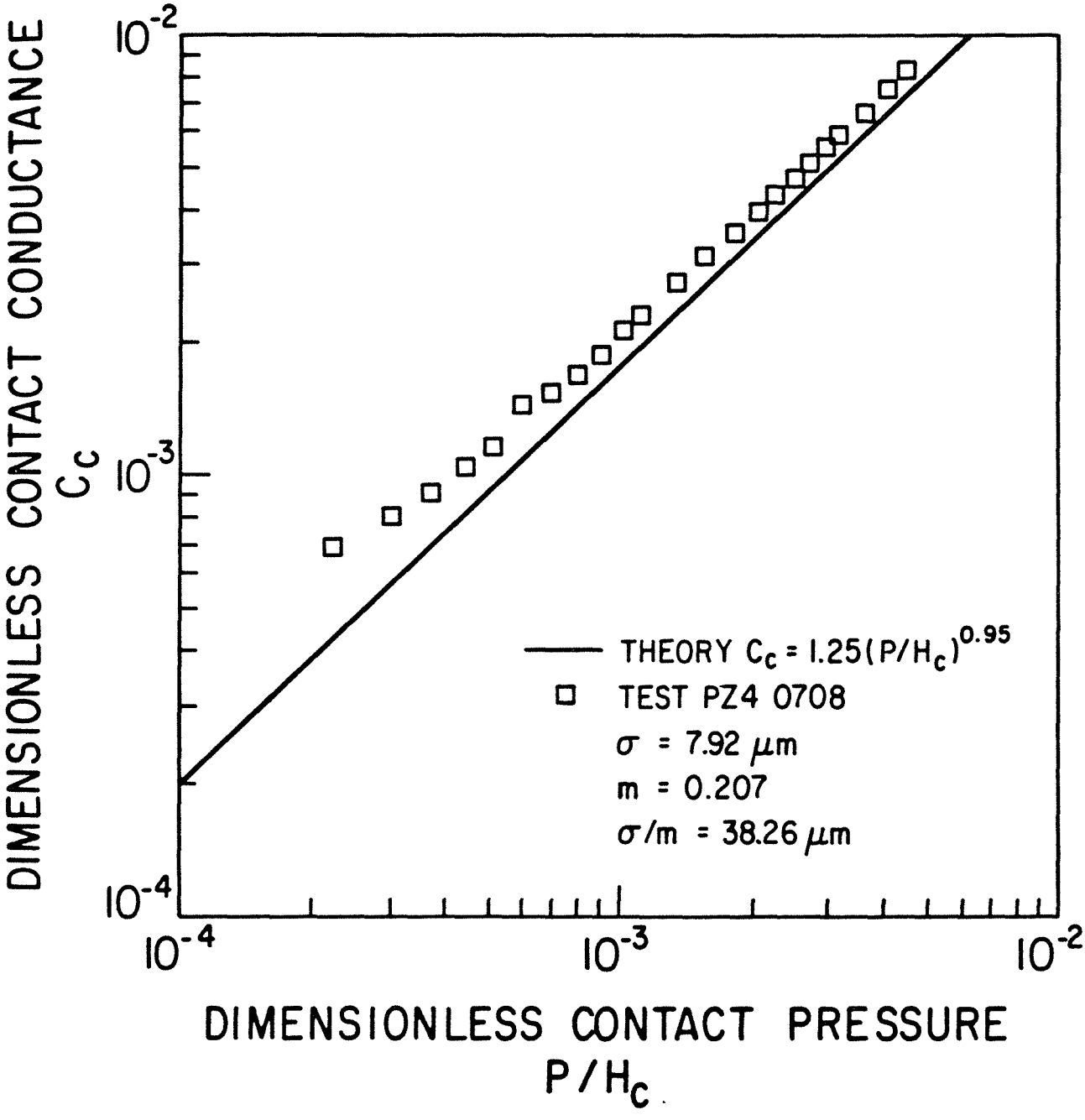

Figure 5.20: Comparison Between Theory and Test Results for Zr-4, Pair PZ40708

expected by approximately 10%. This unexpected increase was due to a partial cooling of the test column as a result of a complete power failure caused by a thunderstorm.

Close examination of Tables C.29-C.30 and Tables C.33-C.34 reveals that the experimental data of pairs PZ40506 and PZ40708 are quite consistent with each other over the whole load range. This lends support to the previously offered explanation and emphasizes the importance of the appropriate hardness value for accurate thermal predictions.

To demonstrate this point further, the dimensionless contact conductance data of pairs PZ40102 and PZ40708 are plotted against the contact pressure in Figure 5.21. For the purpose of comparison, the predictions from the proposed model assuming the macro-hardness value are also included in this figure. The experimental results of pair PZ40102 show very clearly that, when the appropriate hardness value was employed, very good agreement between the predictions and the experiments was obtained. However, if the macro-hardness value was used, the predictions would exceed the measurements by approximately 38%. On the other hand, the experimental data of pair PZ40708 are in excellent agreement with the predictions assuming the macro-hardness value and only in fair agreement with the proposed model. This indicates that the estimated contact

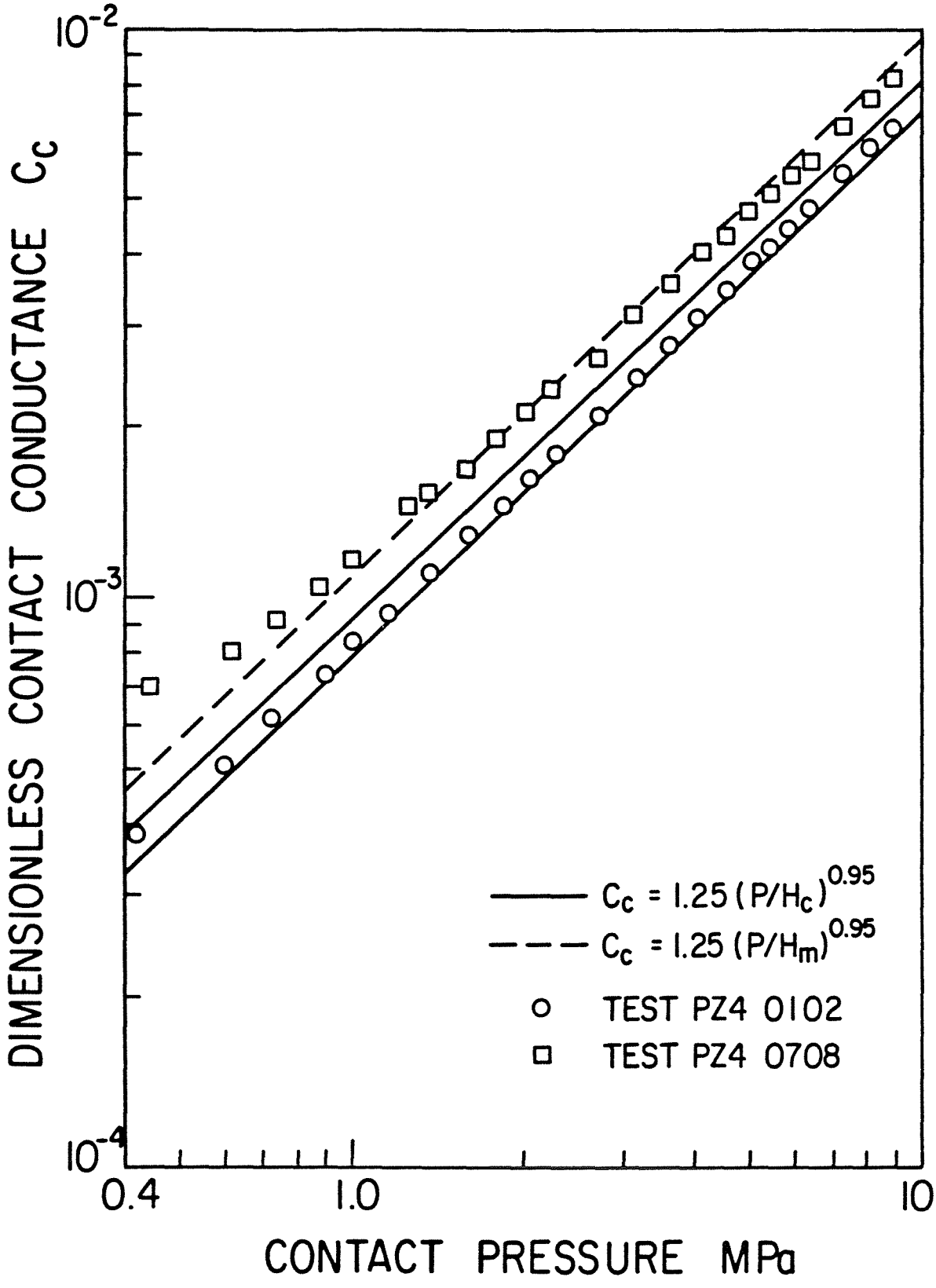

Figure 5.21: Prediction Dependence upon the Appropriate Hardness Value

hardness for this pair is inadequate and conclusively confirms that changes occurred in the contacting surfaces by the acid mixture. In light of the above discussion, the test data of pairs PZ40506 and PZ40708 should not be considered as detrimental to the proposed contact conductance model. In fact, these data should be used as a good example for demonstrating the important role of the surface hardness in accurate prediction of the joint conductance between conforming rough surfaces.

5.2.6 General Discussion of Vacuum Results

The experimental results and their comparisons with the proposed model demonstrate clearly the importance of the surface micro-hardness variation for accurate thermal predictions. Also, the test results verify the contact conductance model, as well as the assumptions made over a broad range of geometric, mechanical and thermal parameters. The ranges of these parameters are:

1. Effective surface RMS roughness from 0.478μm to 13.94μm.

2. Effective surface mean absolute slope from 0.049 to 0.233.

3. Critical surface parameter σ/m from 6.64μm to 59.83μm.

4. Contact pressure from 409 kPa to 8886 kPa.

5. Surface macro-hardness from 1010 MPa to 1727 MPa.

6. Contact hardness from 1972 MPa to 4113 MPa.

7. Heat flux from 22 kW/m^2 to 96 kW/m^2.

8. Interface temperature difference from 2.6°C to 122°C.

9. Mean interface temperature from 98°C to 179°C.

10. Thermal conductivity from 16 W/m°C to 77 W/m°C.

Figure 5.22 shows a photograph of a typical smooth surface after the thermal test had been completed. As can be seen from the figure, the contacts were made through penetration of the smooth surface by the contacting asperities of the harder rough surface. Since the joint was formed between two similar materials possessing the same macro-hardness value, the following conclusions may be drawn:

1. The asperities of the rough surface are harder than the top layer of the smooth surface due to the bead blasting process.

2. The bead blasting process is similar to any machining process which leads to changes in the surface hardness within a thin layer from the machining surface.

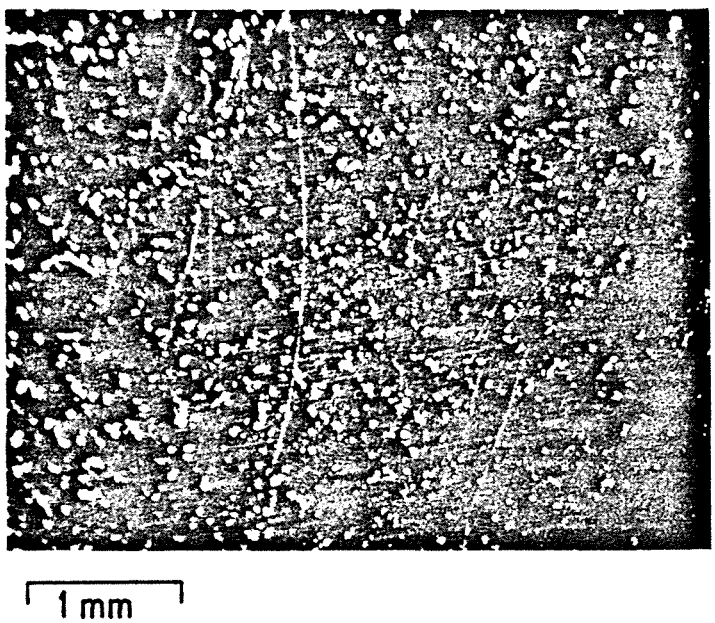

Figure 5.22: Photograph of Smooth Surface After Testing - Magnification 20X

3. Surface micro-hardness is a real phenomenon.

4. The asperities of the hard surface act like micro-hardness indenters.

The experiments emphasize the important role of the surface parameters and show clearly how crucial their estimation is to accurate thermal predictions. It is our belief that the surface parameters have a significant impact upon the thermal predictions since they directly affect the evaluation of the contact hardness and the joint conductance. The consistency of the test results of each series indicates that the methodology used in estimating the surface parameters was satisfactory and yielded quite reasonable information. The overall good agreement between the experimental and theoretical values provides further support for the preceding conclusion.

The test results of pairs PZ40304 and PZ40708 illustrate an important feature of the thermal contact conductance problem. As previously mentioned, a noticeable increase in the contact conductance value was observed when the thermal flux through the test column was disturbed for a period of time. This noticeable increase, of course, reflects a real change occurring within the contacting surfaces caused by decreasing and then increasing the interface mean temperature. In other words, the effect of

increasing the interface mean temperature from a low value to a high value may have resulted in an increase in the size and in the number of contacts due to thermal strain or some other factors.

In general, it is very difficult at this stage to make any firm conclusions regarding the increase in the number or size of the contacts. However, there exists evidence and data showing a marked increase in the contact conductance as the interface mean temperature increases. The heat flux was held as steady as possible during any particular test, specifically to eliminate this effect. Also, it should be mentioned that the magnitude of this increase in conductance decreases with increasing applied contact pressure. The test results of pairs PSS1314 and PSS1516, as well as the data of Ref.[74], shows this phenomenon clearly. In light of this discussion, the deviation between the light load data and the contact conductance model could be partly attributed to this phenomenon since the first load contact was formed at room temperature.

The deviation between the experiments and the predictions at light loads can also be attributed to several other factors. Close inspection of the Ni200 and SS304 results reveals that the light load deviations in the Ni200 data are smaller in magnitude than those of the SS304 in spite of the fact that these pairs are geometrically similar. Since these pairs were prepared identically and tested

using the same equipment and test procedure, a possible explanation for this observation may be based on the differences in the thermo-physical properties of these two metals. The same magnitude of deviation observed at light loads for Zirconium alloys furnishes a good reason for this explanation since their thermal conductivity and macro-hardness values are quite close to those of SS304.

As discussed in Section 5.2.3, it appears that the deviation at light loads increases with increasing surface roughness. Of course, this can be attributed to the increase in the flatness deviation due to the roughening process. However, there is insufficient data to support this line of reasoning. It should also be remembered that the interface temperature difference increased with increasing joint roughness since the input power for any particular series of tests was maintained relatively constant. On this basis, it would seem reasonable to conclude that thermal strain has a major role in this light load deviation.

Further, the deviation between the experimental and theoretical values at light loads can be attributed to the specimens' original out-of-flatness. Obviously, this is true to some extent, since the model was developed for two ideal flat surfaces while all the tested surfaces exhibit flatness deviation of less then 1μm. If this is the case, the very good agreement between the experiments and the predictions at moderate and high contact pressures suggests that as

the applied load increased the out-of-flatness effect becomes negligible. Therefore, it seems possible that the surface flatness deviation is important only at light loads while at moderate and high contact pressures the surface roughness is dominant and overwhelms the out-of-flatness effect.

In light of the above discussions and the experimental evidence, all the previously offered explanations are plausible. Therefore, no definite conclusion regarding the deviation between the experiments and the predictions at light loads can be made. However, further work is recommended to clarify this point.

5.2.7 Correlation of Light Load Data

As already mentioned, the deviation between the light load data and the predictions decreases with increasing applied load. However, a noteworthy feature in Figures 5.1 through 5.21 is that for relative contact pressure higher than approximately $6*10^{-4}$ this deviation lies within the data uncertainty. Also, it can be seen that there is a progressive increase in the slope of the conductance data with increasing relative contact pressure up to a value of approximatly $6*10^{-4}$. This phenomenon has been observed and reported in the literature by a number of investigators [87-90]. Therefore, a correlation for the light load data should be of special interest to thermal design engineers.

In Figure 5.23, the light load dimensionless contact conductances are plotted against the relative contact pressure in the range of $1*10^{-4}$ to $6*10^{-4}$. In light of the discussion presented in Section 5.2.5, the experimental data of pairs PZ40506 and PZ40708 are excluded from the figure. This results in a total of 117 data points which are correlated by the following expression:

$$C_c = 0.23\ (P/H_c)^{0.72} \qquad (5.8)$$

with an overall RMS% difference of 11.2%.

From Figure 5.34, it is interesting to observe that the experimental data are divided into two groups by the broken line which represents Eq.(5.8). The first group lies between the solid and the broken lines and includes the data of Ni200 and the very smooth pairs. The second group is above the broken line and includes the data of SS304 and Zirconium alloys. In other words, the classification of these two groups may be based on the behaviour of the joints, i.e., good or poor conductor joints. This classification, of course, takes into account the effect of the joint surface roughness and thermophysical properties.

Since the main contribution to the data uncertainty is due to the uncertainty in the surface parameters, it is desirable to

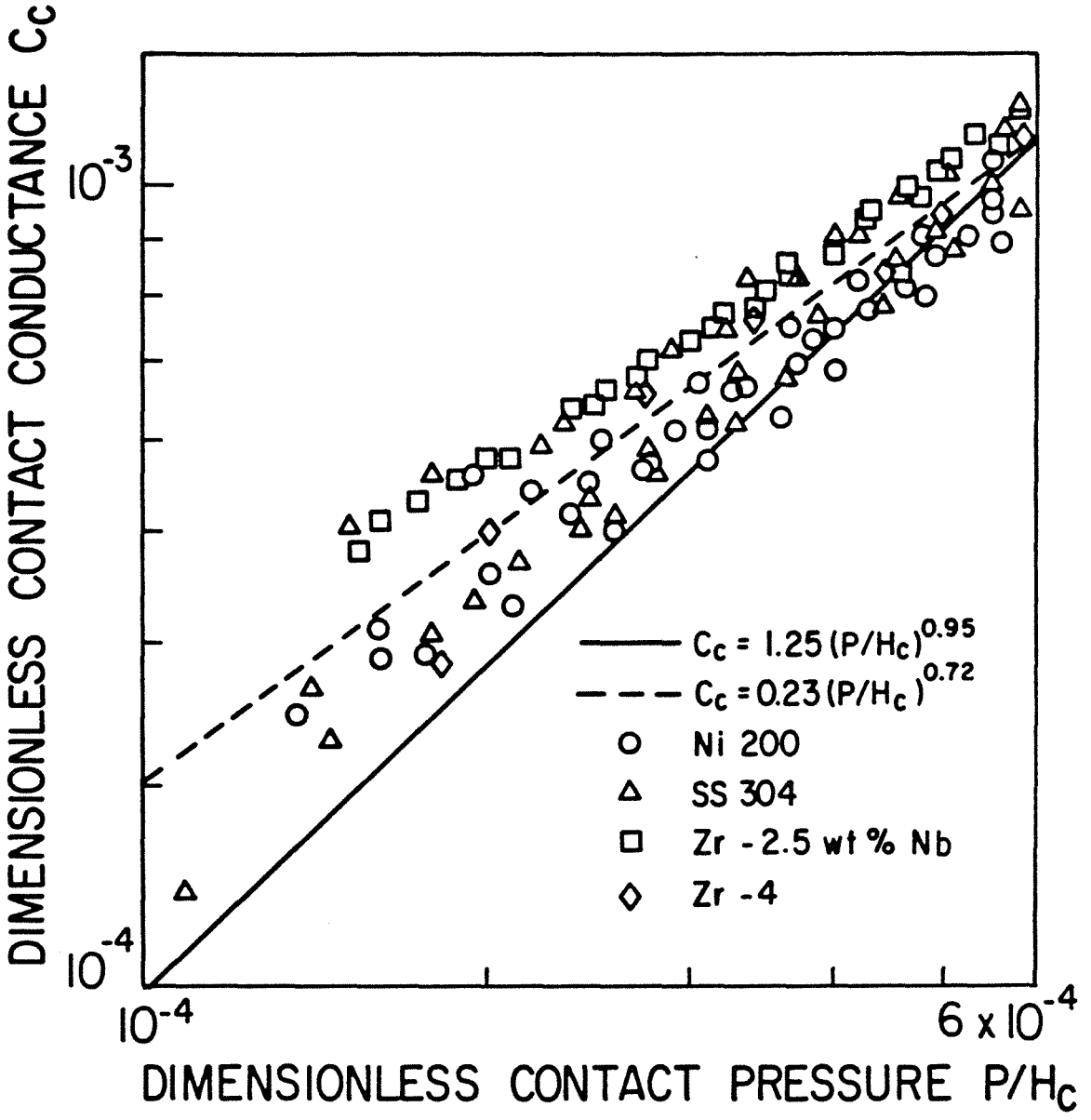

Figure 5.23: Light Load Thermal Contact Conductance Data

compensate for this uncertainty. The compensation can be made by adjusting the experimental data of a particular test by the average percent difference observed at the last five data points, i.e., the high relative contact pressure test results. This is logical since the uncertainty in the relative contact pressure is minimum.

A least-squares fit of the 117 data points after compensation resulted in the following correlation:

$$C_c = 0.22\ (P/H_c)^{0.714} \tag{5.9}$$

with RMS% difference of 8.5%. The compensated test results, as well as the predictions from Eq.(5.9), are shown in Figure 5.24. It is interesting to note that the predictions from Eq.(5.8) or Eq.(5.9) are quite similar, with a maximum percent difference of 1% occurring at $P/H_c = 1*10^{-4}$. This indicates that the estimation of the surface parameters is quite accurate and the deviation at light loads does not depend upon the data uncertainty.

Finally, it should be pointed out that the appearance of the experimental data in two distinct groups, as shown in Figures 5.23 and 5.24, lends support to the previously offered explanations. Thus, we can conclude that the deviation between the experiments and the predictions at light loads depends upon the joint thermo-physical properties, surface roughness, contact pressure, thermal flux, and/or local thermal gradient.

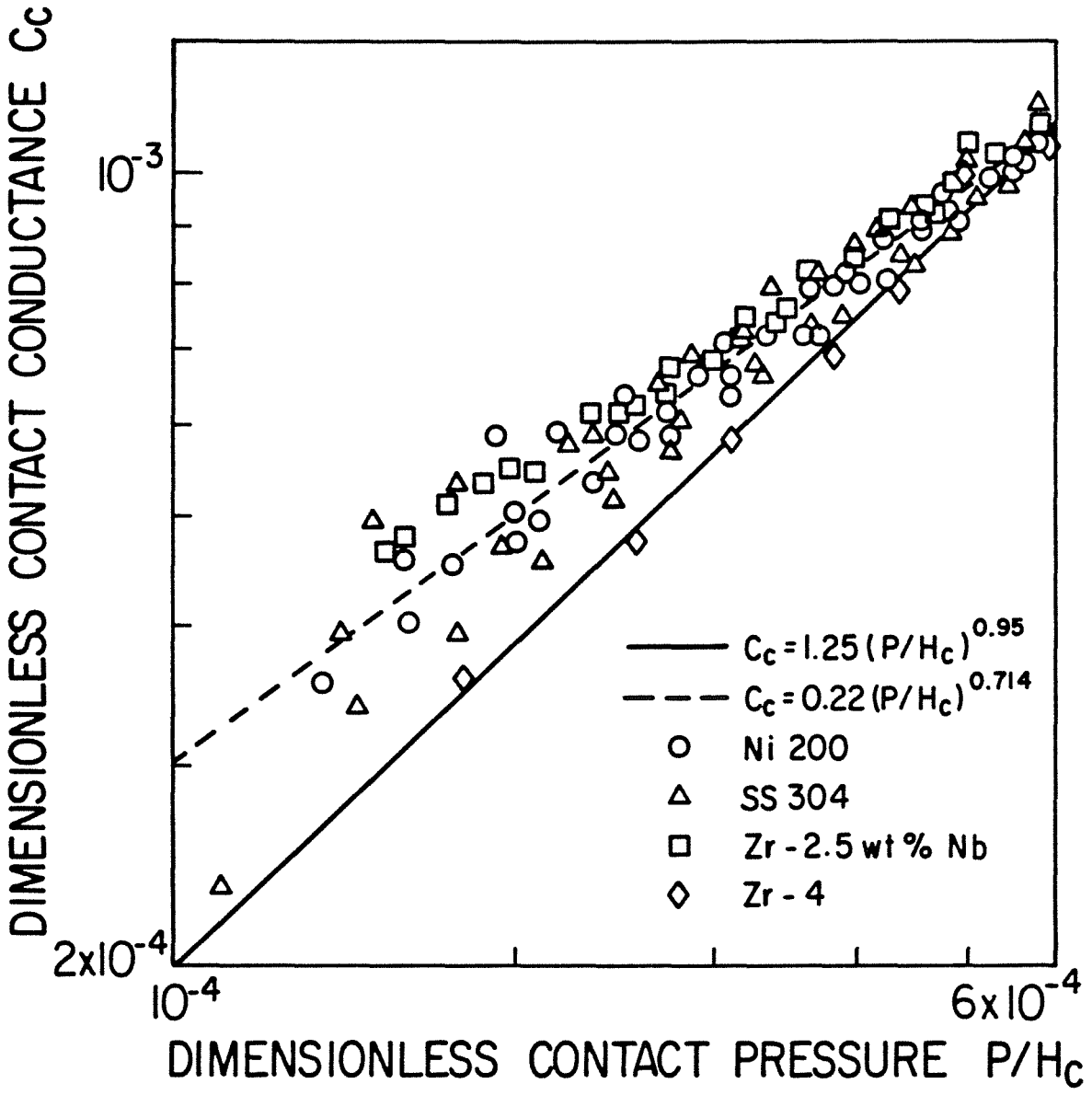

Figure 5.24: Light Load Thermal Contact Conductance Data after Compensation

5.3 Gas Tests

This group of experiments consists of four tests performed on joints made of SS304 and tested in Nitrogen and Helium. Although stainless steel is relatively hard and a poor conductor, this combination of test gases and material represents a reasonable set of extremes for verification of the gap model. Also, SS304 has the advantage that duplicate surfaces free of oxide may be easily prepared.

The thermal properties of Helium and Nitrogen are collected from a number of texts, handbooks, and many other references, and are reported in Table 5.5 for convenience. The thermal

Table 5.5: Nitrogen and Helium Properties

Property	Nitrogen	Helium
k_g W/mK	$2.502 * 10^{-2} + 5.844 * 10^{-5}$ T(°C)	$14.543 * 10^{-2} + 3.24 * 10^{-4}$ T (°C)
α	0.9	0.425 - $2.3 * 10^{-4}$ T (K)
γ	1.405	1.667
Λ_o nm	63.0	186
Pr	0.691	0.667

Note: Λ_o values are at 288K and 760 torr, and the gas purity is 99.7% for Nitrogen and 99.995% for Helium

conductivity expressions for Nitrogen and Helium are obtained by correlating the data reported in Ref.[71] in the range of $27°C \leq T \leq 400°C$. These expressions are accurate to within ±1% in the above specified temperature range.

Thermal accommodation coefficients for Helium and Nitrogen have been measured experimentally for a number of different materials and reported in the literature. Most of these measurements are made on very smooth and atomically clean surfaces specially prepared for this purpose. Unfortunately, very little experimental data are available for engineering surfaces which are in contact and, therefore, the listed values in Table 5.5 are selected with care.

The accommodation coefficient for Nitrogen is taken to be 0.9 based upon the results of Dickins [75]. This value is quite consistent with the data reported in Ref.[76] for air on machined cast iron. For Helium, the accommodation coefficient expression, shown in Table 5.5, was determined by Ullman et al [77] for Helium on Stainless Steel 303. Since no attempt had been made to polish or clean the surface, this expression is felt to be reasonable for Helium on SS304 rough surfaces. Also, this expression is in agreement with very recent experimental data reported in Refs.[78-79] for Zircalloy-2 and Uranium Dioxide.

As can be seen from Table 5.5, Helium and Nitrogen possess quite different properties. At room temperature, for example, there is a factor of 5.8 between their thermal conductivities and a factor of approximately 0.39 between their accommodation coefficients, as well as a factor of approximately 3 between their mean free path values.

This group of tests has been conducted as a function of the gas type, the surface parameters, and the contact pressure. The test procedure used in performing these experiments is fully discussed in Chapter 4. To reduce the readial heat loss from the test column, the upper Armco iron heat-flux meter was removed and the heat flux across the joint was assumed to be the mean of the thermal fluxes through the SS304 specimens. The heat flux through the test specimen was determined from the axial temperature gradient along it and the mid-plane thermal conductivity. The initial test plan for this group of tests was to prepare duplicate SS304 vacuum joints and test each pair only in Nitrogen or Helium. However, the test plan was modified in light of the experimental results of pair PSS1112.

The range of geometric, mechanical and thermal parameters of the tested pairs are tabulated in Table 5.6. The test results and the comparison with the prediction for each pair are reported in detail in Appendix C. The experimental results of each pair will

Table 5.6: Geometric, Mechanical and Thermal Parameters of SS304 Pairs - Gas Tests

PAIR	PSS0910	PSS1112	PSS1314	PSS1516
σ μm	5.65	5.61	6.29	4.02
m	0.153	0.151	0.195	0.168
σ/m μm	36.93	37.15	32.26	23.93
a_c μm	14.03	14.12	12.26	9.09
d_v μm	35.08	35.29	30.65	22.73
H_c MPa	2777	2773	2217	2377
H_m MPa	1472	1472	1472	1472
P_{mx} kPa	8769	8829	4076	8769
P_{mn} kPa	459	470	461	430
10^3 $P/H_{c,mx}$	3.162	3.187	1.840	3.692
10^3 $P/H_{c,mn}$	0.165	0.170	0.280	0.181
$T_{m,mx}$ °C	166.8	222.5	230.6	230.9
$T_{m,mn}$ °C	157.8	194.1	181.5	190.1
ΔT_{mx} °C	19.3	27.3	148.2	124.1
ΔT_{mn} °C	7.5	9.6	14.1	7.3
$h_{j,mx}$ W/m^2K	6219	7202	4979	10154
$h_{j,mn}$ W/m^2K	2303	3016	245	366
Environment	N_2	H_e,N_2,Vac.	Vac.,N_2,H_e	Vac.,N_2,H_e
$H_v(d_v)$ MPa	$6271\ d_v^{-0.229}$		$4922\ d_v^{-0.233}$	
k(T) W/mK	$17.02 + 1.52 * 10^{-2}$ T (°C)			

be discussed separately and compared graphically with the predictions in the following sections. Then, a general discussion of the main features of these experiments will follow. Before discussing the experimental results, it should be mentioned that the gas properties were determined at the interface mean temperature.

5.3.1 Pair PSS0910

This pair was tested in Nitrogen over the whole load range. The test was run in automatic mode and the Nitrogen pressure was maintained as constant as possible between 564 and 574 torr.

Pair PSS0910 was almost identical to pair PSS0506 which was tested under vacuum conditions. The effective surface roughness for pair PSS0910 was 5.6μm, while the effective surface mean absolute slope was 0.153. The range of the interface mean temperature was 168-158°C, associated with a temperature drop of 19.3-7.5°C, and heat flux was approximately 44.8 kW/m^2. The test duration for this pair was 5 days.

The experimental results of pair PSS0910 are reported in Table C.35 in Appendix C, and compared with the predictions in Table C.36. Figure 5.25 shows a graphical comparison between the experimental and theoretical joint conductances. The theoretical predictions from the contact and gap models are also included in the figure for convenience.

As can be seen from Figure 5.25, the experimental joint conductance data points are slightly above the theoretical values for all relative contact pressures by approximately 12%. In light of the uncertainty analysis, Appendix E, this difference should be considered satisfactory. Hence, it can be concluded that the agreement between the experiments and the predictions is very good. The RMS% difference for the 23 data points is only 12.1%.

Qualitatively, this pair was tested in the continuum flow regime because the gap-temperature jump parameter, YH, is in the range of $29.3 \leq YH \leq 38.5$.

5.3.2 Pair PSS1112

Pair PSS1112 is a duplicate of pair PSS0910 and has identical surface textures, as is shown in Table 5.6. However, this pair was mainly tested in Helium. The thermal test consisted of two parts. The first part was conducted in Helium only up to load level 19 and run in automatic mode. The second part was performed in vacuum, Nitrogen and Helium up to the highest contact pressure using a semi-automatic mode. The Helium and Nitrogen pressures were kept constant in the range of 40 ± 1 torr, while the vacuum pressure was always better than 10^{-5} torr. It should be pointed out that the heat flux in the upper and lower specimens

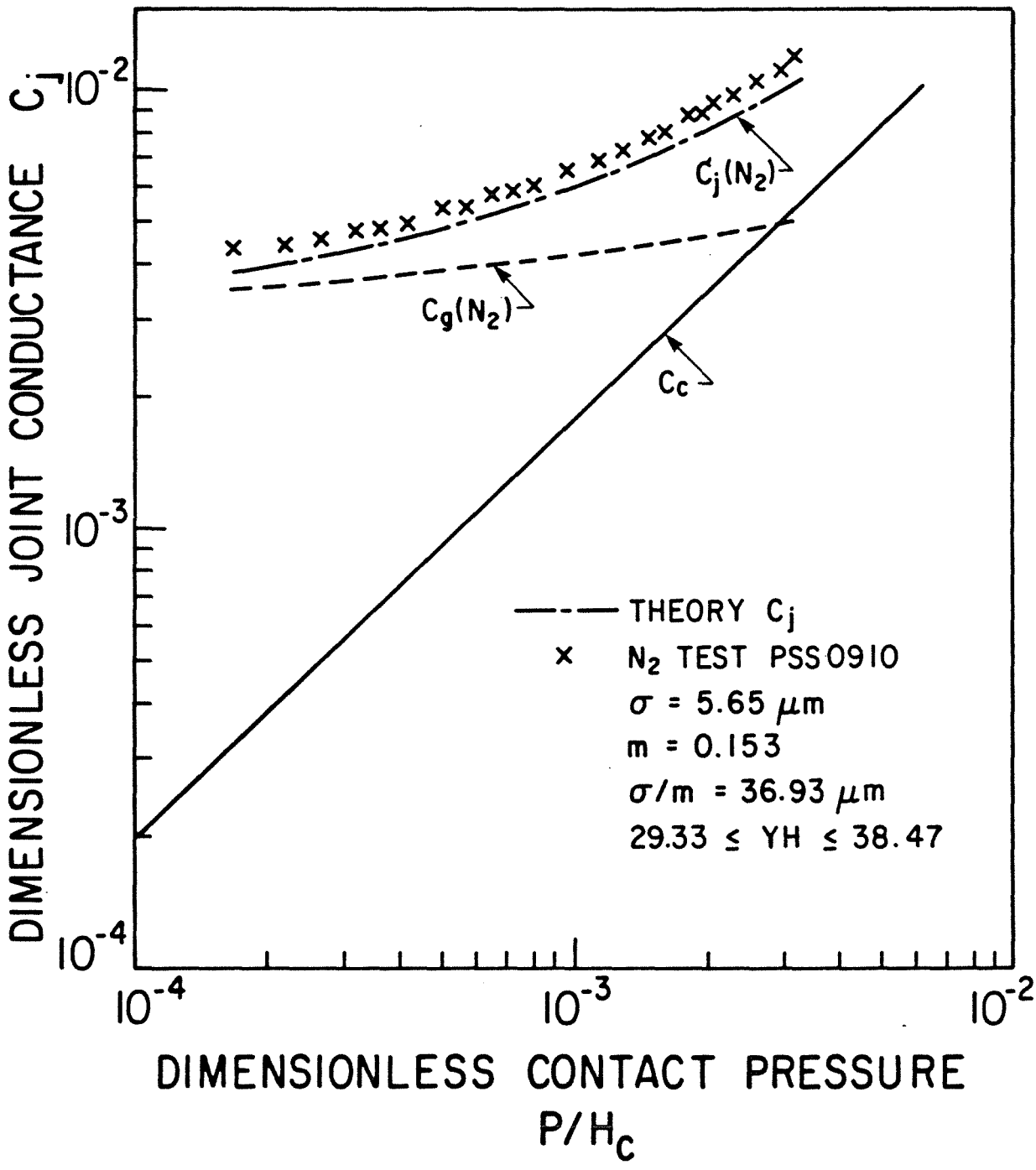

Figure 5.25: Comparison Between Theory and Test Results for SS304, Pair PSS0910 - Gas Tests

agreed poorly at Helium pressures greater than 40 torr. The test duration for this pair was one week.

For the first part, the interface mean temperature ranged from approximately 202°C to 194°C, while the temperature drop across the interface ranged from 19.9 to 11.5°C. The heat flux input to the test column was maintained constant, equal to 60 kW/m^2. For the second part of the test, the interface mean temperature varied from 210°C up to 222°C depending upon the test environment, the heat flux, and the applied load. The interface temperature difference varied between 27 and 9.6°C, while the heat flux varied between 60 and 70 kW/m^2. The test data and the comparison between the experimental and theoretical joint conductances are tabulated in Tables C.38-C.39 and listed in the order of determination.

Experimental and theoretical dimensionless joint conductance versus relative contact pressure is plotted in Figure 5.26. Also, the theoretical values predicted by the contact and gap models are shown in the figure. From Figure 5.26, it can be seen that the first 19 data points are significantly higher than the predictions. The error ranges from approximately 71% for the first data point down to approximately 46% for the nineteenth data point.

At this stage of the test, the poor agreement between the experimental and the theoretical values were thought to be due

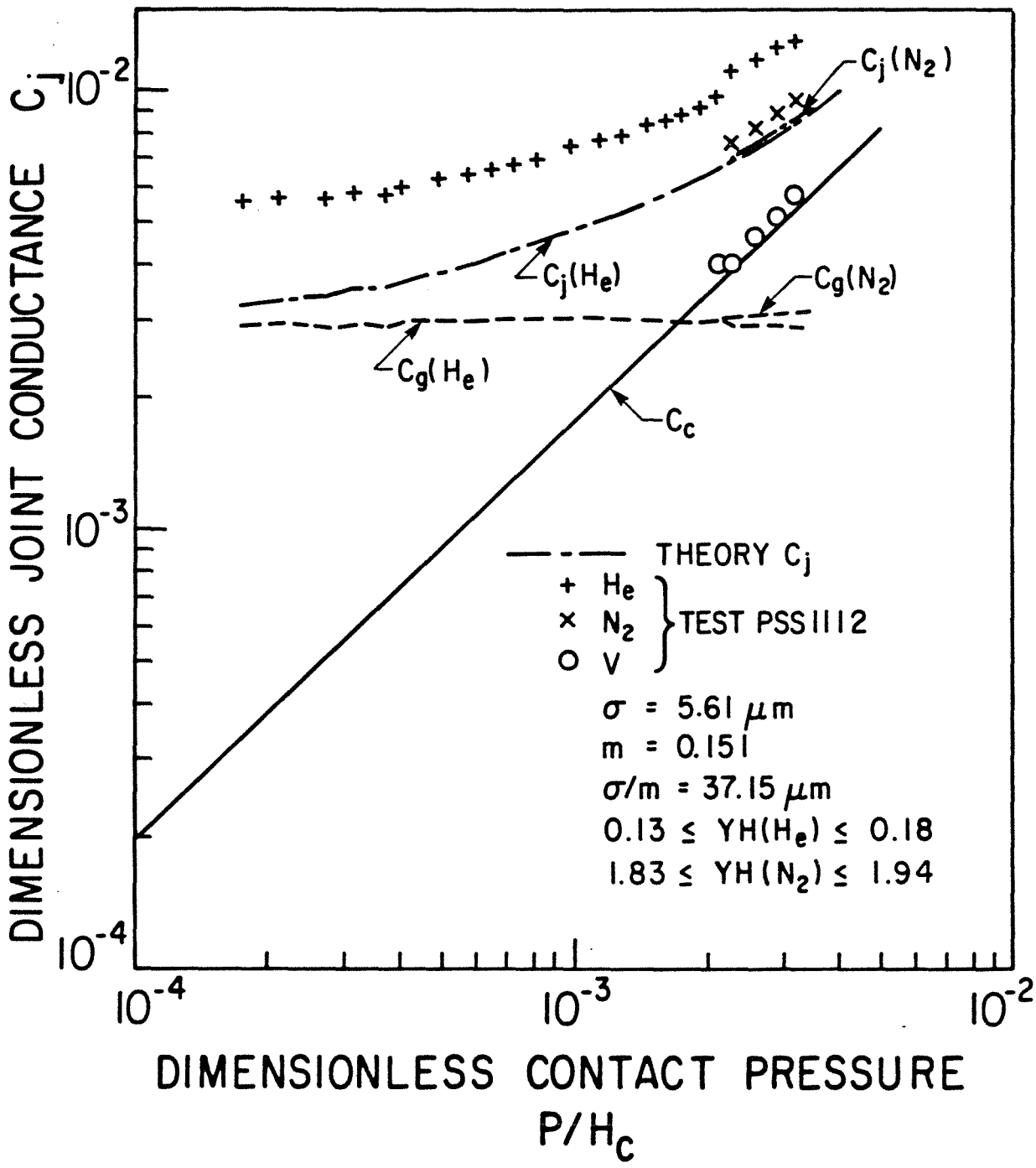

Figure 5.26: Comparison Between Theory and Test Results for SS304, Pair PSS1112 - Gas Tests

mainly to an inadequate estimation of the surface parameters. To eliminate any doubts, it was decided to continue the test up to the maximum permissible contact pressure and test the joint in vacuum and Nitrogen as well as in Helium. As can be seen from Figure 5.26, the measured joint conductances in vacuum and Nitrogen are in very good agreement with the predictions. Both the vacuum and Nitrogen data are slightly above the predictions by approximately 6.5% and 10%, respectively. This good agreement indicates, essentially, that the surface parameters are accurate and this deviation is limited to the Helium measurements.

It is interesting to note that the Helium experimental results of runs 1-19 are quite consistent although they are significantly higher than the predictions. More interesting are the results of runs 20-23, which are even higher and also consistent within themselves. Since this substantial increase in the last four data points was observed after admitting the Nitrogen into the test chamber, therefore this increase can be attributed to the presence of absorbed Nitrogen film on the joint surfaces.

Table C.40, Appendix C, shows a comparison between the Helium measurements and the predictions from the gap model. Helium experimental conductances for runs 1-19 are calculated by subtracting the theoretical contact conductances after multiplying

by a factor of 1.065 from the experimental joint conductances. This factor represents the average percent difference for the last four contact conductance data points. From the table, it is clear that the first 19 data points are higher than the prediction by approximately $83 \pm 6\%$. The percent difference for runs 20-23 increases from 137% up to 156%.

In light of the above results, and knowing that the Helium accommodation coefficient is very sensitive to the surface conditions, it is evident that the accommodation coefficient used in predicting the Helium conductance is inappropriate. In Table C.41, the gap model is used in predicting the Helium accommodation coefficient from the thermal results. As can be seen the predicted coefficient value is between 0.56 and 0.58 for runs 1-19, increases suddenly to 0.7 for run 20, then increases slowly up to 0.74 for run 23. This sudden increase in the Helium conductance, or the predicted accommodation coefficient value, supports the argument for the presence of Nitrogen absorbed film on the contacting surfaces.

Table C.42 shows the range of the geometric and thermophysical dimensionless parameters for this pair. As can be seen from the table, the mean plane relative separation, Y/σ, varied from 3.57 at the lightest load down to 2.73 at the maximum load.

The gas parameter, M/σ, was approximately constant around 20.5 ± 0.5 for Helium, and around 1.5 for Nitrogen. The gap-temperature jump parameter, YH, ranged from 0.178 to 0.127 for Helium and from 1.94 to 1.83 for Nitrogen. Qualitatively, the joint was tested in the transition regime in Helium and in the slip regime in Nitrogen.

5.3.3 Pair PSS1314

This pair was tested under vacuum conditions up to load level 5 and then tested in vacuum, Nitrogen, and Helium envrionments up to load level 14. The test was discontinued after this run due to severe air leaks. The joint was formed between a rough surface and a ground surface with surface micro-hardness variation as reported in Table 5.6. Also, Table 5.6 shows the range of mechanical and thermal parameters for this pair.

The purpose of this experiment was to repeat the previous test in order to ensure that the disagreement between the Helium measurements and the predictions was not an isolated incident. The Helium or the Nitrogen pressure was kept almost constant in the range of 40.5 ± 0.5 torr. The contact conductance measurements were obtained in vacuum pressure better than 10^{-5} torr and the test duration was 11 days.

The experimental data of pair PSS1314 are reported in Table C.43 in Appendix C, and tabulated in the order of determination. Tables C.44 through C.46 contain the comparisons between the experimental joint conductances and the theoretical predictions of contact, Nitrogen, and Helium conductances, respectively.

The experimental joint conductances in vacuum and Nitrogen are plotted against the relative contact pressure in Figure 5.27. It can be seen that there is excellent agreement between the vacuum results and the predictions. The RMS% difference is 7.2%. The data of runs 7-9 show a noticeable increase in the conductance over the rest of the data points. This can be attributed to the thermal strains, as discussed previously in Section 5.2.6. Figure 5.27 also shows the excellent agreement between the Nitrogen joint conductances and the predictions; the RMS% difference is only 6.6%. The RMS% difference between the Nitrogen conductances and the predictions from the gap model, Table C.45, is 7.8%. From Table C.45 it is interesting to note that the noticeable increase in the contact conductance also affected the Nitrogen joint conductance.

The dimensionless joint conductances measured in Helium are compared with the theoretical predictions in Figure 5.28.

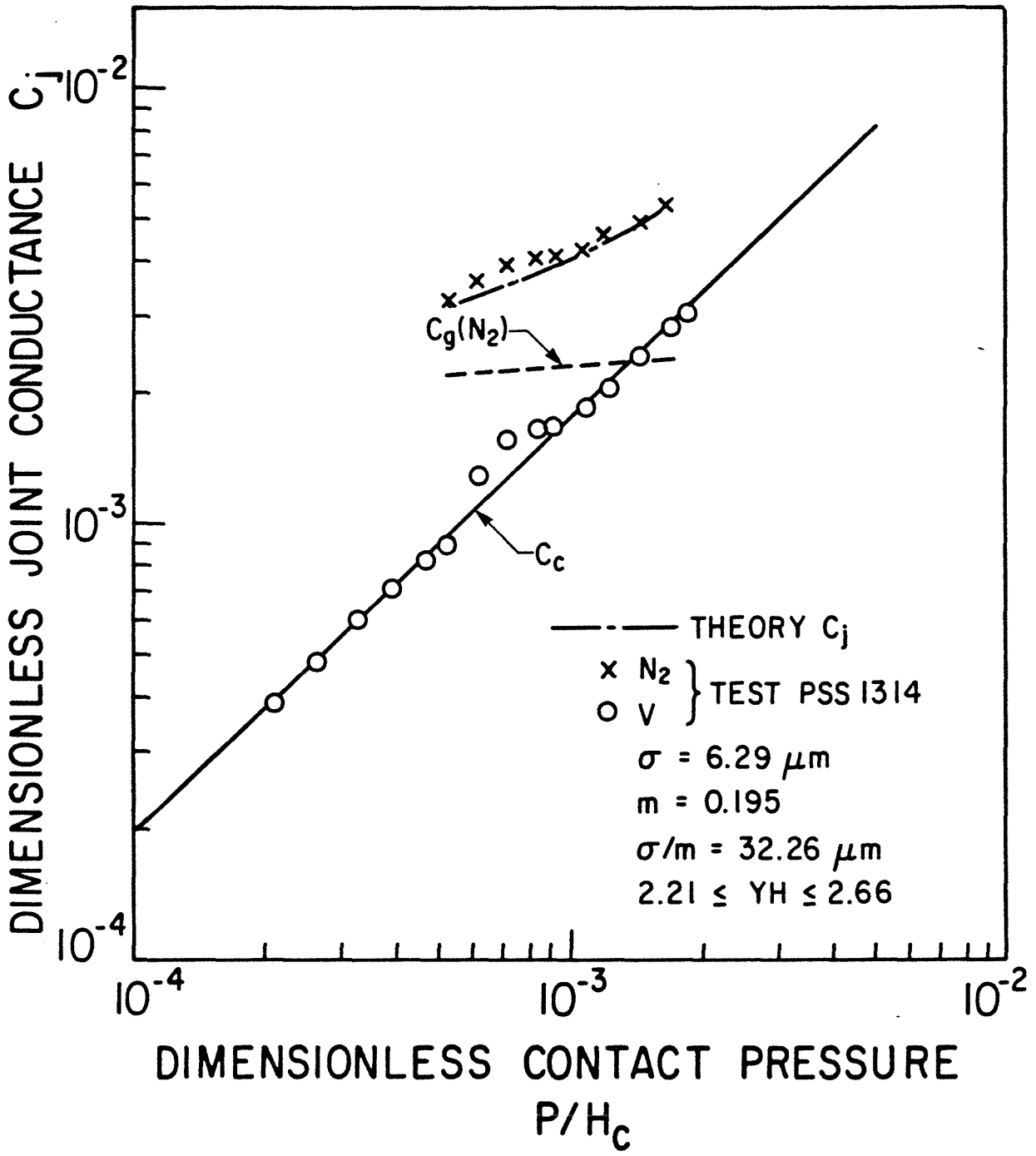

Figure 5.27: Comparison Between Theory and Test Results for SS304, Pair PSS1314 - Nitrogen Data

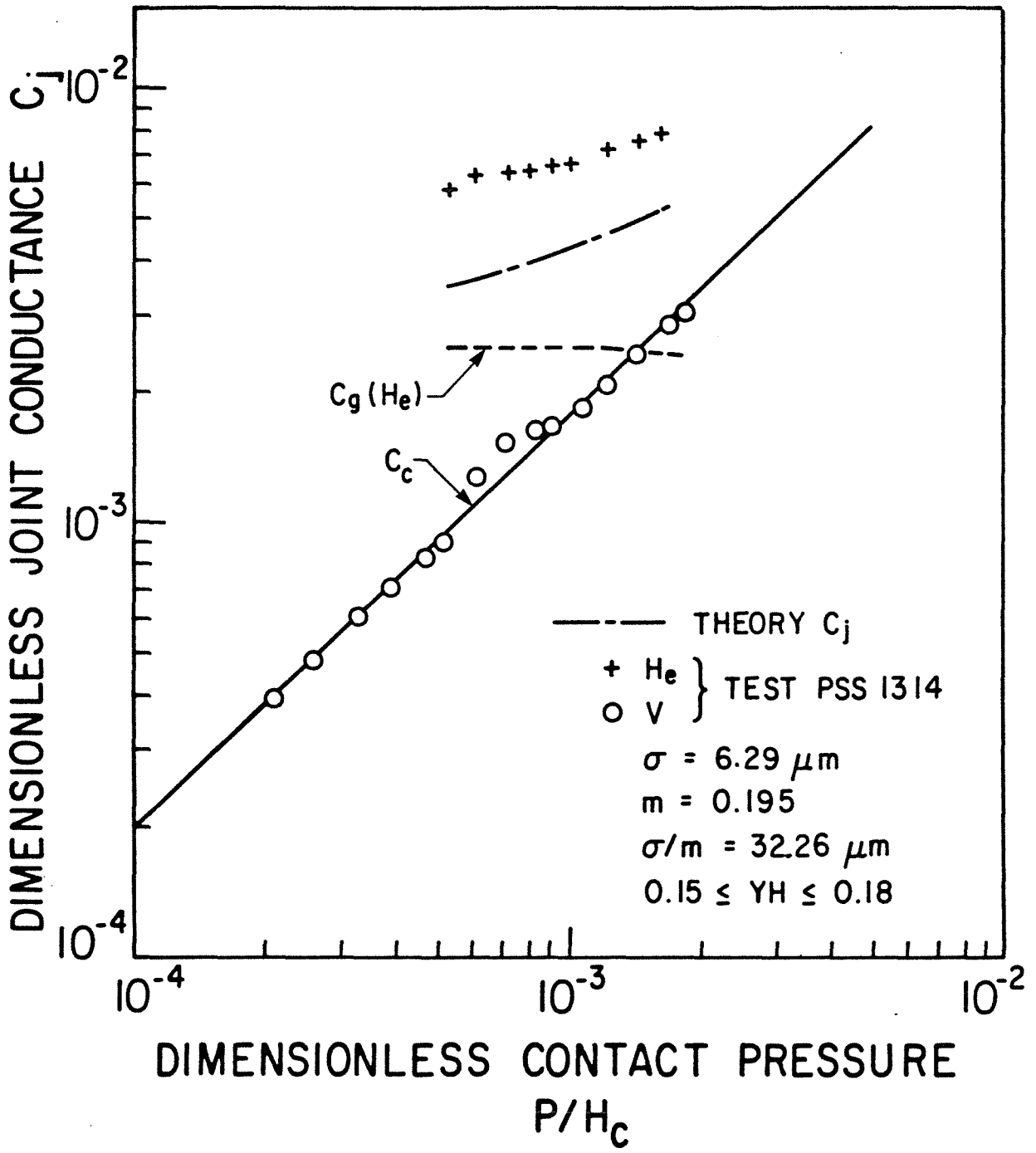

Figure 5.28: Comparison Between Theory and Test Results for SS304, Pair PSS1314 - Helium Data

Similar to the previous pair, it can be seen that the Helium experimental conductances agree poorly with the theoretical predictions. Also, Table C.46 shows that the Helium experimental conductances exceed the predictions from the gap model by approximately 100%; the RMS% difference is 99%.

It is of interest to note that if the gap model is employed in predicting the Helium accommodation coefficient from the thermal measurements, this coefficient would be of the order of 0.61, as shown in Table C.47. Also, it is important to mention that after the test was completed visual inspection of the joint surfaces indicated some yellow discoloration on the smooth surface.

Finally, this pair was tested in the transition flow regime under Helium conditions, and in the slip flow regime under Nitrogen conditions, as is shown in Table C.48.

5.3.4 Pair PSS1516

Similar to the previous pair, this pair was tested under vacuum conditions up to a contact pressure of 1330 kPa, and then tested in vacuum, Nitrogen and Helium up to the maximum contact pressure. However, this pair was relatively smoother than the previous pair. The surface characteristics, as well as the mechanical and thermal parameters, are given in Table 5.6.

The gas pressure inside the test chamber was in the range of 40.7 ± 0.25 torr, while the vacuum measurements were obtained at pressures better than 10^{-5} torr. The test duration of this pair was 18 days.

The experimental data of pair PSS1516 are tabulated in Table C.49 in Appendix C, and listed in order of determination. The comparison between the experiments and the predictions are reported in Table C.50. Table C.51 includes the comparison between the Nitrogen experimental conductances and the predictions from the gap model, while Table C.52 includes a similar comparison for the Helium data.

Figure 5.29 shows a graphical comparison between the experimental and theoretical dimensionless joint conductances in Nitrogen and in a vacuum. It can be seen that the experimental contact conductances are above and below the theoretical values with RMS% difference of 7.3%. Also, the data of runs 1, 9-10 show a marked increase in the contact conductances relative to the rest of the data. Figure 5.29 also shows the excellent agreement between the Nitrogen joint conductances and the predictions. The RMS% difference is only 4.6%. The RMS% difference between the Nitrogen conductances and the theoretical values predicted from the gap model is 9.9%.

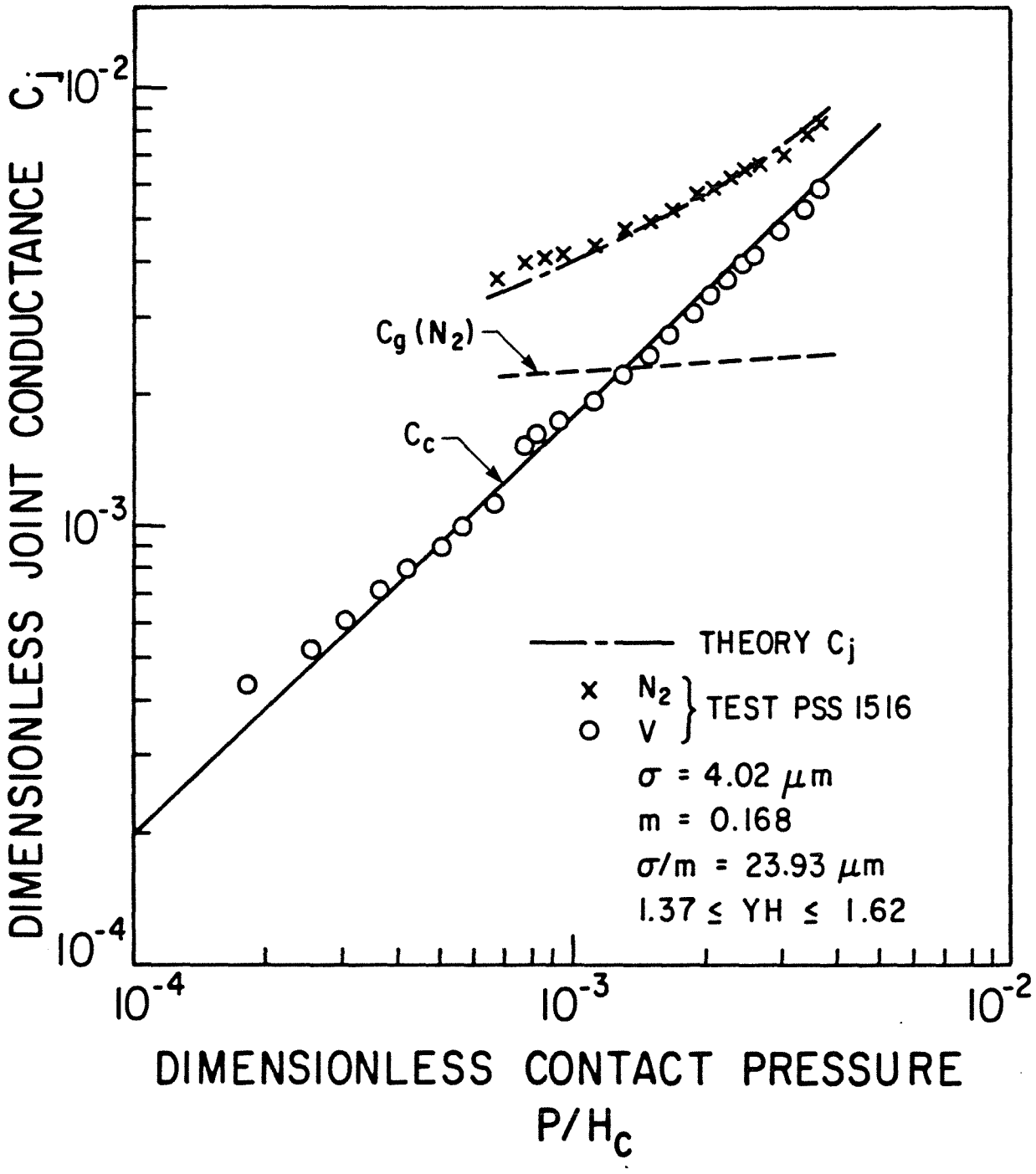

Figure 5.29: Comparison Between Theory and Test Results for SS304, Pair PSS1516 - Nitrogen Data

The pertinent test results in Helium are shown in Figure 5.30, where the dimensionless joint conductance data is plotted against the relative contact pressure. From this figure, as well as from Table C.50, it can be seen that the experimental results are significantly higher than the predictions for all contact pressures. The difference ranges from approximately 77% at run 8 down to 48% at run 23. However, Table C.52 shows that the difference between the Helium conductances and the predictions from the gap model varies from 130% at run 8 up to 213% at run 23. The corresponding Helium accommodation coefficient predicted from the conductance meansurements using the gap model ranges from 0.7 to 0.8, Table C.53. These results demonstrate clearly how sensitive the prediction of the Helium conductance is to the accommodation coefficient value. This point will be discussed further in the next section.

The geometrical and thermal dimensionless parameters reported in Table C.54 show that the Nitrogen results were obtained in the slip flow regime, while the Helium results were obtained in the transition as well as in the free molecule regimes.

Finally, it should be mentioned that, after the test was completed, the joint was disassembled and the contacting surfaces were examined. Visual inspection indicated yellow discoloration on the smooth surface.

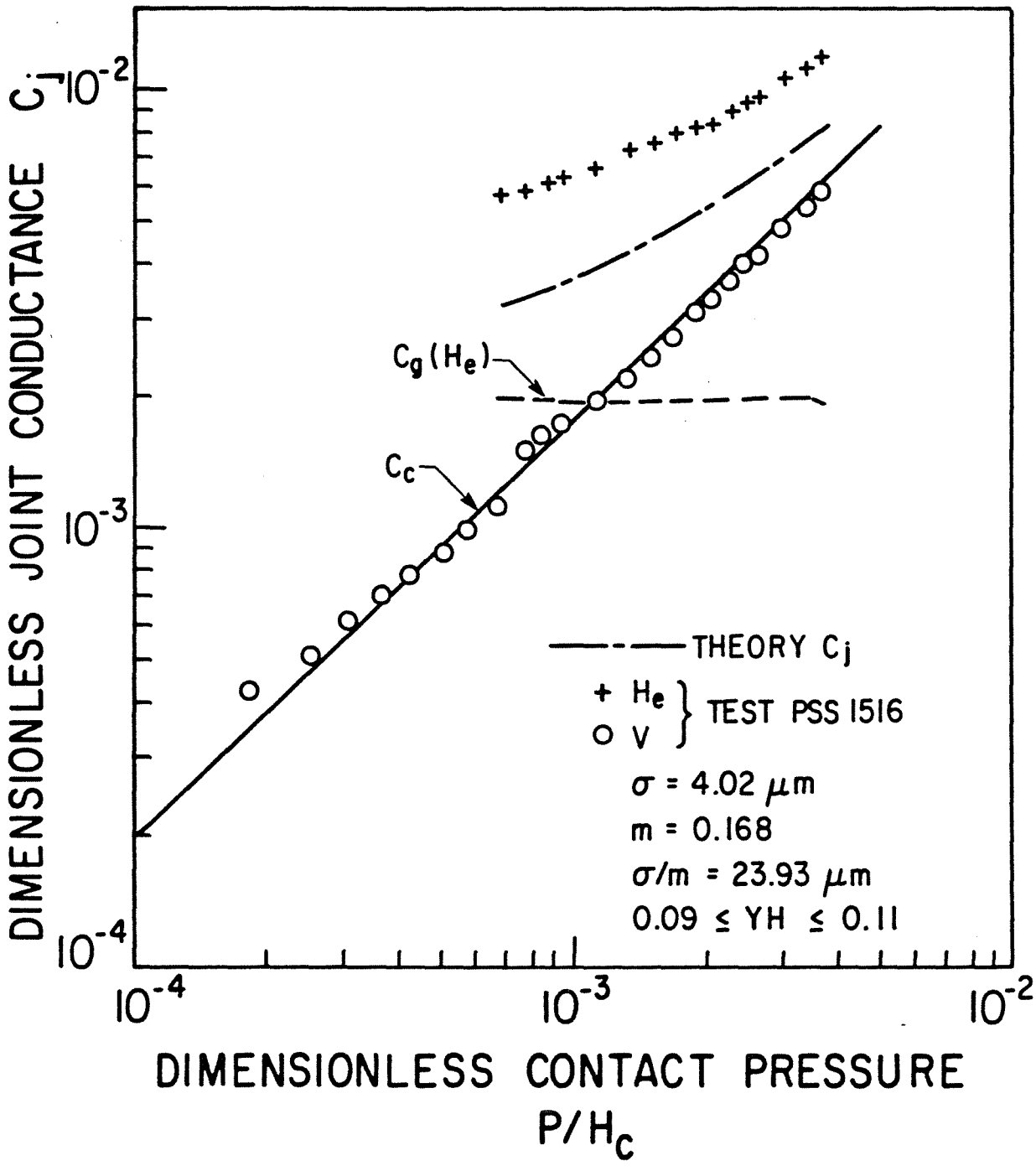

Figure 5.30: Comparison Between Theory and Test Results for SS304, Pair PSS1516 - Helium Data

5.3.5 General Discussion of Gas Results

Four tests were conducted in Nitrogen and Helium using Stainless Steel 304 joints to verify the proposed gap model. The experimentally measured Nitrogen conductances were found to be in excellent agreement with the predicted values. This excellent agreement holds over a wide range of contact pressure and for different surface textures as well as for two different gas pressures.

On the other hand, the Helium experimental results are significantly higher than the predictions and the agreement is poor. However, this difference highlights the importance of the light gas accommodation coefficient values, in general, for adequate thermal predictions. There appears to be a number of possible explanations for the observed disagreement which will be discussed later.

As expected, for this type of test the presence of a gaseous fluid in the interface gap greatly increased the joint conductance. This increase is more pronounced at light loads, since at high contact pressures the contact conductance dominates. This point is fully illustrated by the test results of pair PSS0910 which was tested in Nitrogen. As can be seen from Table C.36 or Figure 5.25, the ratio between the gap conductance to the contact

conductance ranges from approximately 12 at $P/H_c = 1.6*10^{-4}$ down to 4 at $P/H_c = 5*10^{-4}$.

The excellent agreement between the measured and predicted Nitrogen joint conductances verifies the validity of the gap conductance model over two important and critical ranges of the parameter YH, as was discussed in Section 3.4. The test data of pair PSS0910, which cover the range of $29 < YH < 39$, confirm the validity of the gap model in the range of $10 < YH < 100$ and demonstrate clearly that the gap conductance predictions are fully dependent upon the relative mean plane separation in this range of YH. On the other hand, the test data of pairs PSS1314 and PSS1516, which cover the range of $1.3 < YH < 2.7$ show that accurate knowledge of the mean plane separation and the effective temperature jump distance (or gas thermal parameters) is essential to accurate gap conductance predictions in the range of $1 < YH < 10$.

One of the reasons for examining the gap conductance model in Helium was to verify the gap conductance model in the range of $10^{-2} < YH < 1$ without strengthening the prediction dependence upon the contact conductance value especially at light loads. Theoretically, the parameter YH for the tested pairs was in the range of $0.09 < YH < 0.18$. Since in this range of YH the gap conductance is fully dependent upon the gas thermal parameters, it can be

concluded that the poor agreement in Helium is not attributable to uncertainties in the joint surface parameters or in the mechanical and thermal properties of the tested specimens or in the model which assumes that the contact and gap conductances can be added linearly to give the joint conductance. It is believed that the discrepancy in the Helium data is most possibly caused by over-estimation of the effective temperature jump distance due to under-estimation of the Helium accommodation coefficient for such types of joints. The excellent agreement between the measurements and the predictions for the same joints in vacuum and Nitrogen supports this argument as well as the following discussion.

Tables C.38, C.43 and C.49, in Appendix C, show that the Helium measured conductances were obtained at a gas pressure of approximately 40 torr and a mean interface temperature of approximately 210°C. Since these two parameters were accurately measured, and the Helium thermal parameters are accurately known except the accommodation coefficient, as discussed earlier, it can be concluded that the measured Helium conductances were fully dependent upon the accommodation value and were also very sensitive to the uncertainties associated with the appropriateness of the expression used in determining this coefficient.

To demonstrate this point further, the theoretical Helium conductance is plotted in Figure 5.31 against the relative contact pressure for different accommodation coefficient values. The surface parameters and the contact hardness values used in plotting this figure are those of pair PSS1112. The interface mean temperature, Helium pressure, and the harmonic mean thermal conductivity are chosen to be 200°C, 40 torr, and 20 W/mK, respectively. As can be seen from Figure 5.31, the prediction of the Helium conductance is very sensitive to the value of the accommodation coefficient. This observation is true for any joint regardless of the gas type whenever the effective temperature jump distance is greater than the mean separation between the contacting surfaces.

Generally speaking, the accommodation coefficient value of a particular gas depends strongly upon the nature of the gas, as well as the material and surface conditions. Most of the data reported in the literature has been obtained for very smooth and atomically clean surfaces. Thus, for engineering surfaces the accommodation coefficient is expected to be higher than those reported in the literature. Hartnett [80], among many others [81], has pointed out that, when a surface becomes contaminated with an absorbed gas layer, the Helium accommodation coefficient may increase by as much as a factor of 3. Since no attempt had been made to clean the tested surfaces of adsorbed gas layers, this may be a plausible explanation

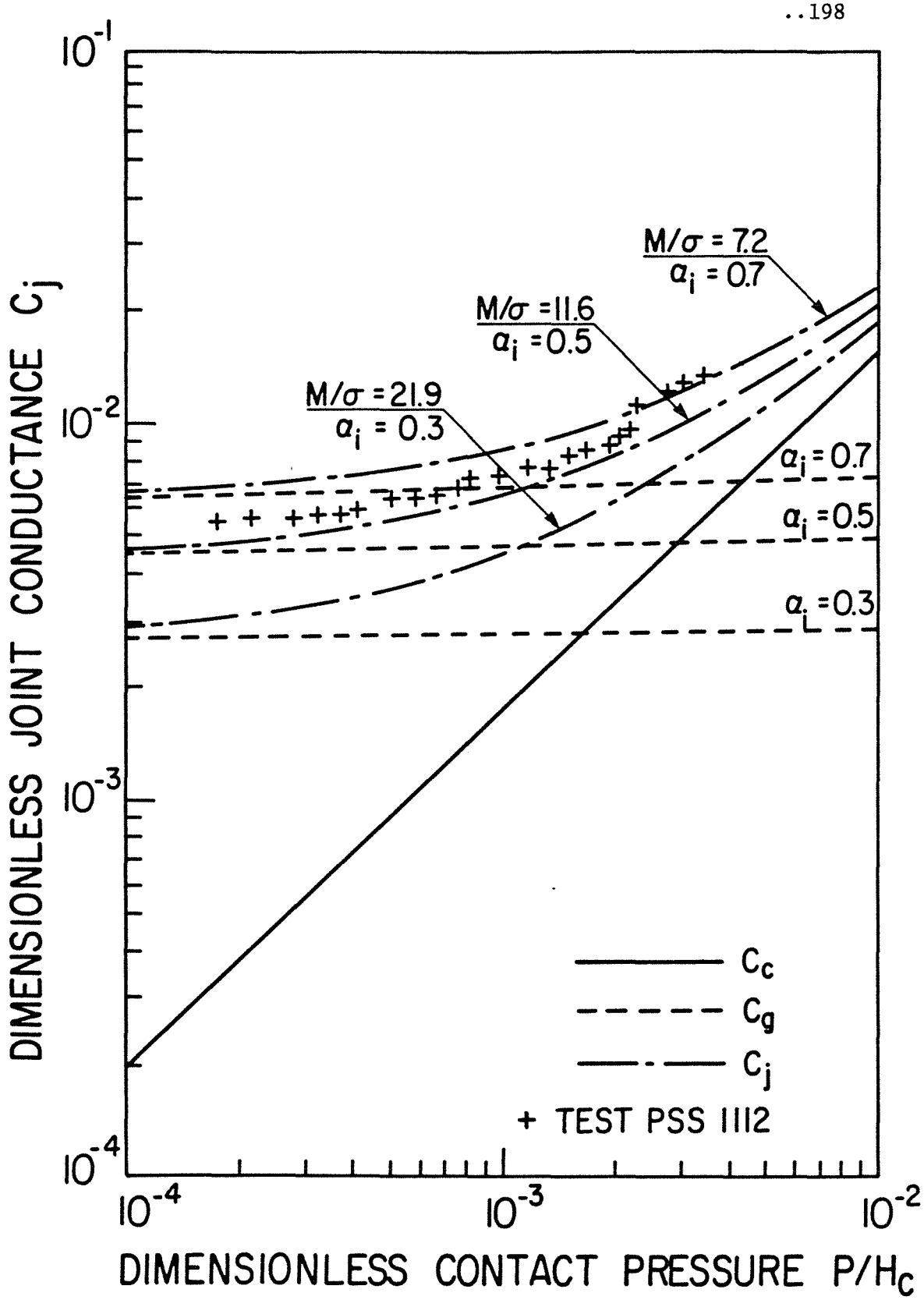

Figure 5.31: Helium Conductance Dependence upon the Accommodation Coefficient Value

for the observed disagreement in the Helium. The substantial increase in the Helium joint conductance observed after testing pair PSS1112 in Nitrogen supports this explanation.

For a rough surface, Roberts [82] has shown that, if the gas molecule strikes the surface in n different places before leaving it, the apparent accommodation coefficient, α_{app}, for the rough surface is larger than the accommodation coefficient of the smooth surface, and they can be related to each other by the following expression:

$$\alpha_{app} = 1 - (1-\alpha)^n \qquad (5.10)$$

The majority of the accommodation data reported in the literature are obtained for smooth, small wires or metal specimens (spheres or flat surfaces) to minimize the possibility of multiple collisions of the gas molecules with the surface. Hence, another plausible explanation and, perhaps the most important one for the poor agreement in Helium, can be based upon this fact as discussed hereafter.

Figure 4.5 shows that the roughened surfaces consist of a large number of microscopic cavities of different sizes. Thus, the possibility of multiple collisions of the gas molecules within a single cavity is high and, therefore, account must be taken of

this possibility. However, the good agreement between the Nitrogen data and the predictions indicates that the effect of multiple collisions can be considered negligible for heavy gases. This fact is fully demonstrated in Table 5.7.

In Table 5.7, the effect of multiple collisions upon the apparent accommodation coefficient value was determined using Eq.(5.10) for different accommodation values in the range of 0.1 to 0.9. The first four lines represent the accommodation coefficient values observed for the light gases, such as Hydrogen and Helium, while the last two lines represent the range of the measured values for Argon and Nitrogen, i.e., heavy gases. As can be seen from Table 5.7, the effect of multiple collisions is more pronounced for light gases than for heavy gases. As an example, if a light gas has an accommodation coefficient equal to 0.1, the heat exchange between the gas molecule and the surface can be increased by 90% due to double collisions, or by 170% due to triple collisions. In contrast, the heat exchange between the heavy gas molecule, such as Nitrogen, and the surface can be increased only by 10% due to double collisions and, in this case, the energy will be completely exchanged.

It is interesting to note that at 210°C the Helium accommodation coefficient expression, Table 5.5, gives a value approximately equal to 0.3. From Table 5.7, the apparent

Table 5.7: Effect of Multiple Collisions Upon the Apparent Accommodation Coefficient Value

	n = 1		n = 2		n = 3	
α_i	α_{app}	α	α_{app}	α	α_{app}	α
0.1	0.1	38.0	0.19	19.1	0.27	12.8
0.2	0.2	18.0	0.36	9.1	0.49	6.2
0.3	0.3	11.3	0.51	5.8	0.66	4.1
0.4	0.4	8.0	0.64	4.3	0.78	3.1
0.5	0.5	6.0	0.75	3.3	0.87	2.6
0.6	0.6	4.7	0.84	2.8	0.94	2.3
0.7	0.7	3.7	0.91	2.4	0.97	2.1
0.8	0.8	3.0	0.96	2.2	0.99	2.0
0.9	0.9	2.4	0.99	2.0	1.0	2.0

apparent accommodation coefficient value corresponding to 0.3 is equal to 0.51 for double collisions and equal to 0.66 for triple collisions which is in agreement with the values predicted by the gap conductance model. In our opinion, this finding confirms the validity of the gap conductance model and, therefore, it is recommended that the gap conductance model be used for determining the apparent accommodation coefficient value of a light gas for this type of contacts or, in general, for engineering joints.

A second interesting observation in Table 5.7 is that the accommodation parameter, α, of a particular combination of light gas and joint of similar materials is very sensitive to small changes in the accommodation coefficient value. This is in contrast to the accommodation parameters of heavy gases. Thus, it can be concluded that the gap conductance predictions will be very sensitive to the uncertainty in the accommodation coefficient value of any light gas. Actually, this sensitivity is overpowered by the accommodation parameter expression, Eq.(3.55).

According to Eggleton and Tompkins [83], the accommodation coefficient value of a particular gas often increases during an experimental test due to the formation of foreign atom layers on the surface as a result of the gas impurity. This may explain the yellow discoloration found on the tested surfaces after the thermal

tests had been completed and supports the expected increase in the Helium accommodation coefficient.

Finally, if any firm conclusion must be drawn on the basis of the above discussion, it would be that the prediction of the gas conductance critically depends upon the gas accommodation coefficient whenever the effective temperature jump distance is larger than the separation between the contacting surfaces. Therefore, the gap conductance becomes difficult to predict accurately due to the uncertainty associated with the accommodation coefficient value of a particular combination of gas and engineering joint.

It is recommended that further work be done to explain the discrepancy between the experiments and the predictions in Helium. Also, it is recommended that further experimental data be obtained to verify the validity of the gap model over a broad range of gas pressure and surface roughness using different types of gases and materials.

CHAPTER 6

COMPARISON OF CONTACT AND GAP CONDUCTANCE MODELS WITH THE PRESENT MODELS

6.1 Contact Conductance Models

During the past three decades numerous researchers from several countries have proposed a number of models and correlations for predicting thermal contact conductance (TCC) between conforming rough surfaces. Some of these models have limited usefulness because either they are proposed for certain types of metallic contacts or they require information about certain contact parameters which must be determined graphically or experimentally. Therefore, these models will not be considered in the following comparison.

The objectives of this section are:

a) to review briefly the available general correlations in the open literature to show their similarities and differences, and

b) to compare them graphically with the present contact conductance model.

The comparison will be made possible by plotting the dimensionless contact conductance C_c against the contact pressure for some

nominal values of surface parameters, contact hardness, macro-hardness and contact pressure. The nominal values of these parameters are those of pairs PNI0102 and PSS0708 which represent two limiting cases. The first pair represents contact between two smooth, relatively soft, good conductivity materials, while the second pair represents contact between one rough and one smooth, relatively hard, poor conductivity materials.

6.1.1 Cooper, Mikic and Yovanovich Correlation

Based upon statistical analysis, a theoretical correlation for predicting TCC between rough surfaces was obtained by Cooper et al [20]. In the analysis, the distribution of both asperity heights and the asperities over the apparent area were assumed to be Gaussian. Assuming plastic deformation of the asperities, the following correlation was proposed:

$$C_c = 1.45\ (P/H)^{0.985} \qquad (6.1)$$

where H is the micro-hardness of the softer material. The authors claimed that a good agreement between the predictions and the limited experimental data, at that time, was evident in the following ranges of variables:

$$3.6 * 10^{-4} < P/H < 1.0 * 10^{-2}$$

$1.0\ \mu m < \sigma < 8.5\ \mu m$

$0.08 < m < 0.16$

Since the authors did not specify the type of micro-hardness test, nor under what load this micro-hardness was to be determined, it is impossible to make any direct comparison between this correlation and the present model.

6.1.2 Tien Correlation

A semi-empirical correlation for predicting TCC had been developed by Tien [27] in terms of three dimensionless groups. These groups are characterized, respectively, by the dimensionless contact conductance, relative contact pressure, and the surface parameters. A straightforward application of the Pi theorem led to the conclusion that the correlation could be logically expressed and related as:

$$(\sigma\, h_c/k_s) = f\, \dot{m}^g\, (P/H)^d \qquad (6.2)$$

where $\dot{m}$ is the RMS slope; f, g, and d are constants to be determined from the experimental results.

Tien plotted conductance data of various investigators in terms of $(\sigma h_c/k_s)$ and (P/H) on a log-log basis and determined the exponent d to be equal to 0.85. In light of the analysis

of Ref[18], Tien assigned a value of 1.0 to the RMS slope exponent g. With these given values for g and d, as well as from the experimental results, the constant f was estimated to be 0.55. Thus, the proposed correlation is:

$$\sigma\, h_c/k_s = 0.55\, \dot{m}\, (P/H)^{0.85} \tag{6.3}$$

For Gaussian rough surfaces, the relationship between the RMS slope $\dot{m}$ and the mean absolute slope m is given by:

$$m = \sqrt{2/\pi}\, \dot{m} \tag{6.4}$$

so that Eq.(6.3) becomes:

$$\sigma\, h_c/k_s = 0.69\, m\, (P/H)^{0.85} \tag{6.5}$$

Although the author realized the importance of the material micro-hardness in correlating the experimental results he stated that, "It may be conveniently represented by three times the tensile yield stress, i.e., $H = 3S_y$". Therefore, Eq.(6.5) can be rewritten as:

$$C_c = 0.69\, (P/3S_y)^{0.85} \tag{6.5}$$

Since the material macro-hardness is larger than $3S_y$, it can easily be concluded that the predictions from the above correlation will be in very poor agreement with the present contact conductance model.

6.1.3 Veziroglu Correlation

Based upon the early work of Cetinkale and Fishenden [10] and various experimental results reported by several investigators, Veziroglue [26] developed the following semi-empirical correlation for estimating the thermal joint conductance:

$$U = 1 + \frac{BC}{K \tan^{-1}\left[\frac{1}{C}\sqrt{1-\frac{1}{U}} - 1\right]} \qquad (6.6)$$

where

B = gap number

C = constriction number

K = conductivity number = k_f/k_s

U = conductance number = $h_j\, t_e/k_f$

t_e = effective gap thickness

Veziroglu also outlined the following procedure for predicting the joint conductance:

1. Calculate the effective gap thickness t_e from:

$$t_e = 3.56(CLA_1 + CLA_2) \quad \text{if} \quad (CLA_1 + CLA_2) < 7.5\mu m$$

or

$$t_e = 0.528(CLA_1 + CLA_2) \quad \text{if} \quad (CLA_1 + CLA_2) > 7.5\mu m \ .$$

2. Calculate the effective fluid conductivity k_f from:

$$k_f = \frac{k_g}{1 + M/t_e} + \frac{4t_e \, \sigma_{st} \, E_1 \, E_2}{E_1 + E_2 - E_1 E_2} \, T_m^3$$

where σ_{st} is the Stefan-Boltzman constant, and E_i is the surface emissivity.

3. Calculate the conductivity number K.

4. Calculate the constriction number $C = \sqrt{P/H_M}$ where H_M is the Mayer hardness.

5. Calculate the gap number B using the results obtained in 1) and 4), from the following expression:

$$B = 0.355 \, C^{2.92 t_e^{-0.18}}$$

where t_e is in μin.

6. Calculate the conductance number from Eq.(6.6) using an iteration procedure since it is a transcendental equation.

The author claimed that the correlation was good for estimating the joint conductance for a large variety of metals and surface finishes as well as over a wide range of contact pressures and temperatures.

Under vacuum conditions with negligible radiation, i.e., $k_f = 0$, Eq.(6.6) can be written as:

$$h_c = \frac{k_s}{t_e} \frac{BC}{\tan^{-1}(1/C - 1)} \tag{6.7}$$

The comparison between the predicted C_c values, using Eq.(6.7) and the present model, can be made by plotting C_c values versus the contact pressure, as shown in Figure 6.1, for pairs PNI0102 and PSS0708. As can be seen, the predicted C_c values, using Eq.(6.7), are below the predictions given by the present model for the smoother pair PNI0102. The error ranges from approximately 60%, at a contact pressure of 0.4 MPa, down to 30% at a contact pressure of 10 MPa. In contrast, Eq.(6.7) overpredicts TCC values for the rougher pair, PSS0708, for all contact pressures. The error ranges from approximately 21% at a contact pressure of 0.4 MPa up to 85% at a contact pressure of 10 MPa.

In light of this comparison, it can be concluded that the Veziroglu correlation fails to adequately predict TCC for reasonably smooth and very rough joints. However, the correlation confirms the fact that for nominal rough surfaces in contact

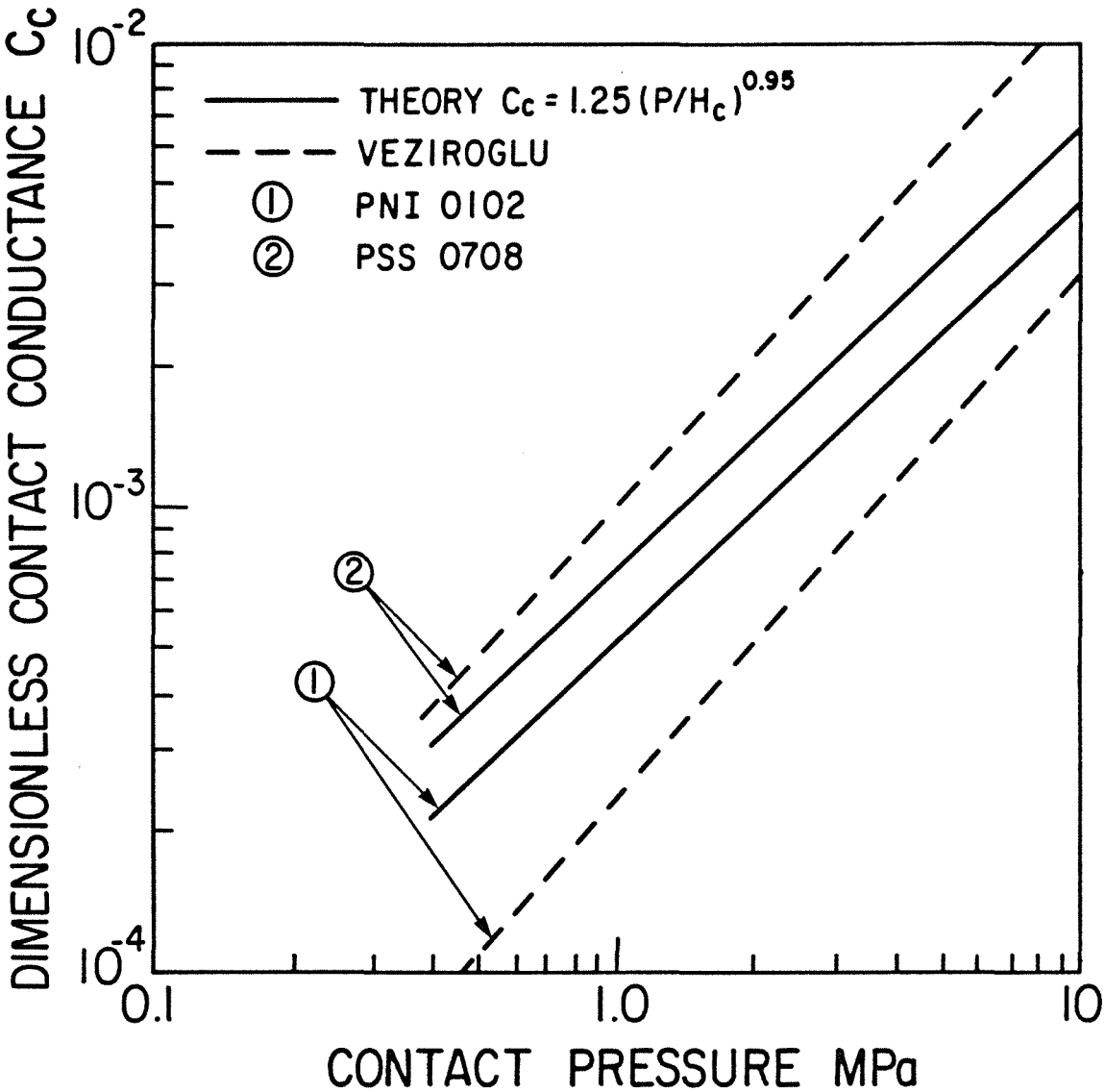

Figure 6.1: Comparison of Different Predictions:
Theory vs. Veziroglu Model

the TCC varies almost linearly with the contact pressure. Hence, it can be said that the Veziroglu correlation agrees with the present model in this one respect.

6.1.4 Shlykov and Ganin Correlation

Shlykov and Ganin [23] developed a semi-empirical correlation for TCC predictions between similar or dissimilar rough surfaces in contact. Experimentally, they found that the contact spot sizes for different materials, such as steel, copper, aluminum, nickel, uranium, etc., are approximately constant, independent of the applied load and the surface roughness. Following Boechoten and Van der Held [32], they assumed the average contact spot radius to be equal to 30μm. Assuming plastic deformation of the contact spots and an asperity flow pressure equal to $3S_u$, the following correlation was proposed:

$$h_c = 2.1 * 10^4 k_s (P/3S_u) \qquad (6.8)$$

The authors pointed out that, for metals with a high degree of cold work such as copper, the asperity flow pressure should be equal to $5S_u$. No details, however, were given to incorporate this effect in their correlation.

Since the material macro-hardness is nearly equal to $3S_u$ [39], Eq.(6.8) can be written in dimensionless form as:

$$C_c = 2.1 * 10^4 (\sigma/m)(P/H_m) \qquad (6.9)$$

Close inspection of Eq.(6.9) reveals that this correlation will be in agreement with the present model if the contacting surfaces are very rough and the softer surface contact hardness is close to the material macro-hardness. Otherwise, the Shlykov and Ganin correlation will be in very poor agreement with the present model. This fact is clearly demonstrated in Figure 6.2 for pairs PNI0102 and PSS0708.

6.1.5 Shlykov Correlation

Shlykov [25] also assumed a fixed average contact spot radius equal to 40μm in developing his correlation, independent of the surface roughness and applied contact pressure. Apart from the use of $3S_u$ for the asperity flow pressure, he considered the effect of the average roughness heights separately. As he pointed out, a large volume of published experimental data for similar and dissimilar machined materials, such as aluminum, uranium, iron, magnox, steel, duralumin and niobium, was correlated to an accuracy of ±20 percent by the following correlation:

$$h_c\, a/k_s = 0.32\, (z\, P/3S_u)^{0.86} \qquad (6.10)$$

where z is a constant which depends upon the average height of the surface roughness and is defined by:

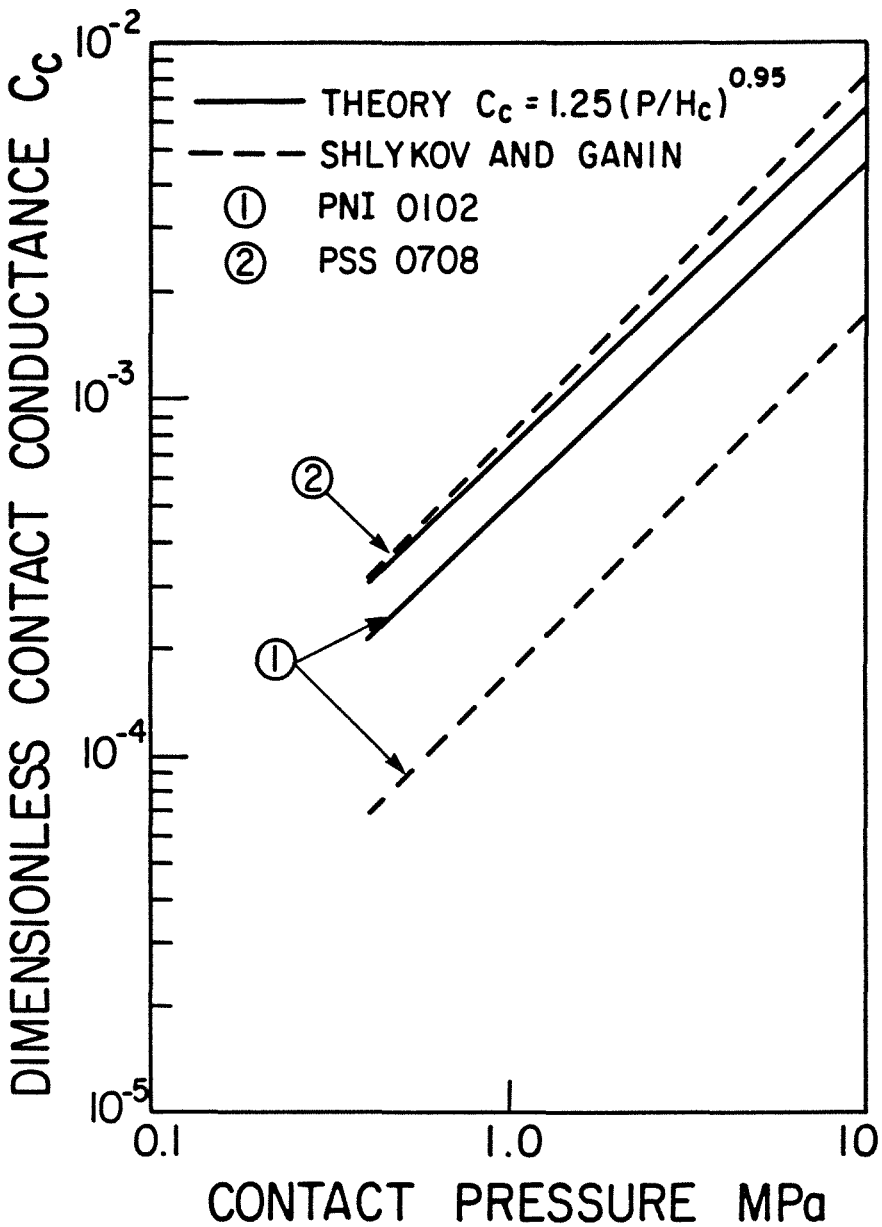

Figure 6.2: Comparison of Different Predictions: Theory vs. Shlykov and Ganin Model

$$
\left.
\begin{array}{lll}
z = 1 & \text{when} & CLA_1 + CLA_2 > 30\mu m \\
z = \left[\dfrac{30}{CLA_1 + CLA_2}\right]^{1/3} & \text{when} & 10\mu m \leq CLA_1 + CLA_2 \leq 30\mu m \\
z = \dfrac{15}{CLA_1 + CLA_2} & \text{when} & CLA_1 + CLA_2 < 10\mu m
\end{array}
\right\} \quad (6.11)
$$

The author claimed that the correlation is valid up to a relative contact pressure, $(zP/3S_u)$, of $2.5*10^{-2}$ and a temperature in the contact zone not higher than 0.3 of the fusion point.

If the parameter $3S_u$ is considered to be equal to H_m and normalizing Eq.(6.10), with respect to (σ/m), such that

$$C_c = 8.0 * 10^3 \, (\sigma/m)(z\,P/H_m) \quad (6.12)$$

then Eq.(6.12) can be used in predicting TCC for pairs PNI0102 and PSS0708. As shown in Figure 6.3, Eq.(6.12) overpredicts TCC for both pairs. The error ranges between 300% to 200% for pair PNI0102 and between 97% to 48% for pair PSS0708. It is also evident from the figure that the disagreement between the two models decreases with increasing joint roughness, therefore, it can be concluded that the Shlykov correlation may be adequate for very rough joints or joints having negligible micro-hardness variation.

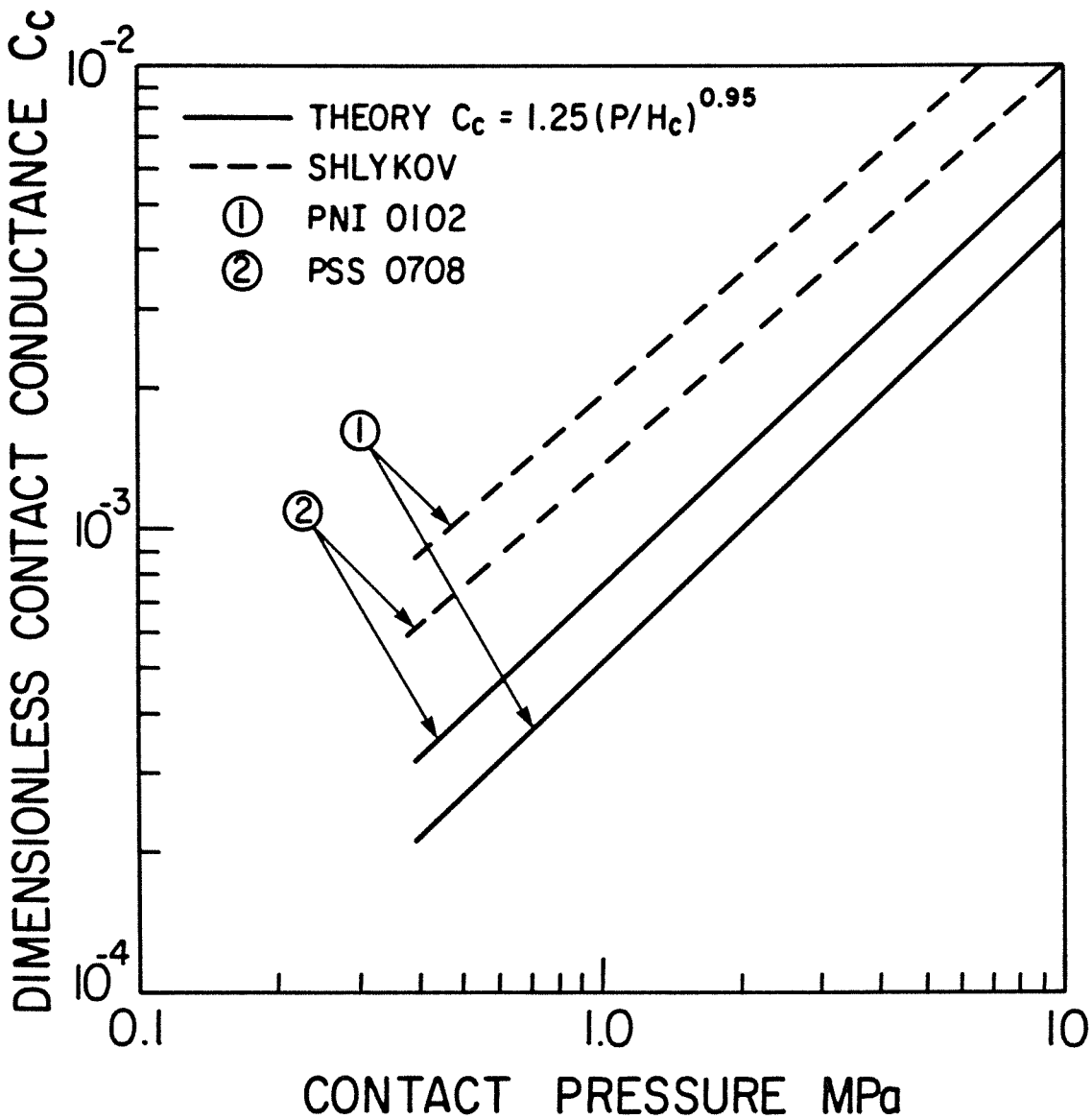

Figure 6.3: Comparison of Different Predictions:
Theory vs. Shlykov Model

6.1.6 Mal'kov Correlation

In the range of moderate contact pressures, Mal'kov [29] proposed a semi-empirical correlation for predicting TCC between engineering surfaces. His development was based upon Shlykov's analysis [25], and the average contact spot radius of 40μm was again considered to be the characteristic dimension. A least squares fit to 92 experimental data points of different materials prepared, using various machining processes such as turning, grinding and lapping, resulted in the following correlation:

$$h_c\, a/k_s = 0.118\ (z\ P/3S_u)^{0.66} \qquad (6.13)$$

in the range of relative contact pressure

$$2 * 10^{-4} \leq (z\ P/3S_u) \leq 8 * 10^{-3}$$

where z is a function of the surface roughness height and is defined by Eqs.(6.11).

Obviously, the major difference between Eq.(6.13) and the Shlykov correlation (Eq.(6.10)) appears in the relative contact pressure exponent value. This unrealistic exponent, especially for ground and lapped surfaces, may very well be attributed to the error associated with the determination of the temperature drop across the interface. As stated by Mal'kov, the first thermocouple

was located at 2mm from the interface, i.e., in the disturbance region, and only four thermocouples were employed to determine the temperature gradient along the specimen, 20mm high. The author also pointed out that the specimens were made from stainless steel and molybdenum and the temperature in the contact zone ranged from 250°C to 520°C. For such poor conductivity materials, as well as these high working temperatures, attention must be paid to creep which increases the contact size and, in turn, TCC. This may be another possible explanation for such an unrealistic relative contact pressure exponent value.

Finally, it can be concluded that the Mal'kov correlation is totally inadequate and unrealistic for predicting TCC between conforming rough surfaces.

6.1.7 Bochorishvili and Ganin Correlations

Bochorishvili and Ganin [84] proposed two expressions for the prediction of TCC between metallic rough surfaces. They also considered the average contact spot radius to be a fixed parameter, equal to 30μm regardless of the type of materials in contact and their surface roughnesses. Further, they used the term $(3S_u)$ for the softer material flow pressure. According to the authors, the prediction from the two correlations was found to be in satisfactory agreement with the experimental data. However,

they suggested the following correlation:

$$h_c = 2.1 * 10^4 \, k_s \, (P/3S_u) \tag{6.14}$$

to be employed when fairly rigid metallic materials are in contact provided that $(P/3S_u) \ll 1$.

For contacts involving both hard and soft metallic surfaces or under heavy mechanical loads, such as $(P/3S_u) > 0.15$, they recommended the use of the following expression:

$$h_c = 6.67 * 10^4 \, (k_s/\phi)(P/3S_u) \tag{6.15}$$

where ϕ is the "form factor" given by:

$$\phi = \left(\varepsilon + \frac{1}{\varepsilon}\right) \ln\left(\frac{1+\varepsilon}{1-\varepsilon}\right) + 2 \ln\left(\frac{1-\varepsilon^2}{4\varepsilon}\right) \tag{6.16}$$

and ε is defined by:

$$\varepsilon = (P/3S_u)^{0.5} \tag{6.17}$$

Eq.(6.14) is identical to the Shlykov and Ganin correlation, Eq.(6.8), therefore, the comparison with the present model and the discussion presented in Section 6.1.4 hold for this equation. For the second expression, Eq.(6.15), its validity is beyond the scope of the present work, hence, no comparison or conclusion is possible regarding it.

6.1.8 Popov Correlation

Following the method of Cooper et al [20], a semi-empirical correlation for predicting TCC between nominally flat rough surfaces was proposed by Popov [84]. Similar to Shlykov [25], the effect of the surface roughness height was considered separately and the average contact spot radius was assumed to be constant, equal to 30μm. Popov correlated a large number of experimental results of various engineering materials prepared using different machining process, and obtained the following correlation:

$$h_c\, a/k_s = 0.81\,(z\,P/3S_u)^{0.956} \tag{6.18}$$

where

$$\left.\begin{aligned} z &= \frac{12}{MRH_1 + MRH_2} && \text{for} \quad 1\mu m \leq MRH_1 + MRH_2 \leq 5\mu m \\ z &= \left[\frac{20}{MRH_1 + MRH_2}\right]^{0.63} && \text{for} \quad 5\mu m \leq MRH_1 + MRH_2 \leq 10\mu m \\ z &= \left[\frac{30}{MRH_1 + MRH_2}\right]^{0.4} && \text{for} \quad 10\mu m \leq MRH_1 + MRH_2 \leq 30\mu m \end{aligned}\right\} \tag{6.19}$$

and MRH_i is the height of the highest peaks from the surface mean line.

Substituting 30μm for 'a' and considering $3S_u$ equal to H_m, Eq.(6.18) can be written as:

$$h_c = 2.7 * 10^4 k_s (z P/H_m)^{0.956} \quad (6.20)$$

or in terms of the dimensionless contact conductance C_c, as:

$$C_c = 2.7 * 10^4 (\sigma/m)(z P/H_m)^{0.956} \quad (6.21)$$

A graphical comparison between the present model and the Popov correlation Eq.(6.21) is presented in Figure 6.4. Pair PZN0708 was employed in the comparison instead of pair PSS0708 since the latter possesses a maximum roughness height greater than 30μm. From Figure 6.4 it can be seen that Eq.(6.21) overpredicts TCC especially for the smoother pair. The error ranges from approximately 135% for pair PNI0102 down to 20% for pair PZN0708. This suggests that Popov's correlation may be adequate for very rough or unworked surfaces, similar to the previous Russian correlations.

6.1.9 Thomas and Probert Correlations

Thomas and Probert [30] considered that the apparent contact area did not play a significant role in the variation of the TCC and they replaced it by the surface RMS roughness. Their dimensionless analysis yielded the following two groups:

$$C^* = 1/R\ \sigma\ k_s \quad \text{and} \quad W^* = W/\sigma^2\ H \quad (6.22)$$

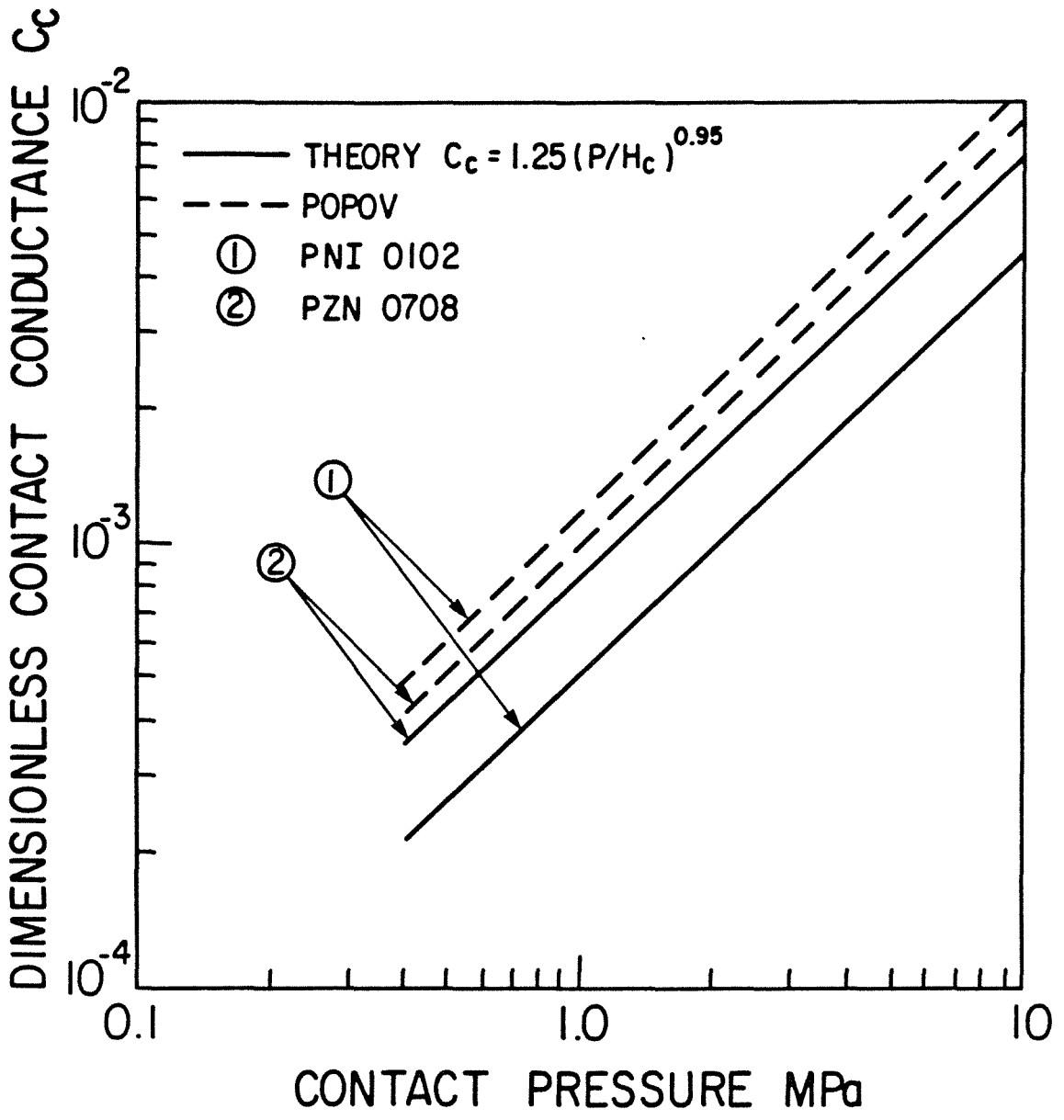

Figure 6.4: Comparison of Different Predictions:
Theory vs. Popov Model

where W is the contact load, and H is the surface hardness. The experimental results of ten investigators for stainless steel and aluminum contacts were correlated into the following two expressions, respectively:

$$C^* = 9.5\ (W^*)^{0.74} \tag{6.23}$$

$$C^* = 1.9\ (W^*)^{0.72} \tag{6.24}$$

The authors stated that, "Clearly, the dimensional analysis is incomplete" and "The fact that the data for two different materials falls into two well-defined groups indicates that the missing parameter or parameters must represent the intrinsic properties of the material". The authors, also, pointed out that the good agreement between the slopes of the correlations is evidence that the other variable involved is dimensionless and may be specific to a particular surface, i.e., another surface parameter.

Since the authors did not specify what hardness value should be employed in their correlations, it is impossible to make any direct comparison between these correlations and the present model. However, it is evident, as the authors stated in their study, that these correlations are inadequate.

6.1.10 O'Callaghan and Probert Correlations

Two empirical correlations for predicting TCC between flat smooth surfaces were developed by O'Callaghan and Probert [85]. Similar to Thomas and Probert [30], they correlated their experimental data as a function of the two dimensionless groups C* and W* and proposed the following correlation:

$$C^* = 3.91\ (W^*)^{0.67} \tag{6.25}$$

The authors combined the experimental data of Ref.[30] with their measurements and obtained the following correlation:

$$C^* = 3.73\ (W^*)^{0.66} \tag{6.26}$$

which they considered the best correlation since it covers a wide range of materials and possesses the least scatter.

For the purpose of comparison, Eq.(6.26) can be written as:

$$C_c = \frac{3.73}{m} \left(\frac{\sigma^2}{A_a}\right)^{0.34} \left(\frac{P}{H}\right)^{0.66} \tag{6.27}$$

where H is the Vickers micro-hardness. Since the authors did not state what load value or values should be used to determine the surface micro-hardness, the graphical comparison between Eq.(6.27) and the present model will be made as a function of the relative contact pressure P/H.

Figure 6.5 shows the predicted dimensionless TCC values plotted against the relative contact pressure for pairs PNI0102 and PSS0708. As is evident from the figure, Eq.(6.27) remarkably underpredicts TCC for the smoother pair over the whole load range. This, in spite of the fact that Eq.(6.27), was primarily developed for smooth joints. On the other hand, Eq.(6.27) overpredicts TCC for pair PSS0708 by approximately 28% at $P/H = 10^{-4}$, and underpredicts TCC by approximately 66% at $P/H = 10^{-2}$.

Based upon this comparison, it can be concluded that the O'Callaghan and Probert correlation is inappropriate for TCC predictions. It can be added that the low value of the relative contact pressure exponent indicates that the experimental data obtained and used for this correlation are improperly determined. As pointed out by the authors, the greatest source of error arose from the temperature extrapolation procedure and the temperature drop across the contacts was, in general, small.

6.2 Gap Conductance Models

As pointed out in Chapter 3, the gap conductance between two smooth flat parallel surfaces separated by a distance t can be expressed, in general, as:

$$h_g = \frac{k_g}{t + M} \tag{6.28}$$

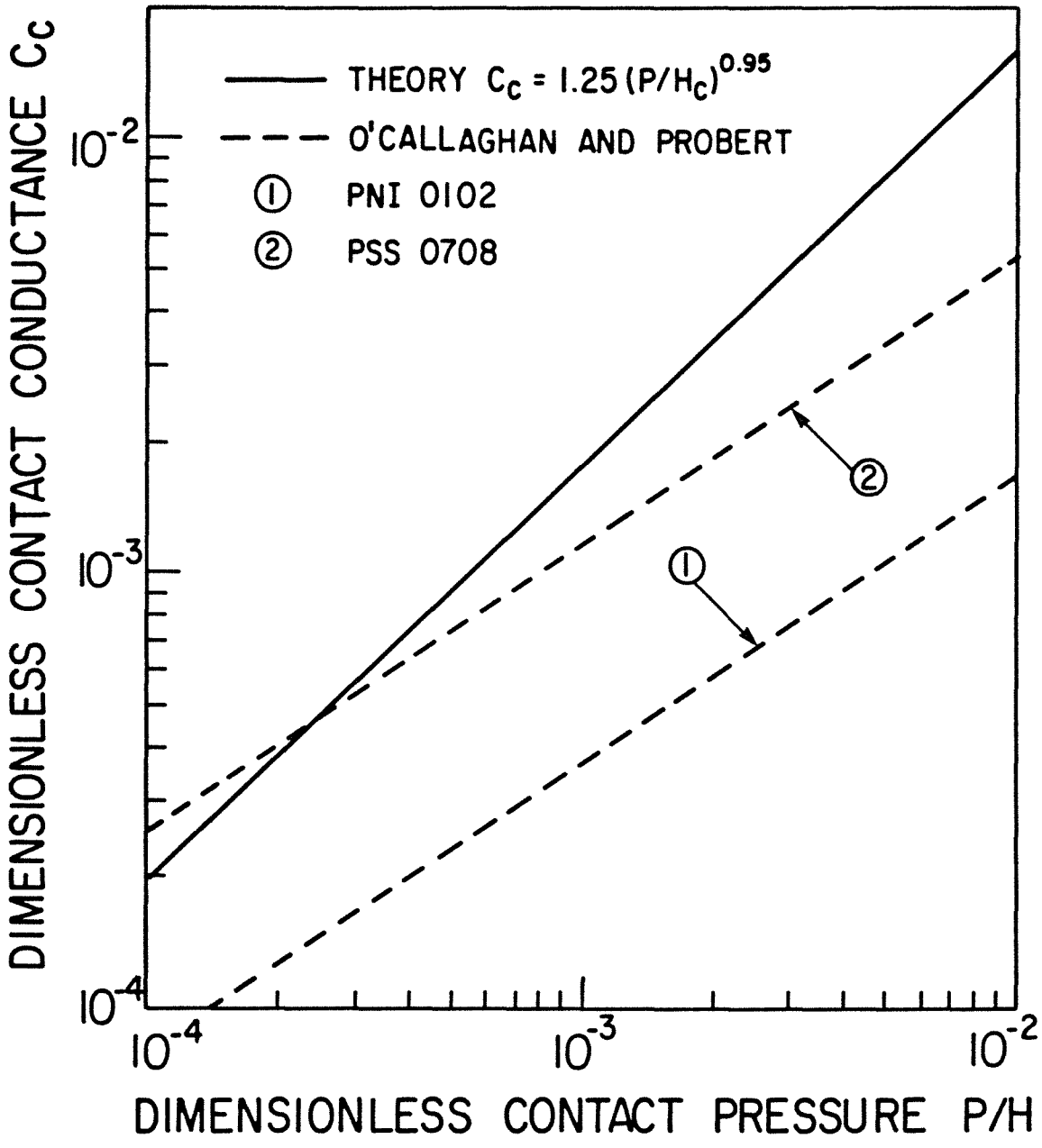

Figure 6.5: Comparison of Different Predictions:
Theory vs. O'Callaghan and Probert Model

where M is the effective temperature jump distance. This simple expression represents the basic idea for all the models proposed for predicting gap conductance between two rough surfaces in contact. In this case, however, account must be taken of the local variation in the gap thickness due to the surface roughness, as well as the effect of the applied contact pressure. Therefore, Eq.(6.28) can be written as:

$$h_g = \frac{k_g}{t_e + M} \tag{6.29}$$

where t_e is an effective thickness for the gap between the two surfaces and is a function of the surface roughness, as well as the applied load.

Cetinkale and Fishenden [10], in one of the earlier analytical and experimental studies on joint conductance, conducted a number of experiments with steel, brass and aluminum surfaces ground to different degrees of surface finish, in air and other fluids. Based upon their experiments, they concluded that the effective gap thickness is independent of the applied contact pressure up to 5.5 MPa and it can be assumed constant for higher load values since the contact conductance becomes predominant. From their measurements the authors proposed the following expression:

$$t_e = 0.61\ (CLA_1 + CLA_2) \tag{6.30}$$

for the effective gap thickness.

Based upon the analytical work of the previous study [10], and following the same procedure of data reduction, Veziroglu [26] compiled a large amount of experimental data taken from different references and developed the following correlations:

$$\left.\begin{aligned} t_e &= 3.56\ (CLA_1 + CLA_2) \quad \text{if} \quad (CLA_1 + CLA_2) < 7.5\mu m \\ t_e &= 0.528\ (CLA_1 + CLA_2) \quad \text{if} \quad (CLA_1 + CLA_2) > 7.5\mu m \end{aligned}\right\} \tag{6.31}$$

for the effective gap thickness. Obviously, the above expressions are independent of the contact pressure and similar to Eq.(6.30) but with different constants.

Yovanovich [31] considered the effective gap thickness to be equivalent to the separation between the mean planes, Y, and, therefore, expressed the effective gap thickness as:

$$t_e = Y = 1.184\ \sigma[-\ell n(3.132\ P/H)]^{0.547} \tag{6.32}$$

In contrast to the previous relationships this expression accounts for the effect of both surface roughness and contact pressure upon the gap conductance.

A different approach exists in the literature which accounts for the variation in the local gap thickness due to the surface roughness only, by defining a "global gap thickness", δ, such that

$$h_g = k_g/\delta \tag{6.33}$$

where δ is some function of the surface roughness and the effective temperature jump distance. Therefore, this function can be determined either experimentally or theoretically.

Rapier et al [13] investigated the thermal joint conductance of uranium dioxide and stainless steel contacts in vacuum and with different types of gases such as Helium, Argon and Neon. The gas pressure in these tests varied from 7 torr up to 1226 torr, while the contact pressure ranged from zero to 3.9 MPa. The mean roughness height of the tested surfaces was in the range of 0.14μm to 14.2μm. The authors correlated the experimentally determined gap conductances, obtained by subtracting the contact conductance from the joint conductance, to get the following semi-empirical expression:

$$\frac{b_t\, h_g}{k_g} = \frac{0.6}{1 + (1/2X)} + 0.4\ \ell n\ (1+2X) \tag{6.34}$$

The parameters b_t and X are defined by:

$$b_t = 2(CLA_1 + CLA_2) \tag{6.35}$$

and

$$X = b_t/M \tag{6.36}$$

The authors claimed that Eq.(6.34) correlated their own measurements quite well, along with the experimental data available at that time. Also, it should be pointed out that the authors proposed four integral expressions which can be used to determine the global gap thickness, as well as the results for three idealized surface profiles.

Shlykov [25] presented a theoretical expression for determining the global gap thickness of a particular joint using one of the integral expressions proposed in the previous work [13]. However, he incorporated the approximate "bearing-surface curve" expression proposed by Shvets and Dyban [24] to describe the variation of the local gap thickness. Shlykov's expression for the gap conductance takes the form:

$$\frac{b_t\, h_g}{k_g} = \frac{10}{3} + \frac{10}{X} + \frac{4}{X^2} - 4\left(\frac{1}{X^3} + \frac{3}{X^2} + \frac{2}{X}\right) \ell n(1+X) \tag{6.37}$$

where b_t and X are defined by Eqs.(6.35) and (6.36). Graphically, Shlykov showed that his expression was in good agreement with a large number of experimental data points obtained

by different investigators for various types of metallic contacts in Helium, air and other gases.

All mentioned models for predicting gap conductance between rough surfaces are summarized in comparable format in Table 6.1 to show their differences and similarities. The present gap conductance model proposed by Yovanovich et al [55] is also included in Table 6.1 for purposes of comparison. It is clear from the table that these models can be classified into two groups. The first group includes the models of Cetinkale and Fishenden, Rapier et al, Shlykov and Veziroglu, while the second group includes the Yovanovich and Yovanovich et al models.

In the first group of models, the gap conductance was considered to be independent of the contact pressure and a function only of the sum of the arithmetic mean of the surface roughness of the joint members. This sum was also used in normalizing the gap conductance. The second group of models accounted for the variation of the gap thickness with contact pressure, and also, considered the effect of the surface roughness. However, in group two the RMS surface roughness is the characteristic dimension used to normalize the gap conductance.

To facilitate the graphical comparison between this variety of models, we define a new dimensionless gap conductance parameter C_g^*, as:

Table 6.1: Summary of Gap Conductance Models

Author(s)	The Model
Cetinkale & Fishenden	$\frac{b_t\, h_g}{k_g} = \frac{1}{0.305 + \frac{1}{X}}$
Rapier et al	$\frac{b_t\, h_g}{k_g} = \frac{0.6}{1 + \frac{1}{2X}} + 0.4 \quad \ell n\ (1+2X)$
Shlykov	$\frac{b_t\, h_g}{k_g} = \frac{10}{3} + \frac{10}{X} + \frac{4}{X^2} - 4\left(\frac{1}{X^3} + \frac{3}{X^2} + \frac{2}{X}\right) \ell n\ (1+X)$
Veziroglu	$\frac{b_t\, h_g}{k_g} = \frac{1}{0.264 + \frac{1}{X}}$ if $b_t/2 > 7.5\mu m$
	$\frac{b_t\, h_g}{k_g} = \frac{1}{1.78 + \frac{1}{X}}$ if $b_t/2 < 7.5\mu m$
Yovanovich	$\frac{\sigma\, h_g}{k_g} = \frac{1}{Y/\sigma + M/\sigma}$
Yovanovich et al	$\frac{\sigma\, h_g}{k_g} = \frac{1}{\sqrt{2\pi}} \int_0^\infty \frac{\exp[-(Y/\sigma - t/\sigma)^2/2]}{[t/\sigma + M/\sigma]}\, d(t/\sigma)$

$$C_g^* = \left(\frac{b_t}{\sigma}\right)\left(\frac{\sigma\, h_g}{k_g}\right) = f(X) \qquad (6.38)$$

Therefore, all the aforementioned models can be expressed as functions of the parameter X for comparison. Also, the ratio (b_t/σ) will be assumed equal to 1.7, based upon the surface roughness measurements of the tested pairs. Further, the relative separation, Y/σ, between the mean planes will be considered equal to 3.09, i.e., $P/H = 10^{-3}$, since most of these models were developed to correlate several hundred data points obtained around this value of relative contact pressure. A summary of all the models, in terms of the dimensionless parameters C_g^* and X after employing the above values for (b_t/σ) and (Y/σ), is presented in Table 6.2. The graphical comparison of these reduced expressions is shown in Figure 6.6 over the range of $10^{-2} \leq X \leq 10^3$. The Nitrogen and Helium experimental data of the tested pairs corresponding to the above specified (Y/σ) value are also included in the figure for comparison purposes.

As is evident from Figure 6.6, the first four expressions listed in Table 6.2 predict very similar conductance values in the range of $1 \leq X \leq 10^3$. However, these conductance values are in poor agreement with the Nitrogen data and with the predictions from the last three expressions in Table 6.2. Thus,it can be concluded that the Veziroglu expression for moderate rough surfaces ($b_t < 15\mu m$) and the Yovanovich model are in agreement with the present model,

Table 6.2: Summary of C_g^* Expressions for Comparisons

Author(s)	The Expression
Cetinkale & Fishenden	$C_g^* = \dfrac{1}{0.305 + \frac{1}{X}}$
Rapier at al	$C_g^* = \dfrac{0.6}{1 + \frac{1}{2X}} + 0.4 \quad \ell n\ (1+2X)$
Shlykov	$C_g^* = \dfrac{10}{3} + \dfrac{10}{X} + \dfrac{4}{X^2} - 4\left(\dfrac{1}{X^3} + \dfrac{3}{X^2} + \dfrac{2}{X}\right) \ell n\ (1+X)$
Veziroglu	$C_g^* = \dfrac{1}{0.264 + \frac{1}{X}}$ if $b_t/2 > 7.5\mu m$
	$C_g^* = \dfrac{1}{1.78 + \frac{1}{X}}$ if $b_t/2 < 7.5\mu m$
Yovanovich	$C_g^* = \dfrac{1}{1.816 + \frac{1}{X}}$
Yovanovich et al	$C_g^* = 0.678 \int_0^\infty \dfrac{\exp[-(Y/\sigma - t/\sigma)^2/2]}{[t/\sigma + 1.7/X]} d(t/\sigma)$

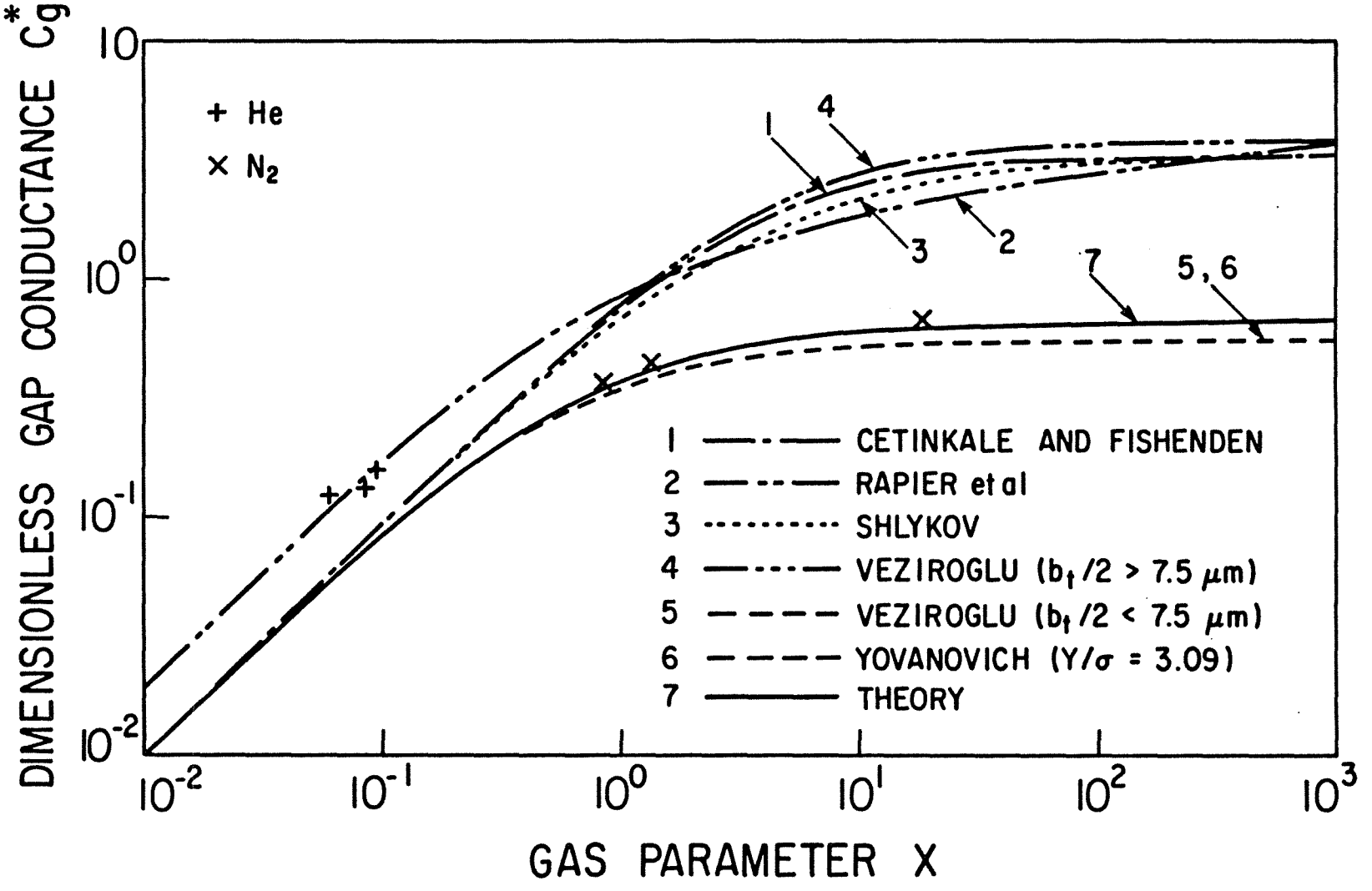

Figure 6.6: Comparison of Different Predictions

as well as with the experimental results over this range of the parameter X.

On the other hand, Figure 6.6 shows that all the gap models, except that of Rapier et al, are in agreement with each other in the range of $10^{-2} \leq X \leq 10^{-1}$. This can be explained by the fact that the effective temperature jump distance M is greater than any local gap thickness and, in turn, the gap conductance is independent of the gap separation; this is the free molecule regime. In this regime the Rapier et al model overpredicts the gap conductance by 100% as a result of multiplying the gas parameter X by a factor of 2.

As the authors stated, this factor was used to correlate the Hydrogen and Helium data in this range of the parameter X. The Helium accommodation coefficient value which was used in their investigation was around 0.3 similar to the value used in the present work. This explains why the Helium data, as shown in Figure 6.6, are in excellent agreement with their model. Also, this confirms that the Helium accommodation coefficient for the joints considered in the present work is around 0.55 as predicted by the gap conductance model.

CHAPTER 7

CONCLUSIONS AND RECOMMENDATIONS

7.1 Conclusions

Based upon the present experimental study, the following conclusions can be drawn:

1. From the thermal viewpoint, very little attention has been given in the past three decades to understanding the effect of surface micro-hardness variation, in spite of its great importance to accurate thermal predictions.

2. In general, none of the joint conductance models that have been proposed by previous investigators account for the effect of surface micro-hardness variation.

3. Hardness investigation had demonstrated clearly that engineering surfaces exhibit micro-hardness variation which depends primarily upon the material type and secondarily upon the machining process.

4. For the tested materials, a semi-general micro-hardness variation has been proposed as a function of the macro-hardness value. This expression will prove extremely useful to thermal analysts.

5. A mechanical model for predicting the appropriate contact hardness value has been developed, incorporating the joint surface parameters and Vickers micro-hardness variation. This mechanical model is applicable for the majority of engineering systems which operate in the range of $10^{-4} \leq P/H_c \leq 10^{-2}$.

6. The comparisons between the measured and predicted contact conductances justify the assumptions made in developing the mechanical model and affirm its applicability over the above specified range of relative contact pressures.

7. For any particular joint, the experimental data indicates that the contact hardness value is independent of the applied load over the above specified range of relative contact pressures. However, the principles of the mechanical model may also be applied to a joint which operates beyond the specified range of relative contact pressure.

8. The analysis and the experiments confirm that the contact spot area, not the shape of the contact, is important for both thermal and mechanical problems. This fact has been overlooked in the past.

9. The excellent agreement between the measured and predicted contact conductances verifies the validity of the contact conductance model over a broad range of surface roughnesses and contact pressures for materials possessing a wide range of thermophysical properties.

10. Also, the excellent agreement between the experimental and theoretical contact conductances demonstrates clearly that:

    a) the methodology used in estimating the surface parameters is satisfactory, yielding adequate information about the joint surface topography;
    b) for a particular joint, accurate estimation of the surface parameters is not only crucial for determining the appropriate contact hardness value, but is very important to the prediction of thermal conductance.

11. The deviations between the light load contact conductance data and the theoretical predictions are not a result of uncertainty in the thermal measurements, surface parameters, thermal or mechanical properties of the tested joints. The experimental evidence shows, however, that the joint thermophysical properties, surface parameters, mean temperature, and contact pressure all contributed to the observed deviations.

12. For engineering joints operating in a gaseous environment, the theoretical analysis showed that the gap-temperature jump parameter, YH, is more appropriate than the inverse of the Knudsen number, $1/K_n$, for characterizing the gas conduction mode in the gap. This new gap parameter accounts for the gas properties, temperature, and pressure in the gap as well as the joint geometric and mechanical parameters.

13. For the relatively limited range of parameters investigated, the Nitrogen conductance data agree extremely well with the predictions by the gap model. In contrast, the Helium data agree poorly with the predictions.

14. The excellent agreement between the measured and predicted Nitrogen conductances, as well as the internal consistency of the Helium data, lend support to the investigated gap model of Yovanovich et al.

15. The Nitrogen conductance data demonstrates that knowledge of the appropriate relative separation value is essential to accurate gap conductance predictions. This fact increases the importance of determining an adequate contact hardness value for any particular joint.

16. The observed apparent disagreement between the measured and predicted Helium conductances does not disprove the gap conductance model but highlights the importance of the light gas accommodation coefficient for accurate gap conductance predictions. In general, the gap conductance predictions will be very sensitive to the accommodation coefficient value whenever the gas effective temperature jump distance is larger than the separation between the contacting surfaces.

17. Based upon the comparisons of the Nitrogen and Helium experimental data with the theoretical predictions, it can be said that joint surface conditions, such as roughness, cleanliness, presence of films, etc., exert first order effects on the value of the light gas accommodation coefficient and, in turn, on the predicted gap conductance. These conditions, by contrast, have little effect on the heavy gas accommodation coefficient and the predicted gap conductance.

18. For engineering joints which operate in a light gas environment and under very light loads, a controlled amount of surface roughness can enhance the joint thermal conductance.

19. The present work explains the apparent contradictory experimental results obtained by a number of investigators for nominally similar materials and raises doubts regarding the validity of other theoretical or empirical models which have been advanced as general models.

7.2 Recommendations

1. This work considered the case of bead blasted surfaces in contact with flat smooth surfaces. It is recommended, therefore, that further work be done to extend the validity of the investigated models to contacts between similar and dissimilar rough surfaces.

2. Since most engineering joints have machined rough surfaces, it is recommended that these types of joints be examined to extend the applicability of these thermal conductance models. The experimental data from the smooth pair tests (lapped surfaces) strongly supports this extension.

3. The light load experimental data indicated that several factors other than the joint out-of-flatness significantly influenced the thermal measurements. It is recommended, therefore, that theoretical and experimental studies be undertaken to investigate the significant enhancement

effects of these factors. Of course, these studies will provide an explanation for the increase in the measured conductance observed when the thermal flux across the joint was disturbed.

4. A thorough experimental investigation over a broader range of surface roughness and gas pressures, employing different types of materials and gases is recommended to affirm the validity of the gap conductance model for different types of contacts.

5. Based upon the experimental evidence, it is suggested that the Helium accommodation coefficient value is between 0.55 and 0.65 for practical engineering joints. However, it is recommended that further work be done to determine more accurate and reliable accommodation coefficient data for different combinations of gases and engineering surfaces.

REFERENCES

[1] Graff,W.J., "Thermal Conductances Across Metal Joints", Machine Design, Vol.32, 1960, pp.166-172.

[2] Minges, M.L., "Thermal Contact Resistance", USAF Report AFML-TR-65-375, 1966.

[3] Thomas, T.R. and Probert, S.D., "Thermal Contact of Solids", Chemical and Process Engineering, Vol.47, 1966, pp.51-60.

[4] Fry, E.M., "Contact Thermal Conductance", Bell Telephone Laboratories, Report No.101, 1966.

[5] Atkins, H., "Bibliography on Thermal Metallic Contact Conductance", NASA - George C. Marshal Space Flight Center, Technical Report X-53227, 1965.

[6] Wong, H.Y., "A Survey of the Thermal Conductance of Metallic Contacts", Aeronautical Research Council Report C.P.973, HSMO, London, 1968.

[7] Hsieh, C.K. and Davis, F.E., "Bibliography on Thermal Contact Conductance", USAF Report AFML-TR-69-24, 1969.

[8] Moore, C.J., Atkins, H. and Blum, H.A., "Subject Classification Bibliography for Thermal Contact Resistance Studies", ASME Paper 68-WA/HT-18, New York, 1968.

[9] Madhusudana, C.V. and Fletcher, L.S., "Thermal Contact Conductance: A Review of Recent Literature", Mech. Eng. Dept., Texas A&M Univeristy, September 1981.

[10] Cetinkale, T.N. and Fishenden, M., "Thermal Conductance of Metal Surfaces in Contact", Proc. of General Discussion on Heat Transfer, Inst. of Mech. Eng., London, 1951, pp.271-275.

[11] Holm, R., Electrical Contacts Handbook, 3rd Ed., Springer-Verlag, Berlin, 1958.

[12] Lang, P.M., "Calculating Heat Transfer Across Small Gas-Filled Gaps", Nucleonics, Vol.20, 1962, pp.62-63.

[13] Rapier, A.C., Jones, T.M. and McIntosh, J.E., "The Thermal Conductance of Uranium Dioxide/Stainless Steel Interfaces", Int. Jr. of Heat and Mass Transfer, Vol.6, 1963, pp.397-416.

[14] Fenech, H. and Rohsenow, W.M., "Prediction of Thermal Conductance of Metallic Surfaces in Contact", Jr. of Heat Transfer, Trans. ASME, Series C, Vol.85, No.1, February 1963, pp.15-24.

[15] Henry, J.J., "Thermal Contact Resistance", Ph.D. Thesis, MIT, 1964.

[16] Clausing, A.M. and Chao, B.T., "Thermal Contact Resistance in a Vacuum Environment", University of Illinois, Report ME-TN-242-1, August 1963.

[17] Yovanovich, M.M. and Fenech, H., "Thermal Contact Conductance of Nominally Flat Rough Surfaces in a Vacuum Environment", AIAA Progress in Astronautics and Aeronautics, Vol.18, 1965, pp.773-794.

[18] Mikic, B.B. and Rohsenow, W.M., "Thermal Contact Resistance", MIT Report No.4542-41, September 1966.

[19] Dutkiewicz, R.K., "Interfacial Gas Gap for Heat Transfer Between Two Randomly Rough Surfaces", Proc. of the 3rd. Int. Heat Transfer Conf., Vol.IV, 1966, pp.118-126.

[20] Cooper, M.G., Mikic, B.B. and Yovanovich, M.M., "Thermal Contact Conductance", Int. Jr. of Heat and Mass Transfer, Vol.12, 1969, pp.279-300.

[21] Mikic, B.B., "Analytical Studies of Contact of Nominally Flat Surfaces: Effect of Previous Loading", Jr. of Lub. Tech., 1971, pp.451-459.

[22] Mikic, B.B., "Thermal Contact Conductance: Theoretical Considerations", Int. Jr. of Heat and Mass Transfer, Vol.17, 1973, pp.205-214.

[23] Shlykov, Yu.P and Ganin, Ye.A., "Thermal Resistance of Metallic Contacts", Int. Jr. of Heat and Mass Transfer, Vol.7, 1964, pp.921-929.

[24] Shvets, I.T. and Dyban, E.P., "Contact Heat Transfer Between Plane Metal Surfaces", Int. Chem. Eng., Vol.4, No.4, October 1964, pp.621-624.

[25] Shlykov, Yu.L., "Calculation Thermal Contact Resistance of Machined Metal Surfaces", Teploenergetika, Vol.12, 1965, pp.102-108.

[26] Veziroglu, T.N., "Correlation of Thermal Contact Conductance Experimental Results", AIAA Paper No.67-317, AIAA Thermophysics Specialist Conference, New Orleans, Louisiana, April 17-20, 1967.

[27] Tien, C.L., "A Correlation for Thermal Contact Conductance of Nominally Flat Surfaces in a Vacuum", Proc. 7th Thermal Conductivity Conf., U.S. Bureau of Standards, 1968, pp.755-759.

[28] Hsieh, C.K. and Touloukian, Y.S., "Correlation and Prediction of Thermal Contact Conductance for Nominally Flat Surfaces", Proc. of the 8th Thermal Conductivity Conf., Plenum Press, New York, N.Y., 1969.

[29] Mal'kov, V.A., "Thermal Contact Resistance of Machined Metal Surfaces in a Vacuum Environment", Heat Transfer - Soviet Research, Vol.2, No.4, July 1970, pp.24-33.

[30] Thomas, T.R. and Probert, S.D., "Correlations for Thermal Contact Conductance in Vacuo", Trans. ASME, Jr. of Heat Transfer, August 1972, pp.276-281.

[31] Yovanovich, M.M., "Thermal Contact Correlations", Spacecraft Radiative Transfer and Temperature Control, Ed. by Thomas E. Horton, Vol.83 of Progress in Astronautics and Aeronautics, New York, 1982.

[32] Boeschoten, F. and Van der Held, E.F.M., "The Thermal Conductance of Contacts Between Aluminum and Other Metals", Physica, Vol.23, 1957, pp.37-44.

[33] Laming, L.C., "Thermal Conductance of Machined Contacts", ASME Int. Heat Transfer Conf., Part 1, No.8, Boulder, Colorado, 1961, pp.65-76.

[34] Mott, M.A., Micro-Indentation Hardness Testing, Butterworths Scientific Publications, London, 1956.

[35] Yovanovich, M.M., Hegazy, A.A. and DeVaal, J., "Surface Hardness Distribution Effects Upon Contact, Gap and Joint Conductances", AIAA Paper No.82-0887, AIAA/ASME 3rd Joint Thermophysics, Fluids, Plasma and Heat Transfer Conf., June 7-11, 1982, St.Louis, Missouri.

[36] Schankula, M.H., Patterson, D.W. and Yovanovich, M.M, "The Effect of Oxide Films on the Thermal Resistance Between Contacting Zircaloy Surfaces", Proc. of Materials in Nuclear Energy Conf., Am. Soc. of Metals, Metals Park, OH, 1982, pp.106-111.

[37] Yovanovich, M.M, Hegazy, A.A. and Antonetti, V.W., "Experimental Verification of Contact Conductance Models Based Upon Distributed Surface Micro-Hardness", AIAA Paper No.83-0532, AIAA 21st Aerospace Sciences Meeting, January 1983, Reno, NE.

[38] Yovanovich, M.M. and Hegazy, A.A., "An Accurate Universal Contact Conductance Correlation for Conforming Rough Surfaces With Different Micro-Hardness Profiles", AIAA Paper No.83-1434, AIAA 18th Thermophysics Conf., June 1983, Montreal, Canada.

[39] Tabor, D., The Hardness of Metals, Oxford, 1952.

[40] O'Neill, H., Hardness Measurements of Metals and Alloys, Chapman and Hall, Ltd., 2nd Ed., London, 1967.

[41] Glazov, V.M. and Vigdorovich, V.N., Microhardness of Metals and Semi-Conductors, Consultants Bureau, New York-London, 1971.

[42] Buckle, H., "Use of Hardness Test to Determine Other Material Properties", The Science of Hardness Testing and Its Research Applications, Ed. by J.H. Westerbrook and H. Conrad, Am. Soc. of Metals, Metals Park, OH, 1973, pp.453-494.

[43] Bowden, F.P. and Tabor, D., The Friction and Lubrication of Solids, Part II, Oxford, 1964.

[44] Pethica, J.B., Hutchings, R. and Oliver, W.C., "Hardness Measurement at Penetration Depths as Small as 20nm", Phil. Mag., Vol.48, No.4, 1983, pp.593-606.

[45] Gane, N. and Cox, J.M., "The Micro-Hardness of Metals at Very Low Loads", Phil. Mag., Vol.22, 1970, pp.881-891.

[46] Shaw, M.C., "A Yield Criterion for Ductile Metals Based Upon Atomic Structure", Franklin Inst. Jr., Vol.24, August 1952, pp.109-131.

[47] Bochorishvili, M.M. and Ganin, E.A., "Method of Calculating the Thermal Resistance of a Contact Between Metal Surfaces", Sov. Phys. Jr., Vol.1, No.1, January 1976, pp.18-22.

[48] Greenwood, J.A., "Constriction Resistance and the Real Area of Contact", Brit. Jr. Applied Phys., Vol.17, 1966, pp.1621-1632.

[49] Longard, K., "Das Elektrolytische Aetzpolieren von Metalloberflächen und seine Bedeutung bei der Mikrohärteprüfung", Archiv. für Metallkunde, Vol.3, No.11, November 1949, pp.381-386.

[50] Metals Handbook, 9th Edition, Am. Soc. of Metals, Metals Park, OH, Vols.1 & 3, 1982.

[51] Tsukizoe, T. and Hisakado, T., "On the Mechanism of Contact Between Metal Surfaces - The Penetrating Depth and the Average Clearance", Jr. of Basic Eng., Vol.87, No.3, September 1965, pp.666-674.

[52] Tsukizoe, T. and Hisakado, T., "On the Mechanism of Contact Between Metal Surfaces: Part 2 - The Real Area and the Number of the Contact Points", Jr. of Lub. Tech., Vol.40, No.1, January 1968, pp.81-88.

[53] Tsukizoe, T. and Hisakado, T., "On the Mechanism of Heat Transfer Between Metal Surfaces in Contact: Part 1 - Theoretical Analysis and Experimental Justification of Theory", Heat Transfer - Japanese Res., Vol.1, No.1, January-March 1972, pp.104-112.

[54] Tsukizoe, T. and Hisakado, T., "On the Mechanism of Heat Transfer Between Metal Surfaces in Contact - 2nd Report, Thermal Contact Resistance Between Metal Surfaces in Vacuum", Heat Transfer-Japanese Res., Vol.1, No.2, April-June 1972, pp.23-31.

[55] Yovanovich, M.M., DeVaal, J. and Hegazy, A.A., "A Statistical Model to Predict Thermal Gap Conductance Between Conforming Rough Surfaces", AIAA Paper No.82-0888, AIAA/ASME 3rd Joint Thermophysics, Fluids, Plasma and Heat Transfer Conf., June 1983, St. Louis, Missouri.

[56] Roess, L.C., "Theory of Spreading Conductance", Appendix to Weills, N.D. and Ryder, E.A., "Thermal Resistance Measurements on Joints Formed Between Stationary Metal Surfaces", presented at Semi-Annual ASME Heat Transfer Division Meeting, Milwaukee, Wisc., 1948.

[57] Yovanovich, M.M., "General Expressions for Circular Constriction Resistances for Arbitrary Heat Flux Distribution", Progress in Astronautics and Aeronautics: Radiative Transfer and Thermal Control, Ed. by A.M. Smith, Vol.49, New York, 1976, pp.301-308.

[58] Gibson, R.D., "The Contact Resistance for a Semi-Infinite Cylinder in Vacuum", Applied Energy, Vol.2, 1976, pp.57-65.

[59] Greenwood, J.A. and Williamson, J.B.P., "Contact of Nominally Flat Surfaces", Proc. Royal Soc. London A, Vol.295, 1966, pp.300-319.

[60] Williamson, J.B.P., Pullen, J. and Hunt, R.T., "The Shape of Solid Surfaces", Surface Mechanics, Ed. by F.F. Ling, Am. Soc. of Mech. Eng., New York, 1969, pp.24-35.

[61] Whitehouse, D.J. and Archard, J.F., "The Properties of Random Surfaces in Contact", Surface Mechanics, Ed. by F.F. Ling, Am. Soc. of Mech. Eng., New York, 1969, pp.36-57.

[62] Kimura, Y., "Estimation of the Number and the Mean Area of Real Contact Points on the Basis of Surface Profiles", Wear, Vol.15, 1970, pp.47-55.

[63] Yovanovich, M.M., Burde, S.S. and Thompson, J.C., "Thermal Constriction Resistance of Arbitrary Planer Contact with Contact Flux", AIAA Ppaer No.76-440, AIAA 11th Thermophysics Conf., San Diego, California, July 1976.

[64] Rubenstein, C., "A Critical Appraisal of Static Hardness Measurements", Jr. of Applied Mechanics, Vol.48, December 1981, pp.796-802.

[65] Mulhearn, T.O., "The Deformation of Metals by Vickers-Type Pyramidal Indenters", Jr. of Mech. Phys. Solids, Vol.7, 1959, pp.85-96.

[66] Kubo, M., "Statistical Analysis of Surface Roughness Waveforms", Annals of C.I.R.P., Vol.XIV, 1967, pp.279-288.

[67] Reti, P., "Bestimmung der Mikroharte nach neuem Sowjestischen verfahren", Feingeraetetechnik, Vol.1, September 1952, pp.259-260.

[68] Williams, S.R., Hardness and Hardness Measurements, Am Soc. of Metals, Cleveland, OH, 1942.

[69] Kennard, E.H., Kinetic Theory of Gases, McGraw-Hill, New York, 1938.

[70] Zwart, J., Personal Communications.

[71] Journal of Physical and Chemical Reference Data, Vol.3, 1974, Supplement No.1.

[72] Fisher, N.J., "Analytical and Experimental Studies of the Thermal Contact Resistance of Sphere/Layered Flat Contacts", M.A.Sc. Thesis, Department of Mechanical Engineering, University of Waterloo, 1985.

[73] DeVaal, J.W., "Thermal Contact Conductance of Rough Surfaces", M.A.Sc. Thesis, Department of Mechanical Engineering, University of Waterloo, 1983.

[74] Antonetti, V.W., "On the Use of Metallic Coatings to Enhance Thermal Contact Conductance", Ph.D. Thesis, Department of Mechanical Engineering, University of Waterloo, 1983.

[75] Dickins, B.G., "The Effect of Accommodation on Heat Conduction Through Gases", Proc. Royal Soc. A, Vol.143, 1934, pp.517-540.

[76] Wiedmann, M.L. and Trumpler, P.R., "Thermal Accommodation Coefficients", Trans. Am. Soc. of Mech. Eng., Vol.68, 1946, pp.57-64.

[77] Ullman, A., Acharya, R. and Olander, D.R., "Thermal Accommodation Coefficients of Inert Gases on Stainless Steel and UO_2", Jr. Nucl. Mater., Vol.51, 1974, pp.277-279.

[78] Thomas, L.B. and Loyalka, S.K., "Determination of Thermal Accommodation Coefficients of Helium, Argon, and Xenon on a Surface of Zircaloy-2 at Above 25°C", Nucl. Tech., Vol.57, 1982, pp.213-219.

[79] Thomas, L.B. and Loyalka, S.K., "Determination of Thermal Accommodation Coefficients of Inert Gases on a Surface of Vitreous UO_2 at ~ 35°C", Nucl. Tech., Vol.59, 1982, pp.63-69.

[80] Hartnett, J.P., "A Survey of Thermal Accommodation Coefficients", Rarefied Gas Dynamics, Ed. by L. Tablot, Academic Press, 1961.

[81] Kaminsky, M., Atomic and Ionic Impact Phenomena on Metal Surfaces, Academic Press, 1965.

[82] Roberts, J.K., "The Exchange of Energy Between Gas Atoms and Solid Surfaces", Proc. Royal Soc. A, Vol.129, 1930, p.146.

[83] Eggleton, A.E.J. and Tompkins, F.C., "The Thermal Accommodation Coefficient of Gases and Their Adsorption on Iron", Trans. Faraday Soc., Vol.48, 1958, p.738.

[84] Popov, V.M., "Concerning the Problem of Investigating Thermal Contact Resistance", Power Eng., Vol.14, No.3, 1976, pp.158-163.

[85] O'Callaghan, P.W. and Probert, S.D., "Thermal Resistance and Directional Index of Pressed Contacts Between Smooth Non-Wavy Surfaces", Jr. of Mech. Eng. Sci., Vol.16, No.1, pp.41-55.

[86] Schenck, H., Theories of Engineering Experimentation, 3rd Ed., Hemisphere Pub. Corp., Washington, 1979.

[87] Fried, E., "Study of Interface Thermal Contact Conductance", Summary Report, No.64SD652, Contract No.NAS8-5207, May 1964.

[88] Fried, E., "Study of Interface Thermal Contact Conductance", Summary Report, No.65SD4395, Contract No.NAS8-11247, 27 March 64 - 27 March 65.

[89] Bloom, M.F., "Thermal Contact Conductance in a Vacuum Environment", Douglas Report SM-47700, 13 December 1964.

[90] Mikic, B.B., Yovanovich, M.M. and Rohsenow, W.M., "The Effect of Surface Roughness and Waviness upon the Overall Thermal Contact Resistance", Technical Report No.76361-43, Department of Mechanical Engineering, MIT, October 1966.

[91] Sherman, F.S., "A Survey of Experimental Results and Methods for the Transition Regime of Rarefied Gas Dynamics", Rarefied Gas Dynamics, Ed. by J.A. Lauermann, Academic Press, New York, 1963.

APPENDIX A: HARDNESS TESTS

A.1 Brinell Hardness Test

A.1.1 Definition

A hard ball of diameter D(mm) is pressed gently into a smooth flat metal surface under a known load L(N), and the diameter of the resulting indentation d(mm) is measured by means of a microscope. The Brinell hardness (BH) is expressed as the load L(N) divided by the curved area of the indentation in mm^2, so that

$$BH = \frac{2L}{\pi D(D - \sqrt{D^2 - d^2})} \text{ MPa} \quad . \qquad (A.1)$$

A.1.2 Indentation Size

The indentation diameter d is determined from the mean of two diameter measurements made at right angles to each other and the indentation size should be such that $d/D = 0.25 - 0.6$.

A.1.3 Loads and Loading Times

The load must be applied without shock or vibration in a direction at right angles to the test specimen and the full load must be maintained for 30 sec. for steels and other materials

of similar hardness. For brasses, bronzes and other softer metals the full load must be maintained for at least 60 sec. The British Standards for Brinell ball tests on metals [B.S.240:Part 1:1962], as well as ASTME Specifications [ASTME E10], specify the following loads and loading ratios (L/D^2) for various metals:

Specimen Suggested Range of BH/9.81	Loading Ratio $L/9.81D^2$	Load (L/9.81)N for D = 1mm	D = 2mm	D = 5mm	D = 10mm
over 100	30	30	120	750	3000
30 - 200	10	10	40	250	1000
15 - 100	5	5	20	125	500
3 - 20	1	1	4	25	100

Brinell hardness values for the various metals which were employed in this investigation were determined using a 10mm diameter steel ball and 29.43 kN load.

A.1.4 Test Specimen

Test specimen thickness should be not less than 10 times the indentation depth and no marking should appear on the side of the specimen apposite the indentation. Also, it is required that the centre of any indentation must be not less than 3 times the indentation diameter d from the free edge of the test specimen.

The distance between the centers of any adjacent indentations must be not less than 4 times the indentation diameter to prevent error due to interference between the strain-hardened zones around the indentations. The surface of the test specimen should be flat and reasonably well polished, otherwise difficulty will be experienced in making an accurate determination of the diameter of the indentation.

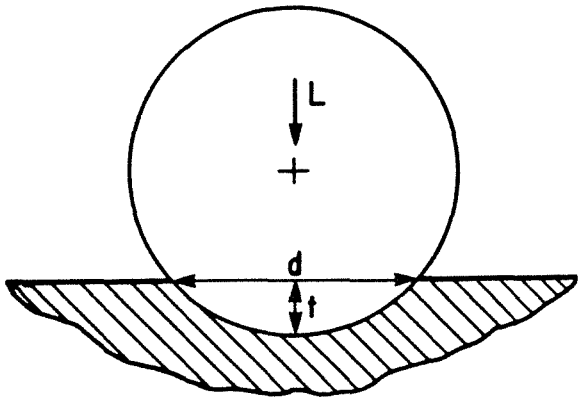

$$BH = \frac{2L}{\pi D\left(D-\sqrt{D^2-d^2}\right)} = \frac{L}{\pi Dt}$$

Figure A.1: Deformation of a Flat Surface by a Brinell Ball Indenter

A.2 Rockwell Hardness Test

A.2.1 Definition

The Rockwell test is a static indentation test similar to the Brinell test. It differs in that it measures the permanent increase in the indentation depth from the depth reached under a minor load of 98.1N, due to the application of an additional load. Measurement is made after recovery which takes place following the removal of this additional load. The Rockwell hardness number is a direct reading (in units of 0.002mm) from the dial gauge attached to the Rockwell machine while the minor load is still imposed.

A.2.2 Indenters

According to the material being tested, the indenter may be a 120° diamond cone with a blending spherical apex of 0.2mm radius or a steel ball indenter. The steel ball indenter is normally 1.588mm in diameter, but others of larger diameters such as 3.175, 6.350, or 12.7 mm may be employed for soft materials.

A.2.3 Loads and Scales

Rockwell machines are constructed to apply a fixed minor load of 98.1N which is used to establish the measurement datum. This is followed by an additional load, within 2-8 sec., which may be

0.49, 0.88, or 1.37 kN. The combination of the three loads and five indenters gives fifteen conditions of test; each has its own hardness scale. These conditions and scales are standardized by the ASTM [ASTM E18].

There is no Rockwell hardness value designated by a number alone because it is necessary to indicate which indenter and load have been used in making the test. Therefore, a prefix letter is employed to designate the scale and test condition. Of these scales, B and C are the most widely used. For B scale, a 0.88 kN additional load with a 1.588mm diameter steel ball indenter is used, while a 1.37 kN and a diamond cone indenter are employed in scale C. Scale B was used in measuring the hardness of the materials employed in the present investigation.

The Rockwell scales are divided into 100 divisions, each equivalent to 0.002mm of recovered indentation. Since the scales are reversed, the number is higher the harder the material, as shown by the following expressions which define the Rockwell B and C numbers:

$$\text{Rockwell B} = \text{RB} = 130 - \frac{\text{depth of penetration (mm)}}{0.002} \qquad \text{(A.2)}$$

and

$$\text{Rockwell C} = \text{RC} = 100 - \frac{\text{depth of penetration (mm)}}{0.002} \qquad \text{(A.3)}$$

A.2.4 Test Specimen

In general, the thickness of the test specimen must be such that no bulge or other marking appears on the surface of the specimen opposite the indentation, since in such cases, the depth of the indentation is noticeably affected by the supporting anvil. For very hard materials, the thickness may be as little as about 0.254mm. For steels and other materials of similar hardness, the specimen thickness should be not less than 2mm. The distance between the centers of adjacent indentations or to the edge of the test specimen should be at least:

a : 1.6mm for 65 - 59 RC

b : 3.2mm for 55 - 20 RC, 100 - 80 RB

c : 4.8mm for 60 - 40 RB

The surface of the test specimen, as well as the surface in contact with the anvil, must be smooth, flat and free from scale, oxide films, pits and foreign materials that might crush or flow under the test pressure and so affect the results.

A.3 Vickers Hardness Test

A.3.1 Definition

A polished pointed square-based right diamond pyramid is pressed into a smooth flat metal surface under a static load L(N) and the mean diagonal of the resultant indentation, d_v(mm), is measured by means of a microscope. The Vickers hardness is equal to the applied load divided by the pyramid indentation area. Since the diamond pyramid has an angle of 136° between opposite faces and 148° between the opposite edges, the Vickers hardness is given by:

$$VH = \frac{2L \sin 68}{d_v^2} = \frac{1.8544\ L}{d_v^2} \text{ MPa} \qquad (A.4)$$

A.3.2 Loads and Loading Times

For macro-hardness tests, the loads usually range from 98.1N to 1.18 kN in increments of 49.05N. However, a 98.1N load is commonly used and 294.3N load is seldom exceeded. For micro-hardness tests, the loads are commonly less than 9.81N. Loads most frequently employed in Vickers micro-hardness measurements lie in the range 4.91N to 0.05N. The typical loads used in the present work were 4.905, 2.943, 1.962, 0.981, 0.491, 0.245, and 0.147N.

For steel and other materials of similar harness, the full load must be maintained for 10-15 sec. and then removed without distorting the indentation. For softer materials, a load duration between 15 sec. and 30 sec. is recommended. The velocity of load application must be between 0.003mm/sec. to 0.012mm/sec.

A.3.3 Test Specimen

The specimen thickness must be at least 1.5 times the indentation diagonal and the distance between the centre of the indentation and any edge of the test specimen or any other indentations must not be less than 2.5 times the indentation diagonal. The test surface must be polished to provide high reflectivity and the RMS surface roughness must not exceed 0.1μm. Also, the selected spot for micro-hardness measurements must be free from scratches that interfere with the diagonal measurements. For further details the reader is referred to ASTM Specifications [ASTM E92] or the British Standards, [B.S.427: Part 1:1961].

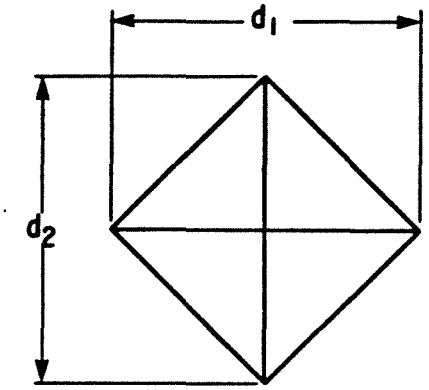

(b)

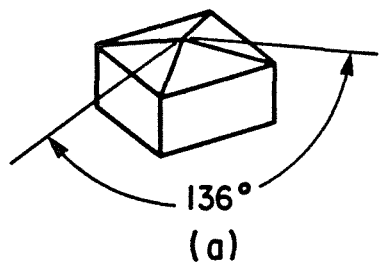

(a)

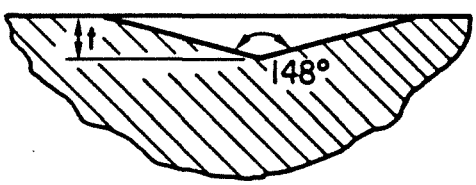

(c)

$d_v = (d_1 + d_2)/2$, $d_v/t = 7$

Figure A.2: Vickers Indenter and Indentation Geometry
a) Indenter, b) Indentation,
c) Indentation Geometry.

Table A.1: Vickers Micro-Hardness Measurements

		Indenter Load, N						
Material	H_v,MPa	4.905	2.943	1.962	0.981	0.491	0.245	0.147
Zr-4	Max.	1924	1928	2029	2232	2520	2776	3121
	Min.	1905	1907	1986	2171	2442	2691	3056
	Ava.	1915	1919	2013	2200	2468	2742	3102
Zr-2.5wt%Nb	Max.	1956	2074	2246	2477	2839	3185	3332
	Min.	1883	1976	2118	2406	2587	2691	3224
	Ava.	1900	2043	2177	2441	2767	2941	3274
Ni200	Max.	2114	2264	2455	2620	3057	3294	3564
	Min.	1973	2273	2308	2542	2871	3266	3524
	Ava.	2073	2268	2419	2597	2995	3272	3555
SS304	Max.	2457	2630	2807	3158	3361	3658	3914
	Min.	2397	2557	2731	3031	3301	3530	3733
	Ava.	2414	2579	2758	3056	3325	3607	3804
Armco iron	Max.	1501	1526	1626	1717	1946	2134	2118
	Min.	1430	1448	1540	1645	1821	1943	1960
	Ava.	1460	1506	1590	1678	1859	2018	2054
Zr-4	Max.	1794	1893	1945	2042	2092	2256	2429
	Min.	1777	1817	1914	1988	2196	2193	2318
	Ava.	1782	1858	1928	2023	2163	2227	2362

APPENDIX B: CONTACT SURFACE PREPARATION AND PARAMETERS

B.1 Bead Blasting Device

Preliminary thermal tests were carried out on surfaces roughened in a sandblasting machine charged with glass beads. Surface roughness was accomplished by directing normal to the surface, in random fashion, a blasting gun which produced a jet of air containing glass beads. This technique dramatically altered the surface flatness and resulted in uneven temperature gradient along the test specimen. Moreover, the previous thermal results could not be repeated when the same pair was re-assembled.

To overcome this problem, the device shown in Figure B.1 was designed by the writer and used to prepare the roughened surfaces. The device consisted of a steel nozzle mounted in a stationary holder and connected to a bead chamber. The bead chamber was also connected to an 827 kPa air line by means of a regulating valve. An adjustable specimen holder was attached to the device base parallel to the nozzle so that the distance between the nozzle outlet and the specimen surface could be adjusted. By filling the bead chamber with the desired beads and pressurizing it a jet of high velocity glass beads could be projected normal to the specimen surface.

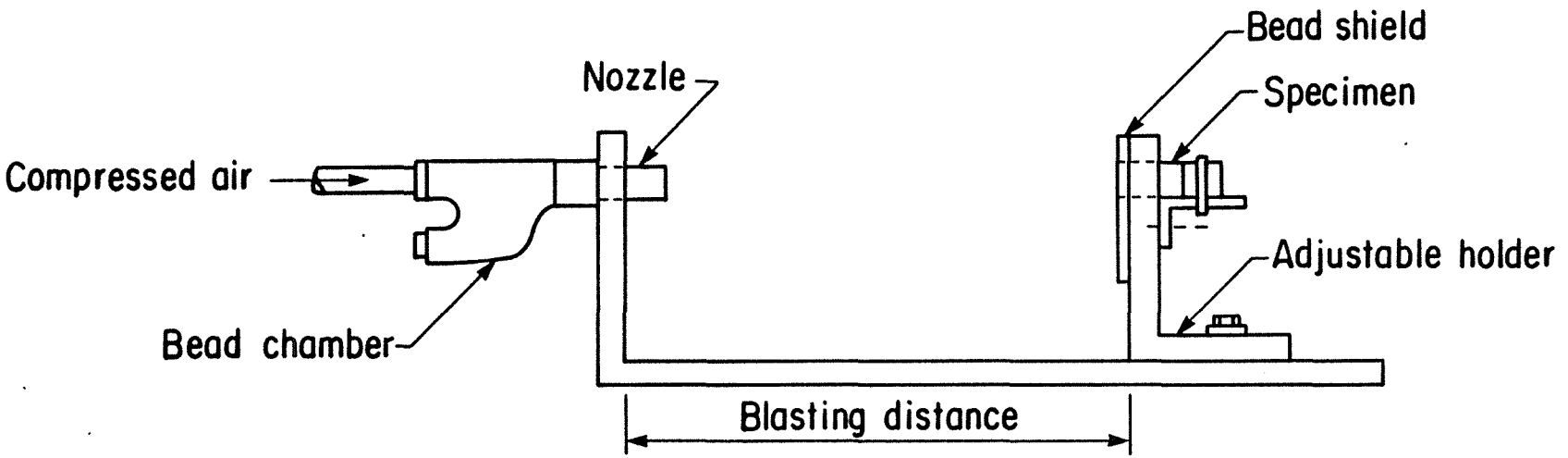

Figure B.1: Schematic of Glass Bead Blasting Device

In general, this device was used inside the sandblasting machine cabinet to prevent the glass dust from contaminating the air. Different surface textures were obtained by: a) using different grades of glass beads, b) varying the blast pressure, and c) varying the distance between the nozzle holder and the specimen surface. Due to the different sizes and weights of the glass beads, as well as the specimen materials, it is very difficult to make firm recommendations about the quantity of beads, the blast pressure, or the distance between the specimen surface and the nozzle holder. However, some simple, but necessary experimentation is recommended for any particular material. The different grades of glass beads as well as their size ranges are shown in Table B.1.

Table B.1: Glass Bead Grades

Bead Number	U.S. Sieve Size	Glass Size Range, μm	Minimum Sphere Count
1	140 - 230	105 - 62	90%
2	60 - 80	250 - 177	80%
3	40 - 50	420 - 297	70%
4	20 - 30	840 - 590	65%

B.2 Estimation of Surface Parameters

For a particular joint, the prediction of the thermal conductance requires, among many other parameters, knowledge about the topographical parameters of the joint before assembly. This is usually obtained by means of a stylus profilometer. However, accurate measurement of surface parameters depends upon a number of factors. The most important one is the ability to specify the appropriate sampling length for the surface under consideration.

Sampling length can be defined as the physical length of the surface over which the parameter is to be measured. It must be large enough to have statistical significance without being so long as to include irrelevant details. The profilometer built in sampling length is called the cut-off length. Usually, several measurements over consecutive cut-off lengths are made by the instrument and the length is called the assessment length. Generally, the assessment length is shorter than the stylus traverse length to allow the electrical and mechanical elements to attain steady operation before the measurement is taken.

Many instruments offer a range of cut-off lengths so that it is necessary to select the appropriate one which suits the surface under examination. In other words, we will be able to measure a particular surface parameter if one of the instrument cut-off lengths

is equal to the surface sampling length. Practically speaking, this is a very difficult problem as it is impossible to specify or determine the appropriate cut-off length for a particular parameter in advance.

From an extensive series of measurements on surfaces having different textures it was observed that the measurements of a particular parameter made with a progressive increase in the cut-off length would reach a value beyond which an increase in the cut-off length would lead to a slight increase in the value of this parameter. In light of this observation, as well as the definition of the surface physical sampling length, it was decided that a particular surface parameter could be estimated by averaging all the values which agreed within $\pm 10\%$. This technique was used in estimating the joint topographical parameters for the thermal predictions. An actual illustration of this technique is given in Tables B.2 and B.3.

Finally, it is desirable to call attention to the importance of instrument calibration and measurement procedures as recommended by the manufacturer. It is also recommended that some experimentation with "Roughness Comparison Specimens" may be useful, especially for a new operator.

Table B.2: Surface Parameters Estimation for Surface SS 02

Cut-off Length, mm	0.08	0.25	0.80	2.50	8.00
Traverse Length, mm	2.16	3.50	7.20	10.0	8.00
σ , μm	0.157	0.181	1.181	0.180	0.232
m	0.047	0.047	0.047	0.021	0.047

Estimated values are: σ = 0.181 μm, m = 0.047

Table B.3: Surface Parameters Estimation for Surface SS 07

Cut-off Length, mm	0.08	0.25	0.80	2.50	8.00
Traverse Length, mm	2.16	3.50	7.20	10.0	8.00
σ , μm	1.96	5.02	8.92	10.44	11.46
m	0.158	0.180	0.183	0.148	0.190

Estimated values are: σ = 10.95 μm, m = 0.184

B.3 Surface Preparation and Parameters

Table B.4 contains the necessary information about test surface preparation after turning, and the estimated surface characteristics. Throughout this table only, the following abbreviations are used for:

BD = Blast Distance, cm

BN = Bead Number, Table B.1

BP = Blast Pressure

G = Ground

HL = Hand Lapped

L = Mechanically Lapped

Table B.4: Surface Preparation and Parameters

Surface	Machining	BN/BP/BD -/kPa/cm	σ μm	10^3 m	CLA μm	MRH μm
NI 01	G,L,G,HL	-----	0.767	95	0.57	1.695
NI 02	G,L,G,HL	-----	0.474	55	0.338	1.097
NI 03	G,L,G,HL	1/207/27	3.427	185	2.8	10.80
NI 04	G,L,HL	-----	0.202	45	0.136	0.50
NI 05	G,L,G,HL	2/276/27	4.237	186	3.405	13.03
NI 06	G,L,HL	-----	0.23	26	0.148	0.35
NI 07	G,L,G,HL	3/689/27	9.522	223	7.66	28.2
NI 08	G,L,HL	-----	0.225	48	0.144	0.473
NI 09	G,L,G,HL	4/689/27	13.94	232	11.39	35.07
NI 10	G,L,HL	-----	0.23	26	0.146	0.348
SS 01	G,L,G,HL	-----	0.442	54	0.315	1.06
SS 02	G,L,HL	-----	0.181	47	0.127	0.633
SS 03	G,L,G,HL	2/276/27	2.708	114	2.137	9.228
SS 04	G,L,HL	-----	0.18	21	0.125	0.314
SS 05	G,L,G,HL	3/689/27	5.864	136	4.715	17.81
SS 06	G,L,G,HL	-----	0.426	52	0.305	1.06
SS 07	G,L,G,HL	4/689/27	10.95	184	8.88	30.0
SS 08	G,L,HL	-----	0.223	47	0.166	0.90
ZN 01	G,L,G,HL	-----	0.865	77	0.615	2.52
ZN 02	G,L,HL	-----	0.319	31	0.228	0.803

Continued...

Table B.4 (continued..)

Surface	Machining	BN/BP/BD -/kPa/cm	σ µm	10^3 m	CLA µm	MRH µm
ZN 03	G,L,G,HL	2/276/27	2.447	154	1.958	8.26
ZN 04	G,L,G,HL	-----	0.533	50	0.416	1.18
ZN 05	G,L,G,HL	3/413/27	5.959	177	4.81	17.73
ZN 06	G,L,G,HL	-----	0.598	51	0.425	1.61
ZN 07	G,L,G,HL	4/413/27	8.781	193	7.057	24.11
ZN 08	G,L,G,HL	-----	0.692	53	0.513	1.70
Z4 01	G,L,G,HL	-----	0.469	38	0.368	1.39
Z4 02	G,L,G,HL	-----	0.389	31	0.284	1.21
Z4 03	G,L,G,HL	2/276/27	2.663	136	2.112	8.10
Z4 04	G,L,G,HL	-----	0.694	58	0.51	1.76
Z4 05	G,L,G,HL	3/413/27	3.076	119	2.484	9.03
Z4 06	G,L,G,HL	-----	0.642	50	0.463	1.65
Z4 07	G,L,G,HL	4/276/20	7.892	203	6.347	19.62
Z4 08	G,L,G,HL	----	0.679	40	0.519	1.65
SS 09	G,L,G,HL	3/551/27	5.648	149	4.498	18.19
SS 10	G,L,G,HL	-----	0.252	36	0.191	0.76
SS 11	G,L,G,HL	3/551/27	5.607	148	4.489	17.67
SS 12	G,L,G,HL	-----	0.186	28	0.138	0.51
SS 13	G,HL	3/413/27	6.283	190	5.028	20.42
SS 14	G,HL	----	0.23	42	0.168	0.55

Continued...

Table B.4 (continued...)

Surface	Machining	BN/BP/BD -/kPa/cm	σ μm	10^3 m	CLA μm	MRH μm
SS 15	G,HL	2/413/27	4.015	163	3.201	12.61
SS 16	G,HL	-----	0.211	40	0.157	0.51

CLA = arithmetic mean of roughness heights from the surface mean line

MRH = height of the highest peaks from the surface mean line

m = surface mean absolute slope

σ = RMS surface roughness

APPENDIX C

THERMAL TEST RESULTS AND COMPARISONS

Table C.1: Test Results of Pair PNI0102

Run No.	P kPa	T_m °C	ΔT °C	k_s W/mK	Q W	h_c W/m²K
1	495	115.7	20.8	75.6	32.5	3183
2	588	114.1	18.6	75.7	32.7	3583
3	734	111.6	15.9	75.8	33.0	4229
4	861	110.1	14.0	75.9	33.0	4785
5	1008	109.7	12.7	76.0	33.0	5277
6	1134	109.0	11.8	76.0	33.1	5691
7	1355	107.9	10.3	76.1	33.0	6507
8	1573	106.6	9.3	76.2	33.0	7256
9	1803	105.9	8.3	76.2	33.1	8116
10	2020	105.0	7.5	76.3	33.1	9037
11	2251	104.3	6.9	76.3	33.1	9724
12	2677	103.4	6.0	76.4	33.0	11228
13	3138	102.3	5.3	76.4	32.9	12762
14	3596	101.8	4.8	76.5	32.9	13941
15	4085	142.2	5.7	73.8	46.6	16589
16	4481	141.5	5.3	73.9	46.5	17918
17	4916	140.6	4.8	73.9	46.4	19569
18	5388	139.6	4.2	74.0	46.3	22316
19	5802	138.8	4.0	74.0	46.2	23621
20	6299	138.1	3.6	74.1	45.9	26062
21	7176	137.2	3.2	74.1	45.8	29352
22	8058	136.2	2.8	74.2	45.6	33175
23	8830	135.6	2.6	74.3	45.5	35957

Table C.2: Test Results of Pair PNI0304

Run No.	P kPa	T_m °C	ΔT °C	k_s W/mK	Q W	h_c W/m²K
1	477	118.9	36.8	75.3	31.7	1750
2	591	116.8	33.7	75.5	31.8	1922
3	732	114.3	28.7	75.6	32.1	2275
4	865	112.5	25.6	75.8	32.2	2562
5	998	110.9	23.4	75.9	32.2	2797
6	1140	109.9	21.3	75.9	32.3	3085
7	1361	108.2	18.8	76.0	32.4	3524
8	1634	107.2	16.5	76.1	32.4	4000
9	1814	106.6	15.2	76.2	32.6	4372
10	2018	105.4	14.1	76.2	32.7	4720
11	2260	104.5	12.7	76.3	32.7	5225
12	2734	102.7	10.5	76.4	32.5	6283
13	3150	101.8	9.3	76.5	32.6	7172
14	3586	101.2	8.1	76.5	32.5	8163
15	4069	100.6	7.2	76.6	32.5	9235
16	4495	99.7	6.3	76.6	32.4	10457
17	4929	98.9	5.9	76.7	32.4	11237
18	5377	98.2	5.6	76.7	32.4	11814
19	5837	98.0	5.0	76.7	32.4	13083
20	6305	97.8	4.7	76.7	32.2	13999
21	7252	134.8	5.8	74.3	44.9	15655
22	8050	134.4	5.3	74.3	44.9	17149
23	8800	134.4	4.8	74.3	44.9	19091

Table C.3: Test Results of Pair PNI0506

Run No.	P kPa	T_m °C	ΔT °C	k_s W/mK	Q W	h_c W/m²K
1	493	124.4	48.7	75.0	31.1	1303
2	586	123.2	44.8	75.0	31.4	1425
3	723	119.8	38.6	75.3	31.8	1678
4	870	118.0	33.8	75.4	31.8	1915
5	1008	117.5	30.3	75.4	31.9	2148
6	1131	116.5	28.2	75.5	32.0	2317
7	1350	113.8	24.5	75.7	32.3	2685
8	1579	112.0	22.0	75.8	32.5	2999
9	1808	110.6	20.0	75.9	32.5	3307
10	2031	108.9	17.8	76.0	32.5	3729
11	2346	108.1	15.3	76.1	32.2	4293
12	2694	107.9	13.5	76.1	32.4	4881
13	3124	106.2	11.6	76.2	32.5	5713
14	3594	105.6	10.2	76.2	32.4	6451
15	4021	104.1	9.1	76.3	32.6	7345
16	4489	103.1	8.1	76.4	32.5	8153
17	4940	102.6	7.5	76.4	32.6	8836
18	5362	101.9	6.9	76.5	32.6	9655
19	5832	101.6	6.4	76.5	32.5	10306
20	6284	102.9	5.9	76.4	32.3	11114
21	7165	102.1	5.2	76.5	32.3	12792
22	8074	101.7	4.6	76.5	32.3	14375
23	8886	138.6	6.2	74.2	45.1	14901

Table C.4: Test Results of Pair PNI0708

Run No.	P kPa	T_m °C	ΔT °C	k_s W/mK	Q W	h_c W/m²K
1	461	131.1	61.0	74.5	29.7	994
2	596	128.7	57.2	74.7	30.2	1075
3	727	125.3	51.2	74.9	30.4	1209
4	868	122.7	46.0	75.1	30.5	1351
5	1000	120.2	42.2	75.2	30.8	1489
6	1139	118.0	38.3	75.4	31.0	1646
7	1368	116.0	33.2	75.5	31.1	1908
8	1591	114.6	29.6	75.6	31.2	2148
9	1827	113.5	26.9	75.7	31.4	2384
10	2033	112.8	24.7	75.8	31.4	2592
11	2248	110.7	22.2	75.9	31.7	2904
12	2685	108.3	18.7	76.0	31.8	3469
13	3138	107.2	16.0	76.1	31.8	4065
14	3598	105.5	14.3	76.2	31.9	4548
15	4053	104.5	12.9	76.3	31.9	5024
16	4534	104.0	11.5	76.3	31.8	5629
17	4929	103.6	10.7	76.4	31.7	6051
18	5389	109.5	10.6	76.0	31.7	6473
19	5836	109.4	9.8	76.0	33.9	7081
20	6273	108.7	9.0	76.0	34.1	7716
21	7164	107.6	8.1	76.1	34.1	8561
22	8055	107.3	7.2	76.1	34.1	9672
23	8779	106.0	4.5	76.2	34.0	10716

Table C.5: Test Results of Pair PNI0910

Run No.	P kPa	T_m °C	ΔT °C	k_s W/mK	Q W	h_c W/m²K
1	473	134.2	84.0	74.2	27.6	670
2	592	133.6	80.9	74.3	28.0	703
3	727	129.9	71.1	74.6	28.6	819
4	859	125.8	63.1	74.8	29.0	937
5	995	123.2	57.7	75.2	29.2	1029
6	1133	120.9	52.5	75.2	29.4	1141
7	1390	118.5	44.4	75.4	29.7	1362
8	1590	116.6	40.3	75.5	29.9	1508
9	1823	114.5	35.2	75.6	29.9	1730
10	2031	114.1	32.7	75.6	30.2	1884
11	2255	111.4	29.3	75.8	30.3	2112
12	2716	109.4	24.7	76.0	30.5	2517
13	3127	107.2	21.4	76.1	30.7	2922
14	3592	105.5	19.0	76.2	30.8	3298
15	4069	104.6	16.8	76.3	30.9	3751
16	4509	103.5	15.0	76.4	30.7	4158
17	4947	103.3	14.0	76.4	30.7	4458
18	5412	102.3	12.7	76.4	30.8	4925
19	5816	101.7	11.9	76.5	30.7	5243
20	6280	100.9	11.1	76.5	30.7	5636
21	7184	100.2	9.6	76.6	30.8	6498
22	8083	99.6	8.6	76.6	30.7	7283
23	8792	99.1	8.0	76.7	30.8	7895

Table C.6: Comparison Between Theory and Test Results of Pair PNI0102

Run No.	P kPa	10^3 P/H_c	10^3 C_c Test	10^3 C_c Theory	% Diff.
1	495	0.135	0.345	0.263	31.2
2	588	0.161	0.388	0.311	24.8
3	734	0.200	0.457	0.383	19.3
4	861	0.235	0.517	0.446	15.9
5	1008	0.275	0.570	0.518	10.0
6	1134	0.310	0.614	0.580	5.9
7	1355	0.370	0.701	0.687	2.0
8	1573	0.429	0.781	0.790	- 1.1
9	1803	0.492	0.873	0.900	- 3.0
10	2020	0.552	0.972	1.004	- 3.2
11	2251	0.615	1.045	1.113	- 6.1
12	2677	0.731	1.206	1.311	- 8.0
13	3138	0.857	1.369	1.525	-10.2
14	3596	0.982	1.495	1.735	-13.8
15	4085	1.115	1.843	1.958	- 5.9
16	4481	1.223	1.989	2.138	- 7.0
17	4916	1.342	2.171	2.335	- 7.0
18	5388	1.471	2.473	2.548	- 2.9
19	5802	1.584	2.618	2.733	- 4.2
20	6299	1.720	2.884	2.956	- 2.4
21	7176	1.959	3.246	3.345	- 3.0
22	8058	2.200	3.666	3.734	- 1.8
23	8830	2.411	3.971	4.074	- 2.5

Table C.7: Comparison Between Theory and Test Results of Pair PNI0304

Run No.	P kPa	10^3 P/H_c	10^3 C_c Test	10^3 C_c Theory	% Diff.
1	477	0.160	0.420	0.310	35.5
2	591	0.199	0.460	0.381	20.7
3	732	0.246	0.543	0.466	16.5
4	865	0.291	0.611	0.547	11.7
5	998	0.336	0.666	0.627	6.2
6	1140	0.383	0.734	0.709	3.5
7	1361	0.458	0.837	0.841	- 4.8
8	1634	0.550	0.949	1.001	- 5.2
9	1814	0.610	1.037	1.104	- 6.1
10	2018	0.679	1.119	1.222	- 8.4
11	2260	0.760	1.237	1.360	- 9.0
12	2734	0.920	1.486	1.631	- 8.9
13	3150	1.060	1.695	1.866	- 9.2
14	3586	1.206	1.928	2.110	- 8.6
15	4069	1.369	2.180	2.380	- 8.4
16	4495	1.512	2.466	2.615	- 5.7
17	4929	1.658	2.648	2.854	- 7.2
18	5377	1.809	2.783	3.101	-10.3
19	5837	1.963	3.081	3.351	- 8.1
20	6305	2.121	3.296	3.607	- 8.6
21	7252	2.439	3.807	4.119	- 7.6
22	8050	2.708	4.169	4.549	- 8.4
23	8800	2.960	4.641	4.950	- 6.2

Table C.8: Comparison Between Theory and Test Results of Pair PNI0506

Run No.	P kPa	10^3 P/H_c	10^3 C_c Test	10^3 C_c Theory	% Diff.
1	493	0.176	0.392	0.339	15.6
2	586	0.209	0.429	0.399	7.5
3	723	0.258	0.503	0.487	3.3
4	870	0.310	0.573	0.580	- 1.2
5	1008	0.360	0.627	0.669	- 6.3
6	1131	0.403	0.693	0.745	- 7.0
7	1350	0.482	0.801	0.883	- 9.3
8	1579	0.563	0.893	1.023	-12.7
9	1808	0.645	0.983	1.164	-15.6
10	2031	0.724	1.107	1.299	-14.8
11	2346	0.837	1.274	1.491	-14.6
12	2694	0.961	1.448	1.700	-14.8
13	3124	1.114	1.693	1.956	-13.4
14	3594	1.282	1.910	2.236	-14.6
15	4021	1.434	2.172	2.487	-12.7
16	4489	1.601	2.409	2.761	-12.8
17	4940	1.762	2.610	3.024	-13.7
18	5362	1.913	2.850	3.270	-12.8
19	5832	2.080	3.041	3.541	-14.1
20	6284	2.241	3.284	3.800	-13.6
21	7165	2.556	3.776	4.306	-12.3
22	8074	2.880	4.242	4.823	-12.1
23	8886	3.170	4.532	5.283	-14.2

Table C.9: Comparison Between Theory and Test Results of Pair PNI0708

Run No.	P kPa	10^3 P/H_c	10^3 C_c Test	10^3 C_c Theory	% Diff.
1	461	0.193	0.557	0.370	50.5
2	596	0.250	0.602	0.473	27.3
3	727	0.305	0.674	0.571	18.0
4	868	0.364	0.752	0.676	11.2
5	1000	0.420	0.827	0.774	6.9
6	1139	0.478	0.912	0.876	4.1
7	1368	0.574	1.055	1.042	1.3
8	1591	0.668	1.187	1.204	- 1.4
9	1827	0.767	1.316	1.372	- 4.1
10	2033	0.853	1.429	1.518	- 5.9
11	2248	0.943	1.599	1.670	- 4.3
12	2685	1.127	1.906	1.978	- 3.6
13	3138	1.317	2.231	2.294	- 2.8
14	3598	1.510	2.493	2.612	- 4.6
15	4053	1.701	2.751	2.925	- 6.0
16	4534	1.903	3.081	3.254	- 5.3
17	4929	2.069	3.311	3.523	- 6.0
18	5385	2.260	3.560	3.831	- 7.1
19	5836	2.449	3.893	4.135	- 5.9
20	6273	2.633	4.240	4.429	- 4.3
21	7164	3.006	4.701	5.023	- 6.4
22	8055	3.380	5.309	5.615	- 5.5
23	8779	3.684	5.876	6.094	- 3.6

Table C.10: Comparison Between Theory and Test Results of Pair PNI0910

Run No.	P kPa	10^3 P/H_c	10^3 C_c Test	10^3 C_c Theory	% Diff.
1	473	0.218	0.540	0.415	30.1
2	592	0.273	0.566	0.514	10.1
3	727	0.335	0.657	0.625	5.1
4	859	0.396	0.749	0.732	2.3
5	995	0.459	0.819	0.843	- 2.9
6	1133	0.523	0.908	0.954	- 4.8
7	1390	0.641	1.081	1.157	- 6.6
8	1590	0.734	1.195	1.316	- 9.2
9	1823	0.841	1.369	1.498	- 8.6
10	2031	0.937	1.490	1.660	-10.2
11	2255	1.040	1.666	1.833	- 9.1
12	2716	1.253	1.982	2.188	- 9.4
13	3127	1.443	2.297	2.502	- 8.2
14	3592	1.657	2.589	2.853	- 9.3
15	4069	1.877	2.942	3.211	- 8.4
16	4509	2.080	3.258	3.541	- 8.0
17	4947	2.283	3.492	3.868	- 9.7
18	5412	2.497	3.855	4.212	- 8.5
19	5816	2.684	4.102	4.511	- 9.1
20	6280	2.898	4.407	4.852	- 9.2
21	7184	3.315	5.077	5.513	- 7.9
22	8083	3.730	5.688	6.166	- 7.8
23	8792	4.057	6.163	6.679	- 7.7

Table C.11: Test Results of Pair PSS0102

Run No.	P kPa	T_m °C	ΔT °C	k_s W/mK	Q W	h_c W/m²K
1	446	151.8	47.8	19.3	16.6	706
2	592	148.3	36.5	19.3	17.1	954
3	730	145.1	30.1	19.2	17.3	1171
4	866	143.1	26.3	19.2	17.5	1356
5	1008	141.2	23.0	19.2	17.4	1540
6	1133	140.0	20.9	19.1	17.4	1695
7	1362	137.8	18.0	19.1	17.3	1966
8	1592	136.6	16.0	19.1	17.4	2221
9	1859	136.0	14.4	19.1	17.5	2470
10	2012	135.0	13.6	19.1	17.5	2620
11	2250	134.3	12.3	19.1	17.4	2879
12	2691	132.3	10.4	19.0	17.4	3415
13	3148	131.5	8.9	19.0	17.4	3969
14	3590	130.2	7.9	19.0	17.2	4457
15	4050	129.7	6.7	19.0	17.3	5124
16	4493	129.3	6.1	19.0	17.3	5736
17	4931	128.6	5.7	19.0	17.2	6129
18	5372	128.2	5.3	19.0	17.2	6591
19	5741	164.3	5.8	19.5	21.9	7691
20	6248	164.5	5.6	19.5	21.8	7973
21	7153	163.5	4.9	19.5	21.8	9001
22	8053	163.0	4.4	19.5	21.8	10125
23	8820	162.5	3.9	19.5	21.7	11321

Table C.12: Test Results of Pair PSS0304

Run No.	P kPa	T_m °C	ΔT °C	k_s W/mK	Q W	h_c W/m²K
1	431	156.0	94.5	19.4	13.9	300
2	597	152.9	82.0	19.3	14.5	359
3	738	150.1	72.8	19.3	14.8	413
4	863	147.7	65.6	19.3	14.8	460
5	1008	146.5	59.2	19.2	14.9	513
6	1125	144.4	55.5	19.2	15.2	557
7	1353	142.3	49.0	19.2	15.4	638
8	1577	140.4	44.2	19.1	15.6	718
9	1789	138.7	41.1	19.1	15.6	775
10	2016	137.1	36.8	19.1	15.8	876
11	2242	135.7	33.9	19.1	15.9	954
12	2677	133.2	28.8	19.0	15.9	1122
13	3153	131.8	24.7	19.0	16.0	1624
14	3604	130.9	21.7	19.0	15.9	1485
15	4042	129.4	19.2	19.0	16.1	1706
16	4482	128.5	17.4	19.0	16.0	1866
17	4929	127.6	16.0	19.0	16.0	2045
18	5375	126.8	14.8	19.0	16.2	2227
19	5855	125.8	13.6	18.9	16.1	2419
20	6275	124.9	12.6	18.9	16.0	2595
21	7187	124.6	11.2	18.9	16.0	2895
22	8115	123.5	9.7	18.9	15.9	3339
23	8824	123.7	9.0	18.9	16.0	3638

Table C.13: Test Results of Pair PSS0506

Run No.	P kPa	T_m °C	ΔT °C	k_s W/mK	Q W	h_c W/m²K
1	409	147.7	103.9	19.2	12.3	241
2	603	144.4	92.0	19.2	12.7	280
3	727	141.4	83.7	19.1	13.0	316
4	866	138.5	75.2	19.1	13.1	355
5	1008	136.0	68.6	19.1	13.3	394
6	1145	134.0	63.3	19.0	13.4	431
7	1359	130.9	55.6	19.0	13.5	494
8	1580	128.7	50.1	19.0	13.6	554
9	1810	127.1	45.3	18.9	13.7	618
10	2066	124.6	40.7	18.9	13.8	690
11	2243	123.4	38.3	18.9	13.9	738
12	2719	121.1	32.3	18.9	14.0	883
13	3123	119.3	28.7	18.8	14.0	998
14	3571	117.6	25.1	18.8	14.0	1138
15	4052	116.6	22.4	18.8	14.0	1270
16	4536	115.5	20.4	18.8	14.0	1404
17	4939	115.0	18.9	18.8	14.1	1514
18	5363	114.3	17.6	18.8	14.1	1638
19	5888	113.8	16.2	18.7	14.2	1785
20	6287	112.9	15.4	18.7	14.1	1868
21	7173	111.7	13.5	18.7	14.0	2112
22	8084	111.1	12.0	18.7	13.9	2365
23	8819	110.2	11.2	18.7	13.9	2543

Table C.14: Test Results of Pair PSS0708

Run No.	P kPa	T_m °C	ΔT °C	k_s W/mK	Q W	h_c W/m²K
1	445	141.4	114.9	19.1	10.4	185
2	584	138.5	106.4	19.1	10.7	205
3	722	135.2	95.8	19.0	11.2	238
4	844	133.3	86.7	19.0	11.7	274
5	1002	133.7	81.9	19.0	12.0	298
6	1135	132.2	76.3	19.0	12.1	322
7	1412	129.8	67.2	19.0	12.2	369
8	1577	128.0	61.2	19.0	12.5	418
9	1791	125.3	56.1	18.9	12.8	564
10	2054	124.1	51.2	18.9	12.8	508
11	2237	122.8	47.2	18.9	13.0	560
12	2672	120.1	40.5	18.8	13.2	661
13	3134	117.8	35.1	18.8	13.2	766
14	3642	116.7	30.4	18.8	13.2	886
15	4058	115.2	28.3	18.8	13.4	960
16	4483	114.2	25.8	18.8	13.4	1059
17	4921	113.6	23.8	18.7	13.5	1151
18	5363	112.7	22.0	18.7	13.5	1248
19	5841	112.2	20.2	18.7	13.5	1361
20	6275	111.5	19.1	18.7	13.5	1439
21	7182	110.3	16.8	18.7	13.4	1627
22	8083	109.4	14.9	18.7	13.4	1837
23	8775	108.8	14.0	18.7	13.5	1964

Table C.15: Comparison Between Theory and Test Results of Pair PSS0102

Run No.	P kPa	10^3 P/H_c	10^3 C_c Test	10^3 C_c Theory	% Diff.
1	446	0.109	0.243	0.215	13.0
2	592	0.144	0.329	0.280	17.5
3	730	0.178	0.404	0.343	17.8
4	886	0.211	0.469	0.403	16.4
5	1008	0.245	0.534	0.464	15.1
6	1133	0.276	0.588	0.520	13.1
7	1362	0.331	0.683	0.618	10.5
8	1592	0.387	0.772	0.717	7.7
9	1859	0.452	0.859	0.830	3.5
10	2012	0.490	0.913	0.897	1.8
11	2250	0.548	1.003	0.997	0.6
12	2691	0.655	1.192	1.181	0.9
13	3148	0.766	1.386	1.371	1.1
14	3590	0.874	1.557	1.554	0.2
15	4050	0.986	1.791	1.742	2.8
16	4493	1.093	2.006	1.921	4.4
17	4931	1.200	2.145	2.100	2.1
18	5372	1.307	2.308	2.277	1.4
19	5741	1.397	2.618	2.426	7.9
20	6248	1.520	2.713	2.628	3.2
21	7153	1.741	3.064	2.990	2.5
22	8053	1.960	3.454	3.346	3.2
23	8820	2.146	3.856	3.647	5.7

Table C.16: Comparison Between Theory and Test Results of Pair PSS0304

Run No.	P kPa	10^3 P/H_c	10^3 C_c Test	10^3 C_c Theory	% Diff.
1	431	0.140	0.363	0.273	33.0
2	597	0.194	0.434	0.372	16.7
3	738	0.240	0.501	0.455	10.1
4	863	0.280	0.559	0.527	6.1
5	1008	0.327	0.624	0.611	2.1
6	1125	0.365	0.678	0.678	0.0
7	1353	0.439	0.779	0.808	- 3.6
8	1577	0.512	0.878	0.935	- 6.1
9	1789	0.581	0.948	1.054	-10.1
10	2016	0.655	1.073	1.181	- 9.1
11	2242	0.728	1.170	1.306	-10.4
12	2677	0.869	1.379	1.545	-10.7
13	3153	1.024	1.624	1.806	-10.1
14	3604	1.170	1.829	2.050	-10.8
15	4042	1.313	2.103	2.287	- 8.1
16	4482	1.455	2.301	2.521	- 8.7
17	4929	1.601	2.525	2.761	- 8.6
18	5375	1.745	2.751	2.997	- 8.2
19	5855	1.901	2.991	3.250	- 8.0
20	6275	2.038	3.211	3.473	- 7.5
21	7187	2.334	3.582	3.950	- 9.3
22	8115	2.635	4.136	4.433	- 6.7
23	8824	2.865	4.506	4.799	- 6.1

Table C.17: Comparison Between Theory and Test Results of Pair PSS0506

Run No.	P kPa	10^3 P/H_c	10^3 C_c Test	10^3 C_c Theory	% Diff.
1	409	0.150	0.505	0.291	73.5
2	603	0.222	0.588	0.423	39.0
3	727	0.267	0.665	0.504	31.9
4	866	0.318	0.748	0.595	25.7
5	1008	0.371	0.832	0.688	20.9
6	1145	0.421	0.912	0.776	17.5
7	1359	0.500	1.047	0.914	14.6
8	1580	0.581	1.177	1.054	11.7
9	1810	0.666	1.314	1.200	9.5
10	2066	0.760	1.470	1.360	8.1
11	2243	0.825	1.573	1.471	6.9
12	2719	1.000	1.886	1.766	6.8
13	3123	1.148	2.134	2.013	6.0
14	3571	1.313	2.437	2.287	6.6
15	4052	1.490	2.722	2.579	5.5
16	4536	1.668	3.012	2.871	4.9
17	4939	1.816	3.250	3.112	4.4
18	5363	1.972	3.518	3.366	4.5
19	5888	2.165	3.835	3.678	4.3
20	6287	2.312	4.016	3.915	2.6
21	7173	2.638	4.545	4.437	2.4
22	8084	2.973	5.093	4.971	2.5
23	8819	3.243	5.479	5.399	1.5

Table C.18: Comparison Between Theory and Test Results of Pair PSS0708

Run No.	p kPa	10^3 P/H_c	10^3 C_c Test	10^3 C_c Theory	% Diff.
1	445	0.178	0.558	0.343	62.7
2	584	0.233	0.619	0.442	40.1
3	722	0.288	0.721	0.541	33.3
4	844	0.337	0.831	0.628	32.3
5	1002	0.400	0.903	0.739	22.2
6	1135	0.453	0.977	0.832	17.4
7	1412	0.564	1.121	1.025	9.4
8	1577	0.630	1.272	1.138	11.8
9	1791	0.715	1.418	1.284	10.4
10	2054	0.820	1.550	1.462	6.0
11	2237	0.893	1.711	1.586	7.9
12	2672	1.067	2.024	1.878	7.8
13	3134	1.251	2.349	2.184	7.6
14	3642	1.454	2.718	2.520	7.9
15	4058	1.620	2.950	2.792	5.7
16	4483	1.790	3.256	3.070	6.1
17	4921	1.964	3.541	3.353	5.6
18	5363	2.141	3.841	3.639	5.6
19	5841	2.332	4.192	3.947	6.2
20	6275	2.505	4.434	4.225	5.0
21	7182	2.867	5.019	4.802	4.5
22	8083	3.227	5.670	5.374	5.5
23	8775	3.503	6.065	5.809	4.4

Table C.19: Test Results of Pair PZN0102

Run No.	P kPa	T_m °C	ΔT °C	k_s W/mK	Q W	h_c W/m²K
1	484	125.5	35.1	19.7	14.8	858
2	588	124.8	31.2	19.7	15.0	982
3	737	122.8	27.3	19.7	15.2	1132
4	862	121.3	24.8	19.7	15.2	1247
5	998	119.7	22.8	19.7	15.2	1361
6	1138	118.6	20.8	19.7	15.3	1501
7	1350	116.8	18.7	19.6	15.4	1673
8	1578	115.8	16.9	19.6	15.3	1849
9	1821	115.0	15.1	19.6	15.3	2055
10	2027	114.7	14.0	19.6	15.2	2212
11	2250	113.9	12.6	19.6	15.2	2450
12	2692	112.5	11.0	19.6	15.2	2822
13	3142	110.9	9.3	19.6	15.2	3325
14	3583	110.4	8.3	19.6	15.1	3706
15	4028	108.9	7.5	19.6	15.2	4096
16	4510	108.1	6.9	19.6	15.1	4439
17	4961	107.5	6.2	19.6	15.1	4929
18	5379	107.4	5.9	19.6	15.1	5226
19	5848	107.5	5.4	19.6	15.0	5643
20	6187	158.0	7.1	20.0	23.0	6557
21	7142	156.9	6.2	20.0	23.0	7523
22	8033	156.8	5.7	20.0	23.0	8267
23	8749	155.9	5.2	20.0	23.0	8931

Table C.20: Test Results of Pair PZN0304

Run No.	P kPa	T_m °C	ΔT °C	k_s W/mK	Q W	h_c W/m²K
1	462	158.9	58.4	20.0	18.8	656
2	596	158.6	52.4	20.0	19.3	749
3	727	156.2	46.1	20.0	19.4	856
4	861	155.2	42.0	20.0	19.5	944
5	1000	153.5	38.4	20.0	19.6	1038
6	1136	152.3	35.7	20.0	19.7	1124
7	1366	150.5	31.7	19.9	19.7	1262
8	1578	149.1	28.5	19.9	19.6	1402
9	1813	147.9	25.5	19.9	19.7	1571
10	2076	148.8	22.9	19.9	20.1	1793
11	2332	150.6	21.5	19.9	20.6	1949
12	2666	165.4	20.3	20.1	23.2	2325
13	3133	163.9	17.7	20.1	23.1	2659
14	3632	163.3	15.6	20.1	23.1	3026
15	4050	162.0	13.8	20.0	23.1	3410
16	4457	169.4	13.1	20.1	24.3	3765
17	4923	168.6	12.1	20.1	24.3	4088
18	5401	167.7	11.3	20.1	24.3	4396
19	5872	166.4	10.3	20.1	24.3	4795
20	6287	165.5	9.6	20.1	24.3	5175
21	7208	165.9	8.5	20.1	24.2	5799
22	8059	166.5	7.7	20.1	24.3	6453
23	8738	164.8	7.1	20.1	24.3	7007

Table C.21: Test Results of Pair PZN0506

Run No.	P kPa	T_m °C	ΔT °C	k_s W/mk	Q W	h_c W/m²K
1	409	165.4	102.4	20.1	16.5	327
2	583	161.5	88.0	20.0	17.1	395
3	739	158.2	77.6	20.0	17.4	457
4	857	155.6	69.9	20.0	17.5	511
5	1003	153.6	63.2	20.0	17.7	572
6	1153	152.0	57.8	20.0	17.8	628
7	1370	151.6	51.4	20.0	18.0	714
8	1574	149.5	46.3	19.9	18.3	803
9	1873	149.5	40.6	19.9	18.3	917
10	2021	149.5	37.9	19.9	18.3	982
11	2262	145.1	35.1	19.9	18.5	1077
12	2706	142.6	29.5	19.9	18.7	1287
13	3067	158.7	28.9	20.0	21.1	1487
14	3580	156.2	25.7	20.0	21.3	1687
15	4073	154.9	22.8	20.0	21.4	1918
16	4482	153.4	20.6	20.0	21.3	2105
17	4966	153.6	18.8	20.0	21.4	2318
18	5401	153.3	17.4	20.0	21.3	2492
19	5910	160.4	17.0	20.0	22.5	2693
20	6262	160.4	16.1	20.0	22.7	2881
21	7163	159.5	14.3	20.0	22.9	3258
22	8065	158.0	12.6	20.0	22.8	3678
23	8785	157.3	11.7	20.0	22.6	3943

Table C.22: Test Results of Pair PZN0708

Run No.	P kPa	T_m °C	ΔT °C	k_s W/mK	Q W	h_c W/m²K
1	429	172.9	122.1	20.1	15.9	265
2	586	168.7	107.4	20.1	16.4	310
3	738	166.0	96.7	20.1	16.9	357
4	868	163.3	87.2	20.0	17.2	402
5	999	160.8	78.9	20.0	17.4	450
6	1146	158.7	72.1	20.0	17.7	499
7	1373	156.9	63.2	20.0	18.0	580
8	1581	155.8	57.2	20.0	18.4	656
9	1795	152.9	52.2	20.0	18.5	724
10	2013	157.8	49.6	20.0	19.5	802
11	2252	156.2	45.6	20.0	19.5	873
12	2728	154.6	38.3	20.0	19.9	1059
13	3165	152.5	33.4	20.0	19.9	1216
14	3581	151.8	29.8	20.0	20.0	1369
15	4026	150.1	26.9	19.9	20.3	1541
16	4518	148.7	24.5	19.9	20.2	1684
17	4925	146.8	22.2	19.9	20.1	1841
18	5429	146.6	20.3	19.9	20.2	2018
19	5856	156.8	20.2	20.0	21.7	2191
20	6353	155.8	19.2	20.0	21.9	2325
21	7151	154.2	16.8	20.0	21.7	2623
22	8102	154.5	14.9	20.0	21.8	2968
23	8851	153.7	13.6	20.0	21.7	3248

Table C.23: Comparison Between Theory and Test Results of Pair RZN0102

Run No.	P kPa	10^3 P/H_c	10^3 C_c Test	10^3 C_c Theory	% Diff.
1	484	0.154	0.483	0.299	61.5
2	588	0.188	0.553	0.361	53.2
3	737	0.235	0.638	0.446	43.1
4	862	0.275	0.703	0.518	35.7
5	998	0.319	0.768	0.596	28.9
6	1138	0.363	0.848	0.674	25.8
7	1350	0.431	0.946	0.794	19.1
8	1578	0.504	1.046	0.921	13.6
9	1821	0.581	1.163	1.054	10.3
10	2027	0.647	1.251	1.168	7.1
11	2250	0.718	1.386	1.289	7.5
12	2692	0.859	1.599	1.528	4.7
13	3142	1.003	1.884	1.771	6.4
14	3583	1.144	2.100	2.006	4.7
15	4028	1.286	2.324	2.242	3.7
16	4510	1.439	2.518	2.495	0.9
17	4961	1.583	2.798	2.732	2.4
18	5379	1.717	2.966	2.951	0.5
19	5848	1.867	3.203	3.195	0.3
20	6187	1.975	3.640	3.371	8.0
21	7142	2.280	4.180	3.863	8.2
22	8033	2.564	4.594	4.319	6.4
23	8749	2.792	4.963	4.683	6.0

Table C.24: Comparison Between Theory and Test Results of Pair PZN0304

Run No.	P kPa	10^3 P/H_c	10^3 C_c Test	10^3 C_c Theory	% Diff.
1	462	0.161	0.507	0.311	63.0
2	596	0.208	0.579	0.397	45.8
3	727	0.253	0.662	0.478	38.5
4	861	0.300	0.730	0.563	29.7
5	1000	0.349	0.804	0.650	23.7
6	1136	0.396	0.870	0.732	18.9
7	1366	0.476	0.978	0.872	12.2
8	1578	0.550	1.087	1.001	8.6
9	1813	0.632	1.219	1.142	6.7
10	2076	0.724	1.391	1.299	7.1
11	2332	0.813	1.511	1.450	4.2
12	2666	0.929	1.791	1.646	8.8
13	3133	1.092	2.050	1.920	6.8
14	3632	1.266	2.333	2.209	5.6
15	4050	1.412	2.630	2.450	7.4
16	4457	1.554	2.895	2.684	7.9
17	4923	1.716	3.145	2.949	6.7
18	5401	1.883	3.382	3.221	5.0
19	5872	2.047	3.693	3.487	5.9
20	6287	2.192	3.986	3.721	7.1
21	7208	2.513	4.466	4.237	5.4
22	8059	2.809	4.967	4.710	5.5
23	8738	3.046	5.399	5.087	6.1

Table C.25: Comparison Between Theory and Test Results of Pair PZN0506

Run No.	P kPa	10^3 P/H_c	10^3 C_c Test	10^3 C_c Theory	% Diff.
1	409	0.174	0.531	0.335	58.5
2	583	0.248	0.642	0.470	36.6
3	739	0.314	0.774	0.587	26.7
4	857	0.364	0.832	0.676	23.1
5	1003	0.427	0.932	0.787	18.4
6	1153	0.490	1.025	0.897	14.3
7	1370	0.583	1.165	1.058	10.1
8	1574	0.669	1.311	1.205	8.8
9	1873	0.797	1.498	1.423	5.3
10	2021	0.860	1.604	1.530	4.8
11	2262	0.962	1.762	1.702	3.5
12	2706	1.151	2.108	2.018	4.5
13	3067	1.304	2.420	2.272	6.5
14	3580	1.523	2.747	2.648	3.7
15	4073	1.732	3.125	2.975	5.0
16	4482	1.906	3.433	3.259	5.3
17	4966	2.112	3.778	3.592	5.2
18	5401	2.297	4.064	3.890	4.5
19	5910	2.513	4.378	4.237	3.3
20	6262	2.663	4.682	4.477	4.6
21	7163	3.046	5.297	5.087	4.1
22	8065	3.430	5.986	5.694	5.1
23	8785	3.736	6.417	6.176	3.9

Table C.26: Comparison Between Theory and Test Results of Pair PZN0708

Run No.	P kPa	10^3 P/H_c	10^3 C_c Test	10^3 C_c Theory	% Diff.
1	429	0.198	0.580	0.379	53.0
2	586	0.270	0.680	0.509	33.6
3	738	0.340	0.783	0.634	23.5
4	868	0.400	0.883	0.739	19.5
5	999	0.461	0.990	0.846	17.0
6	1146	0.528	1.098	0.963	14.0
7	1373	0.633	1.277	1.144	11.6
8	1581	0.729	1.446	1.308	10.6
9	1795	0.828	1.597	1.476	8.2
10	2013	0.928	1.766	1.645	7.4
11	2252	1.038	1.923	1.829	5.1
12	2728	1.358	2.335	2.196	6.3
13	3165	1.459	2.683	2.528	6.1
14	3581	1.651	3.022	2.843	6.3
15	4026	1.856	3.405	3.177	7.2
16	4518	2.083	3.723	3.545	5.0
17	4925	2.271	4.072	3.849	5.8
18	5429	2.503	4.464	4.221	5.8
19	5856	2.700	4.827	4.536	6.4
20	6353	2.929	5.122	4.901	4.5
21	7151	3.297	5.785	5.484	5.5
22	8102	3.735	6.545	6.174	6.0
23	8851	4.081	7.163	6.716	6.7

Table C.27: Test Results of Pair PZ40102

Run No.	P kPa	T_m °C	ΔT °C	k_s W/mK	Q W	h_c W/m²K
1	419	171.4	67.9	16.6	17.2	517
2	594	168.4	53.7	16.6	18.0	682
3	724	165.7	44.5	16.6	18.2	832
4	893	164.5	37.8	16.6	18.4	989
5	1007	163.6	33.6	16.6	18.5	1123
6	1145	162.3	30.2	16.6	18.6	1253
7	1359	161.9	25.6	16.6	18.8	1492
8	1580	160.5	22.3	16.6	19.0	1729
9	1826	159.4	20.0	16.6	19.1	1942
10	2031	158.4	17.9	16.6	19.1	2176
11	2286	158.0	16.2	16.6	19.1	2397
12	2688	156.5	13.7	16.5	19.1	2831
13	3171	157.0	12.0	16.5	19.2	3272
14	3591	156.5	10.5	16.5	19.3	3735
15	4026	155.1	9.3	16.5	19.3	4194
16	4503	154.4	8.4	16.5	19.3	4682
17	4964	154.2	7.5	16.5	19.2	5216
18	5397	178.6	8.1	16.7	22.6	5669
19	5801	176.7	7.6	16.7	22.5	6044
20	6321	175.5	7.0	16.7	22.6	6542
21	7169	175.6	6.1	16.7	22.5	7522
22	8094	176.0	5.4	16.7	22.4	8411
23	8816	174.6	5.0	16.7	22.3	9144

Table C.28: Test Results of Pair PZ40304

Run No.	P kPa	T_m °C	ΔT °C	k_s W/mK	Q W	h_c W/m²K
1	436	175.1	76.7	16.7	17.0	450
2	598	172.1	62.0	16.7	17.6	577
3	742	170.1	53.4	16.6	17.9	682
4	877	167.4	47.1	16.6	18.0	778
5	1007	166.2	42.3	16.6	18.1	870
6	1097	170.5	40.9	16.6	18.8	938
7	1356	168.7	35.2	16.6	19.1	1107
8	1574	167.6	31.3	16.6	19.1	1241
9	1790	166.1	28.0	16.6	19.2	1398
10	2011	164.4	25.4	16.6	19.2	1546
11	2243	177.3	24.7	16.7	20.9	1722
12	2674	175.7	21.1	16.7	21.0	2024
13	3141	175.0	18.0	16.7	21.1	2391
14	3590	173.0	16.2	16.7	21.1	2655
15	4022	172.3	14.5	16.7	21.1	2957
16	4536	171.9	13.0	16.7	21.2	3313
17	4928	171.1	12.0	16.7	21.2	3614
18	5361	170.9	10.9	16.7	21.3	3964
19	5836	170.0	10.0	16.6	21.3	4346
20	6275	170.1	9.6	16.6	21.3	4533
21	7235	169.2	7.6	16.6	21.3	5679
22	8112	168.4	7.5	16.6	21.3	5795
23	8764	168.9	7.1	16.6	21.3	6163

Table C.29: Test Results of Pair PZ40506

Run No.	P kPa	T_m °C	ΔT °C	k_s W/mK	Q W	h_c W/m²K
1	415	167.4	77.2	16.6	16.4	432
2	602	166.4	65.3	16.6	16.9	526
3	742	165.5	57.3	16.6	17.3	614
4	882	162.4	50.2	16.6	17.2	699
5	1002	162.6	45.8	16.6	17.6	783
6	1138	161.6	41.8	16.6	17.7	862
7	1362	161.7	37.1	16.6	18.1	992
8	1569	159.6	33.2	16.6	18.1	1112
9	1813	159.2	29.7	16.6	18.4	1256
10	1986	161.4	28.1	16.6	18.8	1359
11	2245	161.1	25.6	16.6	18.9	1504
12	2716	160.0	21.9	16.6	19.1	1775
13	3153	158.0	19.1	16.6	18.9	2023
14	3646	160.6	17.0	16.6	19.4	2323
15	4015	161.3	15.7	16.6	19.7	2549
16	4523	161.5	14.3	16.6	19.8	2822
17	4949	160.6	13.1	16.6	19.8	3080
18	5376	161.5	12.2	16.6	19.9	3337
19	5794	160.3	11.2	16.6	20.0	3619
20	6248	159.5	10.4	16.6	19.8	3893
21	7256	160.4	9.2	16.6	20.0	4452
22	8055	158.6	8.2	16.6	19.9	4958
23	8775	157.1	7.5	16.6	19.8	5419

Table C.30: Test Results of Pair PZ40708

Run No.	P kPa	T_m °C	ΔT °C	k_s W/mK	Q W	h_c W/m²K
1	442	167.6	99.6	16.6	14.8	303
2	606	165.2	88.5	16.6	15.3	352
3	733	163.0	78.5	16.6	15.5	403
4	871	161.1	70.4	16.6	15.9	461
5	1014	160.3	64.2	16.6	16.1	510
6	1206	165.8	55.9	16.6	17.4	634
7	1367	166.4	53.4	16.6	17.6	673
8	1574	165.9	48.6	16.6	17.8	746
9	1786	164.3	43.7	16.6	18.0	839
10	2017	162.6	39.6	16.6	19.1	934
11	2214	162.8	36.9	16.6	18.5	1020
12	2681	160.8	31.5	16.6	18.6	1205
13	3116	159.4	27.5	16.6	18.7	1382
14	3587	158.6	24.5	16.6	18.8	1565
15	4079	159.9	22.2	16.6	19.1	1758
16	4488	159.6	20.4	16.6	19.2	1912
17	4960	158.8	18.7	16.6	19.2	2087
18	5370	158.4	17.4	16.6	19.3	2257
19	5861	157.6	16.1	16.6	19.4	2446
20	6267	156.9	15.2	16.5	19.3	2590
21	7150	155.5	13.3	16.5	19.3	2949
22	8032	155.0	11.9	16.5	19.4	3326
23	8852	154.8	10.8	16.5	19.3	3644

Table C.31: Comparison Between Theory and Test Results of Pair PZ40102

Run No.	P kPa	10^3 P/H_c	10^3 C_c Test	10^3 C_c Theory	% Diff.
1	419	0.181	0.386	0.348	10.9
2	594	0.256	0.510	0.484	5.4
3	724	0.312	0.623	0.584	6.7
4	893	0.385	0.740	0.713	3.8
5	1007	0.434	0.841	0.799	5.3
6	1145	0.494	0.939	0.904	3.9
7	1359	0.586	1.118	1.063	5.2
8	1580	0.681	1.296	1.226	5.7
9	1826	0.787	1.457	1.406	3.6
10	2031	0.875	1.633	1.555	5.0
11	2286	0.985	1.799	1.741	3.3
12	2688	1.159	2.126	2.031	4.7
13	3171	1.367	2.457	2.376	3.4
14	3591	1.548	2.805	2.674	4.9
15	4026	1.735	3.152	2.980	5.8
16	4503	1.941	3.518	3.315	6.1
17	4964	2.140	3.922	3.638	7.8
18	5397	2.326	4.219	3.937	7.2
19	5801	2.501	4.501	4.218	6.7
20	6321	2.725	4.875	4.576	6.5
21	7169	3.090	5.605	5.157	8.7
22	8094	3.489	6.271	5.787	8.4
23	8816	3.800	6.818	6.276	8.6

Table C.32: Comparison Between Theory and Test Results of Pair PZ40304

Run No.	P kPa	10^3 P/H_c	10^3 C_c Test	10^3 C_c Theory	% Diff.
1	436	0.199	0.502	0.381	31.8
2	598	0.273	0.664	0.514	29.2
3	742	0.339	0.762	0.632	20.6
4	877	0.401	0.870	0.741	17.4
5	1007	0.460	0.974	0.844	15.4
6	1097	0.501	1.048	0.916	14.4
7	1356	0.620	1.237	1.121	10.3
8	1574	0.719	1.388	1.291	7.5
9	1790	0.818	1.565	1.459	7.3
10	2011	0.919	1.732	1.630	6.3
11	2243	1.025	1.919	1.808	6.1
12	2674	1.222	2.256	2.136	5.6
13	3141	1.435	2.666	2.488	7.1
14	3590	1.641	2.963	2.827	4.8
15	4022	1.838	3.300	3.148	4.8
16	4536	2.073	3.700	3.529	4.8
17	4928	2.252	4.036	3.818	5.7
18	5361	2.450	4.427	4.136	7.0
19	5836	2.667	4.857	4.484	8.3
20	6275	2.868	5.066	4.804	5.4
21	7235	3.306	6.346	5.499	15.4
22	8112	3.707	6.480	6.130	5.7
23	8764	4.005	6.891	6.598	4.4

Table C.33: Comparison Between Theory and Test Results of Pair PZ40506

Run No.	P kPa	10^3 P/H_c	10^3 C_c Test	10^3 C_c Theory	% Diff.
1	415	0.197	0.633	0.377	67.9
2	602	0.286	0.771	0.538	43.3
3	742	0.353	0.900	0.657	37.0
4	882	0.419	1.026	0.773	32.7
5	1002	0.476	1.150	0.872	31.9
6	1138	0.541	1.266	0.985	28.5
7	1362	0.647	1.456	1.168	24.7
8	1569	0.746	1.635	1.337	22.3
9	1813	0.862	1.846	1.533	20.4
10	1986	0.944	1.996	1.672	19.4
11	2245	1.067	2.209	1.878	17.6
12	2716	1.291	2.609	2.251	15.9
13	3153	1.498	2.975	2.592	14.8
14	3646	1.733	3.413	2.977	14.6
15	4015	1.908	3.745	3.262	14.8
16	4523	2.149	4.143	3.652	13.4
17	4949	2.352	4.525	3.979	13.7
18	5376	2.555	4.902	4.305	13.9
19	5794	2.754	5.317	4.622	15.0
20	6248	2.969	5.722	4.965	15.3
21	7256	3.448	6.540	5.723	14.3
22	8055	3.828	7.292	6.320	15.4
23	8775	4.170	7.975	6.856	16.3

Table C.34: Comparison Between Theory and Test Results of Pair PZ40708

Run No.	P kPa	10^3 P/H_c	10^3 C_c Test	10^3 C_c Theory	% Diff.
1	442	0.224	0.698	0.426	63.8
2	606	0.307	0.811	0.575	41.0
3	733	0.372	0.929	0.690	34.6
4	871	0.442	1.064	0.813	30.9
5	1014	0.515	1.177	0.940	25.2
6	1206	0.612	1.461	1.107	32.0
7	1367	0.694	1.550	1.248	24.2
8	1574	0.799	1.719	1.423	20.8
9	1786	0.906	1.933	1.608	20.2
10	2017	1.023	2.154	1.804	19.4
11	2214	1.123	2.353	1.971	19.4
12	2681	1.360	2.781	2.365	17.6
13	3116	1.581	3.192	2.728	17.0
14	3587	1.820	3.616	3.119	15.9
15	4079	2.070	4.060	3.524	15.2
16	4488	2.277	4.415	3.858	14.4
17	4960	2.517	4.823	4.244	13.6
18	5370	2.725	5.212	4.576	13.9
19	5861	2.974	5.649	4.973	13.6
20	6267	3.180	5.988	5.299	13.0
21	7150	3.628	6.819	6.006	13.5
22	8032	4.075	7.695	6.707	14.7
23	8852	4.492	8.431	7.357	14.6

GAS RESULTS

Table C.35: Test Results of Pair PSS0910

Run No.	P kPa	T_m °C	ΔT °C	k_s W/mK	Q W	P_g torr	h_j W/m²K
1	459	166.8	19.3	19.5	21.9	574	2303
2	597	165.7	19.0	19.5	21.9	568	2346
3	734	165.3	18.3	19.5	21.9	565	2427
4	872	164.2	17.7	19.5	21.9	568	2514
5	1008	163.6	17.3	19.5	21.8	567	2565
6	1142	163.0	16.8	19.5	21.9	567	2665
7	1382	163.9	16.1	19.5	22.2	564	2802
8	1581	163.2	15.6	19.5	22.2	562	2896
9	1805	162.7	14.9	19.5	22.2	567	3034
10	2021	161.5	14.4	19.5	22.1	568	3119
11	2245	160.9	13.9	19.5	22.0	570	3238
12	2688	160.2	12.9	19.4	22.0	568	3470
13	3133	159.5	12.2	19.4	22.0	564	3687
14	3587	159.2	11.5	19.4	22.0	565	3892
15	4047	158.2	11.0	19.4	21.9	567	4072
16	4472	157.8	10.4	19.4	21.9	567	4261
17	4958	164.6	10.3	19.5	23.0	572	4568
18	5368	164.6	9.9	19.5	23.1	569	4748
19	5801	163.7	9.5	19.5	23.0	568	4915
20	6262	163.7	9.1	19.5	23.0	567	5144
21	7148	163.2	8.5	19.5	23.0	570	5501
22	8039	162.9	8.0	19.5	23.0	570	5888
23	8769	162.6	7.5	19.5	23.0	568	6219

Table C.36: Comparison Between Theory and Test Results of Pair PSS0910

Run No.	10^3 P/H_c	10^3 C_j Test	10^3 C_c Theory	10^3 C_g Theory	10^3 C_j Theory	% Diff.
1	0.165	4.353	0.320	3.491	3.810	14.2
2	0.215	4.439	0.411	3.571	3.982	11.5
3	0.265	4.592	0.500	3.641	4.140	10.9
4	0.314	4.762	0.588	3.701	4.289	11.0
5	0.364	4.861	0.675	3.753	4.428	9.8
6	0.412	5.053	0.760	3.801	4.561	10.8
7	0.498	5.307	0.911	3.882	4.793	10.7
8	0.570	5.488	1.035	3.938	4.973	10.4
9	0.651	5.753	1.174	3.998	5.172	11.2
10	0.729	5.920	1.307	4.048	5.355	10.6
11	0.809	6.149	1.444	4.098	5.542	11.0
12	0.969	6.593	1.714	4.188	5.902	11.7
13	1.130	7.009	1.983	4.267	6.250	12.1
14	1.293	7.398	2.255	4.343	6.598	12.1
15	1.459	7.749	2.528	4.412	6.940	11.7
16	1.612	8.112	2.780	4.473	7.253	11.8
17	1.788	8.648	3.066	4.566	7.632	13.9
18	1.936	8.989	3.307	4.618	7.925	13.4
19	2.091	9.314	3.559	4.668	8.227	13.2
20	2.258	9.748	3.827	4.721	8.549	14.0
21	2.577	10.425	4.340	4.819	9.159	13.8
22	2.898	11.164	4.853	4.908	9.761	14.4
23	3.162	11.792	5.270	4.975	10.245	15.1

Table C.37: Geometric and Thermophysical Parameters of Pair PSS0910

Run No.	10^3 P/H_c	Y/σ	P_g torr	10^2 M/σ	YH
1	0.165	3.582	574	9.31	38.5
2	0.215	3.513	568	9.39	37.4
3	0.265	3.458	565	9.42	36.7
4	0.314	3.412	568	9.35	36.5
5	0.364	3.373	567	9.36	36.0
6	0.412	3.339	567	9.34	35.7
7	0.498	3.286	564	9.41	34.9
8	0.570	3.248	562	9.43	34.4
9	0.651	3.211	567	9.33	34.4
10	0.729	3.179	568	9.29	34.2
11	0.809	3.149	570	9.25	34.0
12	0.969	3.096	568	9.26	33.4
13	1.130	3.051	564	9.32	32.7
14	1.293	3.011	565	9.30	32.4
15	1.459	2.975	567	9.25	32.2
16	1.612	2.945	567	9.23	31.9
17	1.788	2.913	572	9.30	31.3
18	1.936	2.888	569	9.34	30.9
19	2.091	2.864	568	9.34	30.7
20	2.258	2.840	567	9.36	30.4
21	2.577	2.799	570	9.29	30.1
22	2.898	2.761	570	9.29	29.7
23	3.162	2.733	568	9.32	29.3

Table C.38: Test Results of Pair PSS1112

Run No.	P kPa	T_m °C	ΔT °C	k_s W/mK	Q W	P_g torr	h_j W/m²K
$1H_e$	470	201.6	19.9	20.1	29.5	41.3	3016
$2H_e$	593	200.6	19.7	20.1	29.4	41.3	3050
$3H_e$	743	200.3	19.7	20.1	29.4	39.8	3038
$4H_e$	869	200.2	19.0	20.1	29.4	40.8	3152
$5H_e$	1001	200.8	19.1	20.1	29.3	39.9	3133
$6H_e$	1113	199.2	18.4	20.0	29.4	40.7	3258
$7H_e$	1352	198.7	17.7	20.0	29.4	40.6	3375
$8H_e$	1585	198.7	17.4	20.0	29.4	40.1	3454
$9H_e$	1801	197.8	16.8	20.0	29.4	40.7	3556
$10H_e$	2025	197.2	16.2	20.0	29.4	41.2	3684
$11H_e$	2243	196.7	15.9	20.0	29.4	41.3	3757
$12H_e$	2693	196.4	15.0	20.0	29.4	41.3	3990
$13H_e$	3150	196.1	14.4	20.0	29.5	41.0	4183
$14H_e$	3590	196.6	14.1	20.0	29.5	39.7	4272
$15H_e$	4039	196.2	13.5	20.0	29.4	40.1	4460
$16H_e$	4479	196.1	13.1	20.0	29.4	39.5	4587
$17H_e$	4935	195.6	12.5	20.0	29.5	39.4	4790
$18H_e$	5415	194.9	12.1	20.0	29.4	39.5	4952
$19H_e$	5808	194.1	11.5	20.0	29.3	40.6	5175
19V	5879	210.8	27.3	20.2	29.2	--	2181

(continued...)

Table C.38: Test Results of Pair PSS1112 (continued...)

Run No.	p kPa	T_m °C	ΔT °C	k_s W/mK	Q W	P_g torr	h_j W/m²K
20V	6251	210.1	27.0	20.2	29.1	--	2195
$20N_2$	6315	210.2	15.3	20.2	30.6	40.4	4074
$20H_e$	6327	211.3	11.1	20.2	32.6	40.2	5981
21V	7181	207.3	23.6	20.2	29.1	--	2514
$21N_2$	7215	213.5	14.4	20.3	31.3	40.5	4413
$21H_e$	7219	209.7	10.3	20.2	32.3	40.5	6417
22V	8026	204.3	21.1	20.1	28.7	--	2780
$22N_2$	8009	221.3	13.8	20.4	32.8	40.2	4829
$22H_e$	8167	214.8	9.9	20.3	33.5	40.4	6882
23V	8805	222.5	20.5	20.4	31.8	--	3156
$23N_2$	8875	220.2	12.9	20.4	32.8	40.4	5174
$23H_e$	8829	216.0	9.6	20.3	33.8	40.2	7202

Table C.39: Comparison Between Theory and Test Results of Pair PSS1112

Run No.	10^3 P/H_c	10^3 C_j Test	10^3 C_c Theory	10^3 C_g Theory	10^3 C_j Theory	% Diff.
$1H_e$	0.170	5.581	0.327	2.938	3.266	70.9
$2H_e$	0.214	5.648	0.408	2.952	3.361	68.1
$3H_e$	0.268	5.627	0.506	2.873	3.378	66.5
$4H_e$	0.314	5.839	0.587	2.939	3.526	65.6
$5H_e$	0.361	5.801	0.671	2.882	3.553	63.3
$6H_e$	0.402	6.040	0.742	2.945	3.687	63.8
$7H_e$	0.488	6.259	0.893	2.948	3.841	63.0
$8H_e$	0.572	6.405	1.039	2.922	3.960	61.7
$9H_e$	0.650	6.597	1.173	2.972	4.145	59.2
$10H_e$	0.731	6.839	1.311	3.007	4.318	58.4
$11H_e$	0.810	6.977	1.445	3.019	4.560	56.3
$12H_e$	0.972	7.411	1.719	3.032	4.751	56.0
$13H_e$	1.137	7.773	1.995	3.016	5.011	55.1
$14H_e$	1.296	7.936	2.258	2.935	5.194	52.8
$15H_e$	1.458	8.286	2.526	2.971	5.497	50.7
$16H_e$	1.617	8.523	2.787	2.934	5.721	49.0
$17H_e$	1.781	8.903	3.056	2.933	5.989	48.7
$18H_e$	1.955	9.208	3.337	2.951	6.289	46.4
$19H_e$	2.097	9.629	3.568	3.029	6.597	46.0
19V	2.122	4.007	3.609	---	3.609	11.04

(continued...)

Table C.39: Comparison Between Theory and Test Results of Pair PSS1112 (continued...)

Run No.	10^3 P/H_c	10^3 C_j Test	10^3 C_c Theory	10^3 C_g Theory	10^3 C_j Theory	% Diff.
20V	2.257	4.036	3.825	---	3.825	5.5
$20N_2$	2.280	7.489	3.863	3.005	6.868	9.0
$20H_e$	2.284	10.986	3.869	2.912	6.782	62.0
21V	2.592	4.632	4.364	---	4.364	6.1
$21N_2$	2.604	8.093	4.384	3.041	7.425	9.0
$21H_e$	2.606	11.800	4.386	2.942	7.328	61.0
22V	2.897	5.134	4.851	---	4.851	5.8
$22N_2$	2.891	8.804	4.841	3.058	7.899	11.5
$22H_e$	2.948	12.607	4.932	2.910	7.842	60.8
23V	3.179	5.749	5.297	---	5.297	8.5
$23N_2$	3.161	9.440	5.269	3.083	8.351	13.0
$23H_e$	3.187	13.181	5.311	2.897	8.208	60.6

Table C.40: Comparison Between Helium Measured and Predicted Conductances of Pair PSS1112

Run No.	10^3 P/H_c	10^3 C_j Test	10^3 C_c Test	10^3 C_g Test	10^3 C_g Theory	% Diff.
1	0.170	5.581	0.348	5.233	2.938	78.1
2	0.214	5.648	0.435	5.213	2.952	76.6
3	0.268	5.627	0.539	5.088	2.873	77.1
4	0.314	5.839	0.625	5.214	2.939	77.4
5	0.361	5.801	0.715	5.086	2.882	76.5
6	0.402	6.040	0.790	5.250	2.945	78.3
7	0.488	6.259	0.951	5.308	2.948	80.1
8	0.572	6.405	1.107	5.298	2.922	81.3
9	0.650	6.597	1.249	5.348	2.972	80.0
10	0.731	6.839	1.396	5.443	3.007	81.0
11	0.810	6.977	1.539	5.438	3.019	80.1
12	0.972	7.411	1.831	5.580	3.032	84.0
13	1.137	7.773	2.125	5.648	3.016	87.3
14	1.296	7.936	2.405	5.531	2.935	88.4
15	1.458	8.286	2.690	5.596	2.971	88.3
16	1.617	8.523	2.968	5.555	2.934	89.3
17	1.781	8.903	3.255	5.648	2.933	92.6
18	1.955	9.208	3.554	5.654	2.951	91.6
19	2.097	9.629	3.800	5.829	3.029	92.4
20	2.284	10.986	4.082	6.904	2.912	137.1
21	2.606	11.800	4.655	7.145	2.942	142.9
22	2.948	12.607	5.220	7.387	2.910	153.8
23	3.187	13.181	5.764	7.417	2.897	156.0

Table C.41: Predicted Helium Accommodation Coefficient Values for Pair PSS1112

Run No.	10^3 C_g Test	Y/σ	k_s W/mK	T_m °C	P_g torr	α_i
1	5.233	3.575	20.1	201.6	41.3	0.56
2	5.213	3.514	20.1	200.6	41.3	0.55
3	5.088	3.455	20.1	200.3	39.8	0.55
4	5.214	3.413	20.1	200.2	40.8	0.55
5	5.086	3.374	20.1	200.8	39.9	0.55
6	5.250	3.345	20.0	199.2	40.7	0.55
7	5.308	3.292	20.0	198.7	40.6	0.56
8	5.298	3.247	20.0	198.7	40.1	0.56
9	5.348	3.211	20.0	197.8	40.7	0.56
10	5.443	3.178	20.0	197.2	41.2	0.56
11	5.438	3.148	20.0	196.7	41.3	0.56
12	5.580	3.095	20.0	196.4	41.3	0.57
13	5.648	3.049	20.0	196.1	41.0	0.58
14	5.531	3.010	20.0	196.6	39.7	0.58
15	5.596	2.975	20.0	196.2	40.1	0.58
16	5.555	2.944	20.0	196.1	39.5	0.58
17	5.648	2.914	20.0	195.6	39.4	0.59
18	5.654	2.885	20.0	194.9	39.5	0.58
19	5.829	2.864	20.0	194.1	40.6	0.59
20	6.904	2.837	20.2	211.3	40.2	0.70
21	7.145	2.795	20.2	209.7	40.5	0.71
22	7.387	2.756	20.3	214.8	40.4	0.73
23	7.417	2.731	20.3	216.0	40.2	0.74

Table C.42: Geometric and Thermophysical Parameters of Pair PSS1112

Run No.	10^3 P/H_c	Y/σ	P_g torr	M/σ	Y/H
$1H_e$	0.170	3.575	41.3	20.1	0.18
$2H_e$	0.214	3.514	41.3	20.0	0.18
$3H_e$	0.268	3.455	39.8	20.7	0.17
$4H_e$	0.314	3.413	40.8	20.2	0.17
$5H_e$	0.361	3.374	39.9	20.7	0.16
$6H_e$	0.402	3.345	40.7	20.2	0.17
$7H_e$	0.488	3.292	40.6	20.2	0.16
$8H_e$	0.572	3.247	40.1	20.5	0.16
$9H_e$	0.650	3.211	40.7	20.1	0.16
$10H_e$	0.731	3.178	41.2	19.9	0.16
$11H_e$	0.810	3.148	41.3	19.8	0.16
$12H_e$	0.972	3.095	41.3	19.7	0.16
$13H_e$	1.137	3.049	41.0	19.9	0.15
$14H_e$	1.296	3.010	39.7	20.6	0.15
$15H_e$	1.458	2.975	40.1	20.3	0.15
$16H_e$	1.617	2.944	39.5	20.6	0.14
$17H_e$	1.781	2.914	39.4	20.7	0.14
$18H_e$	1.955	2.885	39.5	20.5	0.14
$19H_e$	2.097	2.864	40.6	19.9	0.14
19V	2.122	2.860	--	--	--

(continued...)

Table C.42: Geometric and Thermophysical Parameters of Pair PSS1112 (continued...)

Run No.	10^3 P/H_c	Y/σ	P_g torr	M/σ	Y/H
20V	2.257	2.841	--	--	--
$20N_2$	2.280	2.837	40.4	1.5	1.93
$20H_e$	2.284	2.837	40.2	21.2	0.13
21V	2.592	2.797	--	--	--
$21N_2$	2.604	2.795	40.5	1.5	1.90
$21H_e$	2.606	2.795	40.5	21.0	0.13
22V	2.897	2.761	--	--	--
$22N_2$	2.891	2.762	40.2	1.5	1.84
$22H_e$	2.948	2.756	40.4	21.3	0.13
23V	3.179	2.731	--	--	--
$23N_2$	3.161	2.733	40.4	1.5	1.83
$23H_e$	3.187	2.731	40.2	21.5	0.13

Table C.43: Test Results of Pair PSS1314

Run No.	P kPa	T_m °C	ΔT °C	k_s W/mK	Q W	P_g torr	h_j W/m²K
1V	461	202.2	148.2	20.0	17.8	--	245
2V	577	199.4	129.2	20.0	18.8	--	296
3V	715	192.8	106.8	19.9	19.6	--	374
4V	853	188.9	93.6	19.9	20.0	--	436
5V	1035	184.4	81.8	19.8	20.3	--	505
6V	1146	182.4	76.0	19.8	20.5	--	548
$6N_2$	1164	187.4	26.1	19.9	25.7	40.8	2013
$6H_e$	1162	200.3	16.6	20.1	29.9	40.9	3655
7V	1365	189.7	59.5	19.9	23.0	--	787
$7N_2$	1366	195.7	24.7	20.0	27.4	40.5	2260
$7H_e$	1344	206.1	16.2	20.1	31.0	40.9	3897
8V	1577	185.0	50.0	19.8	23.1	--	943
$8N_2$	1572	193.5	22.8	20.0	27.2	40.8	2428
$8H_e$	1584	203.2	15.7	20.1	30.7	40.6	3984
$9H_e$	1790	203.2	15.7	20.1	30.6	40.6	3978
$9N_2$	1843	192.0	22.1	19.9	27.1	40.8	2497
9V	1877	182.2	47.1	19.8	23.0	--	994
10V	2014	181.5	46.1	19.8	22.9	--	1011
$10N_2$	2014	192.5	21.9	19.9	27.2	40.8	2524
$10H_e$	2094	208.5	15.5	20.2	31.6	40.8	4140

(continued...)

Table C.43: Test Results of Pair PSS1314 (continued...)

Run No.	P kPa	T_m °C	ΔT °C	k_s W/mK	Q W	P_g torr	h_j W/m²K
$11H_e$	2239	208.4	15.4	20.2	31.6	41.0	4190
$11N_2$	2340	198.2	21.8	20.0	28.2	41.1	2636
11V	2380	184.7	43.1	19.8	23.7	--	1122
12V	2676	241.3	49.4	20.7	32.7	--	1349
$12N_2$	2701	201.6	20.5	20.1	28.9	40.9	2880
$12H_e$	2722	204.5	14.1	20.1	31.2	40.8	4509
13V	3153	225.7	40.1	20.4	30.5	--	1548
$13N_2$	3181	219.9	20.7	20.4	32.0	40.7	3138
$13H_e$	3184	222.5	14.7	20.4	34.6	40.7	4786
$14H_e$	3584	223.7	14.2	20.3	34.8	40.6	4979
$14N_2$	3660	219.1	19.2	20.3	32.1	40.4	3399
14V	3738	229.2	36.0	20.5	31.7	--	1794
15V	4076	230.6	33.8	20.5	32.1	--	1931

Table C.44: Comparison Between Theory and Test Restuls of Pair PSS1314

Run No.	10^3 P/H_c	10^3 C_j Test	10^3 C_c Theory	10^3 C_g Theory	10^3 C_j Theory	% Diff.
1V	0.208	0.394	0.398	---	0.398	- 0.9
2V	0.260	0.477	0.492	---	0.492	- 2.9
3V	0.323	0.605	0.603	---	0.603	0.3
4V	0.385	0.707	0.713	---	0.713	- 0.8
5V	0.467	0.822	0.857	---	0.857	- 4.1
6V	0.517	0.895	0.944	---	0.944	- 5.2
$6N_2$	0.525	3.267	0.958	2.180	3.137	4.1
$6H_e$	0.525	5.874	0.957	2.530	3.486	68.5
7V	0.616	1.276	1.114	---	1.114	14.5
$7N_2$	0.617	3.645	1.115	2.201	3.316	9.9
$7H_e$	0.607	6.237	1.098	2.511	3.609	72.8
8V	0.712	1.535	1.278	---	1.278	20.1
$8N_2$	0.709	3.922	1.274	2.229	3.503	12.0
$8H_e$	0.715	6.389	1.283	2.514	3.798	68.2
$9H_e$	0.808	6.380	1.442	2.515	3.957	61.2
$9N_2$	0.832	4.038	1.483	2.253	3.736	8.1
9V	0.843	1.620	1.501	---	1.501	7.9
10V	0.909	1.649	1.612	---	1.612	2.3
$10N_2$	0.909	4.080	1.612	2.267	3.879	5.2
$10H_e$	0.925	6.613	1.640	2.506	4.145	59.5

(continued...)

Table C.44: Comparison Between Theory and Test Results of Pair PSS1314 (continued...)

Run No.	10^3 P/H_c	10^3 C_j Test	10^3 C_c Theory	10^3 C_g Theory	10^3 C_j Theory	% Diff.
$11H_e$	1.010	6.693	1.783	2.522	4.305	55.5
$11N_2$	1.056	4.244	1.860	2.282	4.142	2.5
11V	1.074	1.825	1.890	---	1.890	- 3.4
12V	1.208	2.103	2.112	---	2.112	- 0.4
$12N_2$	1.219	4.624	2.132	2.342	4.453	3.8
$12H_e$	1.228	7.224	2.147	2.537	4.684	54.2
13V	1.423	2.441	2.469	---	2.469	- 1.1
$13N_2$	1.436	4.970	2.490	2.351	4.841	2.7
$13H_e$	1.437	7.565	2.492	2.456	4.948	52.9
$14H_e$	1.618	7.863	2.788	2.445	5.233	50.2
$14N_2$	1.652	5.386	2.844	2.369	5.214	3.3
14V	1.687	2.822	2.902	---	2.902	- 2.8
15V	1.840	3.034	3.151	---	3.151	- 3.7

Table C.45: Comparison Between Nitrogen Measured and Predicted Conductances of Pair PSS1314

Run No.	10^3 P/H_c	10^3 C_j Test	10^3 C_c Test	10^3 C_g Test	10^3 C_g Theory	% Diff.
6	0.525	3.267	0.908	2.359	2.180	8.2
7	0.617	3.645	1.277	2.368	2.201	7.6
8	0.709	3.922	1.530	2.392	2.229	7.3
9	0.832	4.038	1.600	2.438	2.253	8.2
10	0.909	4.080	1.649	2.431	2.267	7.2
11	1.056	4.244	1.796	2.448	2.282	7.3
12	1.219	4.624	2.123	2.501	2.342	6.8
13	1.436	4.970	2.463	2.508	2.351	6.7
14	1.652	5.386	2.765	2.621	2.369	10.6

Table C.46: Comparison Between Helium Measured and Predicted Conductances of Pair PSS1314

Run No.	10^3 P/H_c	10^3 C_j Test	10^3 C_c Test	10^3 C_g Test	10^3 C_g Theory	% Diff.
6	0.525	5.874	0.907	4.967	2.530	96.3
7	0.607	6.237	1.257	4.980	2.511	98.3
8	0.715	6.389	1.540	4.849	2.514	92.9
9	0.808	6.380	1.556	4.824	2.515	91.8
10	0.925	6.613	1.677	4.936	2.506	97.0
11	1.010	6.693	1.721	4.972	2.522	97.1
12	1.228	7.224	2.138	5.086	2.537	100.5
13	1.437	7.565	2.464	5.101	2.456	107.7
14	1.618	7.863	2.711	5.152	2.445	110.7

Table C.47: Predicted Helium Accommodation Coefficient Values for Pair PSS1314

Run No.	10^3 C_g Test	Y/σ	k_s W/mK	T_m °C	P_g torr	α_i
6	4.967	3.271	20.1	200.3	40.9	0.61
7	4.980	3.231	20.1	206.1	40.9	0.61
8	4.849	3.184	20.1	203.2	40.6	0.60
9	4.824	3.149	20.1	203.2	40.6	0.59
10	4.936	3.110	20.2	208.5	40.8	0.61
11	4.972	3.084	20.2	208.4	41.0	0.61
12	5.086	3.026	20.1	204.5	40.8	0.62
13	5.101	2.979	20.4	222.5	40.7	0.62
14	5.152	2.943	20.3	223.7	40.6	0.63

Table C.48: Geometric and Thermophysical Parameters of Pair PSS1314

Run No.	10^3 P/H_c	Y/σ	P_g torr	M/σ	YH
1V	0.208	3.522	--	--	--
2V	0.260	3.463	--	--	--
3V	0.323	3.405	--	--	--
4V	0.385	3.357	--	--	--
5V	0.467	3.304	--	--	--
6V	0.517	3.275	--	--	--
$6N_2$	0.525	3.271	40.8	1.2	2.65
$6H_e$	0.525	3.271	40.9	18.0	0.18
7V	0.616	3.226	--	--	--
$7N_2$	0.617	3.226	40.5	1.3	2.55
$7H_e$	0.607	3.231	40.9	18.3	0.18
8V	0.712	3.185	--	--	--
$8N_2$	0.709	3.186	40.8	1.2	2.55
$8H_e$	0.715	3.184	40.6	18.3	0.17
$9H_e$	0.808	3.149	40.6	18.3	0.17
$9N_2$	0.832	3.141	40.8	1.2	2.50
9V	0.843	3.137	--	--	--
10V	0.909	3.115	--	--	--
$10N_2$	0.909	3.115	40.8	1.2	2.50
$10H_e$	0.925	3.110	40.8	18.5	0.17

(continued...)

Table C.48: Geometric and Thermophysical Parameters of Pair PSS1314 (continued...)

Run No.	10^3 P/H_c	Y/σ	P_g torr	M/σ	YH
$11H_e$	1.010	3.084	41.0	18.4	0.17
$11N_2$	1.056	3.071	41.1	1.3	2.40
11V	1.074	3.066	--	--	--
12V	1.208	3.031	--	--	--
$12N_2$	1.219	3.029	40.9	1.3	2.39
$12H_e$	1.228	3.026	40.8	18.2	0.17
13V	1.423	2.982	--	--	--
$13N_2$	1.436	2.980	40.7	1.3	2.25
$13H_e$	1.437	2.980	40.7	19.3	0.15
$14H_e$	1.618	2.943	40.6	19.4	0.15
$14N_2$	1.652	2.937	40.4	1.3	2.21
14V	1.687	2.931	--	--	--
15V	1.840	2.904	--	--	--

Table C.49: Test Results of Pair PSS1516

Run No.	P kPa	T_m °C	ΔT °C	k_s W/mK	Q W	P_g torr	h_j W/m²K
1V	430	221.7	124.1	20.3	22.3	--	366
2V	602	215.5	105.8	20.3	22.9	--	462
3V	727	208.2	90.4	20.2	23.1	--	519
4V	862	204.7	79.7	20.1	23.5	--	600
5V	1008	203.2	72.9	20.1	23.8	--	667
6V	1206	199.1	65.2	20.0	23.9	--	747
7V	1330	194.0	58.1	20.0	23.7	--	830
8V	1577	190.1	51.8	19.9	23.6	--	930
$8N_2$	1594	196.7	19.0	20.0	28.1	40.6	3019
$8H_e$	1623	202.1	13.1	20.1	30.8	40.9	4795
9V	1852	196.7	41.2	20.0	25.7	--	1272
$9N_2$	1854	210.1	18.7	20.2	30.4	40.9	3317
$9H_e$	1861	203.5	12.8	20.1	31.1	40.8	4947
10V	2002	202.3	40.1	20.1	26.8	--	1362
$10N_2$	2036	205.2	18.0	20.1	29.8	40.7	3378
$10H_e$	2057	202.3	12.3	20.1	31.1	40.7	5141
11V	2231	215.6	40.7	20.3	29.5	--	1477
$11N_2$	2252	223.5	18.7	20.4	33.3	40.5	3632
$11H_e$	2256	214.9	12.8	20.3	33.7	40.5	5346
12V	2678	210.3	36.5	20.2	29.0	--	1620

(continued...)

Table C.49: Test Results of Pair PSS1516 (continued...)

Run No.	P kPa	T_m °C	ΔT °C	k_s W/mK	Q W	P_g torr	h_j W/m²K
19V	5826	206.4	18.3	20.2	30.1	--	3362
$19N_2$	5844	217.0	12.2	20.3	33.1	40.9	5524
$19H_e$	5895	214.1	8.7	20.3	34.4	40.8	8015
20V	6251	202.7	17.3	20.1	29.7	--	3495
$20N_2$	6269	212.7	11.6	20.2	32.5	40.7	5692
$20H_e$	6319	209.5	8.4	20.2	33.7	40.8	8138
21V	7155	200.2	14.9	20.1	29.5	--	4032
$21N_2$	7203	213.9	10.9	20.3	32.7	40.8	6085
$21H_e$	7229	213.0	7.8	20.2	34.3	40.8	8900
22V	8031	212.0	14.3	20.2	31.5	--	4487
$22N_2$	8036	244.4	10.4	20.4	34.7	40.9	6811
$22H_e$	8072	214.9	7.2	20.3	34.7	40.9	9756
23V	8725	230.9	14.2	20.5	34.9	--	5024
$23N_2$	8735	225.9	10.0	20.4	35.0	40.8	7160
$23H_e$	8769	227.0	7.4	20.4	37.0	40.8	10154

Table C.49: Test Results of Pair PSS1516 (continued...)

Run No.	P kPa	T_m °C	ΔT °C	k_s W/mK	Q W	P_g torr	h_j W/m²K
$12N_2$	2681	220.0	17.9	20.4	32.8	40.6	3726
$12H_e$	2685	214.4	12.3	20.3	33.7	40.7	5590
13V	3103	210.5	32.0	20.2	29.4	--	1870
$13N_2$	3149	217.7	16.3	20.3	32.6	40.7	4064
$13H_e$	3187	210.8	11.2	20.2	33.3	40.9	6063
14V	3559	219.2	30.3	20.3	30.9	--	2075
$14N_2$	3585	217.0	15.5	20.3	32.6	40.8	4275
$14H_e$	3604	214.6	10.8	20.3	34.0	40.7	6398
15V	4003	206.3	25.8	20.1	29.1	--	2299
$15N_2$	4025	216.9	14.7	20.3	32.6	40.7	4516
$15H_e$	4042	213.5	10.2	20.3	34.0	40.9	6759
16V	4496	207.7	23.2	20.2	29.9	--	2619
$16N_2$	4506	216.0	13.8	20.3	32.7	40.9	4821
$16H_e$	4503	211.7	9.9	20.2	33.8	40.9	6969
17V	4911	208.5	21.8	20.2	30.3	--	2826
$17N_2$	4931	219.0	13.3	20.3	33.3	40.9	5116
$17H_e$	4934	210.4	9.6	20.2	33.5	40.9	7078
18V	5359	207.6	19.9	20.2	30.2	--	3078
$18N_2$	5366	214.8	12.6	20.3	32.6	40.8	5285
$18H_e$	5459	216.1	9.3	20.3	34.5	40.9	7564

(continued...)

Table C.50: Comparison Between Theory and Test Results of Pair PSS1516

Run No.	10^3 P/H_c	10^3 C_j Test	10^3 C_c Theory	10^3 C_g Theory	10^3 C_j Theory	% Diff.
1V	0.181	0.431	0.348	---	0.348	23.8
2V	0.253	0.521	0.479	---	0.479	8.8
3V	0.306	0.617	0.574	---	0.574	7.5
4V	0.363	0.714	0.674	---	0.674	5.9
5V	0.425	0.794	0.782	---	0.782	1.5
6V	0.508	0.893	0.928	---	0.928	- 3.8
7V	0.560	0.995	1.018	---	1.018	- 2.2
8V	0.664	1.119	1.196	---	1.196	- 6.5
$8N_2$	0.671	3.612	1.209	2.184	3.393	6.4
$8H_e$	0.683	5.713	1.230	1.984	3.214	77.7
9V	0.780	1.522	1.394	---	1.394	9.2
$9N_2$	0.781	3.928	1.396	2.206	3.602	9.1
$9H_e$	0.784	5.888	1.401	1.976	3.377	74.4
10V	0.843	1.623	1.501	---	1.501	8.1
$10N_2$	0.857	4.015	1.525	2.215	3.740	7.3
$10H_e$	0.866	6.125	1.540	1.979	3.519	74.0
11V	0.939	1.742	1.664	---	1.664	4.7
$11N_2$	0.948	4.258	1.679	2.222	3.901	9.2
$11H_e$	0.950	6.309	1.682	1.924	3.608	74.9

(continued...)

Table C.50: Comparison Between Theory and Test Results of Pair PSS1516 (continued...)

Run No.	10^3 P/H$_c$	10^3 C$_j$ Test	10^3 C$_c$ Theory	10^3 C$_g$ Theory	10^3 C$_j$ Theory	% Diff.
12V	1.127	1.919	1.978	---	1.978	- 2.9
12N$_2$	1.129	4.380	1.981	2.248	4.230	3.6
12H$_e$	1.130	6.599	1.984	1.937	3.921	68.3
13V	1.307	2.214	2.276	---	2.276	- 2.7
13N$_2$	1.326	4.786	2.308	2.272	4.580	4.5
13H$_e$	1.342	7.176	2.335	1.961	4.296	67.1
14V	1.499	2.441	2.593	---	2.593	- 5.9
14N$_2$	1.510	5.037	2.611	2.294	4.905	2.7
14H$_e$	1.518	7.552	2.625	1.941	4.566	65.4
15V	1.685	2.730	2.899	---	2.899	- 5.8
15N$_2$	1.695	5.322	2.915	2.309	5.223	1.9
15H$_e$	1.702	7.985	2.927	1.955	4.892	63.2
16V	1.893	3.108	3.238	---	3.238	- 4.0
16N$_2$	1.897	5.685	3.245	2.330	5.574	2.0
16H$_e$	1.896	8.243	3.242	1.966	5.208	58.3
17V	2.068	3.352	3.521	---	3.521	- 4.8
17N$_2$	2.076	6.019	3.535	2.342	5.876	2.4
17H$_e$	2.077	8.381	3.536	1.969	5.505	52.2
18V	2.256	3.652	3.825	---	3.825	- 4.5

(continued...)

Table C.50: Comparison Between Theory and Test Results of Pair PSS1516 (continued...)

Run No.	10^3 P/H_c	10^3 C_j Test	10^3 C_c Theory	10^3 C_g Theory	10^3 C_j Theory	% Diff.
$18N_2$	2.259	6.238	3.830	2.355	6.185	0.8
$18H_e$	2.299	8.918	3.893	1.952	5.845	52.6
19V	2.453	3.993	4.141	---	4.141	- 3.6
$19N_2$	2.461	6.508	4.154	2.389	6.522	- 0.2
$19H_e$	2.482	9.464	4.188	1.956	6.143	54.0
20V	2.632	4.162	4.428	---	4.428	- 6.0
$20N_2$	2.640	6.728	4.440	2.377	6.817	- 1.3
$20H_e$	2.661	9.643	4.474	1.975	6.449	49.5
21V	3.013	4.811	5.034	---	5.034	- 4.4
$21N_2$	3.033	7.186	5.066	2.402	7.468	- 3.8
$21H_e$	3.044	10.517	5.084	1.962	7.045	49.3
22V	3.382	5.306	5.618	---	5.618	- 5.6
$22N_2$	3.384	7.980	5.621	2.418	8.039	- 0.7
$22H_e$	3.399	11.513	5.645	1.960	7.605	51.4
23V	3.674	5.859	6.078	---	6.078	- 3.6
$23N_2$	3.678	8.380	6.085	2.429	8.514	- 1.6
$23H_e$	3.692	11.875	6.107	1.914	8.021	48.0

Table C.51: Comparison Between Nitrogen Measured and Predicted Conductances of Pair PSS1516

Run No.	10^3 P/H_c	10^3 C_j Test	10^3 C_c Test	10^3 C_g Test	10^3 C_g Theory	% Diff.
8	0.671	3.612	1.131	2.481	2.184	13.6
9	0.781	3.928	1.524	2.404	2.206	9.0
10	0.857	4.015	1.649	2.366	2.215	6.8
11	0.948	4.258	1.758	2.500	2.222	12.5
12	1.129	4.380	1.923	2.457	2.248	9.3
13	1.326	4.786	2.245	2.541	2.272	11.8
14	1.510	5.037	2.457	2.580	2.294	12.5
15	1.695	5.322	2.745	2.577	2.309	11.6
16	1.897	5.685	3.115	2.570	2.330	10.3
17	2.076	6.019	3.365	2.654	2.342	13.3
18	2.259	6.238	3.657	2.581	2.355	9.6
19	2.461	6.508	4.006	2.502	2.389	4.7
20	2.640	6.728	4.174	2.554	2.377	7.4
21	3.033	7.186	4.842	2.344	2.402	- 2.4
22	3.384	7.980	5.309	2.671	2.418	10.5
23	3.678	8.380	5.865	2.515	2.429	3.5

Table C.52: Comparison Between Helium Measured and Predicted Conductances of Pair PSS1516

Run No.	10^3 P/H_c	10^3 C_j Test	10^3 C_c Test	10^3 C_g Test	10^3 C_g Theory	% Diff.
8	0.683	5.713	1.150	4.563	1.984	130.0
9	0.784	5.888	1.529	4.359	1.976	120.6
10	0.866	6.125	1.665	4.460	1.979	125.4
11	0.950	6.309	1.761	4.548	1.924	136.4
12	1.130	6.599	1.926	4.673	1.937	141.2
13	1.342	7.176	2.271	4.905	1.961	150.1
14	1.518	7.552	2.470	5.082	1.941	161.8
15	1.702	7.985	2.756	5.229	1.955	167.5
16	1.897	8.243	3.112	5.131	1.966	161.0
17	2.077	8.381	3.366	5.015	1.969	154.7
18	2.299	8.918	3.717	5.201	1.952	166.4
19	2.482	9.464	4.038	5.426	1.956	177.4
20	2.661	9.643	4.206	5.437	1.975	175.3
21	3.044	10.517	4.859	5.658	1.962	188.4
22	3.399	11.513	5.332	6.181	1.960	215.4
23	3.692	11.875	5.887	5.988	1.914	212.8

Table C.53: Predicted Helium Accommodation Coefficient Values for Pair PSS1516

Run No.	10^3 C_g Test	Y/σ	k_s W/mK	T_m °C	P_g torr	α_i
8	4.563	3.197	20.1	202.1	40.9	0.67
9	4.359	3.158	20.1	203.5	40.8	0.64
10	4.460	3.129	20.1	202.3	40.7	0.66
11	4.543	3.102	20.3	214.9	40.5	0.67
12	4.673	3.051	20.3	214.4	40.7	0.68
13	4.905	3.000	20.2	210.8	40.9	0.71
14	5.082	2.963	20.3	214.6	40.7	0.73
15	5.229	2.928	20.3	213.5	40.9	0.74
16	5.131	2.895	20.2	211.7	40.9	0.73
17	5.015	2.866	20.2	210.4	40.9	0.71
18	5.201	2.835	20.3	216.1	40.9	0.74
19	5.426	2.811	20.3	214.3	40.8	0.76
20	5.438	2.788	20.2	209.5	40.8	0.76
21	5.658	2.745	20.3	213.0	40.8	0.78
22	6.181	2.710	20.3	214.9	40.9	0.84
23	5.988	2.682	20.4	227.0	40.8	0.82

Table C.54: Geometric and Thermophysical Parameters of Pair PSS1516

Run No.	10^3 P/H_c	Y/σ	P_g torr	M/σ	YH
1V	0.181	3.558	--	--	--
2V	0.253	3.470	--	--	--
3V	0.306	3.419	--	--	--
4V	0.363	3.373	--	--	--
5V	0.425	3.330	--	--	--
6V	0.508	3.280	--	--	--
7V	0.560	3.253	--	--	--
8V	0.664	3.205	--	--	--
$8N_2$	0.671	3.202	40.6	2.0	1.62
$8H_e$	0.683	3.197	40.9	28.3	0.11
9V	0.780	3.159	--	--	--
$9N_2$	0.781	3.159	40.9	2.0	1.56
$9H_e$	0.784	3.158	40.8	28.5	0.11
10V	0.843	3.137	--	--	--
$10N_2$	0.857	3.132	40.7	2.0	1.56
$10H_e$	0.866	3.129	40.7	28.5	0.11
11V	0.939	3.105	--	--	--
$11N_2$	0.948	3.103	40.5	2.1	1.50
$11H_e$	0.950	3.102	40.5	29.7	0.10

(continued...)

Table C.54: Geometric and Thermophysical Parameters of Pair PSS1516 (continued...)

Run No.	10^3 P/H_c	Y/σ	P_g torr	M/σ	YH
12V	1.127	3.052	--	--	--
$12N_2$	1.129	3.051	40.6	2.1	1.50
$12H_e$	1.130	3.051	40.7	29.5	0.10
13V	1.307	3.008	--	--	--
$13N_2$	1.326	3.004	40.7	2.1	1.46
$13H_e$	1.342	3.000	40.9	29.1	0.10
14V	1.499	2.967	--	--	--
$14N_2$	1.510	2.964	40.8	2.1	1.44
$14H_e$	1.518	2.963	40.7	29.5	0.10
15V	1.685	2.931	--	--	--
$15N_2$	1.695	2.929	40.7	2.1	1.43
$15H_e$	1.702	2.928	40.9	29.3	0.10
16V	1.893	2.895	--	--	--
$16N_2$	1.897	2.895	40.9	2.0	1.42
$16H_e$	1.896	2.895	40.9	29.1	0.10
17V	2.068	2.868	--	--	--
$17N_2$	2.076	2.867	40.9	2.1	1.39
$17H_e$	2.077	2.866	40.9	29.0	0.10
18V	2.256	2.841	--	--	--
$18N_2$	2.259	2.840	40.8	2.0	1.39
$18H_e$	2.299	2.835	40.9	29.5	0.10

(continued...)

Table C.54: Geometric and Thermophysical Parameters of Pair PSS1516 (continued...)

Run No.	10^3 P/H_c	Y/σ	P_g torr	M/σ	YH
19V	2.453	2.814	--	--	--
$19N_2$	2.461	2.813	40.9	2.0	1.37
$19H_e$	2.482	2.811	40.8	29.4	0.10
20V	2.632	2.792	--	--	--
$20N_2$	2.640	2.791	40.7	2.0	1.37
$20H_e$	2.661	2.788	40.8	29.0	0.10
21V	3.013	2.749	--	--	--
$21N_2$	3.033	2.746	40.8	2.0	1.35
$21H_e$	3.044	2.745	40.8	29.3	0.09
22V	3.382	2.711	--	--	--
$22N_2$	3.384	2.711	40.9	2.1	1.30
$22H_e$	3.399	2.710	40.9	29.4	0.09
23V	3.674	2.684	--	--	--
$23N_2$	3.678	2.684	40.8	2.1	1.29
$23H_e$	3.692	2.682	40.8	30.5	0.09

APPENDIX D: THERMAL CONDUCTANCE DUE TO RADIATION

If the contacting surfaces are considered as two parallel, gray, plane surfaces, the radiation heat exchange between the two surfaces Q_r is:

$$Q_r = \frac{\sigma_{st} A_a (T_1^4 - T_2^4)}{1/E_1 + 1/E_2 - 1} \tag{D.1}$$

where σ_{st} is Stefan-Boltzmann constant; T_1 and T_2 are the extrapolated temperatures to the contact plane; and E_1 and E_2 are the emissivities of the contacting surfaces. The radiative component of the joint conductance can be written as:

$$h_r = \frac{Q_r/A_a}{\Delta T} = \frac{\sigma_{st}(T_1^4 - T_2^4)}{(1/E_1 + 1/E_2 - 1)(T_1 - T_2)} \tag{D.2}$$

If $T_1 T_2 - T_m^2$ is small, we can write approximately that:

$$T_1^4 - T_2^4 = 4T_m^3(T_1 - T_2) \tag{D.3}$$

where T_m is the joint mean temperature. Thus, Eq.(D.2) becomes:

$$h_r = \frac{4\sigma_{st} T_m^3}{1/E_1 + 1/E_2 - 1} \tag{D.4}$$

Eq.(D.4) shows clearly that the radiation thermal conductance is a function of the joint mean temperature and the emissivities of the contacting surfaces. Assuming $E_1 = E_2 = 0.2$ and $T_m = 414K$ which corresponds to the lowest measured joint conductance value of 185 W/m^2K, then, from Eq.(D.4), h_r is equal to 1.79 W/m^2K. Since this value of h_r is less than 1% of the lowest measured joint conductance, it can be concluded that radiation contribution to the joint conductance, at the temperature levels considered in this work, is negligible.

APPENDIX E: UNCERTAINTY ANALYSIS

E.1 Introduction

The following is a discussion of the analysis made to estimate the maximum uncertainty in the experimental measurements and the theoretical predictions of the joint conductance. It should be mentioned that the accuracy of the measuring system was discussed in detail in Chapter 4 while the procedure and estimation accuracy used for the surface parameters were discussed in Appendix B. Also, the following analysis is based on the procedure described in Ref.[86].

E.2 Uncertainty in the Measured Joint Conductance

The experimental joint conductance, Eq.(2.1), of a particular joint was determined from the estimated heat flux and the temperature drop across the interface. As previously mentioned, the heat flux through the interface was considered to be the mean of the thermal fluxes through the heat meters. The heat loss was less than 5% under vacuum conditions and 10% in a gaseous environment. The estimated uncertainties in the heat flux are, therefore, ±2.5% and ±5% in the vacuum and gaseous tests, respectively.

The uncertainty in the temperature drop across the interface is the result of the uncertainties associated with the thermocouple

readings and the extrapolated temperatures. The thermocouple readings were estimated to be accuracte to ±0.1°C based upon the calibration and the accuracy of the temperature measurement system. The estimated uncertainty in the interface temperature drop by extrapolation of the temperature gradients was approximately ±0.1°C. The overal uncertainty in the temperature drop across the joint is, therefore, ±0.2°C.

The observed maximum temperature drop was as large as 148°C while the minimum value was approximately 5°C. Thus, the fractional uncertainty in the temperature drop could be as small as 0.1% and as much as 4.0%. Using a simple differential error analysis, the estimated uncertainty in the measured joint conductance could be of the order of 4.7% under vacuum conditions, or approximately 6.4% in a gaseous environment. The maximum estimated uncertainty associated with the measurement of the joint conductance for each test is reported in Table E.1.

E.3 Uncertainty in the Contact Conductance Predictions

The uncertainty associated with the prediction of the contact conductance, h_c, is a function of the surface parameters σ and m, contact pressure P, contact hardness H_c, and the material thermal conductivity. For example, the estimated uncertainties in

the Ni200 series parameters are: effective surface roughness ±10%, effective mean absolute slope ±5%, contact hardness ±2.1%, contact pressure ±0.1%, and material thermal conductivity ±2.5%. Using simple differential analysis, the estimated maximum uncertainty in the prediction of the contact conductance is ±11.6%. The estimated maximum uncertainty for the other series of tests are: 11.8% for SS304, 12.4% for Zr-2.5ωt% Nb, and 11.4% for Zr-4. It is important to note that the main contribution to the uncertainty in the predictions is due to the uncertainties in the estimation of the surface parameters σ and m. This emphasizes how crucial the estimates of σ and m are to accurate thermal predictions. It must be pointed out also that the uncertainties in the surface parameters were less than the above specified maximum values for most of the pairs tested.

The estimate of the maximum deviation between the experimental and the theoretical values (overall uncertainty for short) can be obtained from the square root of the sum of the squares of the maximum uncertainties in the measured and predicted contact conductance values. The estimated data uncertainty for each tested pair is reported in Table E.1. However, it must be remembered that the deviation between the experimental and the theoretical values should be considered unsatisfactory if it exceeds the overall uncertainty of a particular test.

Table E.1: Summary of the Maximum Uncertainties Associated with the Measurements and Predictions of Joint Conductance Under Vacuum Conditions

Pair	Measurements	Predictions	Overall
PNI 0102	8.1%	11.6%	14.1%
PNI 0304	4.9%	11.6%	12.6%
PNI 0506	5.0%	11.6%	12.6%
PNI 0708	5.1%	11.6%	12.7%
PNI 0910	3.5%	11.6%	12.1%
PSS 0102	5.7%	11.8%	13.1%
PSS 0304	3.3%	11.8%	12.2%
PSS 0506	3.1%	11.8%	12.2%
PSS 0708	2.9%	11.8%	12.1%
PZN 0102	4.5%	12.4%	13.2%
PZN 0304	3.8%	12.4%	13.0%
PZN 0506	3.0%	12.4%	12.7%
PZN 0708	2.9%	12.4%	12.7%
PZ4 0102	4.7%	11.4%	12.3%
PZ4 0304	3.7%	11.4%	12.0%
PZ4 0506	3.7%	11.4%	12.0%
PZ4 0708	3.1%	11.4%	11.8%
PSS 1112	2.7%	11.8%	12.1%
PSS 1314	2.6%	11.8%	12.1%
PSS 1516	2.9%	11.8%	12.1%

E.4 Uncertainty in the Gap Conductance Predictions

The theoretical prediction of the gap conductance, h_g, is a function of the effective temperature jump distance M, gas conductivity k_g, and the mean plane separation between the surfaces. The gas properties employed in the prediction were compiled from a number of references and assumed to be accurate. However, an estimate of the uncertainty in the gas accommodation coefficient value would be of the order of ±3% since the reported data exhibit some discrepancies. Assuming the contacting surfaces are clean, free of oxides, and foreign films, the uncertainty in the parameter M is estimated to be ±3%, since the uncertainties in the gas pressure and mean temperature are negligible.

For the gas thermal conductivity, the uncertainty is estimated to be ±1% for both Nitrogen and Helium based on the data reported in the literature. Since the uncertainty in the effective surface roughness σ is significantly greater than the uncertainty in the relative contact pressure P/H_c, the uncertainty in σ dominates. Therefore, the estimated uncertainty in the mean plane separation is approximately ±10%.

No explicit analytical function is available for the prediction of the gap conductance, therefore the uncertainty in h_g was determined numerically. From the analysis, the uncertainty in the

prediction of the gap conductance is estimated to be ±10.5%. Thus, the uncertainty in the theoretical joint conductance when the gas is present in the gap is equal to the square root of the sum of the squares of the uncertainties in the predictions of the contact and gap conductances, respectively. For SS304 pairs tested in a gaseous environment, the uncertainty in the theoretical h_j is estimated to be 15.8% at most. The estimated overall uncertainty, i.e., deviation from the theory, for each pair tested in a gaseous environment is reported in Table E.2.

Table E.2: Summary of the Maximum Uncertainties Associated with the Measurements and Predictions of Joint Conductance in Nitrogen and Helium Environments

Pair	Measurements	Predictions	Overall
PSS 0910, N_2	5.7%	15.8%	16.8%
PSS 1112, N_2	5.2%	15.8%	16.6%
PSS 1314, N_2	5.1%	15.8%	16.6%
PSS 1516, N_2	5.4%	15.8%	16.7%
PSS 1112, H_e	5.4%	15.8%	16.7%
PSS 1314, H_e	5.2%	15.8%	16.6%
PSS 1516, H_e	5.7%	15.8%	16.8%